Deposition and characterisation of functional ITO thin films

by

Gaël Giusti

UNIVERSITY OF BIRMINGHAM

A thesis submitted to
The University of Birmingham
for the degree of
Doctor of Philosophy

School of Metallurgy and Materials
The University of Birmingham
May 2011

Abstract

Polycrystalline tin-doped indium oxide (ITO) thin films were prepared by Pulsed Laser Deposition (PLD) with an ITO (In_2O_3-10 wt.% SnO_2) target and deposited on borosilicate glass substrates. By changing independently the thickness, the deposition temperature and the oxygen pressure, a variety of microstructures were deposited.

The impact on thin film physical properties of different gas dynamics is stressed and explained. Films deposited at room temperature (RT) show poorer opto-electrical properties. The same is true for films deposited at low or high oxygen pressure. It is shown that films grown with 1 to 10 mT Oxygen pressure at 200°C show the best compromise in terms of transmittance and resistivity. The influence of the thickness, the substrate temperature and the oxygen pressure on the microstructure and ITO film properties is discussed. A practical application (a Dye Sensitized Solar Cell) is proposed.

Acknowledgements

I would like to acknowledge sincerely to my two Supervisors Prof. Abell and Prof. Jones, for their kindness, excellent explanations and precious suggestions throughout my study but also their sincere support and invaluable help under very special circumstances.

I would also like to express my sincere gratitude to Dr. Bowen for his enlightening ideas and help in ellipsometric and XPS measurements; to Dr. Chu for her patient guidance and help with the FIB; to the staff from Daresbury laboratory for letting me use the impressive SuperSTEM microscope and to Dr. Ramasse for his help performing the EELS measurements and excellent suggestions on data processing; to Dr. Kuznetsov for allowing me to perform electrical measurements at Oxford.

Special thanks are given Dr. Tse and Mr. Stanley for their patience with the TEM sample preparation and SEM respectively, without forgetting Mr. Bradshaw, for his truly incredible technical support during all my experiments.

Special thanks are also given to Dr. Fort, for his kindness and help with correcting the thesis; to Dr. Blackburn for her help and explanations in glancing angle XRD measurements; to Ms. Tian, for her endless support.

Many thanks are given to all staff in School of Metallurgy and Materials and especially to my colleagues of the superconductivity and electron microscopy group, for their help and support duing my Ph.D.

I am very grateful to the EPSRC body and to Prof. Bowen, head of school of Metallurgy and Materials without whom this work would not have been possible.

Lastly, I would like to thank my family and friends for their precious help and encouragements.

Contents

1 Introduction **1**
- 1.1 Semiconductors and Transparent Conducting Oxides . . . 1
- 1.2 Challenges of this project . . . 1
- 1.3 Aims of the project . . . 2
- 1.4 Organisation of the thesis . . . 2

2 Background theory and literature review: ITO thin film deposition, physical properties and microstructure **4**
- 2.1 General background . . . 4
  - 2.1.1 Indium Oxide and Tin-doped Indium Oxide: an overview . . . 4
  - 2.1.2 Indium Oxide and Tin-doped Indium Oxide (ITO) structure . . . 5
- 2.2 Band structure and related electro-optical properties . . . 7
  - 2.2.1 Indium Oxide and ITO band structures . . . 7
  - 2.2.2 Electrical and optical properties of Indium Oxide and ITO . . . 9
    - 2.2.2.1 Electrical properties . . . 9
      - 2.2.2.1.1 General considerations . . . 9
      - 2.2.2.1.2 Scattering mechanisms . . . 10
    - 2.2.2.2 Optical properties . . . 13
      - 2.2.2.2.1 The refractive index and the dielectric constant 13
      - 2.2.2.2.2 UV region . . . 13
      - 2.2.2.2.3 IR region . . . 14
      - 2.2.2.2.4 Visible region . . . 14
- 2.3 Pulsed Laser Deposition . . . 15
  - 2.3.1 Interaction laser/target . . . 15
  - 2.3.2 Interaction laser/evaporated material from the target material . . 16
  - 2.3.3 Expansion of the plume and interaction with the background gas 16
  - 2.3.4 Film growth . . . 18
    - 2.3.4.1 Adsorption and diffusion . . . 18
    - 2.3.4.2 Nucleation and growth . . . 19
      - 2.3.4.2.1 Energetic considerations and supersaturation . 19
      - 2.3.4.2.2 Details of the processes . . . 20
- 2.4 Pulsed Laser Deposition of ITO thin films . . . 21
  - 2.4.1 Substrate temperature . . . 21
  - 2.4.2 Oxygen pressure . . . 22
  - 2.4.3 Film Thickness . . . 24
  - 2.4.4 Stress in thin films . . . 25
    - 2.4.4.1 Thermal stress . . . 25
    - 2.4.4.2 Intrinsic stress . . . 25
  - 2.4.5 Summary . . . 26
- 2.5 ITO by other deposition methods . . . 26
  - 2.5.1 Spray Pyrolysis techniques . . . 26
  - 2.5.2 Sputtering techniques . . . 28
  - 2.5.3 Evaporation techniques . . . 29

2.5.4 Chemical Vapour Deposition (CVD) . . . 29
2.5.5 Sol-gel method . . . 30
2.5.6 Comparison with PLD deposited thin films . . . 31
2.6 Advantages/drawbacks of PLD . . . 31
2.7 Emerging techniques to improve PLD deposition . . . 32
2.7.1 Minimising droplet formation . . . 32
2.7.2 Large-area PLD approaches . . . 33
2.8 Applications of ITO thin films . . . 34

3 EDX/WDX and EELS: background theory and literature review 35
3.1 Energy Dispersive X-Ray microanalysis (EDX) . . . 35
3.1.1 General principles . . . 35
3.1.2 Presentation of the measurement chain . . . 37
3.1.3 Working out the composition . . . 38
3.1.3.1 In the TEM . . . 38
3.1.3.2 In the SEM . . . 39
3.1.3.2.1 Atomic number effect (Z) . . . 39
3.1.3.2.2 Absorption (A) . . . 39
3.1.3.2.3 Fluorescence (F) . . . 40
3.2 Electron Energy-Loss Spectroscopy (EELS) . . . 40
3.2.1 General principles . . . 41
3.2.2 The Electron Energy Loss Spectrum . . . 42
3.2.3 The electron spectrometer . . . 44
3.3 Parameters affecting chemical microanalysis . . . 45
3.3.1 Parameters affecting EDX experiments . . . 45
3.3.1.1 Energy resolution . . . 45
3.3.1.2 Spatial resolution . . . 45
3.3.2 Parameters affecting EELS experiments . . . 46
3.3.2.1 Energy resolution . . . 46
3.3.2.2 Spatial resolution . . . 47
3.3.2.3 Signal-to-noise ratio (SNR) and Signal-to-background ratio (SBR) . . . 47
3.3.2.4 Collection angle . . . 47
3.3.2.5 Deconvolution procedures . . . 48
3.3.2.6 Relativistic effects . . . 48
3.3.3 Parameters affecting both EELS and EDX experiments . . . 49
3.3.3.1 Contamination . . . 49
3.3.3.2 Radiation damage and surface sputtering . . . 50
3.4 Summary of the project . . . 51

4 Experimental method 52
4.1 Pulsed Laser Deposition . . . 52
4.2 X-Ray Diffraction . . . 54
4.2.1 Bragg-Brentano geometry . . . 54
4.2.2 Glancing angle X-Ray Diffraction (GAXRD) . . . 55
4.3 Electron Microscopy . . . 56
4.3.1 Transmission Electron Microscopy (TEM) . . . 56
4.3.1.1 The instrument . . . 56

4.3.1.2 EDX analysis . . . 57
4.3.2 Scanning Electron Microscopy (SEM) . . . 59
4.3.2.1 The instrument . . . 59
4.3.2.2 EDX analysis . . . 60
4.3.2.3 EELS measurements . . . 62
4.3.2.3.1 Measurements at Birmingham . . . 62
4.3.2.3.2 Measurements at Daresbury . . . 64
4.4 Atomic Force Microscopy (AFM) . . . 64
4.5 TEM sample preparation . . . 65
4.6 Electrical measurements . . . 67
4.6.1 Four point probe . . . 67
4.6.2 Hall effect measurements . . . 68
4.7 Optical measurements . . . 70
4.7.1 UV and Visible Spectroscopy . . . 70
4.7.2 Ellipsometry . . . 71
4.7.2.1 The Cauchy model . . . 72
4.7.2.2 The Lorentz model . . . 73
4.8 X-ray photoelectron spectroscopy (XPS) . . . 74

5 **Results** **75**
5.1 Influence of thickness . . . 75
5.1.1 Results from chamber 1 . . . 75
5.1.2 Results from chamber 2 . . . 76
5.1.2.1 Structural property and surface morphology of ITO films deposited by varying the thickness . . . 78
5.1.2.2 Electrical properties of ITO films deposited by varying the thickness . . . 81
5.1.2.3 Optical properties of ITO films deposited for various thicknesses . . . 82
5.1.3 Discussion . . . 83
5.1.3.1 Structural properties . . . 83
5.1.3.2 Electrical properties . . . 84
5.1.3.3 Optical properties . . . 86
5.1.3.4 Optimal thickness . . . 87
5.2 Influence of substrate temperature . . . 87
5.2.1 Electrical properties . . . 87
5.2.1.1 Film microstructure . . . 89
5.2.1.2 Mobility . . . 102
5.2.1.3 Calculations . . . 103
5.2.1.4 Carrier concentration . . . 105
5.2.1.5 Resistivity - Surface resistance . . . 108
5.2.1.6 Summary of the results . . . 110
5.2.1.7 Discussion . . . 110
5.2.1.7.1 Structural properties . . . 110
5.2.1.7.2 Chemistry . . . 113
5.2.1.7.3 Carrier concentration, mobility and resistivity . 114
5.2.1.7.4 Scattering mechanisms . . . 116
5.2.2 Optical properties . . . 118
5.2.2.1 Transmittance and ellipsometric measurements . . . 118
5.2.2.2 Summary of the results . . . 123

5.2.2.3 Discussion . . . 123
5.2.2.4 Optimal substrate temperature . . . 125
5.2.3 Reconciling results from chambers 1 and 2 . . . 126
5.2.3.1 Electrical properties . . . 126
5.2.3.2 Structural properties . . . 127
5.2.3.3 Optical properties . . . 127
5.2.3.4 Summary . . . 128
5.3 Influence of Oxygen pressure . . . 130
5.3.1 Electrical properties . . . 130
5.3.1.1 Film microstructure . . . 131
5.3.1.2 Mobility . . . 141
5.3.1.3 Calculations . . . 142
5.3.1.4 Carrier concentration . . . 144
5.3.1.5 Resistivity - Surface resistance . . . 150
5.3.1.6 Summary of the results . . . 150
5.3.1.7 Discussion . . . 151
5.3.1.7.1 Thickness . . . 151
5.3.1.7.2 Structural properties . . . 151
5.3.1.7.3 Bulk and surface chemistry . . . 152
5.3.1.7.4 Mobility, carrier concentration and resistivity . 155
5.3.1.7.5 Scattering mechanisms . . . 157
5.3.2 Optical properties . . . 159
5.3.2.1 Transmittance and ellipsometric measurements . . . 159
5.3.2.2 Summary of the results . . . 164
5.3.2.3 Discussion . . . 164
5.3.2.4 Optimal oxygen pressure . . . 166
5.3.3 Reconciling chambers 1 and 2 . . . 167
5.3.3.1 Electrical properties . . . 167
5.3.3.2 Structural properties . . . 168
5.3.3.3 Optical properties . . . 169
5.3.3.4 Summary . . . 170

6 Conclusions and future work 172
6.1 Summary . . . 172
6.2 Conclusions . . . 173
6.2.1 Thickness . . . 173
6.2.2 Substrate temperature . . . 174
6.2.3 Oxygen pressure . . . 176
6.2.4 Achievements . . . 177
6.3 Further work . . . 178

A Ellipsometry and EELS: complex refractive index and dielectric function 180
A.1 Method . . . 180
A.2 Ellipsometric data . . . 180
A.3 Low loss EELS data processing of spectra acquired on the SuperSTEM (Daresbury laboratory) . . . 182
A.4 Crystalline and amorphous areas . . . 188
A.5 Results from Birmingham . . . 191
A.6 Discussion . . . 198
A.7 Further work on EELS measurements . . . 200

B One application: Dye-Sensitized Solar Cells 201
B.1 Context and challenges 201
B.2 Principle 202
B.3 Experimental method 204
B.3.1 Resources 204
B.3.2 Preparation of the porous electrode (photoanode) and counter electrode 204
B.3.3 DSSC assembling 206
B.3.4 Characterisation and measurements 207
B.3.4.1 Electrical measurements 207
B.3.4.2 Optical measurements 208
B.4 Summary 209
B.5 Further work on Dye-Sensitized solar cells 209

Bibliography 209

List of Figures

2.1 Indium Oxide structure. 6
2.2 Generic energy-band model for tin doped indium oxide. 8
2.3 Pulsed laser deposition schematic 15
2.4 The three basic modes of thin film growth. 21

3.1 The main mechanism for X-ray production is a consequence of an electron being ejected from an inner shell of an atom by the high energy electron beam. 36
3.2 Typical SEM EDX spectrum in the 0-5 keV range of a 300 nm ITO (In_2O_3:Sn 10 wt.%) thin film. 36
3.3 Schematic of an EDX system on an electron column. 37
3.4 Schematic of an EELS spectrometer (sector magnet type) mounted on a TEM/STEM column. 45
3.5 Definition of the jump ratio of an ionisation edge. 48
3.6 Typical sputtering and displacement energy thresholds (eV) at different accelerating voltages [1]. 51

4.1 The two different PLD set-ups used during the course of the project. . . . 52
4.2 Principle of GAXRD. 55
4.3 Signal generated when a high-energy beam of electrons interacts with a thin specimen. 56
4.4 Scanning Electron Microscope JEOL 7000 at the University of Birmingham. 59
4.5 Monte Carlo modelling of beam trajectories in an In_2O_3 layer with a total thickness 250 nm on a glass substrate at an accelerating voltage of 7 kV. 61
4.6 Monte Carlo modelling of beam trajectories in an In_2O_3 layer with total thickness 350 nm on a glass substrate at an accelerating voltage of 7 kV. 61
4.7 Detected X-ray intensity versus depth for oxygen (K line) at an accelerating voltage of 7 kV. 61
4.8 Atomic Force Microscope principle. 65
4.9 Tripod polisher - South Bay Technology - Model 590 [2]. 66
4.10 Creation of an angle by wedge polishing. 66
4.11 TEM sample preparation: the main steps to make a cross section 67
4.12 Principle of four point probe measurements. 68
4.13 Hall effect principle [3]. 69
4.14 Experimental set-up to determine the sheet resistance [3]. 69
4.15 Hall sample holder used for measurements. 70
4.16 Schematic of a single beam spectrophotometer. 71
4.17 Principle of spectroscopic ellipsometry. 71

5.1 Cross-sectional SEM micrographs of a film grown with 500 pulses (left). 77
5.2 Thickness of ITO thin films deposited in chamber 2 by varying the number of pulses from 500 to 15000; deposition parameters used are listed in Table 5.1. The coefficient correlation R is shown. 77
5.3 XRD patterns of ITO thin films deposited for varying thickness (left); high resolution XRD scan for 2θ=25 - 40° (right). 78

5.4 FWHM of preferred orientation peaks of ITO thin films deposited in chamber 2 and varying thickness from 47 to 1467 nm. 79
5.5 2×2 μm 3-dimensional AFM scans of ITO thin films deposited in chamber 2 by varying the film thickness from 47 to 1467 nm. 80
5.6 RMS roughness of ITO thin films deposited in chamber 2 with varying thickness from 47 to 1467 nm. 80
5.7 Variation of N (left) and μ (right) of ITO thin films deposited in chamber 2 by varying the thickness. 81
5.8 Variation of ρ of ITO thin films deposited in chamber 2 by varying the thickness from 47 to 1467 nm (left). On the right, the variation of ρ with thickness is shown in more detail by omitting the experimental point at t=47 nm. 82
5.9 Optical properties of ITO thin films deposited for varying film thickness in chamber 2. 83
5.10 Average transmittance over the 400 - 1000 nm optical region of ITO thin films deposited with various thicknesses in chamber 2. 83
5.11 Mobility μ versus carrier concentration N of ITO thin films deposited for various film thicknesses. 85
5.12 Variation of thickness (t) with T_s in chamber 1 (black curve) and 2 (blue curve). 89
5.13 XRD patterns of the ITO films deposited at different substrate temperatures in chamber 1. 90
5.14 XRD patterns of the ITO films deposited at different substrate temperatures in chamber 2. 90
5.15 XRD pattern of a bare glass substrate between 2θ=20 and 70°. 91
5.16 XRD pattern in the 25 - 40° region of a sample grown at RT in chamber 1. 91
5.17 Corresponding FWHM of preferred orientation peaks of XRD patterns presented in Figs. 5.13 - 5.14. 91
5.18 Relation between mobility μ and texture quality of ITO thin films grown in chamber 1 (left) and 2 (right). 92
5.19 GAXRD patterns of a sample deposited in chamber 2 at T_s=200°C and P(O_2)=5 mT by varying the incidence angle Ψ from 0.5 to 20°. 93
5.20 Evolution of surface microstructure in chamber 1 observed via low magnification SEM micrographs. 94
5.21 Evolution of surface microstructure in chamber 1 observed by high magnification SEM. 94
5.22 5×5 μm AFM scans of samples grown at (a) RT, (b) T_s=150°C, (c) 175°C, (d) 200°C, (e) 300°C and (f) 400°C at $P_{(O_2)}$=10 mT in chamber 1. . . . 95
5.23 Evolution of surface microstructure in chamber 2 observed by low magnification SEM. The samples were grown at (a) RT, (b) T_s=100°C, (c) 150°C, (d) 200°C, (e) 300°C and (f) 400°C at P(O_2)=10 mT. 96
5.24 Evolution of surface microstructure in chamber 2 observed by high magnification SEM. The samples were grown at (a) RT, (b) T_s=50°C, (c) 150°C, (d) 200°C, (e) 300°C and (f) 400°C at P(O_2)=10 mT. 97
5.25 2×2 μm AFM scans of samples grown at (a) RT, (b) T_s=200°C, (c) 300°C and (d) 400°C at P(O_2)=5 mT in chamber 2. 98
5.26 RMS roughness comparison between samples from chamber 1 (black curve) and 2 (blue curve). 99
5.27 TEM bright-field plan view micrographs of films grown in chamber 1 at (a) T_s=RT, (b) 100°C, (c) 200°C and (d) 400°C. 100

5.28 TEM bright-field plan view micrographs of films grown in chamber 2 at (a) T_s=RT, (b) T_s=200°C and (c) 400°C. 100
5.29 TEM bright-field cross sectional micrographs of films grown in (a) chambers 1 and (b) 2 at T_s=200°C. 101
5.30 TEM bright-field cross sectional micrographs of a film grown at RT in chamber 2. 101
5.31 Variation of μ with T_s. T_s is varied from RT to 400°C. 102
5.32 Calculated mean free path L for ITO thin films grown in chambers 1 (black curve) and 2 (blue curve). 103
5.33 Plot of log(μ) versus 1/T_s for chambers 1 (left) and 2 (right). 104
5.34 Variation of N with T_s when T_s varies from RT to 400°C. 105
5.35 Variation of In/Sn and (In+Sn)/O atomic ratios for chambers 1 and 2 when T_s is varied from RT to 400°C. 106
5.36 STEM EDX linescans. 107
5.37 Variation of ρ (left) and R_s (right) with T_s as T_s is varied from RT to 400°C.109
5.38 Arrhenius plot of log(ρ) versus 1/T_s for chambers 1 and 2. 109
5.39 Relationship between the carrier concentration N and the mobility μ of ITO thin films when T_s varies from RT to 400°C. 117
5.40 Hall mobility μ versus carrier density N for chambers 1 (left) and 2 (right).117
5.41 Transparency in the 400 - 1000 nm region of ITO thin films deposited at varying T_s in chambers 1 and 2. 119
5.42 Transparency in the 275 - 500 nm region for ITO thin films deposited at varying T_s in chambers 1 and 2. 119
5.43 Left: average transparency in the 400 - 1000 nm region of ITO thin films deposited at $T_s's$ from RT to 400°C in chambers 1 and 2. Right: variation of bandgap E_g with T_s. 120
5.44 RMS roughness comparison for chambers 1 and 2. 121
5.45 Variation in the optical bandgap E_g with $N^{2/3}$ in chambers 1 (left) and 2 (right). 122
5.46 Real part of the complex refractive index (n) and extinction coefficient (k) derived from ellipsometric results for ITO films grown at RT, 200 and 400°C in chambers 1 (left) and 2 (right). 122
5.47 Comparison of electrical properties between chambers 1 and 2 in terms. 127
5.48 Comparison between XRD patterns of films grown in chamber 1 (dynamic atmosphere) and 2 (static atmosphere) at four different T_s: RT, 200, 300 and 400°C. 128
5.49 Comparison between chambers 1 and 2 for transmittance over the 300 -1000 nm wavelength range. 129
5.50 Comparison via SEM cross sectional micrographs of the thicknesses of films deposited at $P(O_2)$=0.5 (left) and 50 mT (right) in chamber 2. . . 131
5.51 XRD patterns of ITO films deposited at different oxygen pressures in chamber 1. 132
5.52 XRD patterns of ITO films deposited at different oxygen pressures in chamber 2. 132
5.53 FWHM of preferred orientation (222) (except for red experimental points) peaks as $P(O_2)$ is varied. 133
5.54 Correlation between FWHM and the mobility μ in chambers 1 (left) and 2 (right). T_s was kept at 200°C. The mobility values are taken from the samples corresponding to the X-Ray diffractograms presented in in Figs. 5.51 and 5.52. 133

5.55 Relation between μ and $TC_{(222)}$ - $TC_{(400)}$ in chambers 1 (left) and 2 (right). 134
5.56 Reproducibility of the (222) peak asymmetry for three different samples grown under exact the same conditions. 134
5.57 GAXRD patterns performed on a film grown at $P(O_2)$=20 (left) and 30 mT (right). 135
5.58 Multi peak fitting of the GAXRD peak asymmetry for films grown at $P(O_2)$=20 mT and T_s=200°C in chamber 2. 135
5.59 Low magnification SEM micrographs of samples grown at (a) $P(O_2)$=1 mT, (b) 5 mT, (c) 10 mT, (d) 20 mT, (e) 30 mT, (f) 40 mT and (g) 50 mT in chamber 1. 136
5.60 Low magnification SEM micrographs of samples grown at (a) $P(O_2)$=0.2 mT, (b) 0.5 mT, (c) 1 mT, (d) 5 mT, (e) 50 mT and (f) 70 mT in chamber 2.137
5.61 High magnification SEM micrographs showing the change of surface microstructure at (a) $P(O_2)$=1 mT, (b) 5 mT, (c) 10 mT, (d) 20 mT, (e) 30 mT, (f) 40 mT and (g) 50 mT. 138
5.62 High magnification SEM micrographs showing the surface microstructure evolution at (a) $P(O_2)$=0.2 mT, (b) 0.5 mT, (c) 5 mT, (d) 50 mT and 70 mT (f). 139
5.63 AFM images showing the surface microstructure evolution at (a) $P(O_2)$=1 mT, (b) 10 mT, (c) 30 mT and (d) 50 mT. 139
5.64 AFM images showing the change of surface microstructure evolution at (a) $P(O_2)$=0.2 mT, (b) 5 mT, (c) 20 mT, (d) 30 mT, (f) 50 mT and (g) 70 mT. 140
5.65 RMS roughness of ITO thin films deposited at various oxygen pressures in chambers 1 (black curve) and 2 (blue curve). 141
5.66 Mobility (μ) variation for films grown in chambers 1 and 2 versus $P(O_2)$. 142
5.67 Calculated mean free paths of free carriers for films grown at various $P(O_2)$ in chambers 1 and 2 based on a highly degenerate free electron gas model [4]. 142
5.68 Mean free path versus $P(O_2)$ according to the empirical formula proposed by Mergel et al. [5]. 143
5.69 Carrier concentration (N) variation for chambers 1 and 2 with $P(O_2)$. . . 144
5.70 Dependence on $P(O_2)$ of N. 145
5.71 In/Sn (left) and (In+Sn)/O (right) atomic ratios for chambers 1 and 2 obtained by EDX SEM as $P(O_2)$ is varied from 1 to 50 mT (chamber 1) and 0.2 to 70 mT (chamber 2). 146
5.72 XPS survey of the In, Sn and O peaks for ITO thin films grown in chamber 2.147
5.73 XPS of a sample grown in chamber 2 at $P(O_2)$=0.2 mT. 148
5.74 Evolution of the position of the (222) peak as $P(O_2)$ varies from 0.2 to 7.5 mT (left). 149
5.75 Resistivity (ρ) (left) and surface resistance (R_s) (right) versus $P(O_2)$ for chambers 1 and 2. 150
5.76 Relation between the mobility μ and the carrier concentration N in chambers 1 (left) and 2 (right). 158
5.77 Ionised impurity scattering model developed by Dingle et al. [6] (red and green curves) and comparison with experimental data (blue triangles) in chambers 1 (left) and 2 (right). 158
5.78 Transparency of ITO thin films deposited with varying $P(O_2)$ in chambers 1 (left) and 2 (right). 160

5.79 Variation of the absorption edge in chambers (left) 1 and 2 (right) with $P(O_2)$. 161
5.80 Average transmittance over the 400 - 1000 nm range of ITO thin films deposited at various oxygen pressures in chamber 1 and 2. 161
5.81 Optical bandgap variation of ITO thin films deposited at various oxygen pressures in chambers 1 (black curve) and 2 (blue curve). 162
5.82 Variation in the optical band gap with carrier concentration $N^{2/3}$ in chambers 1 (left) and 2 (right), showing the Burstein-Moss shift in ITO thin films. 162
5.83 Refractive index n (left) and complex coefficient k (right) derived from ellipsometric measurements using a Cauchy model for ITO films grown at 0.2, 1, 5, 20, 50 and 70 mT. 163
5.84 Comparison of the mobility μ , carrier concentration N and resistivity ρ for films from chambers 1 and 2. 168
5.85 XRD pattern comparison for samples grown at T_s=200°C in chambers 1 and 2. 169
5.86 Optical properties comparison in the 250 - 1000 nm range of films grown in chamber 1 and 2 when chamber 2 is operated under a static atmosphere.170

A.1 The real (ε_1) and the imaginary (ε_2) parts of the dielectric function derived from ellipsometric results for ITO films grown at RT, 200 and 400°C in chambers 1 (left) and 2 (right). 181
A.2 The real (ε_1) and the imaginary (ε_2) parts of the dielectric function derived from ellipsometric results for ITO films grown at RT in chamber 2 using the Lorentz model. 182
A.3 HAADF micrographs showing where the line scans were taken from four different regions. 183
A.4 Illustration of how to choose the fitting window for a spectrum acquired in region 1. 185
A.5 Illustration of ZLP loss peak removal from a spectrum acquired from a crystalline area. 186
A.6 Raw EELS signal corresponding to region 2 (crystalline) over the 0 - 10 eV range. 188
A.7 Raw EELS signal corresponding to region 3 (amorphous) over the 0 - 10 eV range. 189
A.8 Raw EELS signal corresponding to region 4 (amorphous) over the 0 - 10 eV range. 189
A.9 Kramers-Kronig analysis results (ε_1 and ε_2) from spectra acquired from regions 1 and 2 (crystalline) and regions 3 and 4 (amorphous) and a comparison with the ellipsometric results (Cauchy and Lorentz models). 190
A.10 Kramers-Kronig analysis results (transmittance) from spectra acquired from regions 1 and 2 (crystalline) and regions 3 and 4 (amorphous) and a comparison with spectrophotometry results. 190
A.11 ZLP loss peak removal from a spectrum acquired with an acceptance angle of 4.2 mrads. 193
A.12 Signal extracted after removal of the ZLP tail of the spectra presented in Fig. A.11. 193
A.19 Reproducibility of the EELS removal procedure illustrated over the 0 - 10 eV region for 6 spectra taken from 6 different regions (1...6). 194

A.20 Summary of the SSD obtained after extrapolation and removal of the ZLP tails from the low-loss EELS signal via a power-law function. 195
A.21 KKA analysis results in terms of dielectric data (ε_1, ε_2) for the 6 SSD spectra presented in Fig. A.20. 196
A.22 KKA analysis results in terms of optical data (transmittance) of the 6 spectra presented in Fig. A.19. 196
A.23 Comparison of EELS and ellipsometric measurements (Cauchy and Lorentz models) over the 1-10 eV range for ε_1 (left) and ε_2 (right). 197
A.24 Comparison between ε_1 (left) and ε_2 (right) obtained after Kramers-Kronig analysis of SSD acquired in Birmingham and in Daresbury. 197

B.1 Schematic of dye sensitized solar cell. Taken from Smestad [7]. 202
B.2 Electron injection and regeneration reaction. Instead of TiO_2 nanocrystals, a porous ITO layer was used in this work. 203
B.3 Plan view SEM micrograph showing the surface microstructure of the porous ITO (left). Cross-sectional SEM micrograph of the same porous ITO/photoanode showing the 284 nm thick conductive ITO thin film on top of which a 1062 nm porous ITO layer was deposited (right). 205
B.4 Plan view SEM micrographs showing the surface microstructure of the porous ITO electrode at two different N_2/O_2 pressure ratios: 140 (left) and 700 (right). 206
B.5 Schematic of how the two electrodes are arranged in the built DSSCs. Two contacts (+ and -) are formed and covered with Ag paint. 207
B.6 Electrical characterisation set-up for the two assembled cells. Cell 1 is on the left while cell 2 is on the right. 208
B.7 Transmittance of cell 1 (left) and 2 (right) over the 300 - 1000 nm wavelength range. 208

List of Tables

2.1 Summary of ITO thin film electro-optical properties deposited by PLD by different authors. 27
2.2 Comparison of different deposition techniques with PLD. 31

4.1 Experimental differences between chamber 1 and 2. “Bottom” refers to the bottom of the deposition chamber where pumping takes place. . . . 53
4.2 Optimal conditions used in chambers 1 and 2. Conditions from previous work [8] are also shown. 53
4.3 Conditions used in acquiring EDX spectra in STEM mode. 57
4.4 In_2O_3 and SnO_2 nanopowder characteristics used as standard specimens. 58
4.5 k(Sn) and k(O) sensitivity factors measured from EDX spectra generated from In_2O_3 and SnO_2 nanopowder specimens. 59
4.6 Experimental conditions used acquiring low-loss spectra in conventional diffraction mode. 64

5.1 Summary of ITO growth parameters by varying the number of pulses . . 76
5.2 Summary of ITO growth parameters by varying number of pulses 76
5.3 Summary of fitted and measured thicknesses for samples deposited in chamber 1 between RT and 400°C. 5000 pulses were fired. 88
5.4 Summary of fitted and measured thicknesses for samples deposited in chamber 2 between RT and 400°C. 5000 pulses were fired. 88
5.5 Average grain size (nm) at T_s= RT, 100°C, 200°C, 300°C and 400°C in chambers 1 and 2. 102
5.6 Generation of free carriers for ITO thin films grown in chambers 1 and 2. 106
5.7 Summary of In/Sn and (In+Sn)/O atomic ratios obtained from the three five point line scans shown in Fig. 5.36). 108
5.8 Summary of ITO growth parameters in chamber 2. $P(O_2)$ was kept at 10 mT. 126
5.9 Summary of ITO growth parameters when varying $P(O_2)$. 131
5.10 Average grain size as $P(O_2)$ is varied from 1 to 50 mT and from 0.2 to 70 mT in chambers 1 and 2 respectively. 141
5.11 Variation with $P(O_2)$ in chamber 2 of the In/Sn and (In+Sn)/O atomic ratios given by XPS. 148
5.12 Summary of ITO growth parameters by varying $P(O_2)$ in chamber 2. T_s was kept at 200°C. 167

A.1 Summary of the chosen fitting windows from region 1 to 4. Relative and absolute thicknesses are specified. 189
A.2 Fitting windows used to derive the spectra presented in Fig. A.19. 195

B.1 Growth conditions used for manufacturing the photoanode in chamber 2. 205

List of symbols, abbreviations and notations

Symbols:

c: speed of light
N: carrier concentration
μ: mobility
R_s: surface resistance
σ: conductivity
ρ: resistivity
ε: dielectric function
ε_∞: high frequency dielectric constant
E_g: band-gap energy
λ_p: plasma wavelength
n: refractive index
k: extinction coefficient

Abbreviations:

TCO: transparent conducting oxide
AFM: atomic force microscopy
ITO: indium tin oxide
LCD: liquid crystal display
FPD: flat panel display
OLED: organic light emitting diode
PLD: pulsed laser deposition
RT: room temperature
SEM: Scanning electron microscopy/microscope
TEM: Transmission electron microscopy/microscope
T-S distance: target to substrate distance
IR: InfraRed
XRD: X-Day Diffraction
UV: UltraViolet
MCA: Multi Channel Analyser
CMP: Chemical Mechanical Polishing
BF: bright field
MFP: mean free path
IMFP: inelastic mean free path
XPS: X-Ray Photolectron spectroscopy
GAXRD: glancing angle X-Ray diffraction
EELS: Electron Energy Loss Spectroscopy
KKA: Kramers-Kronig analysis

Kröger-Vink notation:

$V_{\ddot{O}}$: an oxygen vacancy, with a doubly positive charge.
$e^{'}$: an electron. A site isn't normally specified.
O_o^x: an oxygen ion sitting on an oxygen lattice site, with neutral charge.

Chapter 1

Introduction

1.1 Semiconductors and Transparent Conducting Oxides

A transparent conducting oxide is a semiconducting material combining high conductivity and optical transparency. Within the transparent conducting oxides category, Indium Tin Oxide (ITO) is still the most widely used. Today, it has reached the industrial level mainly via the use of the magnetron sputtering deposition process. Nonetheless, Pulsed Laser Deposition (PLD) presents some unique advantages over magnetron sputtering, which make this technique particularly suitable in the processing of some opto-electronic devices.

The physical characteristics of semiconductors are determined both by the properties of the host crystal and by the presence of impurities and crystalline defects. Dopant impurities, which typically substitute for a host crystal atom, introduce electronic states in the bandgap close to the valence and conduction band edges and thus determine the type and conductivity of the material. These so-called shallow level defects enable a wide range of semiconductor properties. However, crystal lattice defects and other impurities, which introduce electronic states deeper in the bandgap and are referred to as deep level defects, also modify the properties of the semiconductor and thus may make a semiconductor unsuitable for its intended applications. It is then necessary to control carefully the deposition process to adjust the required properties.

1.2 Challenges of this project

The electrical and optical properties of ITO are interrelated and can be tailored to suit a whole range of applications. Obtaining metallic high conductivity means sacrificing optical properties. Moreover, ITO films are extremely sensitive to crystallinity and microstructure. Never-ending demands from technological applications for better quality electronic materials exhibiting higher performance limits involve a deep understanding of the structure (phases, stoichiometry, crystallinity) and morphology (grain size, texture,

roughness) since they determine the mechanical, electrical and optical properties of thin polycrystalline ITO films. This microstructure is itself quite sensitive to the deposition conditions. Controlling the latter is essential to produce films for a given application.

Nonetheless, few studies exist of the crystallisation and growth process of ITO deposited by PLD and above all of the link between microstructure and the observed physical properties. And yet, understanding this link is indispensable to growing high quality thin films.

Several challenges have to be addressed:

1. Careful control of the deposition conditions.
2. Understanding very different microstructures.
3. Making the link between those microstructures and the physical properties.

1.3 Aims of the project

The two main goals of this study are to understand and control:

1. the dependence of microstructure on PLD processing parameters
2. the dependence of the physical properties on the microstructure in order to produce high quality ITO thin films

1.4 Organisation of the thesis

Chapter 2 gives the background theory of ITO and its associated electro-optical properties. The pulsed laser deposition technique is also detailed and explained. A literature review of ITO deposition by PLD and other methods is given and they are compared. The physical properties of pulsed laser deposited ITO thin films are compared with those from other deposition methods. The last section of this chapter gives background theory on thin film deposition (nucleation and growth) and the resulting microstructures.

Chapter 3 focuses on chemical microanalysis. It provides background theory for EDX and EELS.

Chapter 4 contains experimental methods. Machines, methods and procedures will be detailed: for example, ITO thin film deposition, electro-optical measurements and TEM sample preparation.

Chapter 5 contains experimental results for the ITO films. The effects of the thickness (t), the substrate temperature (T_s) and the oxygen pressure ($P(O_2)$) on the conductivity and optical transparency of the films are described and discussed. Microstructural arguments are used to explain changes in physical properties.

Chapter 6 concludes the thesis. The main findings of this project are summarised. The future work which needs to be done is described.

Appendix A presents macro and nanoscale dielectric constant measurements performed on ITO thin films via ellipsometry and EELS respectively, while appendix B describes a practical application: a dye-sensitized solar cell. Its electrodes are made from the best ITO thin film obtained during this study.

Chapter 2

Background theory and literature review: ITO thin film deposition, physical properties and microstructure

2.1 General background

2.1.1 Indium Oxide and Tin-doped Indium Oxide: an overview

Indium Oxide and Indium Tin Oxide (ITO) are metal oxides. They are electrically conductive, even though band theory predicts them to have wide band gaps. This behaviour defines the materials class of "Transparent Conducting Oxides" which includes tin dioxide (SnO_2), especially doped with antimony or fluorine, doped/undoped indium oxide, in particular doped with tin, cadmium oxide, cadmium stannate and doped/undoped zinc oxide. They have large band gaps in the ultraviolet and are transparent over the visible range. Yet, the Fermi level is in (or very close to) the conduction band due to free-carrier producing centres.

Indium Oxide is a direct wide band gap ($>$ 3.5 eV) n-type semiconductor which makes the transmission window between wavelengths 300 nm and 1500 nm, depending on the processing conditions. At short wavelengths (high energies - UV range) electron interband transitions from the valence to unoccupied states in the conduction band limit the transmission up to the band gap. For long wavelengths (low energies - IR range), light is reflected because of the quasi-free electron plasma. Thus, the wavelength cutoff in the IR depends on the charge carrier density. An indirect band of of 2.62 eV has been calculated by Weiher et al. [9] but is not widely reported in the literature.

This carrier density is related to the oxygen stoichiometry, where, in the ideal case, each doubly charged oxygen vacancy contributes two free electrons and to the doping element when the latter is present. These defects create an impurity band that overlaps the conduction band, thereby creating a "degenerate" semiconductor (i.e. its behaviour

approximates that (semi-)metals. Increasing the carrier density also leads to a widening of the band gap known as the Burstein-Moss effect. This effect competes with many body effects (electron-electron interactions) which tend to decrease the band gap. However, it is a double edged sword: doubly charged O vacancies and singly charged Sn on an In site reduce the mobility of charge carriers via ionised impurity scattering. In addition, oxygen vacancies play an important role in all processes related to solid-state diffusion, including recrystallization, grain growth, sintering and phase transformations. They are electrically charged and can be associated with dopant atoms to form neutral or charged complexes.

To summarise, these oxide films are electrically conductive and act optically as a selective transmitting layer, being transparent to visible light and reflective of thermal infrared radiation.

2.1.2 Indium Oxide and Tin-doped Indium Oxide (ITO) structure

The indium oxide (In_2O_3) and the ITO structure are closely related. In_2O_3 is an ionically bound semiconducting oxide. During its synthesis, point defects are formed relatively easily, compared with covalently bonded materials. These defects consist mainly of oxygen vacancies and interstitial indium atoms [10]. The same authors found that these defects are pressure dependent ($P(O_2^x)$) where x=-0.166 and -0.1875 for oxygen vacancies and indium interstitals respectively. It is worth mentioning that these two values are derived from a model assuming a parabolic conduction band and non-degeneracy of the carrier concentration. These vacancies and interstitials are electrically charged, making ionized impurity scattering unavoidable in Indium Oxide and ITO. Indium oxide crystallizes in a cubic bixbyite-type structure with a space group Ia3 [11] and a lattice parameter of 10.118 nm. The unit cell contains 80 atoms. 32 sites are occupied by cations at two types of non-equivalent six-fold coordinated site. One quarter of the cations is located on trigonally compressed octahedral sites, referred to as b sites, while the remaining three quarters are located on highly distorted octahedral d sites. The two different six-fold coordinated sites are called ”b” and ”d”, according to international notation [12]. Indium atoms, on both b and d sites, reside at the centre of a distorted cube with the six corners occupied by oxygen atoms, while the remaining two corners are empty. In the case of the b sites, oxygen vacancies are located along the body diagonal; for the d site they are located along a face diagonal. A schematic representation of the structure including “b” and “d” sites is given in Fig. 2.1.

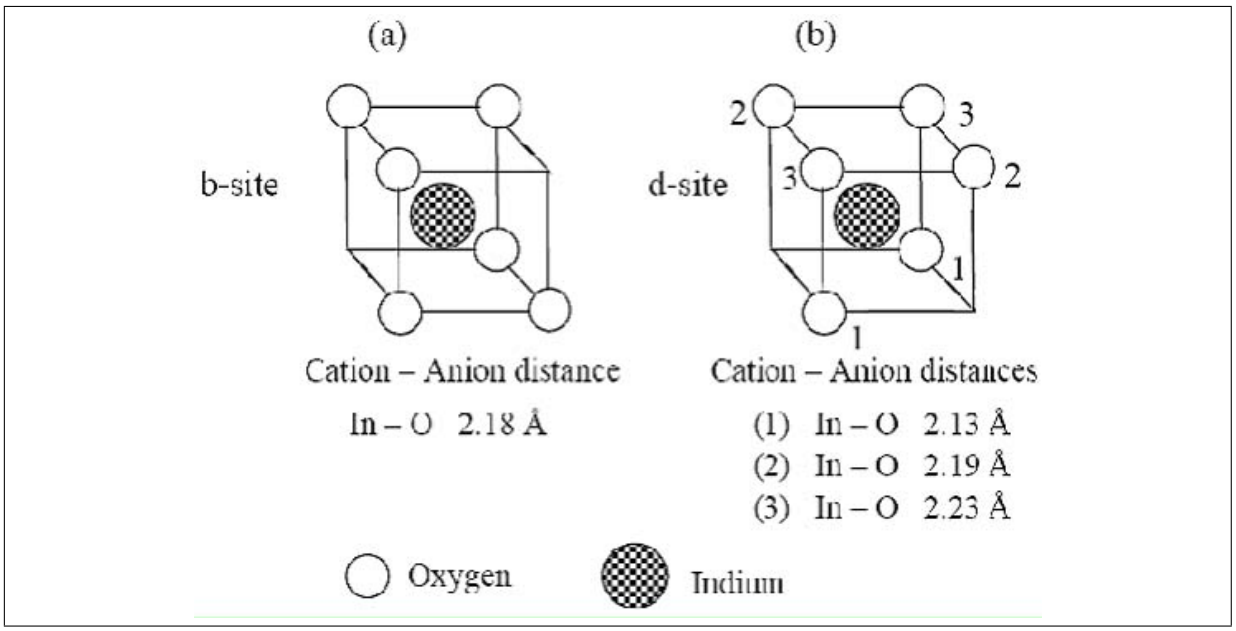

Figure 2.1 Indium Oxide structure - (a) Eight oxygen atoms are situated within compressed octahedra (b site) and have six equidistant oxygen atom neighbours at 2.18 $\mathring{A}$. (b) Eight Indium atoms are situated at the corners of a highly distorted octahedron (d site). For these Indium atoms, there are three possible cation-oxygen distances: 2.13, 2.19 and 2.23 $\mathring{A}$ [11].

Indium Oxide contains intrinsic oxygen vacancies: via in-situ electrical property measurements, De Wit [10] concluded that In_2O_3 is an anion-deficient n-type conductor where the oxygen vacancy population (about 1%) limits the electron concentration. This deficiency persists even under equilibrium growth conditions, at high-temperature. With tin doping a charge imbalance is created due to the different valences of indium and tin. The charge imbalance can be compensated by incorporation of interstitial oxygen atoms or/and oxygen vacancies. Tin cations and interstitial oxygen anions can form cluster defects (charged or not). Frank et al. [13] proposed the existence of such defects rather than isolated point defects in order to explain the conductivity of ITO. These clusters of defects can be overall positive, negative or neutral depending on their stoichiometry. In their work, a defect model is presented in which interstitial and associated Sn-oxide defect complexes such as $[Sn_2O_i^{''}][Sn_2O_4]^x$, depending on the Sn content, are presented. This model does not involve other defects than Sn and interstitial oxygen even if interstitial indium atoms have been discussed in the literature [14][15].

2.2 Band structure and related electro-optical properties

Indium oxide and ITO are most of the time used as thin films. Therefore, in the following sections, the properties of indium oxide and ITO thin films will be detailed.

2.2.1 Indium Oxide and ITO band structures

It is generally accepted, despite the observed high sensitivity of its properties to processing conditions [16], that the electronic band structure is one of the most important factors for understanding the unique interplay between optical and electrical properties in TCOs. Most of the interesting TCO properties are predetermined and can be described satisfactorily on the microscopic level only on the basis of a suficiently detailed and reliable model of the electronic band structure. The plot of electron wave vector against electron energy is called a band structure diagram. The band structure is directly related to the crystal and defect structure of the material. The band structure of indium oxide and above all ITO is extremely complicated to model because of the complexity of the lattice structure and electronic interactions in these compounds. Therefore, the properties are usually discussed in terms of an assumed band structure consisting of an isotropic parabolic condution band [17].

Fan and Goodenough [18] were the first to publish a schematic energy band model for pure indium oxide and ITO (see Fig. 2.2) on the basis of their Electron Spectroscopy for Chemical Analysis (ESCA)/XPS measurements. Even if this band model is largely simplified, it is still the only one allowing a qualitative explanation of the observed concurrent high optical transparency and electrical conductivity in ITO . The only attempt for a similar material structure was based on Eu_2O_3 [19]. This band model exhibits a wide direct band gap (3.5 eV) accounting for the high transmission in the visible range. The conduction band was proposed to be mainly from indium 5s electrons and the valence band from oxygen 2p electrons. The Fermi energy E_f is very close from the conduction band (a few tens of eV).

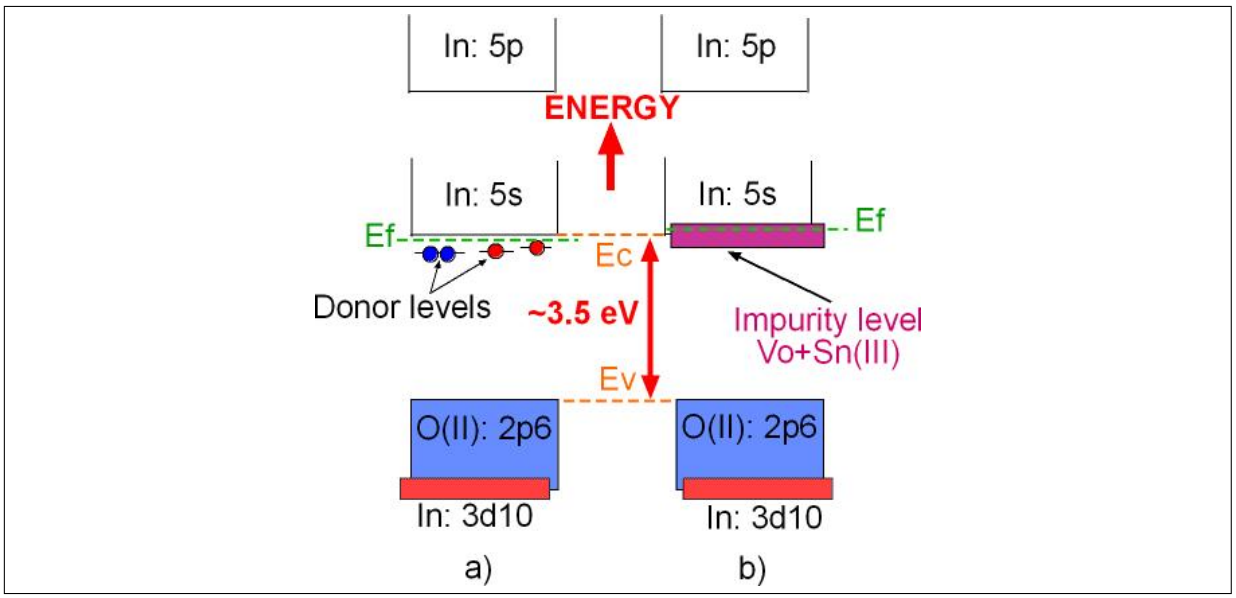

Figure 2.2 Schematic energy-band model for tin doped indium oxide according to [18]. a) Low doping level b) High doping level.

Regarding ITO, the situation is sightly different: a low doping level results in a low density of donor atoms. Under these conditions, donor states are formed just below the conduction band, and the Fermi energy lies between the donor level and the conduction band minimum. However, for very high doping, the donor density increases. The donor states merge with the conduction band at a certain "critical" density n_c. This is the Mott critical density and is defined as: $\frac{{n_c}^{1/3}}{{a_0}^*} = 0.25$ where the effective Bohr radius a_0 is about 1.3 nm for In_2O_3. Therefore,n_c(ITO)=3.43×10^{-19}cm^{-3}. Above the critical Mott density [20], the impurities and the associated electrons occupy the bottom of the conduction band in the form of an electron gas. The material is said to be "degenerate". Electrons present at the lowest states ofthe conduction band prevent or "block" these states resulting in a band gap widening known as the Burstein-Moss shift [21].

The ITO band structure and its relation with the electro-optical properties can be summarized as follows:

1. ITO exhibits a wide direct optical band gap (at least 3.5 eV) prohibiting interband transitions in the visible range and hence making it transparent within this range.
2. Intrinsic dopants (oxygen deficiency) or extrinsic dopants (Sn) donate electrons into the conduction band (n doping - creation of donor level states below the conduction band).
3. A large internal gap in the conduction band prohibits inter-conduction band absorption of photons in the visible range [22].

2.2.2 Electrical and optical properties of Indium Oxide and ITO

2.2.2.1 Electrical properties

2.2.2.1.1 General considerations Transport in polycrystalline semiconductors is much more complex than that in single crystals [23]. In_2O_3 or ITO films consist of amorphous or crystalline phases or a mix of both. Polycrystalline films, which generally display better electro-optical properties than amorphous ones, result when the films are deposited on heated substrates or after annealing of the amorphous films. In ITO films, the presence of Sn lowers the resistivity if thermally "activated", i.e., diffusion of Sn from grain boundaries and/or interstitials to effectively substitute In on an In site. This process adds extra free electrons to the conduction band [24] [25] [26]. However, for RT deposited ITO films, Sn is not efficiently "activated" resulting in generally higher resistivity at lower substrate temperatures compared to In_2O_3 thin films as it can act as an additional scattering centre.

Electrical conductivity (σ) depends on the concentration (N) and mobility (μ) of free carriers as follows:

$$\sigma = N \times \mu \times e \tag{2.1}$$

where e is the electron charge. In order to obtain films with high conductivity, high carrier concentration and mobility should be simultaneously realised. Indium oxide behaves as an insulator in its stoichiometric form, but if prepared in its oxygen-decient form, it can reach high n-type doping levels ($\sim 10^{19}$cm^{-3}) as a result of intrinsic defects (O vacancies). On the contrary, under reducing conditions, oxygen is lost. It is convenient to use the Kröger-Vink notation (see section) when describing In_2O_3/ITO. In_2O_3 can be written as $In_2O_{3-x}(V_{\ddot{O}})_x e'_{2x}$ with x$\sim$0.01. The creation of oxygen vacancies contributes two free electrons to the matrix: $O_o^x \rightarrow \frac{1}{2}O_2(g) + V_o^{\cdot\cdot} + 2e'$. As a consequence, a variety of electrical properties can be obtained: metallic, semiconducting, or insulating behaviour depending on the stoichiometry, without any further impurity doping [27].

Efforts were then made to lower the resistivity by doping and particularly by tin doping. Most of these efforts directed at improving the conductivity of the material have been focused on increasing the effective number of free carriers N (electrons) via tin doping. TCOs have to be doped to a carrier concentration of up to $10^{21} cm^{-3}$ in order to achieve low resistivities ($\rho < 5 \times 10^{-4} \Omega$ cm) [24]. This means that these semiconductors

are degenerately-doped, leading to a Fermi level position within the conduction band. Although this method had some success, it is also self-limiting. As the dopant atoms occupy random In sites in the host lattice, the process of doping certainly impairs the mobility while increasing nN. Hence, obtaining the lowest possible resistivity is a trade-off between carrier concentration and electron mobility. When adding small amounts of Sn to In_2O_3, and if the right conditions are met, the Sn atoms enter substitutionally into the cation sublattice. Since Sn has one valence electron more than indium, a Sn atom substituting for an In atom will be expected to donate one free extra electron to ITO. Incorporation of Sn^{2+} has not been proved by experiments [28] but it is believed to operate [29] [30]. For high Sn content (>12 at.%), complexes and precipitates may form, distorting the lattice and/or adding scattering centres. Carrier generation in ITO is somewhat less efficient than that observed in group IV semiconductors. In TCOs, the chemical dopant concentration is generally much higher than in other typical semiconductors (Si, GaAs etc.), easily reaching 10 wt.% owing to the low doping efficiency of Sn: 10% and 20% only for ITO thin films with 1.9 and 6.7 wt.% SnO_2 respectively [31]. Therefore, the concentration of impurities in the host indium oxide crystal tends to be higher than in other typical semiconductors.

2.2.2.1.2 Scattering mechanisms In order to fully explain the electrical properties of indium oxide and ITO, it is necessary to consider the different mechanisms at play for scattering of electrons. There are several of them:

1. Lattice scattering
2. Ionised impurity scattering
3. Dislocation scattering
4. Grain boundary scattering
5. Neutral impurity scattering

The total mobility can therefore be written as:

$$\frac{1}{\mu_{tot}} = \sum_i \frac{1}{\mu_i} \tag{2.2}$$

The one mechanism that will certainly operate is scattering of the electrons by the ionised impurities which must be present in order to preserve charge neutrality in indium oxide and ITO [32]. This scattering is caused by ionised dopant atoms/clusters and dominates for free carrier concentrations above about $10^{20} cm^{-3}$ owing to the inherently high oxygen vacancy density when depositing in low oxygen environment. The scattering of conduction electrons by ionised impurities has been extensively treated in the Born

scattering approximation by Brooks and Dingle [6]. This model was refined later by Moore [33] and Pisarkiewicz et al. [34]. For high charge carrier densities (degenerate semiconductors),

$$\mu_I = \frac{3(\varepsilon_0\varepsilon_r)^2 h^3 N}{e^3 m^{*2} F(\zeta_d) Z^2 N_i} \tag{2.3}$$

with

$$\zeta_d = \frac{(3\pi^2)^{1/3}\varepsilon_0\varepsilon_r h^2 N^{1/3}}{m^* e^2} \tag{2.4}$$

The screening function F(ζ_d) is given by:

$$F(\zeta_d) = ln(1+\zeta_d) - \frac{\zeta_d}{1+\zeta_d} \tag{2.5}$$

The symbols ε_0, h and e are the dielectric constant in vacuum, Planck's constant and the charge of an electron. ε_r and m^* are the low-frequency relative permittivity and the effective mass of the conduction electrons. N is the carrier density, Z and N_i are the charge and density of the charged scattering centres, respectively. It is also worth mentioning that the theoretical model given above is based on the assumption of a statistically homogeneous distribution of scattering centres (vacancies, dopants etc.) and conduction band parabolicity.

Neutral impurity scattering operates as well. Its origins have been presumed to be two different kinds of crystallographic faults: point defect aggregates which were observed by Transmission Electron Microscopy (TEM) as locally strained small areas and supposed to be a low-grade oxide of In_2O_3 (In_2O_{3-x}) [35] or associated Sn-oxide defect complexes such as ($(Sn_2^{\cdot}O_i^{''})(Sn_2O_4)^x$) which do not contribute to the increase in electron concentration [13]. This scattering gives rise to a mobility μ_N expressed as [36]:

$$\mu_N = \frac{m^* e^3}{20\varepsilon_0\varepsilon_r \hbar^3 N_n} \tag{2.6}$$

where N_n is the concentration of neutral impurities. The symbols ε_0, $\hbar$ and e are the dielectric constant in vacuum, Planck's constant and the charge of an electron. ε_r and m^* are the low-frequency relative permittivity and the effective mass of the conduction electrons.

Scattering by grain boundaries plays a subordinate role if the mean-free path length (L) of electrons in indium oxide and ITO is much smaller than the crystallite size [37] and/or the carrier concentration is high ($\sim 10^{21}$cm^{-3}). L can be calculated from a highly degenerate electron gas model [4]. L is expressed as:

$$L = (3\pi^2)^{1/3}(h/e^2)\rho^{-1}N^{-2/3} \tag{2.7}$$

where h is Planck's constant, e is the electron charge, ρ is the resistivity and N is the carrier concentration. Shigesato et al. [38] found that this mean free path (L) was relatively unchanged with Sn concentration in the amorphous material (L=7 nm), increased in the undoped crystallized sample (L=11 nm), and decreased rapidly with increasing Sn concentration. The mobility of the free carriers can also be significantly affected by surface scattering [39] provided the mean free path is comparable to the film thickness. In conclusion, it appears that the carrier mobilities in crystalline ITO films are mainly dominated by neutral scattering centres which are independent of temperature [40] and above all by ionized scattering centres [6].

The effect on electric conductivity of disordered (amorphous) indium oxide should be substantial. Indeed, a common view in semiconductor physics is that the mobility is highest in semiconductors of high structural quality (large grains, low dislocation density etc.). Nonetheless, it is still questioned [32]. One explanation is the fact that the mean free path of free carriers in indium oxide and ITO is a few nanometres. For comparison, the mean free path in a metal is one order of magnitude less (a few $\mathring{A}$). As a consequence, electrons in indium oxide and ITO might not be strongly scattered by the disorder because it varies rapidly on the scale of an electron wavelength and the electrons experienced only a smoothed out potential. Again, this is not the case for metals since the electron wavelength is of the order of the interatomic spacing. This is confirmed by the fact that the resistivity of RT deposited ITO and particularly indium oxide films (amorphous) is generally low ($\sim 10^{-3}\Omega$ cm) [41][38]. Conduction mechanisms have been proposed for amorphous ITO films. Hopping conduction via localized states, originating in density fluctuations in the material, seems to govern the conductivity. Such a type of conduction was suggested by Korzo et al. [42] for amorphous Indium Oxide films prepared by the CVD method based on the pionneering work of Mott [43].

2.2.2.2 Optical properties

As for electrical properties, optical ones of the spectrally selective In_2O_3 and ITO films are governed by their band structures and its modifications by defects.

2.2.2.2.1 The refractive index and the dielectric constant The absorption and refraction of a medium can be described by a single quantity: the complex refractive index n_c=n+ik. n is the refractive index and it describes the velocity of light v in the medium since n=c/v where c is the speed of light in vacuum. k is called the extinction coefficient and it describes the attenuation of light wave as it goes through a material. k is directly related to the absorption coefficient α of a medium. It is shown that:

$$\alpha = \frac{4\pi k}{\lambda} \tag{2.8}$$

where λ is the vacuum wavelength of light.

The transmittance T is given by:

$$T = A \times exp(\frac{-4\pi kt}{\lambda}) \sim exp(-\alpha t) \tag{2.9}$$

where

$$A = \frac{16 n_0 n_1 (n^2 + k^2)}{((n_0 + n)^2 + k^2) + ((n_1 + n)^2 + k^2)} \tag{2.10}$$

n_0, n and n_1 are the refractive indices of air, film and substrate respectively. k is the extinction coefficient. For TCOs in the visible range, $k^2 < n^2$ and hence A$\sim$1. n and k are interdependent parameters related with the Kramers-Kronig relationships:

$$n(\omega) - 1 = \frac{2}{\pi} P \int_0^\infty \frac{\omega' k(\omega')}{\omega'^2 - \omega^2} d\omega' \tag{2.11}$$

and

$$k(\omega') = -2\frac{2}{\pi\omega} P \int_0^\infty \frac{\omega'^2 [n(\omega') - 1]}{\omega'^2 - \omega^2} d\omega' \tag{2.12}$$

2.2.2.2.2 UV region In the UV region, indium oxide and ITO films show high ultraviolet absorption due to the fundamental direct band gap of about 3.5 eV. This absorption is related to interband transitions. The absorption edge (λ_{gap} or band-gap absorption) is strongly dependent on the method of preparation [44]: it is found to lie between 3.5 and 4.1 eV.

It has been observed [45] that the higher the free electron density (N), the shorter the wavelength of the absoprtion edge. This phenomenon can be explained if the density of free electrons is so high that the conduction band is partially filled up; then, the first observable interband transition occurs for higher photon energy. This shift ΔE can be described by assuming a Fermi free electron gas whereupon:

$$\Delta E = E_{gopt} - E_{g0} = \frac{\hbar^2}{2m^*_{VC}} \times (3\pi^2 N)^{2/3} + \hbar \sum \tag{2.13}$$

and is commonly referred to as the Burstein-Moss shift [21]. E_{gopt} is the direct optical band gap, E_{g0} is the intrinsic band gap, N the free carrier density, $\hbar$ is the reduced Planck's constant and m^*_{VC} is the reduced effective mass of the electron carriers defined by:

$$\frac{1}{m^*_{VC}} = \frac{1}{m^*_c} + \frac{1}{m^*_v} \tag{2.14}$$

where m_c and m_v are respectively the conduction and valence band effective mass of the electrons. $\hbar \sum$ accounts for electron-electron and electron-impurity scattering. Thus, the free electron concentration is a critical parameter in defining optical properties in the UV region.

Muller [46] observed a considerable absorption tail at low photon energies (<3.7 eV) on his sputtered In_2O_3 thin films. This absorption tail was not believed to be caused by direct or indirect interband transitions but rather by lattice defects. Such absorption tails are ascribed to lattice imperfections, for instance: defects near the band edges (band tailing) or statistical variations in the energy gap due to local lattice deformations [47]. The introduction of a high concentration of impurities/defects to a perfect semiconducting crystal causes a perturbation of the band structure with the result that the parabolic distribution will be disturbed and prolonged by a tail extending into the energy gap.

2.2.2.2.3 IR region In the IR region, films exhibit high infrared reflection related to the quasi-free electron plasma [28], with a plasma wavelength λ_p. λ_p is defined by Transmittance=Reflectance, where the dielectric-like transmittance equals the metal-like IR reflectance. Therefore, in the near-IR region, the free carrier absorption becomes important for the transmittance and reflectance of the ITO film. The optical phenomena in this region can be explained on the basis of classical Drude theory [48][49]. As in the UV region, the free electron concentration is a critical parameter in defining optical properties in this range of wavelengths.

2.2.2.2.4 Visible region Between λ_{gap} (the band-gap absorption) and λ_p (the plasma wavelength) there is a region of high transmission, about 80 - 90% (glass substrate included) for the visible spectrum [45] depending on the deposition conditions. The wide optical band gap ($>$ 3.5 eV) prohibits interband transitions, hence the transparency within this range.

2.3 Pulsed Laser Deposition

The PLD process can be described as follows:

1. Interaction laser/target and laser/evaporated material
2. Expansion of the plume and interaction with the background gas
3. Condensation on a substrate: thin film growth

A simplified schematic of the PLD method is given in Fig. 2.3.

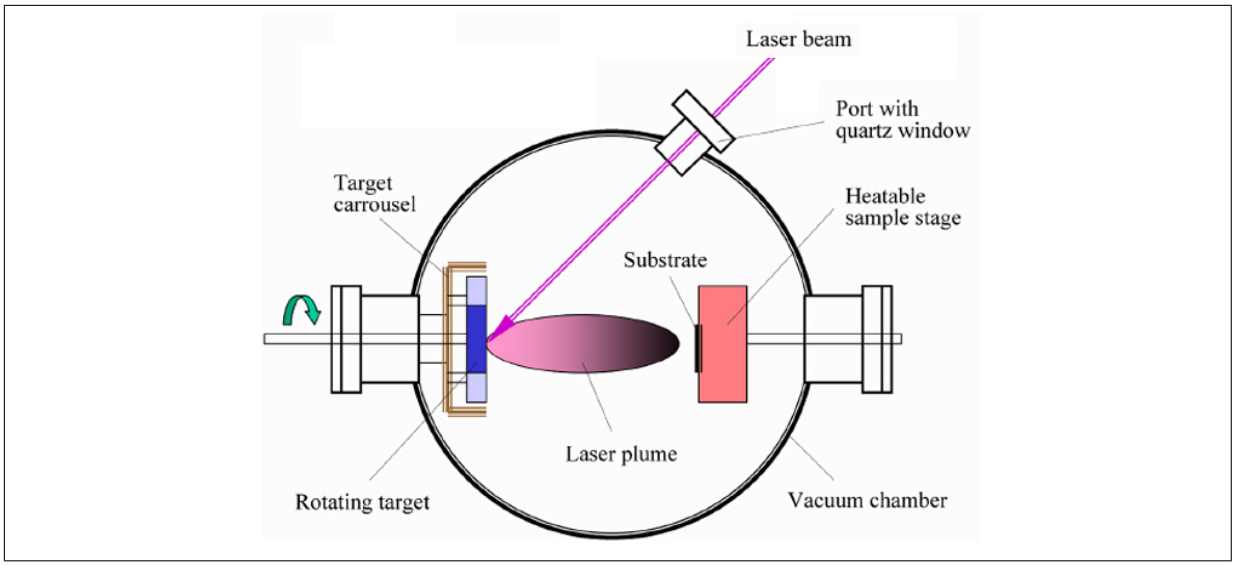

Figure 2.3 Pulsed laser deposition schematic

The next sections detail each of these processes.

2.3.1 Interaction laser/target

Photons from the laser can be absorbed by the target in at least three different ways:

- Volume absorption by electrons and phonons in the solid
- Surface absorption by free carriers in the molten layer
- Absorption by the emitted plume

Optical irradiation of the target causes a strong (typically up to temperatures of more than 5000 K) and fast (a few ns) surface heating [50]. The rate of increase in the

surface temperature depends on the optical penetration depth of the material and the thermal diffusivity of the target. Laser parameters such as the energy density (fluence), pulse duration, wavelength, polarization and laser repetition rate also play a role in the formation and properties of the plasma from the irradiated surface. The underlying non-equilibrium mechanisms involved in this removal are extremely difficult to model. This also makes PLD a non-thermal deposition technique.

Generally, the electronic structure of the target does not really matter since the very high electric fields generated by the laser result in dielectric breakdown. Indeed, at these power densities (10^7 - 10^8 W/cm^2), all materials actually absorb a significant fraction of the radiation, resulting in surface heating and evaporation of all target components at the same time, irrespective of their partial binding energies yielding stoichiometric films.

2.3.2 Interaction laser/evaporated material from the target material

The laser subsequently interacts with plasma via ionisation, energy absorption and radiation transport. The optical absorption of the plasma is a self-regulating process: if the optical absorption of the plasma falls for whatever reasons, its increased transparency will enable further surface exposure to re-populate the plasma and again increase absorption and surface shielding. Thus it could be deduced that an instantaneous equilibrium plasma density, once formed, will try to self regulate against any change in density, temperature or irradiance.

2.3.3 Expansion of the plume and interaction with the background gas

The interaction of laser ablation plumes with a background gas is of importance in PLD, nanoparticle formation and growth [51]. Compared with expansion into a vacuum, the interaction of the plume with an ambient gas is a far more complex gas dynamic process due to the appearance of new physical processes such as deceleration, thermalisation of the ablated species, interpenetration, recombination, formation of shock waves and clustering [52][53][54]. Numerical investigations of PLD have been performed both experimentally and theoretically for decades. Several diagnostic tools have been used to study plume formation and content: they mainly include time-resolved optical spectroscopy and time-of-flight mass spectrometry [55]. Different models describing the expansion of the plume were then developed according to the background gas pressure

range used. Shock wave models are commonly used for the case of ablation in a dense background gas when typically pressures of above a few Pa are used. Nevertheless, a number of gas dynamic aspects of the expansion are not yet fully understood [56].

Optimal properties of films deposited by PLD require the use of a background gas to obtain high-quality ITO films, with both high conductivity and transparency. Background gas influences the kinetic energy distribution of plume constituents when they impact on the substrate. Moreover, oxygen reacts with the ablated metal species of the plume leading to the formation of oxides and oxygen-containing clusters [55]. These reactions play an important role in preserving film stoichiometry and ensuring good functional properties. It was found in [57] that high quality as-deposited superconducting films could be obtained at only a given target-substrate distance (7 cm) and oxygen background pressure (5 mT). Authors related this observation to the velocity distribution uniformity of the various species, ensuring homogeneous substrate surface densities of the constituents and identical coverage rates. As a consequence, there is a better chance for the atoms to rearrange amongst themsleves to form a stoichiometric film. There are narrow ranges of parameters for which a uniform velocity distribution occurs. It was shown in [58] that the velocity distribution of each atomic species could be described very accurately by the following equation (theory of supersonic molecular beams):

$$f(v) = Av^3 \times e^{\frac{m(v-v_0)^2}{2kT_s}} \tag{2.15}$$

where A is normalization constant, v_0 is the so-called stream velocity, m is the mass of the ejected atom or ion under consideration, k is Boltzmann's constant and T_s is a temperature parameter describing the velocity spread.

For laser pulses of some tens of nanoseconds duration, the expansion of the evaporated cloud into the ambient gas starts right after the laser pulse termination. Thus, the evaporation and expansion can be considered separately. The expansion starts from a cloud with the density and temperature uniformly distributed within a half sphere spreading above the surface exposed to the laser beam. The particles in the cloud have a Maxwell-Boltzmann distribution with the temperature [56]. After its formation and until the end of the laser pulse, it can be considered isothermal, with the temperature well exceeding 1000 K. Immediately after irradiation, the plasma will expand away from the target because it is the direction of the greatest density gradient. This expansion pushes any existing gases away from the target, setting up a pressure wave: this is

a shock-wave. There is a threshold pressure above which shock-wave formation can occur [59]. During propagation through a gas, the presence of this shock-wave front causes spatial confinement resulting in a reduced cooling rate of the plume and high ionisation degree of its species. Under such conditions mutual aggregation of plume constituents occurs [60] leading to the formation of clusters which can grow on the substrates if they are larger than a critical size. Expansion of the saturated vapour, combined with heat transfer at the contact surface between the plume and the ambient gas, leads to very rapid cooling. This cooling can occur more rapidly than condensation, leading to exceptionally high saturation ratios (S).

After evaporation from the target, material from the plume is then allowed to recondense on a substrate, where film growth occurs.

2.3.4 Film growth

2.3.4.1 Adsorption and diffusion

After an atom or an ion is adsorbed on a surface, it has two possibilities: it might diffuse across the surface and then escape to the vacuum or it might bond. The diffusion rate of an adatom across a surface at a temperature T is given by a Maxwell-Boltzmann relation:

$$D_s = D_0 \times e^{\frac{-\epsilon_D}{kT}} \tag{2.16}$$

where ϵ_D is the activation energy for diffusion (cal/mole) and D_0 is a constant. In order to grow high quality crystalline film, there must be sufficient surface diffusion to allow adatoms to migrate to thermodynamically stable sites and minimize their surface energy within the time needed to deposit a monolayer of atoms. There are two ways to enhance this surface diffusion: increasing the substrate temperature and/or the kinetic energy of the ablated species. One problem with increasing the surface temperature is the increase in surface-to-bulk diffusion and bulk interdiffusion. This leads to a smearing out of planes so that it can lower the limit to device size [61]. This problem can be overcome by enhancing surface mobility by energy transfer from the species impinging from the plume to the surface. A compromise needs to be found between promoting surface mobility and avoiding bulk displacement phenomena. The arrangement and growth of indium oxide and ITO thin films can be simplified in terms of the stacking of MO_6 coordination groups. Amorphous indium oxide is probably formed during physical vapour deposition processing when MO_6 coordination units, which evolve from the target or are formed while chemisorbed on the growth surface, are incorrectly oriented

when they are incorporated into the growing film. For example, at low temperature, the restricted mobility of the indium oxygen clusters preserves the misorientation of the coordination units and consequent bond distortion [62].

2.3.4.2 Nucleation and growth

2.3.4.2.1 Energetic considerations and supersaturation When a cluster is allowed to diffuse on a given substrate, it will try to minimize its free energy G. G is the free energy function and is a convenient measure of the feasibility of reaction. It is defined as:

$$G = H - TS \tag{2.17}$$

where H is the enthalpy, S the entropy and T the absolute temperature. Thus, if a system changes from some initial (i) to a final (f) state at constant temperature due to a chemical reaction or physical process, a free-energy change ΔG=G_f-G_i occurs given by:

$$\Delta G = \Delta H - T\Delta S \tag{2.18}$$

where ΔH and ΔS are the corresponding entahalpy and entropy changes. Systems naturally tend to minimize their free energy and successively proceed from a value G , to a still lower, more negative value G, until it is no longer possible to reduce G further. When this happens, ΔG =0 . The system is said to have achieved equilibrium and there is no longer a driving force for change. It is convenient to work with the change in chemical free energy per unit volume ΔG_v.

For most deposition processes including pulsed laser deposition, the two main thermodynamic parameters that determine to a great extent the growth mechanism are the substrate temperature T_s and the supersaturation S. Both parameters are involved in the expression for ΔG_v which can be written as [63]:

$$\Delta G_v = -\frac{kT_s}{\Omega} ln(\frac{P}{P_e}) = -\frac{kT_s}{\Omega} ln(S) \tag{2.19}$$

P is the pressure of the arriving atoms and P_e is the equlibrium vapor pressure at the substrate temperature T_s. S is the vapour supersaturation defined by S=P/P_e. Ω is the atomic volume. Without supersaturation, S=0 and hence ΔG_v=0 so that nucleation and growth are impossible. Therefore, any level of gas-phase supersaturation generates a

negative ΔG_v, which makes nucleation possible. A supersaturated solution/vapour is not at equilibrium ($\Delta G_v \neq 0$). In order to relieve the supersaturation and move towards equilibrium ($\Delta G_v = 0$), the solution or the thin film crystallises. Thus, a supersaturated solution/vapour is required for crystallisation to occur. In PLD thin film growth, the degree of supersaturation of the plume (vapour) is mainly controlled by the energy density (E_d) falling on the target. Therefore, it is a critical parameter to control.

On the other hand, the growth orientation is determined by the surface free energy G_s given by:

$$G_s = (\gamma_f - \gamma_s) + \gamma_i - \gamma_e \tag{2.20}$$

where γ_f, γ_s, γ_i and γ_e are respectively the free surface energy for the film-air, substrate-air, film-substrate interfaces and the epitaxial energy gain [64]. The film actually grows along the orientation leading to a minimum value of G_s. The crystal plane with the smallest surface energy tends to be exposed at the surface of the crystal. Crystallisation includes nucleation and growth; the ratio of nucleation to growth controls the grain size distribution. The next paragraph gives more details about these steps.

2.3.4.2.2 Details of the processes All phase transformations, including thin film formation, involve the processes of nucleation and growth. During the earliest stages of film formation, a sufficient number of vapour atoms condense and establish a permanent residence on the substrate. Depending on their size, they will either grow in size or dissociate into smaller entities. After repeated exposures of the substrate to the incident vapour, a uniform distribution of small but highly mobile clusters or islands is observed [65]. If the nucleus size is greater than the critical size, the nuclei incorporate impinging atoms and subcritical clusters and grow in size while the island density rapidly saturates. The next stage involves merging of these islands by a coalescence phenomenon. Then, a second layer can be formed. This the “layer by layer growth” (or Frank-van der Merwe growth) mechanism which is clearly favoured in PLD given the small size of critical nuclei (practically one atom) owing to the high degree of supersaturation. This results in two-dimensional nucleation of mono atomic height islands. Fig. 2.4 illustrates the three main basic modes of thin film growth.

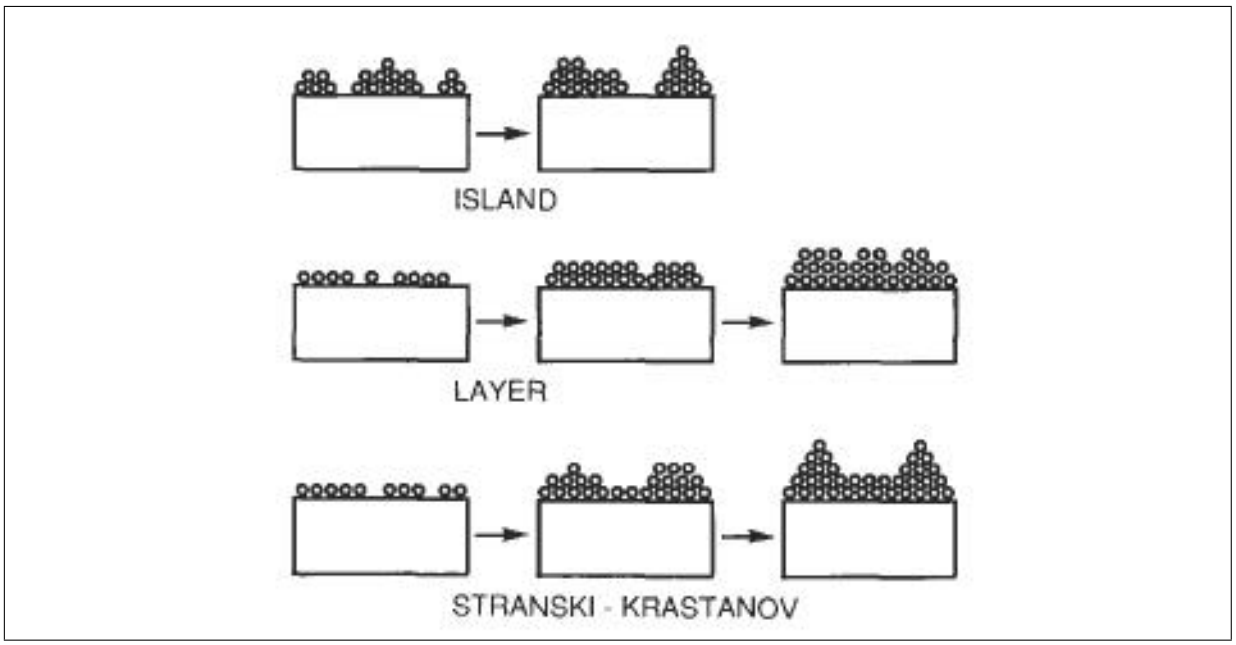

Figure 2.4 The three basic modes of thin film growth: island (or Volmer-Weber), layer (or Frank-van der Merwe) and Stranski-Krastanov (combination of layer and island growth). The layer by layer (Frank-van der Merwe) growth is favoured in PLD growth.

2.4 Pulsed Laser Deposition of ITO thin films

The substrate temperature (T_s) and oxygen pressure ($P(O_2)$) can be easily controlled during deposition to obtain ITO thin films with the required properties. However, parameters also affecting film properties such as film thickness (t) and stress are much more difficult to control. These four parameters are reviewed in the next sections.

2.4.1 Substrate temperature

Much work has been done on ITO films using commonly known fabrication technologies such as sputtering, evaporation, chemical vapour deposition and spray pyrolysis. This will be detailed in the next section. Nevertheless, most of these techniques require elevated temperatures ($T_s > 300$°C) to grow reasonably low resistivity and high transparency films [24]. This requirement may be restrictive for a number of applications such as liquid crystal displays which require low deposition temperature, solar cells (especially photovoltaic devices based on amorphous silicon which may deteriorate seriously at elevated temperature [66]) and in situations where coatings need to be made on polymerized materials (flexible substrates). PLD is then extremely suitable since it allows lower deposition temperatures to be used.

Even at RT, high quality indium oxide thin films can be grown [41]. At RT and 10 mT oxygen pressure, better conductivity films ($2.5 \times 10^{-4}\Omega$ cm) could be obtained from

undoped In_2O_3 material as compared with ITO. Optical transmittance in the visible range in excess of 90% was obtained and the presence of Sn was less critical to the transmittance value. This behaviour is consistent with the fact that it has been reported [38] [24] that at RT, the presence of Sn atoms in the ITO films does not contribute free carriers to the conduction band, rather they act as scattering centres in the films. Sn has to be thermally "activated" effectively to substitute for In and provide free carriers to the matrix [67] resulting in lower resisitity ITO thin films at higher substrate temperatures.

Regarding ITO thin films, the decrease in resistivity with an increase in T_s is also explained in terms of enhanced crystallisation. Grain growth is favoured at higher T_s resulting in better optical properties.

The plasma wavelength (λ_p), related to free carrier cocnentration, was observed to decrease initially with increasing T_s up to $100°$C and then increase slightly up to $300°$C [25]. Usually, post deposition heat-treated films or films deposited on heated substrates (at least above $300°$C) exhibits high near-infrared reflectance. This parameter is extremely important to tailor the optical properties of applications like window layer coatings and solar cells. Such a high near-infrared reflectance was also obtained for films deposited by PLD at temperatures as low as $200°$C [68][69]. T_s also affects the direct optical band gap. It was found [25] that the direct band gap of ITO films increases from 3.89 to 4.21 eV as T_s increases from RT to $300°$C owing to increase in carrier concentration. In another paper [70], Adurodija et al. found that the best films were obtained for oxygen pressures around 10 mT. For this oxygen pressure, resistivities as low as $5.35 \times 10^{-4}\Omega$ cm and $1.75 \times 10^{-4}\Omega$ cm were obtained at RT and $200°$C respectively. Optical transmittance in the visible region of 85% was also achieved.

The substrate temperature is sometimes found to have an effect on thickness [71]. The authors noticed that the thickness decreases from 90 to 44 nm as the substrate temperature increases from RT to $300°$C.

2.4.2 Oxygen pressure

The oxygen flow during the deposition influences the chemical composition, film density, growth rate and layer morphology. $P(O_2)$ is found to affect the PLD deposition rate and hence the film thickness during growth. The deposition rate reduced significantly as $P(O_2)$ increased. It was found [70] to reduce from 15 nm/min under a $P(O_2)$ of 5 mT to 5 nm/min under a $P(O_2)$ of 50 mT. Such a reduction in the growth rate was attributed

primarily to increased collisions of the ablated ITO particles with the ambient oxygen gas. This is a widely shared view among researchers where similar effects of $P(O_2)$ on the growth rate and thickness have been reported, not only for PLD but also for sputtering and electron beam evaporation [72] [73]. Another effect of $P(O_2)$ is to reduce surface mobility. This reduction is so important that at very high $P(O_2)$, ITO films were found to be completely amorphous [68].

The electrical properties are also strongly impacted by oxygen pressure changes. At very low $P(O_2)$, there is a very large number of oxygen vacancies; above a certain threshold, the crystallinity can be greatly impacted, reducing the mobility of the free carriers. At very high $P(O_2)$, the mobility also tends to decrease for two main reasons: oxygen atoms accumulate mainly at grain boundaries and tend to form defects because an Sn^{4+} ion pair may attract an additional oxygen atom, producing a neutral cluster $(SnO_2)_2$ in which the additional oxygen atoms play the role of electron traps and so reduce the carrier mobility [13]. In between, there is a narrow window of oxygen pressure (at a given substrate temperature) where low resistivity thin films can be grown. For instance, several groups found that for RT PLD deposited indium oxide and ITO thin films, the optimal oxygen pressure that yielded the highest conductivity films lies within a narrow range from 10 to 15 mT [73] [25] [69] [70]. This range is about the same for films grown at higher substrate temperatures.

The carrier concentration also plays a role in the increase/decrease in resistivity. The incorporation of oxygen leads to a decrease in oxygen vacancies in the films and hence to a fall in the carrier concentration. Therefore, the resistivity of the ITO film is strongly correlated with the chamber oxygen pressure and the resulting film stoichiometry. Oxygen provides the background gas necessary for optimal PLD growth of complex oxides, and equilibrates the energetic species of the emerging atomic/ionic constituents ablated from the target [74]. A uniform velocity distribution is found to be a key parameter in growing high quality thin films. This gas-dynamic equilibration is even more necessary in the low temperature case, where there is not sufficient surface diffusivity to allow formation of the film after the atomic/ionic species impinge on the substrate and where it mediates enhanced ITO cluster formation within the plume. Zheng et al. [74] observed that at low and high $P(O_2)$, small particles covered the surfaces of their films. They suggested that these small particles are precipitates of indium or of tin. Nonetheless, due to the very small size of the particle, they could not perform accurate energy dispersive X-ray analysis in the SEM. They also noticed that there were no particles on the surface for the films

grown at the optimized pressure. At low $P(O_2)$, ITO films are substoichiometric, [75] which leads to metallic inclusions (metallic indium or tin) and hence to opaque films. These metal-rich dark ITO films also exhibit high carrier concentrations but very low mobilities with the presence of different phases. Optical properties are also impacted because of light scattering.

The density of ITO films is reported [76] to increase as the deposition pressure increases. The incorporation of oxygen leads to a decrease in oxygen vacancy concentration and hence the density increases. Optical properties are affected by this density change: less light is scattered as the film becomes denser, increasing its transparency. This oxygen vacancy concentration change impacts as well on the refractive index n of In_2O_3 films. A decrease in the refractive index with increasing $P(O_2)$ was observed in the thickness range 200-300 nm for pulsed laser deposited indium oxide films [77] and for reactively evaporated indium oxide films[78]. It is suggested that this is due to a change in the number of conduction electrons [79].

2.4.3 Film Thickness

Film thickness is an important parameter for the properties of ITO films. It is directly proportional to the number of laser shots. When the film thickness decreases below a critical value, the electrical properties of the indium oxide and ITO films deteriorate drastically. As films get thinner, the effect of surface scattering becomes more and more predominant over grain boundary [80] than ionised/neutral impurity scattering and tend to be discontinuous. The critical thickness, below which electro-optical properties degrade strongly, depends on the control parameters of the process. Jan et al. [81] also studied the critical thickness of ITO thin films deposited by directly coevaporating metallic In and Sn onto a heated glass substrate. A rapid increase of resistivity with decreasing film thickness below 50 nm was again attributed to 1) the increased importance of carrier scattering from the outer surface of the film due to surface roughness as seen previously but also to: 2) the greater density of grain boundaries due to decrease in grain size [25] and 3) film discontinuities attributed to the formation of islands [82] and extensive voids. Similar studies for pulsed laser deposited films have been published. Kim et al. [25] observed that the resistivity of the ITO thin films initially decreased with an increase in the film thickness, up to 220 nm, but it remains almost constant with further increases in the film thickness up to 870 nm. The resistivity does not change very much for films thicker than 300 nm because both carrier density and mobility become independent of film thickness.

The same authors [25] also reported the effect of thickness on optical transmission. They found that the transmission was not exponentially related to the film thickness as expected from the following relation: $I = I_0 exp(-\alpha t)$ where α is the absorption coefficient, t the film thickness, I the transmitted intensity at a particular wavelength and I_0 the incident intensity, taken to be 100%. Therefore, other parameters affect the optical properties. The one found to have the greatest impact was the grain size, which grew larger with film thickness. But surface roughness might play a role as well as the films grew thicker [83]. It has also been shown that the refractive index depends on the film thickness up to 100 nm, after which it is almost constant [79].

In the range of extremely thin films (a few nanometres), it was reported [84] that reactively evaporated indium oxide films were amorphous below 4 nm, while films thicker than 4 nm were polycrystalline. Finally, adjusting the film thickness has a practical use in applications where the ITO serves as an antireflective layer. In that specific case, the reflectivity losses can be reduced when the layer thickness is adjusted to the wavelength of the light used [85].

2.4.4 Stress in thin films

Virtually all vacuum-deposited coatings are in a state of stress. The total stress is composed of a thermal stress and an intrinsic stress. The thermal stress is due to the difference in the thermal expansion coefficients of the coating and the substrate and is generally independent of the deposition process. The intrinsic stress is due to the cumulative effect of the crystallographic flaws that are built into the coating during deposition.

2.4.4.1 Thermal stress

Strain is invoked due to thermal mismatch between the ITO film (7.2×10^{-6}/°C [86]) and the substrate when the latter is a polymer substrate (from 12×10^{-6}/°C for PET substrates [87] to 39×10^{-6}/°C for polycarbonate substrates [76]). This thermal stress is somewhat less important when ITO films are grown on glass substrates, since the thermal expansion coefficient of glass (4.6×10^{-6}/°C) is close to that of ITO.

2.4.4.2 Intrinsic stress

In PLD, the tailoring of stress in the film becomes possible through the bombardment of the depositing film with the energetic species during film growth. It is indeed possible

to tune the kinetic energy of ablated species through background gas pressure. Few studies have addressed this issue for PLD. One study, though, showed the existence of compressive stress in homoepitaxial growth of $SrTiO_3$ using PLD [88].

Norton et al. [89] studied further the role of ablation energies in determining the film stress in CeO_2 films deposited by PLD. They showed that at very low P(O_2) (0.4 mT), large lattice distortion occured. This was attributed to both the stresses and the defects in the film, mainly due to the large number of oxygen vacancies. They separated the effects of plume kinetic energy from other possible sources of lattice distortion, including the variation in oxygen content by depositing films at constant oxygen pressure but with different background gas pressure (using Ar). They confirmed that the compressive stress decreases as the background gas pressure increases through a reduction in the kinetic energy of ablated species via collisions.

2.4.5 Summary

Table 2.1 sums up the electro-optical properties and deposition conditions of pulsed laser deposited In_2O_3 and ITO thin films as discussed in the above sections:

2.5 ITO by other deposition methods

2.5.1 Spray Pyrolysis techniques

The spray pyrolysis method has been used frequently for the preparation of transparent conducting oxide films for many years [97][98][99]. The conventional spray hydrolysis technique consits of spraying a dilute solution of an appropriate chloride from an atomizer onto a heated substrate under normal atmospheric conditions or controlled atmospheres. High pressure argon, nitrogen, or air are usually used as the spraying gas. ITO films can be formed by mixing $InCl_3$ with a proper amount of $SnCl_4$ [28][97]. The solutions are made usually by dissolving $SnCl_4$ and $InCl_3$ in some solvents such as ethanol [97][99], butyl acetate [100], propanol [101], HCl or H_2O. ITO films deposited by spray hydrolysis adhere strongly to various substrates and can have a very low resistivity of about $5 \times 10^{-4}\Omega$ cm with high transparency of about 90% in the visible and near infrared parts of the spectrum [45]. The deposition rate can be very high, ranging from 200 to 400 nm/min [45]. In another paper [13] it was found that the optimum concentration of Sn atoms, resistivity and carrier concentration were 9 at.%, $1.3 \times 10^{-4}\Omega$ cm and $1.5 \times 10^{21}/cm^3$, respectively. But for some opto-electronic applications such

Table 2.1 Summary of ITO thin film electro-optical properties deposited by PLD by different authors.

ρ (Ω cm)	N (cm^{-3})	μ $(cm^2(Vs)^{-1}$	T(%)	T_s (°C)	$P(O_2)$ (mT)	t (nm)	Sn at.%	Reference
8.45×10^{-5}	1.38×10^{21}	53.5	84.7	400	75	315	5 wt.% SnO_2	[90]
9.4×10^{-5}	1.1×10^{21}	54	>85	200	10	90±25	3 wt.% SnO_2	[91]
1×10^{-3}	8×10^{20}	20	90%	RT	10	150	10 wt.% SnO_2	[41]
1.9×10^{-4}	1.45×10^{21}	29.4	∼92	300	10-15	170	5 wt.% SnO_2	[92]
4.5×10^{-4}	$5 - 8 \times 10^{20}$	12-35	>85	RT	9.75	no data	5 wt.% SnO_2	[68]
1.7×10^{-4}	1.1×10^{21}	33	>85	200	9.75	no data	5 wt.% SnO_2	[68]
5.35×10^{-4}	8.5×10^{20}	19.2	>85	RT	5-10	100	10 wt.% SnO_2	[70]
1.75×10^{-4}	1.2×10^{21}	48.2	>85	200	5-10	100	10 wt.% SnO_2	[70]
2.49×10^{-4}	1.45×10^{21}	35	88	300	15	180	10 wt.% SnO_2	[93]
2.7×10^{-4}	7×10^{20}	32.5	no data	200	1.3	95	5 wt.% SnO_2	[94]
2.1×10^{-4}	6.2×10^{20}	48.2	no data	200	1.3	110	10 wt.% SnO_2	[94]
no data	no data	no data	85	200	2.25	500-800	10 wt.% SnO_2	[69]
2.8×10^{-4}	no data	no data	>90%	RT	15	150	10 wt.% SnO_2	[73]
9.55×10^{-5}	no data	no data	80%	500	20	no data	5 wt.% SnO_2	[95]
1.4×10^{-5}	no data	no data	90%	310	20	190	10 wt.% SnO_2	[74]
3×10^{-4}	5×10^{20}	no data	80%	250	10	no data	10 wt.% SnO_2	[96]

as OLEDs, the layers have too rough a surface, so in such cases more “sophisticated” deposition techniques are needed.

2.5.2 Sputtering techniques

Sputtering is one of the most extensively used techniques for the deposition of ITO films. Various sputtering techniques have been used for deposition of transparent conducting oxide films, including conventional direct current (d.c.), radio frequency (r.f.) and magnetron reactive sputtering of a metal alloy target in the presence of oxygen, as well as r.f. and ion beam sputtering of a pressed oxide powder target. Magnetron sputtering as one deposition method offers the possibility to prepare ITO films at low temperature and on large areas and is the dominant technology in the industry. Indeed, the development of high performance magnetron sputtering sources that provide relatively high deposition rates and large deposition areas [102][103]. However, sputtered films are generally much rougher than PLD deposited films [25]. In particular, the conventional d.c. reactive sputtering process proceeds under elevated working gas pressures (generally in the range 0.8 to 13 Pa or 6 to 97 mT). Such high pressures often cause surface roughness in sputtered films which is inconvenient for some applications like OLEDs.

The magnitude of the deviation from the stoichiometric composition in reactively sputtered oxide layers is another very important issue. Sputtering does not allow the same control over the In/Sn ratio in the film as chemical vapour or pulsed laser deposition. Moreover, reduced yields in reactive sputtering attributed to compound formation on the target are commonly observed. Sputtering in pure O_2 produced a thin film of In_2O_3 and SnO_2 on the In-Sn target surface [104] especially at high oxygen partial pressure. The sputter rate drops substantially since oxides usually sputter more slowly than metals. Pure O_2 and a mixture of O_2 and Ar or N_2 are usually used as the sputtering gas. The use of inert gas ions avoids chemical reactions at the target and substrate. As a result of the difference in the volatility and sputter rates of these oxides, an enrichment in indium of the film is observed. Therefore, the film composition deviates from that of the target. Additionally, the surface topography that develops on the target can be signicantly influenced by ions/surface interactions. Because of the difference in the sputter yields of metallic materials and their corresponding oxides, the deposition rate is very sensitive to the change in the oxidation state of the target. Therefore, control of the oxidation state of the target surface is a primary factor to be considered during sputtering of ITO thin films with good physical properties.

2.5.3 Evaporation techniques

To evaporate In_2O_3/SnO_2 powder, electron beam evaporation and direct thermal evaporation of metallic In and Sn in an O_2 ambient are commonly used. For the latter, since In has a signicantly higher vapour pressure than that of Sn, it will be preferentially vaporized, causing a change in the composition of the Sn+In liquid alloy with time [24]. A much more efficient way to produce low resistivity and high transparency films is to use an electron beam. Low resistivity ITO films processed at low T_s have been reported using reactive electron beam evaporation onto heated glass substrates (300°C and an oxygen pressure above 0.5 mT) [49]. Under optimum conditions, the resistivity was $3\times10^{-4}\Omega$ cm and the average mean transmittance in the visible range was about 84%. Salhei [105] deposited ITO using a thermal evaporation technique without introducing oxygen into the chamber. A transmittance value of more than 80% in the visible region of the spectrum and a resistivity of $9.1\times10^{-4}\Omega$ cm were obtained.

2.5.4 Chemical Vapour Deposition (CVD)

Chemical vapour deposition (CVD) is a process in which a chemical reaction involving gaseous reacting species takes place on, or in the vicinity of, a heated substrate surface. The CVD technique has the advantage of being cost effective with respect to the apparatus. It enables the production of coatings with good properties without the use of high vacuum even on substrates with complicated shapes. In particular, atmospheric pressure CVD (APCVD) is attractive in many applications in the sense that it offers high deposition rates and hence short process time [24]. The deposition of ITO films by the CVD method generally faces difficulties due to a lack of volatile and thermally stable source materials. Maruyama et al. [106] deposited ITO films using the APCVD technique without an oxygen supply. The precursor materials were indium acetate and tin diacetate. Although the transmittance in the visible region exceeded 90%, the films had a relatively high electrical resistivity ($6.93\times10^{-3}\Omega$ cm). This was attributed to the small crystallite size (15 - 20 nm). Later on, Maruyama and Fukui [107] reported the fabrication of ITO films with better electrical properties using indium and tin acetylacetonate. This time, oxygen gas was introduced. The films deposited at 450°C and 215 nm thick had much lower resistivity ($1.8\times10^{-4}\Omega$ cm). Indium 2-ethylhexanoate and tin IV chloride were proposed as precursor materials [108] for obtaining ITO films by APCVD without a supply of oxygen. The ITO film obtained at a reaction temperature of 400°C had a resistivity of $2.9\times10^{-4}\Omega$ cm.

2.5.5 Sol-gel method

Compared to conventional thin film forming processes, films prepared by the sol-gel route require considerably less equipment and are potentially very cost effective. This method offers many other advantages [24]:

- intimate mixing, at the molecular level, of the starting materials resulting in a high degree of film homogeneity, even for multicomponent systems.
- low processing temperature
- dopants, even at a trace level, can be introduced with relative ease.
- easy adjustment of the viscosity, and thereby the thickness per coating, by adequate choice of the solvent, chelating organic ligands, concentration, etc.
- large area coatings with desired thickness and composition are obtainable.

Dip coating [109] is the preparation method favoured in the sol-gel process. ITO films with satisfactory electrical and optical properties can be prepared by the sol-gel method. Gallagher et al. [110] prepared ITO films by dip coating them from an acetylacetone solution of indium and tin acetylacetonate. They studied the solution chemistry and the thermal decomposition of ITO precursors. The best resistivity ($1.01 \times 10^{-3}\Omega$ cm) was obtained after postannealing in forming gas and for a film containing 8 wt.% SnO_2. Maruyama et al. [111] obtained a lower resistivity (4.23$\times 10^{-4}\Omega$ cm) through direct heating in an inert gas. Furusaki et al. [112] used indium 2-ethylhexanoate or indium acetylacetonate and tin 2-ethylhexanoate as starting materials for indium and tin. A relatively high resistivity in the range 3-5$\times 10^{-3}\Omega$ cm was obtained after annealing in vacuum at 550°C. However, they obtained a very good transparency of over 90% in the visible region. Using the same precursors, Xu et al. [113] slightly improved properties (1.08$\times 10^{-4}\Omega$ cm and transparency over 90% in the visible range) for spin coated ITO films annealed at 650°C and without annealing. Similar to the CVD technique, the preparation of ITO films with satisfactory electrical and optical properties by the sol-gel process is restricted to a very limited range of precursors, mainly because of the high cost of the alkoxides which are commonly used and a lack of sufficient solubility. Therefore, better understanding of the solution chemistry, film thermal decomposition and reduction and control of film microstructure are important in the preparation of low electrically resistive films by the sol-gel method.

2.5.6 Comparison with PLD deposited thin films

Table 2.2 sums up the electro-optical properties of ITO thin films deposited by different techniques.

Table 2.2 Comparison of different deposition techniques with PLD.

Technique	ρ (Ω cm)	T(%)	T_s (°C)	t (nm)	Reference
Sputtering	6.8×10^{-5}	>90	370	150	[48]
	4×10^{-4}	84	RT	800	[114]
	7×10^{-4}	84	300	300-1500	[115]
Electron beam evaporation	3×10^{-4}	>84	300	300	[49]
Thermal evaporation	9.1×10^{-4}	>80	80	120	[105]
CVD	6.93×10^{-3}	>90	300	450-700	[106]
	1.8×10^{-4}	>90	450	215	[107]
	2.9×10^{-4}	80	400	430	[108]
Spray-pyrolysis	1.3×10^{-4}	no data	500	300	[13]
	no data	no data	506	280	[97]
Sol-gel	$3 - 5 \times 10^{-3}$	90	550	150	[112]
	4.23×10^{-4}	85	500	no data	[111]
	1.08×10^{-3}	95	650	360	[113]
	1.01×10^{-3}	90	500	273	[110]

2.6 Advantages/drawbacks of PLD

PLD has become one of the most versatile and powerful methods for producing multi-component oxide thin films. PLD has advantages and disadvantages. Major advantages of PLD include [116]:

- Relatively high deposition rates. Film growth rates may also be controlled to any desired level.
- Congruent transfer from the target to the film, provided that appropriate and precise deposition conditions are met.
- The possibility of producing as-deposited films with an appropriate microstructure at relatively low substrate temperature. It is known that energetic particle bombardment of the film surface during growth lowers the crystallisation temperature [117].
- Possibility of producing multilayered films of many different materials.
- Possibility of sharing the laser beam among several deposition systems.
- Reduction of film contamination since the laser beam is focused on the source material during deposition.
- The energy source (laser) is outside the vacuum chamber providing a greater

degree of flexibility in material use and in the geometrical arrangements.
- Almost any condensed matter can be ablated.
- The possibility to produce metastable materials that would be unattainable under thermal conditions.

The main disadvantages are:

- Formation of micron and submicron-sized particulates (droplets) during target ablation.
- The highly focused nature of the laser beam makes it difficult to scale-up the PLD technique to cover large areas (unlike magnetron sputtering for example).
- The necessity to polish the surface of the target for each new film deposition (time consuming).
- Impurities in the target materials.
- Frequent cleaning of the special quartz ultra high vacuum window, used to introduce the laser beam into the deposition chamber.
- Inhomogeneous flux and angular energy distribution within the ablation plume.

2.7 Emerging techniques to improve PLD deposition

Because of the disadvantages listed in the previous section, PLD has not been preferred so far as a manufacturing process, primarily because of two main limitations: the deposition of micron and submicron-sized particulates and a limited area of uniformity in the deposited film. Droplets spoil the surface smoothness and uniformity of the films. Numerous research groups have tried to address these two issues.

2.7.1 Minimising droplet formation

Several techniques can minimise droplet formation. The most successful and easy to set up involves target rotation and/or beam scan across the target. A 10,000 rpm rotating deflector can also be inserted between target and substrate [118] to deflect selectively slow particles and transmit faster moving species. Later on, a similar device was used by Yoshitake et al. [119]. They used a vane velocity filter. They succeeded in eliminating particulates below 0.5 μm diameter at 350 rpm. They also found that particulate maximum velocities become larger as their size decreases (up to 65 m/s for 0.5 μm diameter particulates). Another set up [120] was to use two colliding beams to generate a high pressure zone which expanded towards the substrate. Heavier particles were then forced to miss the surface altogether. A negative substrate bias of several hundred

volts can also reduce considerably similarly charged heavy clusters. This was found to improve the growth of Ge by PLD [121]. A second laser to excite and dissociate the larger particles within the plasma has been successful [122][123]. Sankur et al. [124] adopted a totally different approach: they used a melted Ge target and they managed to produce completely particulate-free films.

2.7.2 Large-area PLD approaches

PLD has now demonstrated the capability to deposit highly uniform films over 150 mm diameter substrates. Variations over the useable area were found to be only 2.3% and 0.5 at.% for thickness and composition, respectively [125]. These latter data presently represent the state of the art for the laser-deposition process and clearly indicate that PLD can be scaled to sizes compatible with mainstream semiconductor processing equipment. Finally, the limits of the PLD process have not yet been reached and it is expected that similar uniformity over even larger substrate sizes will be demonstrated in the near future.

There are three main techniques which have been used to grow large area thin films:

- "Offset" (OS) or off-axis PLD
- Rotational/Translational (R/T) PLD
- Laser-beam rastering over a large diameter rotating target

The first two techniques are static-beam approaches while the last one is dynamic and involves computer-controlled laser beam(s). Laser beam rastering is the oldest of the large-area PLD approaches. High quality YBCO thin films on 7.6 cm diameter (100) $LaAlO_3$ substrates have been grown [126] with this method. It has even been used recently to deposit films on 12.5 cm diameter substrates [127]. In OS PLD, the target is positioned such that the centre of the ablation plume which nominally leaves normal to the target surface, impinges near the outer edge of the rotating substrate. This technique can reduce droplets (improving overall thin film quality) although growth rate is slower than on-axis deposition. It easily accommodates substrate heating, and has been further used to grow high quality films of YBCO in situ on 50 mm diameter $LaAlO_3$ substrates [128]. Furthermore, the OS approach has been scaled up to deposit $Bi_4Ti_3O_{12}$ films over 100 mm diameter Si substrates for RAM applications [129]. In the second static beam approach, R/T PLD, the substrate is both rotated and translated in a linear fashion. A computer controls both substrate motions such that uniform film properties are obtained. Unlike the techniques already described, this approach is not

really suitable for substrate heating. It has been used to deposit YBCO films onto 75 mm diameter $LaAlO_3$ substrates [130].

2.8 Applications of ITO thin films

There are three main applications for ITO thin films:

- Optoelectronic Devices (Solar Cells, Organic light emitting diodes and Flat Panel Displays).
- Electromagnetic shielding.
- Functional glass.

For most opto-electronic applications, ITO thin films are used as a transparent electrode. Manufacturers try to achieve both a high optical transparency and a low resistivity. For OLED devices, there is an additional very important requirement: the surface has to be ultra smooth (a few nanometres roughness at most). Roughness is known to cause colour quality to deteriorate and to reduce the lifetime of the OLEDs (higher electric field at the tip). Much smoother film can be deposited by PLD as compared with magnetron sputtering films [92]. PLD is clearly a promising technique for making OLEDs with better lifetimes. An OLED with an ITO anode grown by PLD at room temperature has been reported to work very well [25]. There is however the problem of scaling up the PLD technique and making it more cost effective but the possibility of producing good quality films even at room temperature makes this technique very attractive indeed [73].

Chapter 3

EDX/WDX and EELS: background theory and literature review

Electron microscopy enables micro and nanochemical analysis, i.e. establishing the chemical composition of small (micron size range) to very small (nanometre size range) volumes of material. Such analysis is performed with EDX or EELS. EDX can be performed both in a TEM and SEM for elemental chemical analysis. The physics underlying the generation and the detection of X-Rays is exactly the same in SEM and TEM. However, since electron transparent specimens are analysed in a TEM while bulk specimens are analysed in a SEM, the achievable spatial resolution and data treatment differ profoundly. Those differences will be stressed. EELS can only be operated in a TEM. Contrary to EDX, not only compositional elemental can be gained from the sample but also bonding information. EDX will be discussed first before moving on to EELS.

3.1 Energy Dispersive X-Ray microanalysis (EDX)

3.1.1 General principles

EDX derives its major elemental analytical signal (X-Rays) from ionisation of the inner electron shells of the atoms, with subsequent de-excitation via various inter and intra-shell transitions of the electrons. This is done through the bombardment of a specimen with a high energy beam of electrons. One product of these transitions is the emission of electromagnetic radiation in the form of X-Rays. The other way for the atom to dissipate its energy excess is to emit a secondary electron or "Auger" electron (see Fig. 3.1).

Generated X-Rays are emitted isotropically but only 1% of those X-Rays are detected due to geometrical constraints on the detector. Since these X-rays are emitted as a result of electron transitions between precisely defined energy levels, the X-Rays produced have specific energies that are characteristic of the atoms involved and thus serve to identify them. Therefore, qualitative analysis is possible. In addition, the intensity of

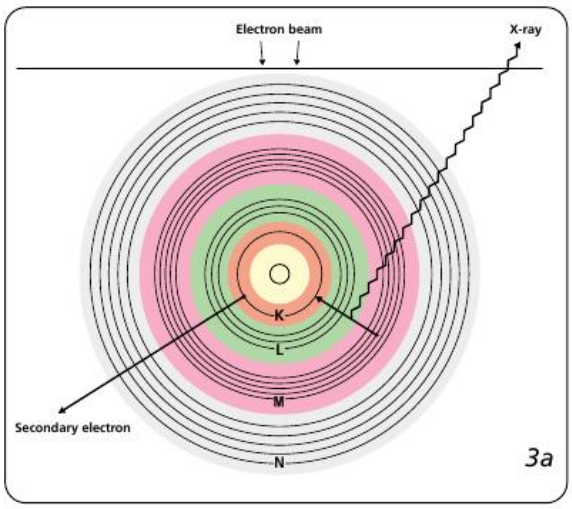

Figure 3.1 The main mechanism for X-ray production is a consequence of an electron being ejected from an inner shell of an atom by the high energy electron beam. The vacancy is subsequently filled by an outer shell electron. The atom finds itself with excess energy which must be dissipated. One way of doing so is by the emission of an X-ray with its energy corresponding to the energy difference between the inner and outer atomic shells. Taken from [131].

the emitted X-ray is directly proportional to the quantity of atoms present in the excited volume. Therefore, it is also possible to perform quantitative analysis. Modern detectors can detect X-Rays for all the elements in the periodic table above Beryllium (Z=4).

Fig. 3.2 shows a typical EDX spectrum acquired with a SEM: it is composed of peaks corresponding to specific X-ray lines. Their intensity varies according to the elements concentration present. Peaks sit on a background consisting of a continuum which decreases with energy. This continuum arises from the X-Rays produced as electrons are slowed down in the coulombic fields of atoms (nucleus) comprising the specimen. Such radiation is called “Bremsstrahlung” or “braking” radiation. The red curve in the same figure is a “reconstructed” spectrum which results from the processing of the experimental one. This is the subject of the next section.

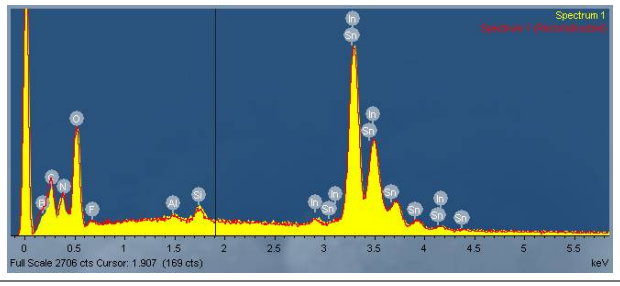

Figure 3.2 Typical SEM EDX spectrum in the 0-5 keV range of a 300 nm ITO (In_2O_3:Sn 10 wt.%) thin film.

3.1.2 Presentation of the measurement chain

The detection and measurement of X-Rays in an electron microscope require a complex measurement chain. It is complemented with a software which allows reliable automatic peak identification and processing through different algorithms. An EDX system (shown in Fig. 3.3) is composed of three basic components designed to work together to achieve optimum results:

1. A solid state X-ray detector (a classical Si(Li) like in Fig. 3.3 or a more "sophisticated" Silicon Drift Detector (SDD)) which detects and converts X-Rays into a charge signal. This charge signal is fed into a Field Effect Transistor (FET), and becomes a voltage signal which is then amplified.
2. A pulse processor or Multi Channel Analyser (MCA) which measures the previously amplified voltage signals to determine accurately and quickly the energy of each X-ray.
3. An analyzer which displays via a Cathode Ray Tube (CRT) and interprets (analytical software) the X-ray data.

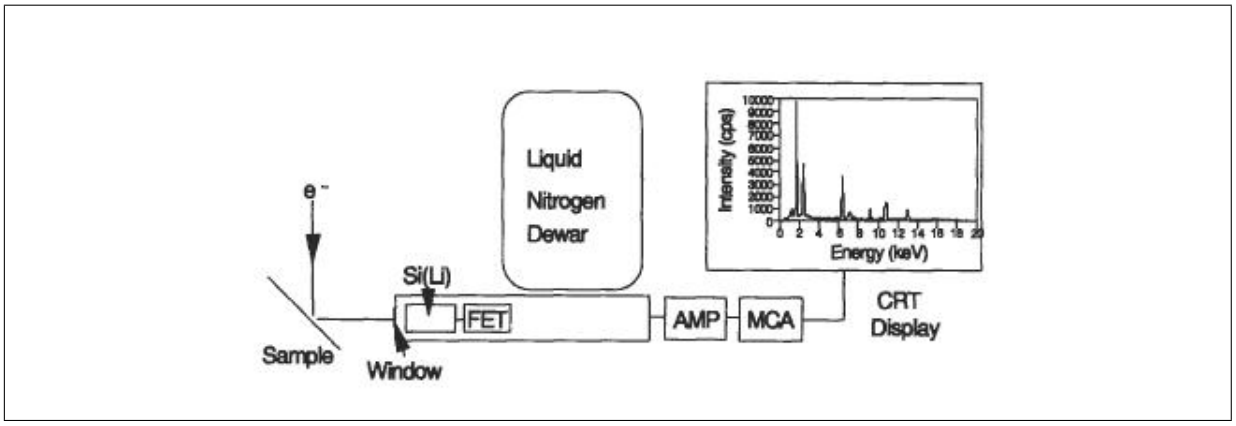

Figure 3.3 Schematic of an EDX system on an electron column. AMP=amplifier, MCA=multi channel analyser and CRT=cathode ray tube.

For information and a sense of scale, it only takes a few μs to "deal" with each X-ray (also called dead time), i.e. detecting it, measuring it and storing it in the MCA. If another X-Ray arrives before the completion of this process, both X-Rays must be ignored or the answer will be some combination of the two energies (pulse pile-up). Therefore, it is important not to overload the detector.

3.1.3 Working out the composition

The correction procedure for bulk microanalysis is often refered to as ZAF corrections. Z represents the atomic number, A and F respectively the absorption and fluoresecence of X-Rays within the specimen. For thin specimens such as those analysed in a TEM, the correction procedure is greatly simplified since to a first approximation (thin film approximation), the A and F factors can be neglected and only the Z correction remains necessary. Both procedures are detailed in the following two sections.

3.1.3.1 In the TEM

Deriving the chemical composition of a specimen involves determining factors relating EDX peak intensities and concentrations. They are called "k-factors". There are two ways one can determine k-factors:

- Calculation from first principles.
- Experimental determination using a standard.

The first way uses a set of stored equations and standard peak profiles built into the software. The calculated value is accurate to within $\pm$20% relative [132]. When a quick answer is required and accuracy is not essential, it is the recommended approach. However, if a suitable standard specimen can be obtained, experimenal k-factors should be determined to increase the previous level of accuracy. In theory, there is no limit to the accuracy of such a method, but generally, accuracy better than a few percent can be achieved. It also makes possible a known level of confidence in the quantification results produced. This is the method of choice if elements with concentration less then 5 wt.% are to be detected with accuracy. The most popular method of quantification was proposed by Cliff and Lorimer [133]. In the case of a specimen whose chemical formula would be AB, it states that: if X-ray absorption (A) and fluorescence (F) in the sample are negligible (known as the thin film approximation), the ratio of the peak intensities I_A/I_B is directly related to the ratio of the concentrations of the two elements C_A/C_B through a factor, generally called a "k-factor", which depends on components A and B, but also on the specific EDX system used to get such measurements. The equation can be written as:

$$\frac{C_A}{C_B} = k_{AB}\frac{I_A}{I_B} \tag{3.1}$$

Owing to the dependence of k-factors on the system used to acquire the data, a k-factor is not a constant. Therefore, it is of the utmost importance first to determine which experimental conditions are to be used and to keep those conditions unchanged when analysing a set of samples. Otherwise, the results cannot be reliably compared. In that sense, EDX is not an absolutely standardless method.

The Cliff-Lorimer equation involves concentration and intensity ratios, hence relative k-factors are determined: "relative" to a standard ratio element which is present or not in the sample. Its k-factor is taken to be 1. The determination procedure is the following: for a standard compound AB of known composition C_A and C_B, the experimental determination of k-factors involves three different steps:

1. Acquisition of a "standard profile", i.e. generating an EDX spectrum of a given standard under precise experimental conditions. A profile stored in the analytical software can also be used.
2. After data processing, values of I_A and I_B are obtained and inserted in the Cliff-Lorimer equation.
3. k-factors are calculated since C_A and C_B are already known.

In a second time, when a specimen of unknown composition is analysed, the now known k-factors enable the calculation of C_A and C_B. I_A and I_B are respectively derived from peaks A and B areas. The latter is calculated from the fitting of stored peak profiles (or previously acquired experimental peaks from a standard specimen). During this matching process, a fit index is calculated and is of particular interest even if it has no absolute significance in itself. It is a figure of merit which allows the user to determine the quality of quantitative microanalysis using experimental k-factors. It is a used as a "diagnostic tool".

3.1.3.2 In the SEM

In a bulk specimen, obtaining compositional data requires a different data treatment. For example, the absorption A and the fluorescence F cannot be neglected anymore. Matrix effects impacting on analytical studies are detailed and explained below.

3.1.3.2.1 Atomic number effect (Z) For some elements, a significant fraction of the beam electrons escape the surface as backscattered electron (elastic scattering). For instance in gold (Au), this is the case for 50% of the electrons. If these electrons had remained in the specimen, they would have generated many more X-Rays.

3.1.3.2.2 Absorption (A) X-Rays are produced over a range of depth into a bulk sample. To be detected, they have to "travel" up to the detector. This propagation takes place along a finite path through the specimen to reach the detector, and they are subject to photoelectric absorption and scattering. As a consequence, the detected X-Ray intensity will be less than the generated intensity and this intensity reduction has to be taken into account in order to give the right chemical composition.

3.1.3.2.3 Fluorescence (F) It was seen previously that absorption of X-Rays on the way to the detector needs to be corrected for. There is is another effect: absorption of X-Rays causes the inner shell ionisation of the absorbing atoms and the subsequent generation of characteristic X-rays from the absorbing atoms. It raises the generated intensity over that produced by the direct action of the beam electrons. Therefore, the detected X-Ray intensity will be more than expected and this intensity increase has to be taken into account to yield the correct chemical composition. This effect can be induced by both characteristic X-Rays and Bremsstrahlung.

When the above three physical processes are taken into account in a quantitative analysis procedure, one is using the ZAF method. A separate correction factor is calculated for each effect (or matrix effects). The characteristic X-Rays measured from the specimen are ratioed to the intensity measured from a standard. The physical models yielding the correction factors Z, A and F described above are used to calculate iteratively inter-element matrix factors that multiply the unknown/standard intensity ratio to yield the concentration of the unknown relative to the standard [134]. Therefore, in a binary compound AB, A and B peak intensities are related to the concentrations of A and B by:

$$\frac{C_A}{C_B} = ZAF \times \frac{I_A}{I_B} \tag{3.2}$$

3.2 Electron Energy-Loss Spectroscopy (EELS)

Electron energy-loss spectroscopy provides a spectrometry complementary to EDX, enabling much better light element detection. It consists of the analysis of the energy disribution of electrons that have interacted inelastically with the specimen. The scattered beam of electrons is spectroscopically analysed to give an energy spectrum for the electrons after the interaction. Energy and hence intensity from the incident electron beam are absorbed by the matter under study. The nature of this energy absorption will depend on the precise composition and electronic structure of the specimen under

investigation. The general principle of EELS will first be explained before moving on to the description of the electron energy loss spectrum and the working principles of the spectrometer.

3.2.1 General principles

Electrons can interact in two manners with matter: elastically and inelastically. During scattering both the amplitude and phase of the incident electron wave may alter. When elastic scattering occurs, the direction of the electron velocity is changed, but its magnitude remains constant, so that the kinetic energy is unchanged. It is also generally coherent. Large angle scattering (greater than 5°) occurs through the coulombic interaction between the incident electron and the nucleus of the atom. It is also known as Rutherford scattering. If the electrons travel much farther from the nucleus and only interact with the screened nuclear field (by electrons) of an atom, then small-angle (a few degrees) elastic scattering occurs.

During an inelastic scattering event, not only is energy transferred to the target atoms and electrons but also any phase relationships between scattered waves are lost (incoherent scattering). As a consequence, the kinetic energy of some beam electrons decreases giving rise to energy losses. An inelastically scattered electron undergoes only slight angular deviation (up to a few mrads/tens of degrees), which means that contrary to EDX, a large fraction of the total possible signal can be collected by an electron spectrometer placed in the forward-scattering direction. It is the energy analysis of these inelastically scattered electrons that forms the basis for EELS.

The main types of inelastic scattering mechanisms are:

- Phonon excitation (heat).
- Plasmon excitation (valence electrons in a solid).
- Single electron excitation (inner and outer shell scattering).
- Direct radiation losses (deceleration of the electron beam in the Coulomb field of an atom (Bremsstrahlung radiation)).
- Excitation of conducting electrons leading to secondary electron (low-energy) emissions.

These different mechanisms are all associated with different energy levels. Some of them cannot even be detected, like phonon excitation. Indeed, the energy resolution of the very best current EELS systems (0.1 eV) is much higher than the phonon scattering

energy (0.03 eV) [135].

If the specimen is sufficiently thin to prevent any multiple inelastic scattering (or if the latter is corrected for), the majority of electrons suffers only a single inelastic scattering event during passage through the specimen. If not, there is a degradation of the ionisation edge information. "Sufficiently thin" means that the specimen thickness must generally lie in the 25-100 nm range (depending on the average atomic number of the specimen and the beam energy). If the specimen thickness is less than 25 nm, surface effects are increasingly likely and can modify low-loss EELS spectra [136]. Thickness is sometimes given as a fraction of the inelastic mean free path (IMFP). This better represents the average distance travelled by an electron between two inelastic scattering events and is inversely proportional to the inelastic cross section. It can be calculated by the use of either classical physics or wave mechanics. A commonly used expression for the IMFP is given by Egerton [137]:

$$IMFP(nm) = \frac{106 \times [(1 + E_0/1022)/(1 + E_0/511)^2 \times (E_0/E_m)]}{ln(2\beta E_0/E_m)} \tag{3.3}$$

where E_0 is the incident beam energy (keV), $E_m = 7.6 \times Z^{0.36}$ (Z is the average atomic number), β is the collection angle (mrad) and $(1+E_0/1022)/((1+E_0/511)^2$ is a relativistic correction factor. IMFP is expressed in nanometres.

The high background in the EELS spectrum generally restricts the relative detection limit to 1% or higher [134]. Quantitative analysis is based on physical models of inelastic electron scattering with empirical corrections for instrumental effects. The next section will detail the different regions of the electron energy loss spectrum.

3.2.2 The Electron Energy Loss Spectrum

The electron energy loss spectrum is composed of two main parts: a low loss and a high loss part. The first region extends from 0 to about 50 eV with several noticeable features. It contains a zero-loss peak (ZLP) which is made up from those electrons which have (1) not been scattered by the specimen, (2) suffered only phonon scattering ($\pm$0.03 eV) or (3) been elastically scattered. The energy width of the zero-loss peak is caused by the energy spread of the electron source (up to $\pm$2 eV for a thermionic W filament) and the energy resolution of the spectrometer. It is an excellent measurement of the energy resolution of a given experiment. A lower intensity peak is observed in the 20-30 eV region. It is associated with bulk plasmon excitations corresponding to collective, resonant oscillations of the valence electrons. Its energy is given by:

$$E_p = \frac{h}{2 \times \pi} \times \sqrt{\frac{Ne^2}{m_e \varepsilon_0}} \tag{3.4}$$

where N is the valence electron density, h the Planck constant, m_e the electron mass, e the electron charge and ε_0 the permittivity of free space.

Plasmon scattering has the largest cross section and it is by far the most common inelastic interaction occurring in materials [138]. The typical mean free path for the generation of a plasmon is about 50 nm, resulting in many electrons suffering from single-plasmon losses: only thicker specimens would show additional peaks at multiples of the plasmon energy, corresponding to the excitation of more than one plasmon by the incident electron. Plasmons can be imagined as soundwaves, since they are longitudinal oscillations which create regions of varying electron density. Other types of plasmons can be observed depending on the material under investigation or its geometry. Samples thinner than 20 nm or nanoparticles generally show surface plasmons. The presence of interfaces parallel to the beam direction (including possible contamination layer(s)) can give rise to interface losses such as interface plasmons [139] and gap states [140]. The low-loss region is generally used for thickness and electron density measurement. It is also used for deriving the dielectric function after Kramers-Kronig analysis of the single scattering distribution (SSD) obtained after zero-loss peak and multiple scattering deconvolution of the low-loss spectrum. It can then be correlated with optical measurements and band gap determinations in semiconductors/insulators.

The second region extends from about 50 eV to 2000 eV. Above a certain critical ionization energy E_c, excitation of electrons from well localised orbitals (core shells) at a single atomic site to previously unoccupied electron energy levels just above the Fermi level of the material arises. This region reflects the atomic character of the specimen, so that compositional data can also be derived. A continuous background on which the characteristic ionisation edges (rather than peaks in the low-loss range) are superimposed is particular to this region. Such a background arises from tails of plasmon excitation(s) combined with those of ionisation edges at lower threshold energies. Qualitative elemental analysis can be carried out simply by measuring the energies of the edges and comparing them with tabulated energies. A classification of EELS ionisation edges can be found in [141]. Since the ionisation process can impart more than the critical ionisation energy E_c needed by the core electron to escape the attraction of the nucleus, the final state of the excited electron will be in the range of possible energy levels above the Fermi level (E_F) giving rise to Energy-Loss Near Edge Structures (ELNES). Some electrons gain enough energy to

leave the atom and act as an electron wave which can be diffracted by the surroundings atoms. In the spectrum, it is seen as weak oscillations and fine structures beyond the first 30-40 eV of an edge and known as Extended Energy Loss Fine Structures (EXELFS). Analysis of this part of the spectrum can be performed to obtain the Radial Distribution Function (RDF).

3.2.3 The electron spectrometer

The intensity of the various electrons, i.e. those transmitted without loss of energy and those that have been inelastically scattered and lost energy, is obtained by dispersing the electrons with a magnetic prism, which separates spatially the electrons of different energies. This is the main feature of an electron spectrometer.

Several types of electron spectrometers are curently in use: the sector magnet spectrometer, the Castaing-Henry prism, the Ω filter and the Mollenstedt analyser. The sector magnet spectrometer is the most commonly used as it can be easily fitted to any TEM column. It consists of a sector magnet generating a homogenous magnetic field normal to the electron beam. According to the Lorentz equation, this causes the electron to bend with a radius R where R=mv/eB due to the magnetic force F defined as F=Bev where v is the electron velocity, B the magnetic vector value and e the electron charge. Therefore, electrons with different kinetic energies undergo a different Lorentz force and hence emerge from the spectrometer spatially dispersed. The object plane of the spectrometer is either the final projector crossover in TEM mode or the virtual image of the specimen in STEM mode. The spectrometer has a focusing action which results in the formation of a line spectrum at the spectrometer image plane and can be thought of as an optical component with its own properties and aberrations. Such aberrations have to be corrected by the user through quadrupole and sextupole magnetic lenses at the entrance and exit faces of the magnet. At the image plane is an array of silicon photodiodes where the whole spectrum is recorded at once in parallel. Like any other photodiode, they need to be calibrated before exposure to electron radiation. A schematic of a sector magnet spectrometer is shown in Fig. 3.4.

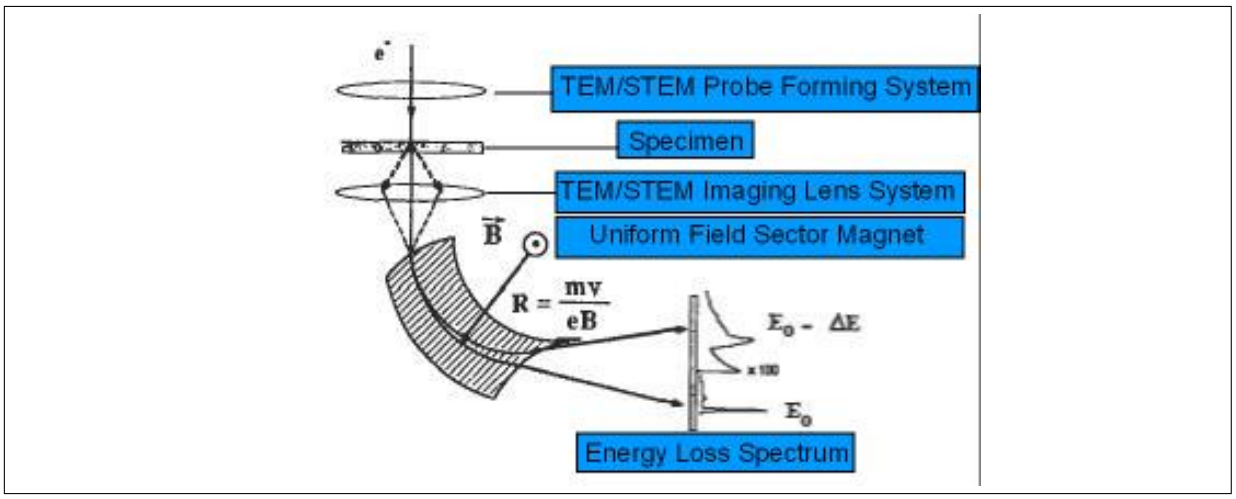

Figure 3.4 Schematic of an EELS spectrometer (sector magnet type) mounted on a TEM/STEM column. The spatial dispersion of different electron energies is obtained with a uniform field sector magnet resulting in the formation of a line spectrum at the spectrometer image plane.

3.3 Parameters affecting chemical microanalysis

3.3.1 Parameters affecting EDX experiments

3.3.1.1 Energy resolution

The FWHMs of the peaks give the energy resolution of the experiment. Depending on the element, the typical resolution of an EDX detector (Si-Li) is around 130 eV. This rather "poor" energy resolution arises from the statistics of electron-hole pair production and electronic noise in the processing chain.

3.3.1.2 Spatial resolution

EDX when performed in a TEM operating in STEM mode allows nanoanalysis to be performed at a much higher spatial resolution than in conventional imaging mode (smaller interaction volume) resulting from the combination of a very small electron probe of diameter d (about 1 nm width in STEM mode) and a very thin specimen limiting (high-angle) elastic scattering (beam spreading b). d is defined as the FWHM of the Gaussian electron density which can be experimentally measured from the viewing screen. The beam spreading/broadening b caused by elastic scattering is described by [142]:

$$b = 0.198 \times (\frac{\rho}{A})^{0.5} (\frac{Z}{E_0}) \times t^{3/2} \tag{3.5}$$

where Z is the atomic number, E_0 is the incident beam energy, ρ is the density, A is the atomic weight and t is the foil thickness. It is worth noting the strong dependence on t. A calculation shows that at 100 keV, a 100 nm thick sample (the typical thickness of a TEM sample) gives a beam broadening of the order of 10 nm. This is rather significant when small electron probes of a few nanometres diameter are used. Beam spreading can be restricted by making the specimen thickness no greater than a few times the elastic mean free path. In crystalline specimens, b can also be limited by orienting it in such a way that electron channelling down atomic columns occurs [143]. By combining d and b, it is now possible to come up with an expression [144] describing the diameter R of the interaction volume midway through the foil:

$$R = \frac{R_{max} + d}{2} \tag{3.6}$$

where

$$R_{max} = (b^2 + d^2)^{1/2} \tag{3.7}$$

is the width of the broadened beam at the exit surface of the specimen.

In a bulk specimen such as those analysed in a SEM, it is the contrary: the dimension of the beam-specimen interaction dominates over the incident beam diameter. Not only is the beam larger (about 10-100 nm) but also and more importantly, the electron beam spreads out in a pear-shaped ”interaction volume” below the sample surface due to elastic and inelastic scattering.

The radius R of the interaction of the interaction volume from which X-Rays are generated is defined as [145]:

$$R(\mu m) = \frac{0.068}{\rho} \times (E_0^{1.68} - E_c^{1.68}) \tag{3.8}$$

where ρ is the material density, E_0 the incident beam energy (keV) and E_c is the critical excitation energy for the characteristic X-Ray of interest.

3.3.2 Parameters affecting EELS experiments

3.3.2.1 Energy resolution

The overall energy resolution is mainly a function of the type of electron source, filament emission current, the spectrometer resolution, external fields and the energy dispersion

at the detector [146]. It is conveniently given by the FWHM of the ZLP for a given experiment.

3.3.2.2 Spatial resolution

In STEM mode, the spatial resolution is determined by eq. 3.6. As discussed previously, elastic scattering causes a broadening (b) of a focused electron probe, by an amount that increases with specimen thickness eventually limiting the spatial resolution of EDX. The effective broadening is less for EELS if an angle-limiting aperture (an SAED aperture) is used to eliminate electrons scattered through larger angles (in imaging or STEM mode). In conventional diffraction mode, the area from which the spectrum is taken is limited by the size of the selected area diffraction aperture (SAED). Nonetheless, the precision of the area selected using the SAED aperture is strongly affected by spherical and chromatic aberration of both the TEM objective and projector lenses. At last, in imaging mode, the diameter D of the analysed area is governed by both magnification M and entrance aperture radius R according to D=(2Rh_v)/(Mh_a) where h_v and h_a are respectively the distance from the projector lens to the viewing screen and spectrometer entrance aperture [146].

3.3.2.3 Signal-to-noise ratio (SNR) and Signal-to-background ratio (SBR)

The SNR or fractional noise is determined by the choice of a suitable detector integration time before data read-out. The integration time is chosen according to the number of electrons arriving at the detector. It is determined by the number of electrons falling on the anlaysed area which is related to: the incident beam energy, the brightness of the source, the emission current, the size of the condenser aperture and the collection angle. The SBR is dependent on the thickness and the collection angle as discussed below and should increase with the accelerating voltage. The SBR is also known as the “jump ratio” (see Fig. 3.5).

3.3.2.4 Collection angle

The collection angle should be chosen to ensure that the optical dipole selection rule is respected. It is so when collected electrons have transferred minor momentum ($\hbar.\overrightarrow{q} \sim 0$ where $\overrightarrow{q} = \overrightarrow{k_0} - \overrightarrow{k_f}$) upon collison with specimen outer shell electrons, limiting the observed electronic transitions to those in which the angular momentum quantum number (l) changes by ± 1. Typical collection angles of 10 mrads are used in the high loss regime while smaller collection angles (5 mrads$<$) are used in the low loss region, in particular

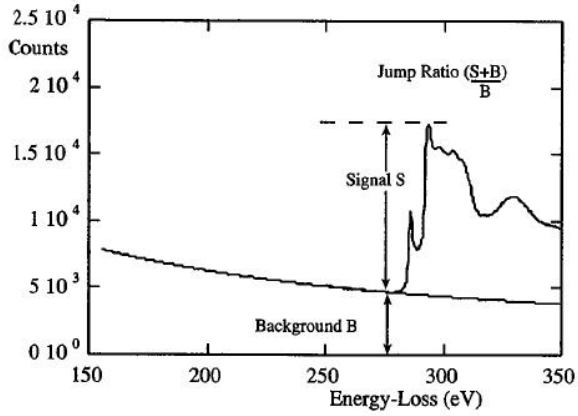

Figure 3.5 Definition of the jump ratio of an ionisation edge. For information, it should be about 5-10 at the carbon K ionisation edge provided the EELS system is aligned correctly [132].

if dielectric data are acquired. These selection rules originate from restrictions imposed on matrix elements of the electric-dipole operator [146].

3.3.2.5 Deconvolution procedures

With increasing sample thickness, there is an increasing probability of multiple inelastic scattering. This constitutes noise and can mask features in the spectrum. It is however possible to remove this multiple inelastic scattering by Fourier transform deconvolution. Two techniques are routinely employed depending on the energy-loss range [137]:

- Fourier-log method
- Fourier-ratio method

Fourier-log deconvolution is usually applied to low-loss spectra while the Fourier-ratio method is more suitable for high loss spectra [147]. If the specimen thickness is greater than 1 IMFP, the multiple scattering has appreciable intensity and gives rise to a redistribution of counts within the spectrum making features like ELNES or EXELFS difficult to observe. This redistribution of counts can be counteracted by deconvolution procedures like the Fourier-Ratio or Fourier-Log routines detailed. In addition, it is also necessary to deconvolute either an experimental spectrum (recommended) or a modeled zero-loss peak (ZLP) to suppress the effects of the ZLP tail on the spectrum. As with all deconvolution procedures, some noise added to the spectra is unavoidable.

3.3.2.6 Relativistic effects

Relativistic effects, also known as retardation effects, are not widely discussed in the literature. Among those are Cerenkov radiation which gives rise to an additional loss

visible on an VEELS spectrum as a bump, typically arising in the band-gap energy region of common semiconductors (2 - 3 eV). This occurs as soon as the speed of the probing electron exceeds the speed of light inside the probed medium [148] (i.e. $v>c_0/n$, n being the refractive index). Consequently, the VEELS spectrum is spoiled by effects which do not purely stem from the interaction beam/specimen impacting negatively on the accuracy at which band-gap measurements can be performed affecting eventually Kramers-Kronig analysis results. A few possibilities exist to circumvent such losses:

- decrease the accelerating voltage
- record VEELS spectra with a non-zero momentum transfer ($\overrightarrow{q} \neq 0$)
- use the difference method described in [149]

The first method is the easiest but is not always experimentally possible (the EELS spectrometer may need some realignment at lower accelerating voltage). The second one is also experimentally difficult but for another reason: the intensity is very weak making the acquisition time much longer. More importantly, optical data from such spectra acquired under those conditions cannot be compared with the standard optical method where $\overrightarrow{q} \sim 0$. The third method is the most versatile. The user can still derive optical data from EELS measurements even if decreasing the accelerating voltage is impossible.

3.3.3 Parameters affecting both EELS and EDX experiments

3.3.3.1 Contamination

Specimen contamination in the electron microscope is a complicated process [150] and is not always well understood. The microscope itself is not really a detectable source of contamination, but dirty specimens definitely are. The contamination of specimens in the electron microscope is due to a complex process involving adsorption of impinging molecules, subsequent migration of the molecules across the surface and finally conversion to carbon film by ionisation and polymerization [151]. This problem of contamination in the normal operation mode of a TEM can be ameliorated by the use of a specimen cold stage. It acts in reducing the partial pressure of hydrocarbons in the vicinity of the specimen [150] and in preventing the build-up of carbonaceous contamination under a small probe by slowing thermally activated hydrocarbon transport across the specimen sufaces. Contamination is an important issue when very small beam diameters are used, as for example in STEM mode [152]. It has been shown that the kinetics of contamination build up depend solely on the beam size (the smaller the

beam, the faster the build up) and not on the current density of the probe [153]. Dirty specimens can also be cleaned by baking in the microscope [154] but this is not always experimentally feasible. A high level of contamination can not only affect the final results but also the spatial resolution of chemical microanalysis since beam spreading in surface contamination layers will also occur with dirty specimens. Such a layer creates an interface with the specimen which could give rise to interface/surface plasmons spoiling EELS spectra.

3.3.3.2 Radiation damage and surface sputtering

In most organic and some inorganic materials, the practical limit to spatial resolution is set by radiation damage. The main damage mechanism is radiolysis or ionisation damage which involves the breaking of chemical bonds as a result of inelastic scattering. Such damage occurs even for low-energy incident electrons as those used in High Resolution Electron Energy Loss Spectroscopy (HREELS) [155]. For metallic and semi-metallic specimens, there is no radiolysis but displacement damage (due to elastic scattering) occurring at high radiation dose above a given displacement energy threshold T_d (10-30 eV range). It arises through a knock-on momentum transfer from the incident electrons to atomic nuclei and results in permanant displacement of the atom from its original site. The energy transferred (T_T) to an atom by a fast incident electron of mass m_0, is given by the expression [156]:

$$T_T = \frac{2E_0(E_0 + 2m_0c^2)sin^2(\phi/2)}{Mc^2} \tag{3.9}$$

where E_0 is the kinetic energy of the incident electron, M is the mass of the nucleus, c is the speed of light and ϕ is the scattering angle.

The displacement of surface atoms, i.e. surface sputtering at the exit surface of a solid, has an even lower energy threshold T_s [157](5-10 eV range). Surface sputtering can become an issue as the specimen thickness decreases which is often wanted for the best images and chemical microanalysis spatial resolution. It can induce changes in the surface chemistry and affect quantitative microanalysis. Sputtering is expected to be quite rapid in a focused aberration-corrected electron probe, where the current density can exceed 106 A.cm^{-2} . Table 3.6 [1] lists some value of T_T, T_d and T_s for several atoms.

Element	<----------T_T----------> (100kV	200kV	300kV	400kV	T_d	T_s
Al	8.93	19.5	31.6	45.3	16	3.5-7.0
Ti	5.00	11.0	17.8	25.5	15	4.9-9.8
V	4.73	10.3	16.72	24.0	29	5.3-10.6
Cr	4.63	10.1	16.38	23.5	21	4.1-8.2
Fe	4.31	9.40	15.25	21.8	16	4.3-8.6
Co	4.08	8.91	14.45	20.7	23	4.4-8.8
Ni	4.10	8.94	14.5	20.8	21	4.5-9.0
Cu	3.79	8.26	13.4	19.2	18	3.5-7.0
Zn	3.69	8.03	13.03	18.7	16	1.4-2.8
Nb	2.59	5.65	9.17	13.2	24	7.5-15.0
Mo	2.51	5.47	8.88	12.7	27	6.8-13.6
Ag	2.23	4.87	7.90	11.3	28	3.0-6.0
Cd	2.14	4.67	7.58	10.9	20	1.2-2.4
Ta	1.33	2.90	4.71	6.75	33	8.1-16.2
Pt	1.23	2.69	4.37	6.26	33	5.9-11.8
Au	1.22	2.67	4.32	6.2	36	3.8-7.6

Figure 3.6 Typical sputtering and displacement energy thresholds (eV) at different accelerating voltages [1].

3.4 Summary of the project

This project will detail electro-optical properties of ITO thin films deposited by PLD under different growth conditions in two different chambers. The thickness, the substrate temperature and the oxygen temperature are varied independently. This enables the determination of sets of optimal growth conditions.

However, this study will give more emphasis on the microstructure rather than on only optimising electro-optical properties. A variety of microstructures can be generated by these different growth conditions which in turn give rise to various physical properties. This link is rarely studied and yet, it is essential to achieve good electro-optical properties. This is what this study is intending to do.

Chapter 4

Experimental method

A description of the experimental techniques and methods will be given in this chapter. Since the project extends from thin film deposition to thin film characterisation, a wide range of techniques were used. They will be described briefly except where particular experimental difficulties were encountered.

4.1 Pulsed Laser Deposition

During the course of the project, two different chambers with a slightly different set-up were used as illustrated in Fig. 4.1.

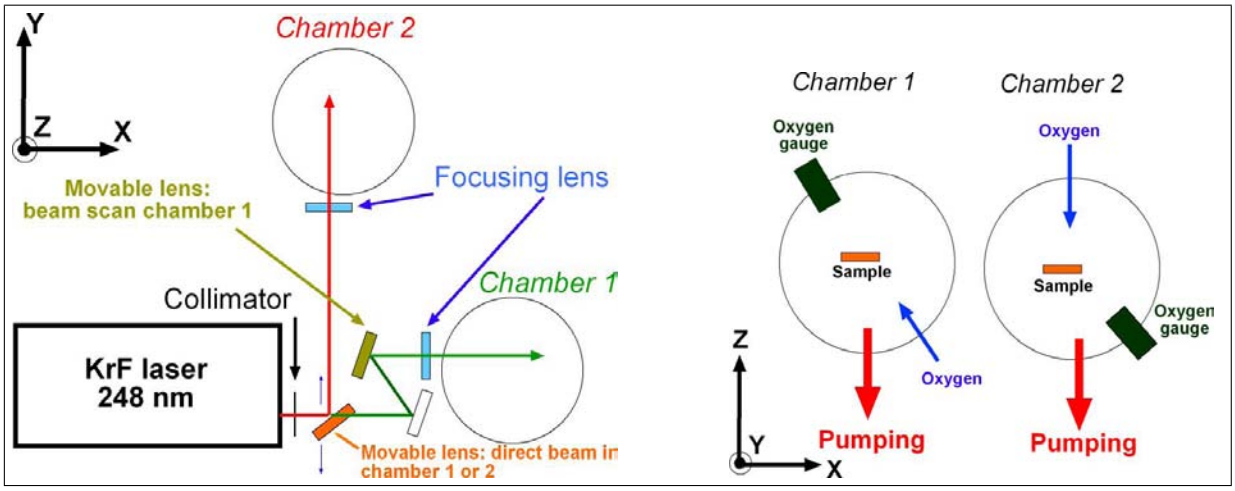

Figure 4.1 The two different PLD set-ups used during the course of the project.

Both chambers are manufactured by Neocera, a US based company. The ”first” and ”second” chamber is simply the chronological order. They will be referred as “chamber 1” and “chamber 2” in the rest of this thesis. Fig. 4.1 illustrates and Table 4.1 sums up the differences between chambers 1 and 2.

In chamber 1, the starting deposition parameters were chosen from previous work at the University of Birmingham [8]. A slightly different set of optimal growth parameters was found. “Optimal” parameters were defined in terms of the highest [Transparency over the visible range]/[resistivity] ratio of the thin film obtained. They are presented in

Table 4.1 Experimental differences between chamber 1 and 2. "Bottom" refers to the bottom of the deposition chamber where pumping takes place.

	Chamber 1	Chamber 2
Oxygen input	Bottom	Directly onto the substrate via a nozzle
Oxygen pressure measurement	Top	Bottom
Lateral beam scan	Yes	No

Table 4.2. Initially, optimal experimental parameters found in chamber 1 were directly transposed to chamber 2. Owing to the slightly difference set-up presented in Fig. 4.1, the parameters were refined. They are also listed in Table 4.2.

Table 4.2 Optimal conditions used in chambers 1 and 2. Conditions from previous work [8] are also shown.

Parameter	Chamber 1 in [8]	Chamber 1	Chamber 2
Oxygen pressure (mT)	10	10	5
Substrate temperature (°C)	300	200	200
Distance target-substrate (mm)	63	63	63
Number of pulses	5000	5000	5000
Energy density (J/cm^2)	14	7.5	10

The oxygen flow rate and pumping speed were identical in both chambers. The ITO films were deposited on 1.1 mm thick glass (Corning 1737) substrates (10×10 mm). Corning 1737 is an Alkaline Earth Boro-Aluminosilicate glass type with a very low content of alkaline ions. This is relevant since such ions can diffuse into the thin films at high temperature and ruin its electrical properties. Boro-Aluminosilicate glass is mainly composed of silica (70 - 80 %), boric oxide (B_2O_3) and aluminium oxide (Al_2O_3). Boron gives greater resistance to thermal shock. These substrates were ultrasonically cleaned using HCl, deionized water, acetone and ethanol sequentially and mounted on a heater with silver paint to ensure good thermal contact. Before depositions, the substrate was kept one hour at a given T_s to ensure that the temperature on the substrate surface is about the same as the one on the thermal heater, i.e. thermal equilibrium is reached. This is important since glass has a low thermal conductivity. The target supplied by π-Kem and manufactured by LTS (Chemical) via Hot Isostatic Pressing (HIP) resulting in a 2 cm diameter sintered ceramic in a slightly reduced oxygen atmosphere. It is composed of 90 wt.% In_2O_3 and 10 wt.% SnO_2, which corresponds to 17 mol % SnO_2, or to a 9.2% contribution of Sn to the total cation content ([Sn]/([Sn]+[In])). It is of high density and purity (>99.9%). The exact same target was used in both chambers. The latter was ablated by a 248 nm KrF excimer laser (Lambda Physik LPX 300).

Energy density (E_d) is a fundamental parameter in PLD thin film growth. The laser energy inside the chamber and the laser beam area on the target were thus carefully monitored prior to each deposition. The laser was focused onto the target within the vacuum chamber through a quartz glass window using a spherical lens with a focal length of 30 cm. The beam was incident at an angle of 45° on a rotating target at 10 rpm. Target rotation was necessary to avoid creating craters on the surface, to maximize material utilization and to produce homogeneous films over a large area. In addition, the laser beam was rastered over the target in chamber 1. Prior to each deposition, the target was polished and pre-ablated with 750 pulses to remove any contaminant from the surface. A base vacuum of less than 10^{-5} Torr was assured by means of a turbomolecular pump. During deposition, oxygen ambient gas was introduced into the chamber to maintain the desired oxygen pressures. The oxygen flow was left on after the deposition and the sample was left to cool to RT at a cooling rate of 3°C/min prior to removal. 5000 laser pulses were fired onto the ITO target. This ensured 250 nm ± 20 nm and 320 nm ± 20 nm thick films in chambers 1 and 2 regardless of the substrate temperature. However, pulse numbers were adjusted accordingly when $P(O_2)$ was varied. No post deposition heat treatment was performed on any of the films reported in this study.

4.2 X-Ray Diffraction

X-Ray diffraction is a powerful non-destructive technique to determine the crystal structure of materials. Two different X-ray set-ups were used: a classical $\theta/2\theta$ Bragg-Brentano and a glancing angle geometry.

4.2.1 Bragg-Brentano geometry

X-Ray diffraction was primarily used to characterize the crystal structure of the films immediately after deposition and was performed on a conventional Bragg-Brentano ($\theta/2\theta$) diffractometer (Philips PW 1120) with CuK_α radiation (1.54 $\mathring{A}$). The spotsize on the sample was about 4 mm^2. Constructive interference of the radiation reflected from successive planes occurs whenever the path difference is an integral number n of wavelengths λ. Thus the condition for constructive reflection of the incident radiation and appearance of a peak is:

$$2dsin\theta = n\lambda \tag{4.1}$$

This equation is known as Bragg's law where d is the lattice inter-planar spacing, λ the

wavelength of the incoming X-ray beam, θ the angle of diffraction and n is an integer. XRD peaks were fitted with a Gaussian profile with Origin 6.1 in order to obtain precise peak parameters such as peak position (related to interatomic spaces) and peak width or FWHM (grain size, strain, crystalinity information). Finally, the preferred orientation of the thin films was qualitatively evaluated by calculating the texture coefficient (TC_{hkl}):

$$TC_{(hkl)} = \frac{I_{(hkl)}}{\sum_{i=1}^{n} I_n(hkl)} \tag{4.2}$$

where $I_{(hkl)}$ is the measured intensity of a particular (hkl) plane, $I_n(hkl)$ is the intensity of the n^{th} peak and n is the number of significant peaks observed in the corresponding diffractogram.

4.2.2 Glancing angle X-Ray Diffraction (GAXRD)

For thin film studies, the "conventional" Bragg-Brentano X-ray diffraction geometry is not always adequate when studying possible other phases or particular peak shapes, for example. This is partly because of the presence of the interfering effect of the substrate giving rise to an amorphous signal which could mask low intensity features. A useful geometry is therefore based on a low (up to a few tens of degrees) X-ray incidence angle, so as to make sure a greater proportion of the signal stems from the thin films alone rather than the substrate plus the thin film. Many thanks to Dr. Blackburn (Physics department, the University of Birmingham) for the opportunity to use the GAXRD diffractometer (Siemens D5000). Cu$K_{\alpha 1}$ radiation (1.54 $\mathring{A}$) were selected and focused by a Ge (111) monochomator. The geometry of such measurements is shown in Fig. 4.2.

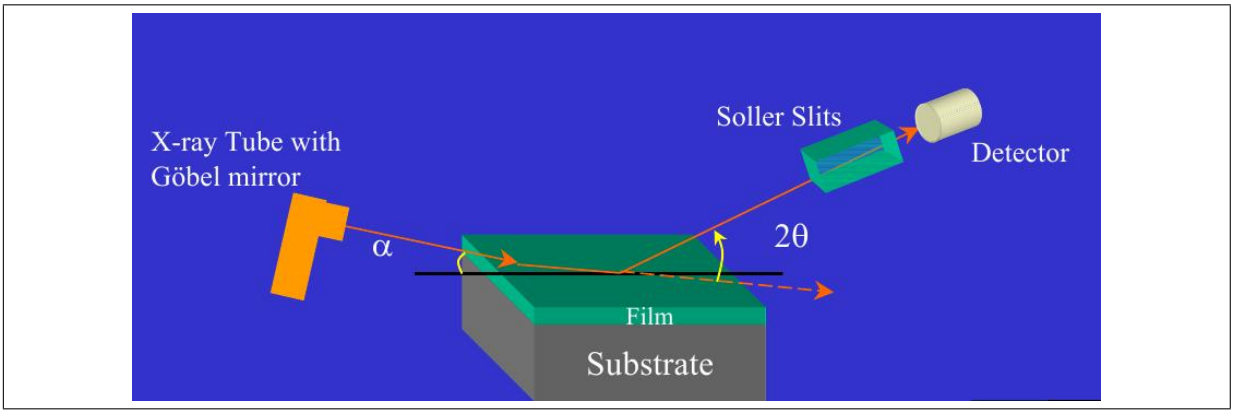

Figure 4.2 Principle of GAXRD: parallel, monochromatic X-Rays fall on a sample surface at a fixed angle of incidence (α) and the diffraction profile is recorded by detector scan.

The penetration depth of the X-Rays is defined as the length at which the field has fallen

by a factor e^{-1}. It is a function of the incidence angle α. The lower the incidence angle, the lower the penetration depth. Such values were obtained from the Center for X-Ray Optics (CXRO) [158]. Peak shape versus thickness probed was investigated via different glancing incident angles from α=0.5 to 20°.

4.3 Electron Microscopy

4.3.1 Transmission Electron Microscopy (TEM)

4.3.1.1 The instrument

An electron micoscope consists of an electron gun and an assembly of lenses all enclosed in an evacuated column. Electrons are charged particles and interact strongly with matter, thus generating a wealth of signals (see Fig. 4.3) all giving specific information about the material under investigation.

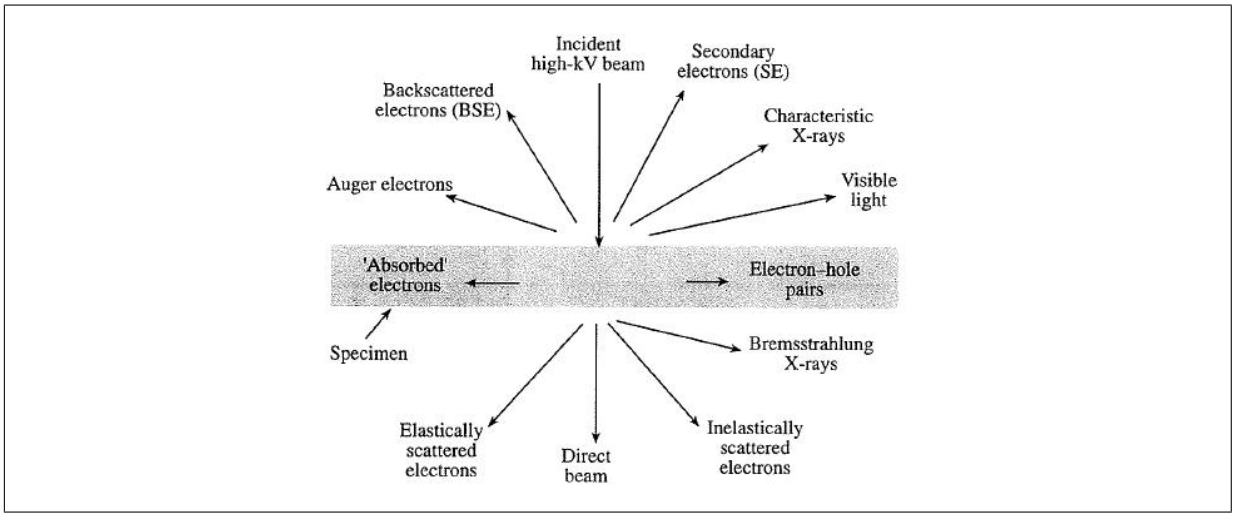

Figure 4.3 Signal generated when a high-energy beam of electrons interacts with a thin specimen. Taken from [138].

TEM imaging and chemical microanalysis were performed on an FEI Tecnai F20 FEG and a Philips CM20 microscope both operating at a beam voltage of 200 kV. TEM can be operated in image and diffraction modes and both modes give complementary information.

Prior to introduction of the sample into the TEM column, it was cleaned by a Fischione Oxygen/Nitrogen plasma cleaner for five to ten minutes to remove contaminants.

4.3.1.2 EDX analysis

EDX analysis was performed on an FEI Tecnai F20. Spectra were acquired using a large area (80 mm^2) X-Max Silicon Drift Detector (SDD) manufactured by Oxford Instruments and interfaced to INCA software. The higher capture angle (or solid angle) corresponding to a large area detector makes possible many more counts than the "classical" 10 mm^2 Si(Li) detector. In addition, its design enables unlimited count rates. More accumulated counts improve very much the statistics of each measurement and make quantification of low concentration elements like Sn in this project more accurate.

Spectra were acquired in STEM mode. The objective aperture was removed during analysis. The microscope was operated with a clean, top-hat C2 diaphragm (30 μm diameter). Prior to each analysis, it was ensured that the hole counts from stray radiation from the illumination system were negligible over the energy range of interest (0 - 40 keV). The specimen was tilted to 17° and an extraction voltage of 4400 V was used. Since sample thickness and roughness affect the measured X-Ray intensity owing to variations in the path lengths of X-Rays emerging from the sample on their way to the detector, relative and absolute sample thicknesses were carefully monitored by EELS measurements to compute an absorption correction factor.

Table 4.3 sums up the experimental conditions used when acquiring EDX spectra in image and STEM mode.

Table 4.3 Conditions used in acquiring EDX spectra in STEM mode. The specimen was tilted to 17° and the display resolution was 20 eV/ch over a 0 - 40 keV energy range.

Microscope parameters	STEM mode
Condenser aperture size (μm)	30
Extraction voltage (V)	4400
Count rate (cps)	3200
Acquisition time (live time) (s)	200

EDX spectra were generated from In_2O_3 and SnO_2 nanopowder specimens manufactured by Alpha Cesar. Their characteristics are listed in Table 4.4. Standard In, Sn and O profiles were made from these spectra to replace the standard profiles initally stored in the software element library.

Table 4.4 In_2O_3 and SnO_2 nanopowder characteristics used as standard specimens.

	In_2O_3	SnO_2
Purity (%)	99.994	99.996
Formula weight (g/mol)	277.64	150.69
Melting point (°C)	850	1630
Density (g/cm^3)	7.18	6.09

Quantifying EDX results also requires careful determination of sensitivity factors or "k-factors" (see section 3.1.3.1). A typical k-factor determination involves taking many spectra from different parts of a specimen to check both the chemical homogeneity and the stability of the specimen under the beam. It was also ensured that there were enough counts (a few tens of thousands typically) in each peak for good count statistics. In order to determine k(In), k(Sn) and k(O), In_2O_3 and SnO_2 nanopowder specimens were used. Spatial resolution was not in that case at all an issue so that the beam was not fully focused during analysis. Indium was always chosen as the ratio standard element, hence k(In)=1. In the first place, k(O) was measured from the analysis of In_2O_3. Then, k(Sn) was measured from SnO_2 using the previously measured k(O). K lines were used for quantification. As mentioned by Bellingham et al. [159], one must be careful about the absorption correction on oxygen as the oxygen content varies (change in density of the films).

A large number of spectra were acquired in image mode from different nanoparticles to ensure they were chemically homogeneous over large areas. The thickness of the analysed area calculated via EELS was in the 60 - 70 nm range and the density was known in each case. This enabled correction of the k factors for X-Ray absorption in the In_2O_3 and SnO_2 specimens. Each measurement corresponded to a different area. The exact same experimental conditions were used for all the measurements. Finally, it was ensured that several measurements made at the exact same place gave the same results. The results of the k factor measurements are listed in Table 4.5.

Table 4.5 k(Sn) and k(O) sensitivity factors measured from EDX spectra generated from In_2O_3 and an SnO_2 nanopowder specimens. The analysed area were 60 - 70 nm thick. This value was fed in the INCA software to account for X-Ray absorption in the In_2O_3 and SnO_2 layers on the way to the EDX detector. Indium was chosen as the ratio standard element: k(In)=1.

	In_2O_3	SnO_2
Area number	k(O)	k(Sn) using k(O)=0.07
1	0.07	1.2
2	0.06	1.1
3	0.08	1.4
4	0.06	1.3
5	0.10	1.2
6	0.07	1.2
7	0.08	1.4
8	0.05	1.3
9	0.09	1.2
10	0.05	1.5
Average	0.07	1.28
Standard deviation	0.02	0.12

Based on Table 4.5, k(Sn)=1.28 and k(O)=0.07 were used for TEM EDX quantification analysis in this study.

4.3.2 Scanning Electron Microscopy (SEM)

4.3.2.1 The instrument

A scanning electron microscope (JEOL 7000, Fig. 4.4) was used to study the surface morphology and chemistry of the films.

Figure 4.4 Scanning Electron Microscope JEOL 7000 at the University of Birmingham.

When the samples were very smooth and hence with low topological contrast, they were

tilted to the maximum angle experimentally possible (5°) with respect to the incident electron beam and the working distance was decreased to 6 mm from 10 mm (default setting). The samples were all mounted on metallic SEM stubs with double-sided sticky tape. Silver paint was used to provide a path for the electrical current from the surface down to the metallic stub, thus preventing charging of the specimen. Prior to introducing the specimen into the SEM column, the surface of the specimen as well as that of the SEM stub was cleaned with ethanol. Spatial resolution can deteriorate drastically by contamination of the specimen, and/or apertures. Contamination results when the beam interacts with organic volatiles (from oil diffusion pumps, rubber vacuum seals, vacuum grease, fingerprints and samples) and causes them to polymerize. Polymerization occurs primarily where the beam is most intense (crossover points), such as at the apertures and above all, on the specimen.

4.3.2.2 EDX analysis

All the EDX analyses were performed on the JEOL 7000. INCA software was used to acquire and process the EDX spectra. The following X-ray lines were used for quantification: In L (3.2870 keV), Sn L (3.4440 keV) and O K (0.5249 keV). The overvoltage parameter, $U=E_0/E_c$ must obviously exceed unity for any X-ray generation to take place. (E_0 is the incident beam energy and E_c is the minimum energy for X-ray generation from a given line). In fact, a value of at least U=2 is desirable [134]. Hence, the microscope was operated at 7 kV resulting in a 96 μA current. This choice was motivated by Monte Carlo simulations of the electron trajectories inside the specimen and above all, the intensity of the detected oxygen X-ray versus depth at 7 kV, since the substrate also contains oxygen. The simulations were performed using CASINO version 2.42 [160]. The model consisted of an Indium Oxide (In_2O_3) layer (thickness 250 nm - chamber 1 and 350 nm - chamber 2) on top of a semi-infinite Alkaline Earth Boro-Aluminosilicate glass substrate. The densities were respectively 7.18 g/cm^3 and 2.40 g/cm^3. The initial beam diameter was 10 nm. The results are presented in Figs. 4.5 and 4.6.

The intensity of the detected oxygen X-ray versus depth at a beam voltage of 7 kV is presented in Fig. 4.7.

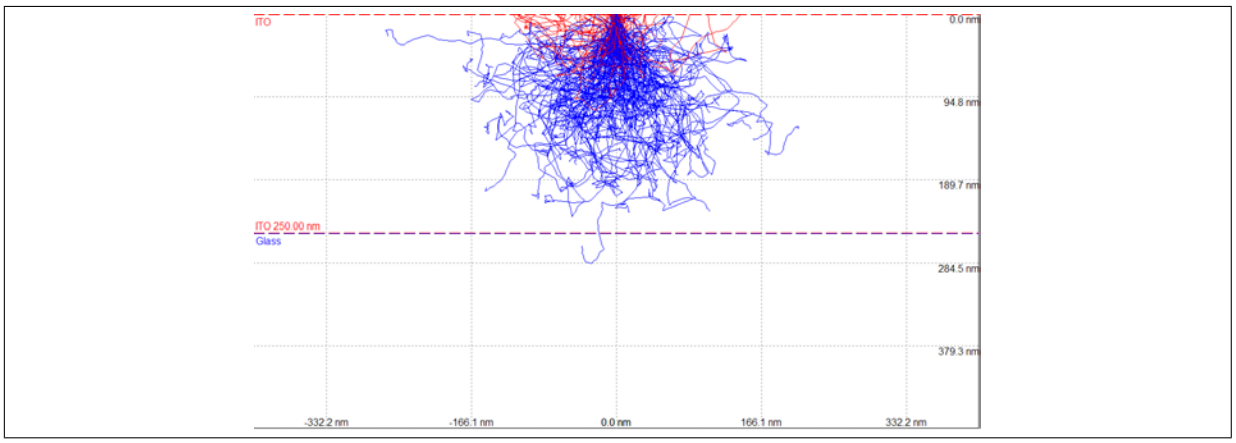

Figure 4.5 Monte Carlo modelling of beam trajectories in an In_2O_3 layer with total thickness 250 nm on a glass substrate at an accelerating voltage of 7 kV. 300 trajectories are represented. Backscattered electrons are represented in red.

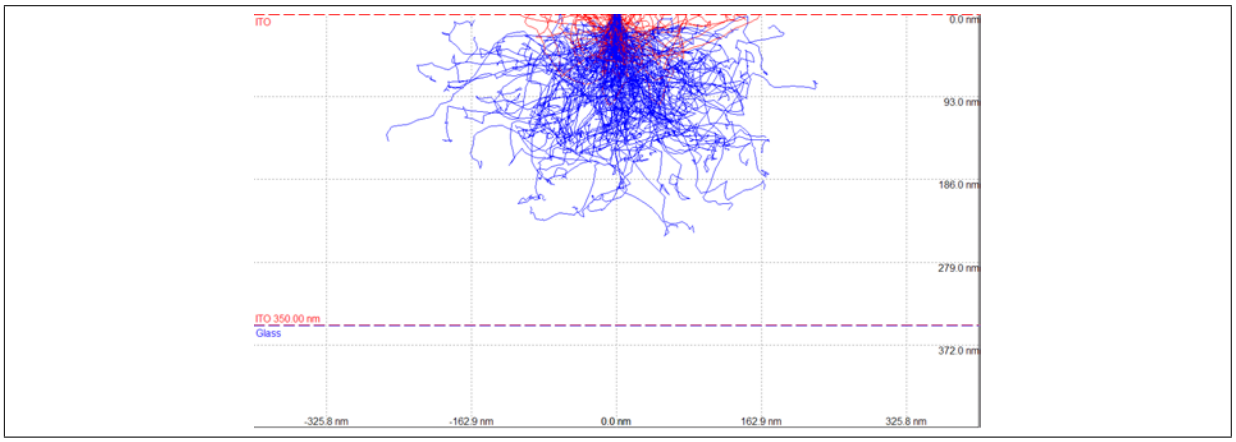

Figure 4.6 Monte Carlo modelling of beam trajectories in an In_2O_3 layer with a total thickness 350 nm on a glass substrate at an accelerating voltage of 7 kV. 300 trajectories are represented. Backscattered electrons are represented in red.

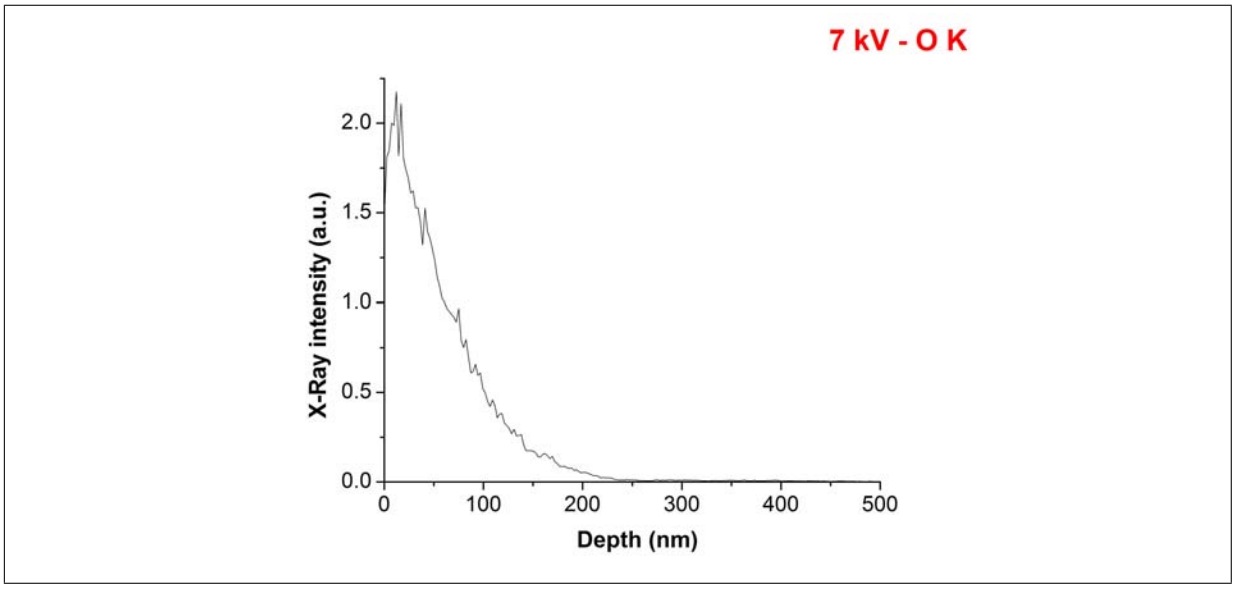

Figure 4.7 Detected X-ray intensity versus depth for oxygen (K line) at an accelerating voltage of 7 kV. Results are derived from previous Monte Carlo modelling for an In_2O_3 layer with total thickness of 350 nm on a glass substrate.

The Monte Carlo simulations (Figs. 4.5 - 4.6) and Fig. 4.7 confirm that the influence of the substrate is minimal (in terms of oxygen contribution) at both 250 and 350 nm, provided an acceleration voltage of 7 kV is used. This was confirmed by the absence of Silicon peaks.

The working distance (the distance of the sample from the objective lens) was kept at 10 mm due to EDX detector - sample stage geometry constraints. A highly polished surface is required for accurate quantitative analysis, since surface roughness would cause undue random absorption of the generated X-ray signal, which is impossible to account for in the quantification procedure. Nonetheless, all our ITO thin films were sufficiently smooth (a few nanometres roughness) that such an effect could be neglected.

Prior to each measurement, the system was optimised ("quant optimisation" option in INCA software) since ambient temperature changes can alter the gain/exact peak positions of the system and the microscope beam current varies with time. It was performed via the acquisition of a spectrum from a pure titanium sample.

The default standard In, Sn and O peaks used during the quantification procedure (matching process) were replaced by In, Sn and O peaks acquired experimentally from InAs, pure Sn and Al_2O_3 standard specimens respectively. Hence, InAs, Sn and Al_2O_3 were used as chemical standards.

The bulk ITO target was not used as a chemical standard because its composition was not exactly known. Finally, when Sn is in solid solution in the In_2O_3 matrix, ITO can be written as $In_{2-x}Sn_xO_3$. Hence the nominal (In+Sn)/O atomic ratio should be 0.66. With 10 wt.% of SnO_2 in the matrix, the nominal In/Sn atomic ratio was calculated to be 9.85.

4.3.2.3 EELS measurements

EELS measurements were performed with a Gatan 666 parallel electron energy-loss spectrometer attached to an FEI Tecnai F20 Schottky field emission gun transmission electron microscope, which offers an energy resolution of 0.8 eV when operating at 200 keV (University of Birmingham). Another set of EELS measurements was performed at Daresbury in the SuperSTEM laboratory (University of Liverpool). Measurement details are presented in the next two paragraphs.

4.3.2.3.1 Measurements at Birmingham The spectrometer consists of a magnetic prism spectrometer where aberrations are corrected using quadrupole and sextupole lenses through the Gatan EL/P software (version 3.0). The microscope was operated in conventional diffraction mode. Only low loss spectra were acquired (0-50 eV). Operating in conventional diffraction mode presents two advantages:

- large enough area can be selected (up to a few hundreds of microns square)
- reduced problem associated with chromatic aberration in the objective and projector lenses which can result in differing collection efficiencies at different energy losses [146].
- the acceptance angle β is easy to compute.

In diffraction mode, the spectrometer object is the demagnified image of the specimen in the final projector lens and so the spectrometer is said to be image coupled. The angle of acceptance at the specimen, β, is defined by the radius of the spectrometer aperture, R, which was selected to be 1 mm. For inellastically scattered electrons in conventional diffraction mode, β is defined as:

$$\beta = \frac{h_V R}{h_A L} \tag{4.3}$$

where L is the camera length (for the viewing screen) and h_V and h_A are the distances from the projector lens crossover to the viewing screen and spectrometer entrance aperture respectively. In an FEI Tecnai F20, $\frac{h_V}{h_A}$=0.718. L was chosen to be 150 mm giving β=4.78 mrads ensuring the dipole selection rule to be verified.

The area from which the spectrum is taken is limited by the size of the selected area diffraction aperture (SAED). The smallest aperture was chosen (10 μm diameter). It is large enough to select several grains/crystallites and associated defects but not too large to select an area where the thickness would not be uniform resulting in less precise deconvolution/background removal procedures. However, the precision of the area selected using the SAED aperture is strongly affected by spherical and chromatic aberration in both the TEM objective and projector lenses. It was not an important issue in this work since “any” area containing a few tens of grains/defects could be selected. The extraction voltage was reduced down to 3800 V to reduce the electron energy spread and hence improve energy resolution. No drift or contamination problems were ancountered as the beam was spread (conventional diffraction mode). The smallest condenser aperture was generally used for several reasons:

- Degree of beam coherency was improved.
- Effective removal of stray scattering which can contribute artefacts to the EELS spectrum.

Table 4.6 sums up the experimental conditions used when acquiring low-loss spectra.

Table 4.6 Experimental conditions used acquiring low-loss spectra in conventional diffraction mode.

Condenser aperture size (μm)	30
Entrance aperture radius (R) (μm)	1
Camera length (mm)	150
Collection angle (mrads)	4.78
Energy resolution (eV)	0.9/1

4.3.2.3.2 Measurements at Daresbury The SuperSTEM used ("SuperSTEM 1") is based on the Cambridge VG HB 501 dedicated STEM and has Quadrupole-Octupole corrector retrofitted within the column. It enables electron-optic aberrations up to 3^{rd} order to be corrected. Spatial resolution up to $1\mathring{A}$ and 0.3 eV energy resolution on a UHV ENFINA spectrometer were achieved. The microscope was operated at 80 kV (cold FEG emitter) to circumvent any Cerenkov radiation spoiling low-loss EELS spectra in TCO materials. A probe semi-convergence angle of 20 mrads was used after aberration correction. The acceptance angle β was chosen to be 6 mrads for consistent Kramers-Kronig analysis. Prior to introduction inside the column, the sample was baked at $100°$C for one hour to remove any residual contaminants. The EELS spectra were all corrected for dark-current and readout noise.

4.4 Atomic Force Microscopy (AFM)

A Dimension 3100 nanoscope AFM (Veeco, UK) was used to study further surface morphology and roughness. Its principle is shown in Fig. 4.8.

It operates Nanoscope v5.12 software for both real-time analysis and post-capture image processing. The AFM was housed on vibration isolation tables and all images were acquired while operating in Contact Mode under ambient conditions, using triangular pyramidal-tipped Si_3N_4 cantilevers (DNP-S, Veeco, UK) with nominal spring constants of 0.58 N.m^{-1} and nominal tip diameters of 20 nm. Contact mode alows direct surface profiling by scanning a tip (Si_3N_4), capable of following topology at atomic-scale resolution. It does so by using a sharp tip mounted on a flexible cantilever. When the tip comes within a few $\mathring{A}$ of the sample's surface, repulsive Van Der Waals forces

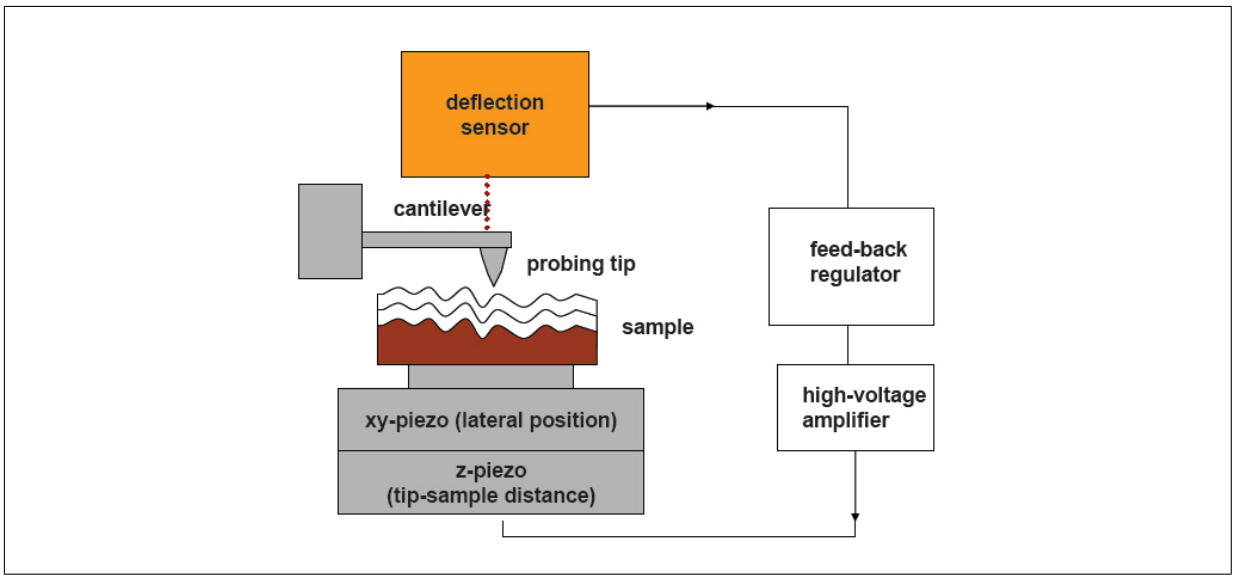

Figure 4.8 Atomic Force Microscope principle. Illustration of the feedback loop [161].

between the atoms on the tip and those on the sample cause the cantilever to deflect. This deflection is monitored by a laser beam falling on the cantilever and reflected onto a position-sensitive photodetector (PSPD). A feedback loop is then formed making the force applied to the cantilever constant. The level of contamination can be important causing image acquisition to deteriorate if no caution is taken. Therefore, each sample was cleaned with ethanol and blown dry with nitrogen gas prior to analysis. Samples were mounted on an SEM stub with with double-sided sticky tape. The roughness of the film can be calculated from the AFM image. The Root Mean Square (RMS) roughness is the standard deviation of the Z values within a given area [162].

$$RMS(mm) = \sqrt{\frac{\sum_{j=1}^{N}(Z_j - Z_m)^2}{N-1}} \tag{4.4}$$

where Z_m is the mean surface level within a given area, Z_i is the current Z value and N is the number of pixels (related to the number of measurements) within a given area.

4.5 TEM sample preparation

TEM preparation from ITO coated onto a glass substrate is challenging due to the nature of glassy materials: cracks inititate very easily and ion milling causes significant heating during the process owing to the low heat conduction of such materials. Specimens were prepared for both plan-view and cross-sectional TEM mainly by the wedge polishing method. When necessary, ion beam milling was used for cleaning purposes. Therefore, only the wedge polishing method will be detailed. A tripod polisher (South Bay Technology - Model 590) on which the specimen was mounted with glue was used. A

lapping machine (South Bay Technology) was also used for the polishing. Fig. 4.9 is an illustration of the tripod polisher used.

Figure 4.9 Tripod polisher - South Bay Technology - Model 590 [2].

For plan-view samples, a set of six diamond films with roughnesses of 30, 15, 6, 3, 1 and 0.5 microns were used sucessively to polish the sample down to a few hundred nanometres. Each step of the polishing should remove the scratches from the previous one. The final stage involved the use of silica solution (Syton) on a velvet cloth. This step is sometimes called chemical mechanical polishing (CMP). Syton HT-50 manufactured by Testbourne Ltd. is a solution of colloidal silica with particles ranging from 0.02 to 0.05 micrometres. The sample was removed from the tripod by dipping in acetone ($\sim$20 minutes). It was then glued onto a copper grid. Post-cleaning can be critical and essential after colloidal silica polishing. Plasma cleaning in combination with ion beam milling (low kV and sputtering angle, five minutes on both sides) were used for that purpose when necessary. For cross-section sample preparation, the same process described above was used except that both sides had to be polished to make the interface flat. Figs. 4.10 and 4.11 sum up the processes:

1. Make an angle by changing the leg graduations (Fig. 4.10)

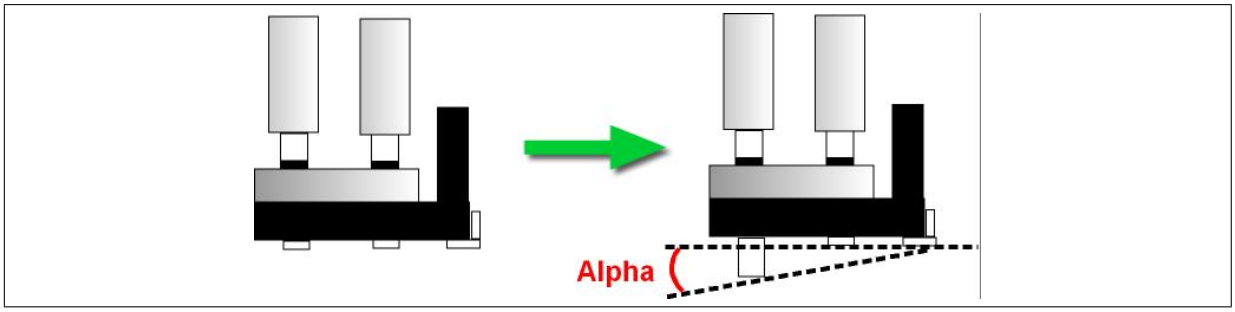

Figure 4.10 Creation of an angle by wedge polishing.

2. Cut a part of the film with a diamond saw into small pieces of approximately 1$\times$3 mm. In order for this part to be representative of the film, it has to be in the middle

of the sample (Fig. 4.11 1)).

3. Glue these two pieces with the film facing each other, thus making a ”sandwich” (Fig. 4.11 2) and 3)).
4. Polish both sides of this “sandwich”.
5. One of the sides is polished down to electron transparency.

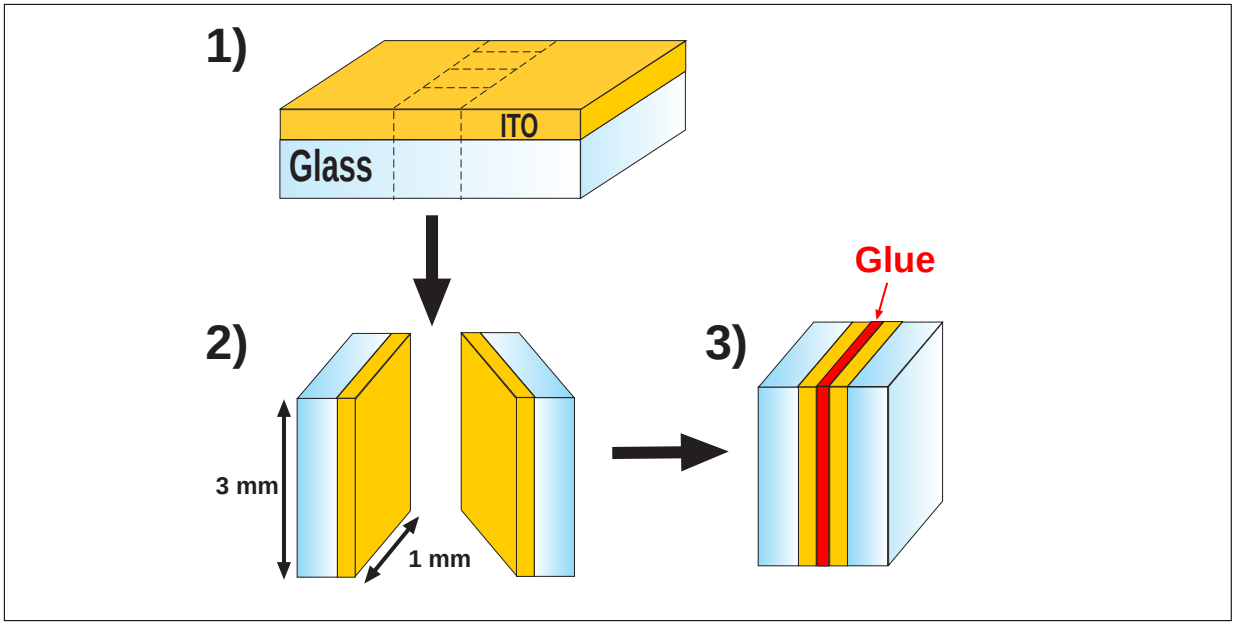

Figure 4.11 TEM sample preparation: the main steps to make a cross section

An optical microscope was regularly used along with the interference fringe technique, a well-established non destructive method [163], to control accurately the specimen thickness during the thinning process. The appearance of black and white interference fringes shows that the specimen thickness is no more than a few tens of nanometres and hence electron transparent. The main advantage of the wedge polishing method is that less structural damage is introduced using tripod polishing as compared to ion milling [164]. By this method, one can get quite a large thin area and a clean surface [165]. However, it is a very time consuming process and the failure rate can be quite high.

4.6 Electrical measurements

4.6.1 Four point probe

The resistivity ρ was measured using a four-point probe. The principle of a Four-Point-Probe is shown in Fig 4.12.

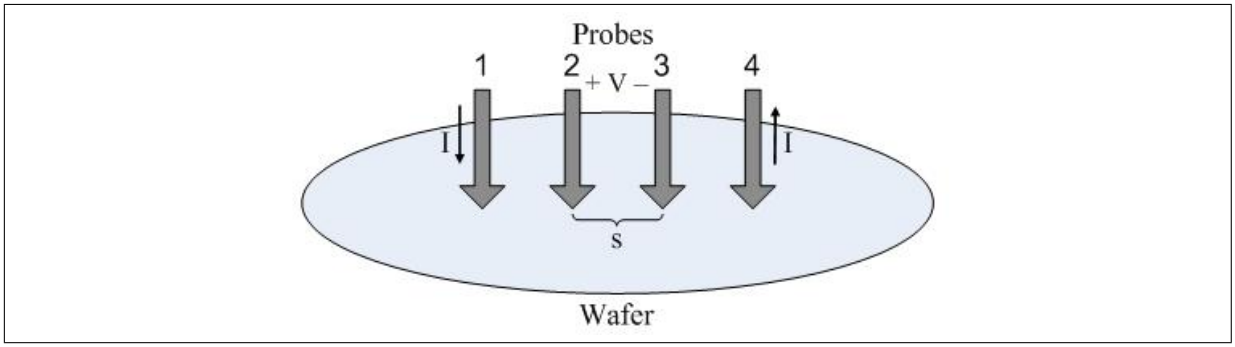

Figure 4.12 Principle of four point probe measurements. A current (I) is passed through two outer probes and the voltage (V) is measured between the inner probes allowing the measurement of the film resistivity when its thickness is known.

A current is passed through through two outer probes and the voltage measured via the inner probes, allowing the measurement of the film resistivity provided the thickness is known. Measurements are made on finite sized areas and therefore correction factors have to be used based on the sample geometry. This correction factor depends on the sample thickness and edge effects (i.e. location of the probe on the sample). Correction factors are well known and tabulated [166]. The resistivity ρ is given by:

$$\rho = \frac{\pi}{ln(2)} t(\frac{V}{I}) f_1 f_2 \tag{4.5}$$

where t is the film thickness, V the potential difference between electrodes 2 and 3 and I the current between electrode 1 and 4. f_1 and f_2 are respectively a finite sample thickness and sample width correction factors. The four-point-probe used has four tungsten carbide tips at 1 mm spacing (s=1 mm). The lateral dimension was d=10 mm (size of the specimen). Since d/s=10, a finite width correction f_2 needs to be applied; according to [166], f_2=0.90. However, since t<<s, f_1=1 (no correction needed).

4.6.2 Hall effect measurements

Hall measurements were performed at the department of Chemistry at the University of Oxford. Special thanks are given to Dr. Kuznetsov for allowing me using the Hall effect measurement set-up. If an electric current flows through a conductor in a magnetic field, the magnetic field exerts a transverse force called a “Lorentz force” on the moving charge carriers. This tends to push them to one side of the conductor. These charges build up at the sides of the conductors and balance the magnetic influence, producing a measurable voltage between the two sides of the conductor. The Hall voltage V_H is given by: $V_H = \frac{IB}{Ned}$ where I and B are respectively the current and magnetic field intensity, N is the density of mobile charges (holes or electrons), e is the electron charge and d is the

film thickness (see Fig. 4.13).

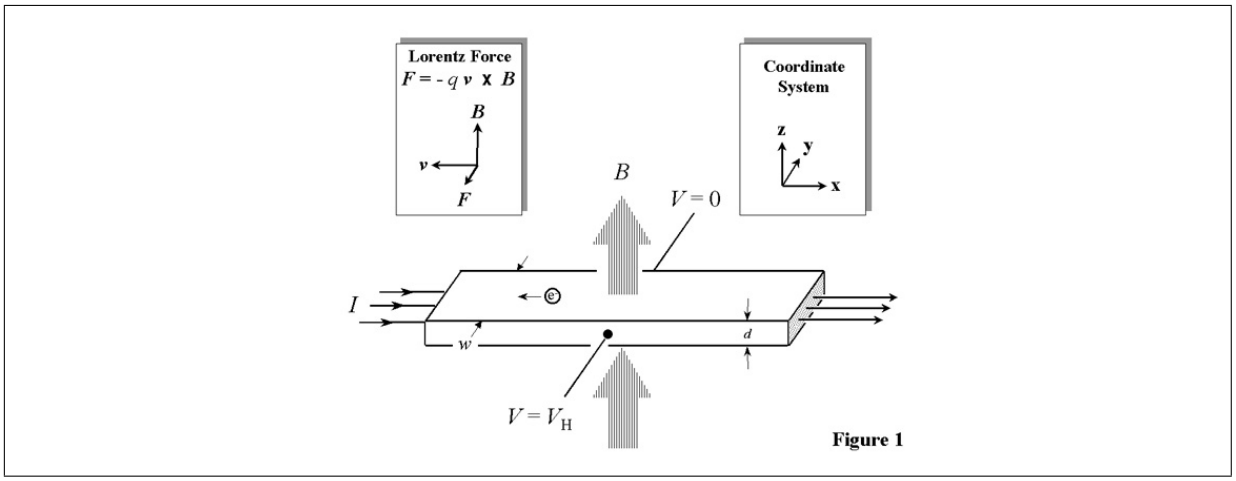

Figure 4.13 Hall effect principle [3].

Thus, by measuring the Hall voltage V_H and from the known values of I, B, q and d, it is possible to determine the carrier density N. As for the Hall mobility, it is given by $\mu_H = \frac{V_H}{R_s I B}$ where R_s, the sheet resistance, can be determined using Ohm's law R_s=V/I (see Fig. 4.14).

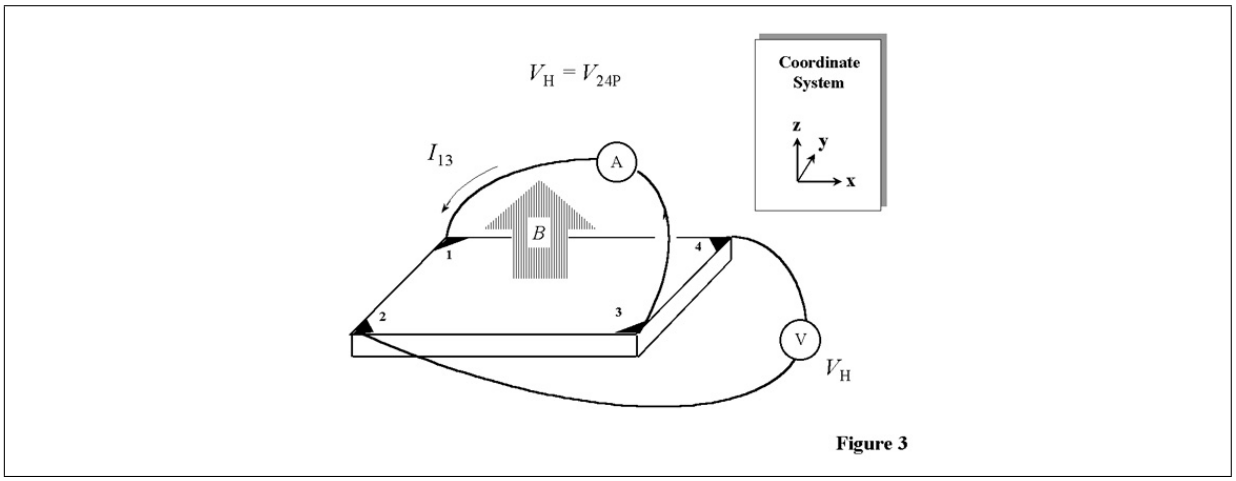

Figure 4.14 Experimental set-up to determine the sheet resistance [3].

Therefore, the bulk resistivity $\rho = R_s d$ can be calculated from R_s. Thus, in order to determine both the carrier density N and the mobility $\mu_H = \mu$, a combination of resistivity and a Hall measurements is needed: this is known as the Van Der Pauw technique. Regarding the ITO sample, it was ensured that the average diameters of the contacts and the sample thickness were much smaller than the distance between the contacts. The contact made with indium metal has to be ohmic so as to obtain consistent and reproducible measurements. The sample is mounted on a holder as shown in Fig. 4.15.

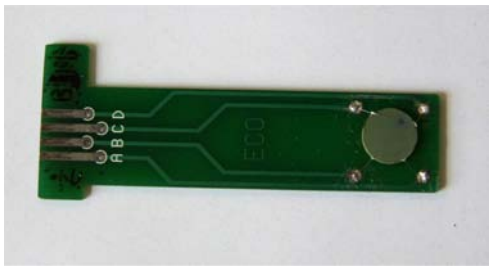

Figure 4.15 Hall sample holder used for measurements. Contacts with the film were made with indium and the wires were made of copper.

Previous formula were intially developed for single crystal materials where the Hall mobility (μ_H) is set equal to the drift mobility (μ_d):

$$\mu_H = r\mu_d \tag{4.6}$$

where r is a scattering factor which lies betwenn 1 and 2 [23]. The simplification r=1 is widely accepeted for polycrystalline and high carrier concentration specimens on the basis that other uncertainties of interpretation are probably greater than any uncertainty in r.

4.7 Optical measurements

The transmittance of the films was measured with a UV-visible spectrometer. An ellipsometer was also used to derive optical constants like the refractive index and extinction coefficient. More details are given in the following two sections.

4.7.1 UV and Visible Spectroscopy

Transmittance measurements were performed on a single beam Jenway 6315 UV/Vis scanning spectrophotometer operating in the 198 to 1000 nm range. Wavelength resolution and accuracy were respectively 1 nm and +/-2 nm. A 2 nm scan interval was used. It consists of a light source (Xenon lamp), a monochromator (diffraction grating to produce a range of wavelengths) and a detector (photodiode). “Direct” transmittance was measured as no integrating sphere (measuring diffuse and hence total transmittance) could be used with this set-up. Calibration was performed prior to each measurement and consisted in taking a reference spectrum with no sample in the measurement chamber. This process also enables residual noise to be effectively suppressed. Finally, the transmittance value measured at a given wavelength for a sample is compared with the transmittance through a reference sample (the air). Fig. 4.16

shows how the different elements of a spectrophotometer are organised.

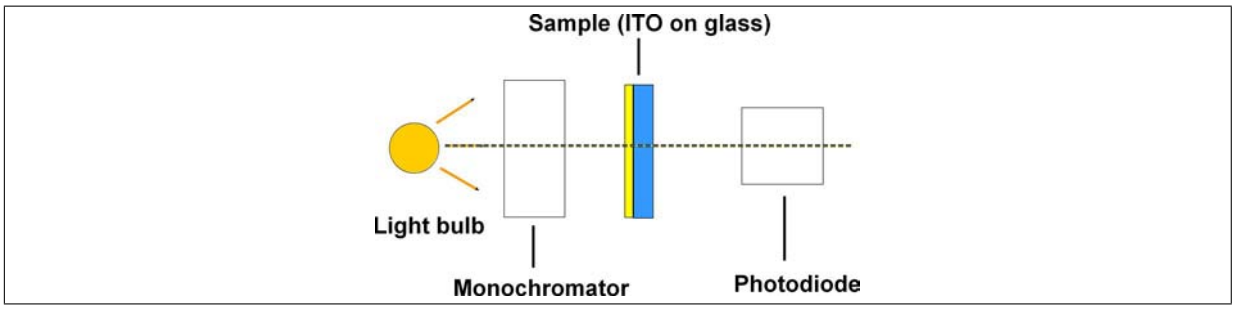

Figure 4.16 Schematic of a single beam spectrophotometer.

4.7.2 Ellipsometry

Ellipsometric measurements were performed at the department of Chemistry at the University of Birmingham. Special thanks are given to Dr. Bowen for all the measurements presented in this study. A spectroscopic ellipsometer (Jobin-Yvon/Horiba, UK) operating with DeltaPsi2 v. 2.0.8 software at an angle of incidence of 70° was used. The wavelength range for the incident light was 250 - 800 nm (or 1.5 - 5 eV). All measurements were made under conditions of ambient temperature, pressure and humidity. Precautions were taken to avoid performing measurements on visibly defective locations on the sample (if any).

The principle of the ellipsometer shown in Fig. 4.17.

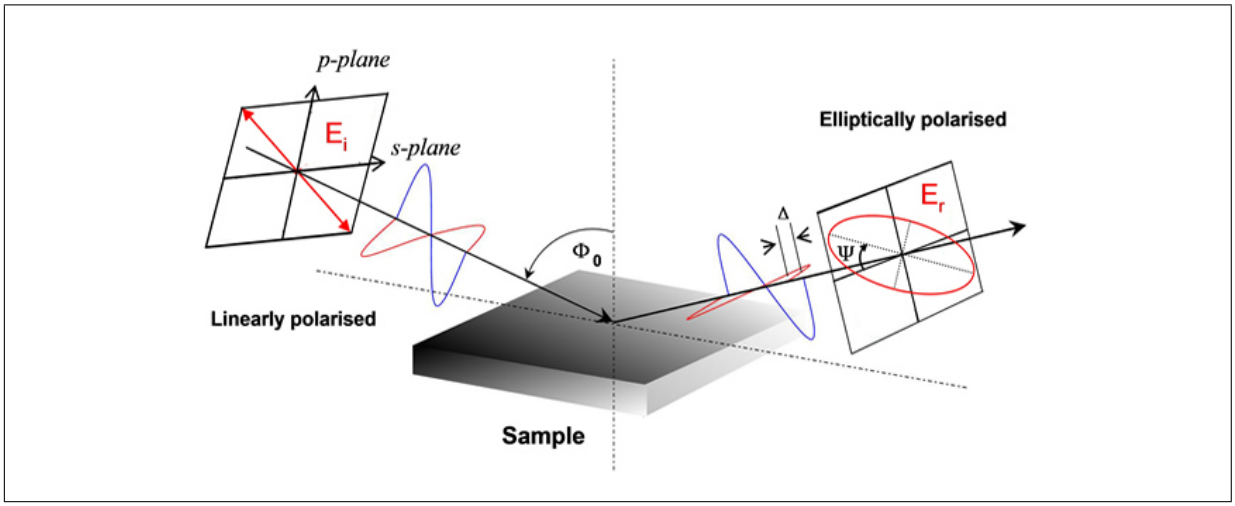

Figure 4.17 Principle of spectroscopic ellipsometry: ellipsometry uses the change in polarisation of light upon reflection from a material to determine optical constants like the real part (refractive index n) and the imaginary part (extinction coefficient k) of the complex refractive index of a material [167].

Linearly polarised light at non-normal angles of incidence becomes elliptically polarised on reflection from the material with asymmetric intensity difference ($\tan(\Psi)$) and phase

difference (Δ). The ellipticity, or ratio of minor to major axis of the ellipse, and the orientation of the reflected beam are determined by the relative phase difference Δ and azimuth Ψ. These values are measured using ellipsometry and they are related to $\frac{R_p}{R_s}$, the complex ratio of the p- and s- polarized components of the reflected amplitudes (complex Fresnel ratio):

$$tan(\Psi)e^{\Delta i} = \frac{R_p}{R_s} \tag{4.7}$$

The ellipticity of the reflected light depends on the optical constants of the thin film and its thickness (i.e. SE is an indirect measurement technique.). It makes it a powerful non-destructive technique to investigate accurately thin film optical properties (complex refractive index n_c/dielectric constant ε) and even non-optical properties (thickness or roughness for example) down to a few $\mathring{A}$. SE derives its sensitivity from the measurement Δ which contains phase information.

Calculation of the film thicknesses was performed for each measurement, based on a three-phase ambient/thin film/glass model, in which the thin film was assumed to be isotropic and modelled using a simple classical layer model, with the initial thickness varied using a multiguess iterative calculation procedure. Surface roughness was not taken into account owing to the very smooth characters of the thin films under investigation (a few nanometre RMS roughness). The correct interpretation of the measured data (Ψ and Δ) relies on theoretical model fittings with sample structure and optical/physical constants previously known (or guessed) by the user. Such a model must be able to describe the interaction of light with the material under investigation. Two models were used in this work: the Cauchy and Lorentz models. The thickness was the by-product of these models and the fitted thickness was initially compared with the measured one (direct measurements made under the SEM and/or TEM) to test how well the simulations are reproducing the physical parameters.

4.7.2.1 The Cauchy model

For dielectric function modelling in a transparent region (ε_2 or k$\sim$0), the Cauchy (or Cauchy absorbent) model is commonly used [168] and n(λ) and k(λ) are defined by:

$$n(\lambda) = A + \frac{B \times 10^4}{\lambda^2} + \frac{C \times 10^9}{\lambda^4} \tag{4.8}$$

$$k(\lambda) = D \times 10^{-5} + \frac{E \times 10^4}{\lambda^2} + \frac{F \times 10^9}{\lambda^4} \tag{4.9}$$

where A, B, C, D, E and F are fitting parameters and λ is the wavelength.

The real (ε_1) and imaginary (ε_2) parts of the dielectric function ε are obtained by data conversion of (n,k) using the two following equations: ε_1=n^2-k^2 and ε_2=2nk

The fitting of the experimental data (Ψ_{Exp} and Δ_{Exp}) to the modelled outputs (Ψ_{Theory} and Δ_{Theory}) is done by minimizing the mean-square error (MSE) χ^2 defined as:

$$\chi^2 = \frac{1}{2n-m-1}\sum_{i=0}^{n}[(tan\Psi^i_{Theory} - tan\Psi^i_{Exp})^2 + (cos\Delta^i_{Theory} - cos\Delta^i_{Exp})^2] \qquad (4.10)$$

where n is the number of Ψ/Δ pairs and m is the number of free parameters. The lowest χ^2 corresponding to the fitting process is taken as the correct model outputs.

4.7.2.2 The Lorentz model

The dielectric function ε of ITO can be divided, in most cases, into a number of terms each representing different excitation mechanisms: ε=ε_∞+ε_s+ε_{FC}+ε_{VE} where ε_{FC} and

ε_{VE} are the dielectric contributions of the valence electrons and free carriers, respectively. ε_s/ε_∞ is the low/high frequency dielectric constant and includes all other polarisation processes at low/high frequency. The contribution of valence and free electrons can be described respectively with Lorentz oscillators and a Drude term. The dielectric function ε is expressed as:

$$\varepsilon = \varepsilon_\infty + \varepsilon_s + \frac{(\varepsilon_\infty - \varepsilon_s)\omega_0^2}{\omega_0^2 - \omega^2 + i\gamma_0\omega} + \frac{\omega_p^2}{-\omega^2 + i\gamma_D\omega} + \sum_{j=1}^{2}\frac{f_j\omega_{0j}^2}{\omega_{0j}^2 - \omega^2 + i\gamma_j\omega} \qquad (4.11)$$

where ε_∞ is the high frequency contribution to the dielectric constant, ε_s is the static dielectric constant (material response to a static electric field), ω is the photon frequency, ω_{0j} is the jth resonant frequency, f$_j$ the jth oscillator strength, and γ_j is the jth damping constant. ω_p is the plasma frequency due to free carriers. The two Lorentzian oscillators describe interband transitions while the Drude term describes the contribution of intra-band transitions (free electron transitions in the conduction band). The fit parameters in eq. 4.11 are ε_∞, ε_s, ω_{tj} and γ_j (including γ_D and γ_0). The fitting of the experimental data (Ψ_{Exp} and Δ_{Exp}) to the modelled outputs (Ψ_{Theory} and Δ_{Theory}) is also done by

minimizing the MSE χ^2.

4.8 X-ray photoelectron spectroscopy (XPS)

The measurements were made at the department of Chemistry at the University of Birmingham. Dr. Bowen is acknowledged for the measurements presented in this work. XPS analysis of the thin films was performed using a custom-built instrument with an Al K_α X-ray source, providing a monochromatic X-ray beam with an incident energy of 1486.68 eV in a vacuum of $\sim 1\times10^{-8}$ mbar and with a circular spot size of ~ 4 mm^2. Samples were immobilised onto stainless steel sample holders using double-sided carbon sticky tape (Shintron tape, Agar Scientific, UK). X-Rays illuminate an area of a sample causing electrons to be ejected with a range of energies and directions.

The electron optics consists of electrostatic lens units to collect a proportion of these emitted electrons due to the X-Ray bombardment. They are transferred through the apertures and focused onto the analyzer entrance slit. Electrostatic fields are established to only allow electrons of a given energy (also called “pass energy”) to arrive at the detector slits and onto the detectors themselves. Low resolution survey spectra were obtained using a pass energy of 150 eV over a binding energy range from 0 to 1200 eV in 1 eV increments. High resolution spectra were obtained using a pass energy of 20 eV with 0.1 eV increments. A dwell time of 1 sec was employed when collecting data from each binding energy increment for all measurements. Peaks were referenced to the C 1s peak (286 eV) so as to correct eventual shifts due to carbon contaminated surfaces.

Chapter 5

Results

In this chapter, the physical properties of the pulsed laser deposited ITO films are reported. These films were deposited under different experimental of conditions. One set was deposited at different thicknesses (t), the second was deposited at various substrate temperatures (T_s) and, in the third set, the oxygen pressure ($P(O_2)$) was varied. Each of the above sets occupies a section. For each of them, any microstructure change and its relationship with physical property change will be systematically exposed and detailed. During the second half of the project, another PLD chamber (referred to as "chamber 2") was used along with a slightly different set-up. Results from this chamber will also be presented and compared with the first chamber ("chamber 1"). Any differencies are discussed. The chapter begins by discussing the influence of thickness and substrate temperature before moving on to the influence of Oxygen pressure on microstructure and physical properties.

5.1 Influence of thickness

5.1.1 Results from chamber 1

Thickness variation and its impact on electro-optical properties were studied in previous work [8] in the department using films deposited in in chamber 1. A brief summary of those results is given below. The interested reader is invited to look at the reference provided for more detailed information. Thickness was changed by varying the number of pulses from 3000 to 30000 and was observed to increase linearly with the number of pulses. Film orientation was influenced as the number of pulses increased: the (222) preferred orientation observed up to 5000 pulses was increasingly changed to a (521) orientation and the film tended to become more polycrystalline. As thickness increased, films tended to show a higher degree of polycrystallinity. Resistivity decreased up to 9000 pulses then remained unchanged from 9000 to 30000 pulses. The optical transparency at 636 nm was also impacted as it decreased almost linearly with increasing thickness. Finally, the film surface was found to be rougher as the number of pulses increased.

Similar work was repeated in the second chamber, although Hall effect and optical measurements over the whole visible spectrum were added and will now be described.

5.1.2 Results from chamber 2

The thickness (t) was changed by varying the number of pulses. In this study, 500 to 15000 pulses in total were fired. Other parameters like $P(O_2)$ and T_s were kept constant. Table 5.1 summarises the growth parameters used in this section. In the following, the number of pulses will be converted into thickness.

Table 5.1 Summary of ITO growth parameters by varying the number of pulses

Temperature	200°C
T-S distance	63 mm
Laser fluence	10 J/cm^2
Laser frequency	10 Hz
Oxygen pressure	5 mT

Table 5.2 summarises samples grown under the conditions listed in Table 5.1.

Table 5.2 Summary of ITO growth parameters by varying number of pulses

Sample number	Number of pulses	Thickness (nm)
110	500	47
91	1000	69
96	2500	172
53	5000	327
100	9200	654
107	15000	1467

The thicknesses listed in the previous table were evaluated via direct measurements. For that purpose, cross-section SEM samples were prepared, micrographs of two examples of which are given in Fig. 5.1. Despite the small thickness of the thinnest sample ($\sim$50 nm), its thickness could still be measured with reasonable confidence.

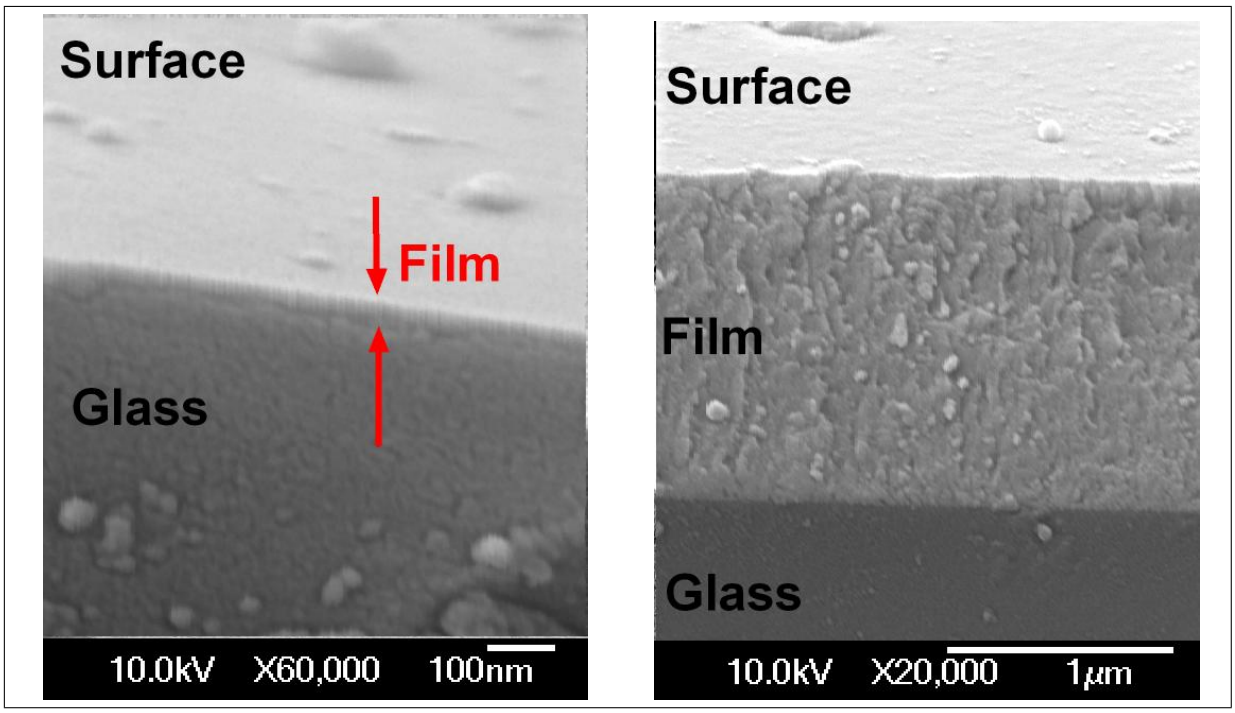

Figure 5.1 Cross-sectional SEM micrographs of a film grown with 500 pulses (left). A resulting thickness of 47 nm is evaluated; when 15000 pulses are fired, a resulting thickness of 1467 nm is observed (right). Other deposition parameters used are listed in Table 5.1.

The results are plotted in Fig. 5.2, which enables the calculation of the deposition rate in chamber 2 at T_s=200°C and P(O_2)=5 mT.

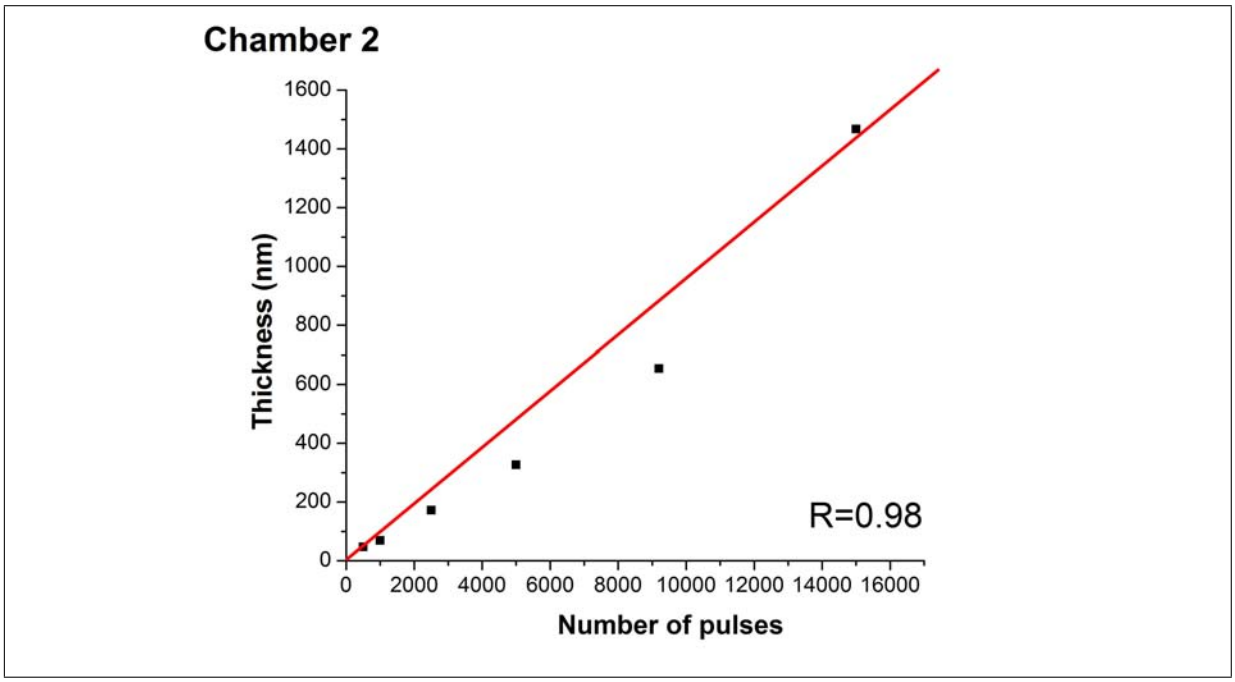

Figure 5.2 Thickness of ITO thin films deposited in chamber 2 by varying the number of pulses from 500 to 15000; deposition parameters used are listed in Table 5.1. The coefficient correlation R is shown.

As in [8], thickness is observed to vary linearly with the number of pulses, a linear regression giving 0.09 nm/pulse. In alternative terms, with a laser frequency of 10 Hz, a deposition rate of 54 nm/min is calculated. The variations of structural and electrical properties with film thickness (t) are now presented taking into account previous results on thickness.

5.1.2.1 Structural property and surface morphology of ITO films deposited by varying the thickness

Structural properties were studied by XRD while surface morphology was studied by AFM. XRD patterns are presented in Fig. 5.3 (left).

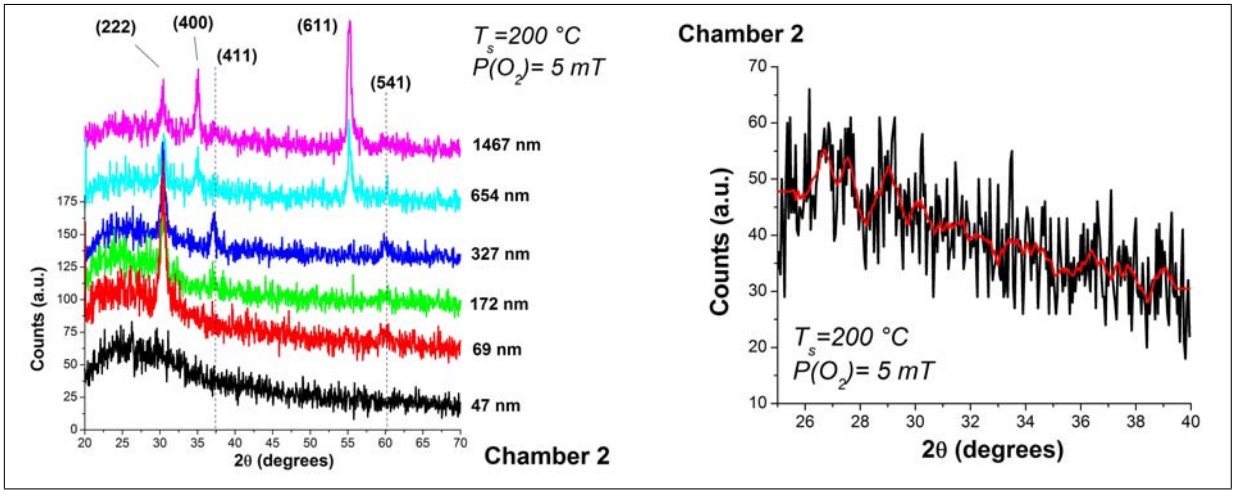

Figure 5.3 XRD patterns of ITO thin films deposited for varying thickness (left); high resolution XRD scan for 2θ=25 - 40° (right) choosing 10s/step (step size=0.05) instead of 1s/step for the sample deposited with 500 pulses (t∼47 nm). A Savitzky-Golay smoothing [169] is also shown on the same graph (red curve). The thickness varied from 47 to 1467 nm; other deposition parameters used are listed in Table 5.1.

At 47 nm, no evidence for crystallisation is evident, based on the XRD pattern presented in Fig. 5.3 (right). That means that the film is either amorphous or its thickness is so low that any XRD peak would be difficult to identify above the noise level resulting from the glass substrate and the instrument. This last hypothesis is unlikely, as an increase in acquisiton time failed to show any peak. However, between 69 and 327 nm, films developed a strong (222) orientation. As the ITO films grow thicker, they become increasingly polycrystalline with a slight (611) texture. This is in agreement with previous results obtained at the University of Birmingham in chamber 1 [8]. However, in this previous work, a slightly different preferred orientation was found ((521)) as thickness increased.

FWHM results are illustrated in Fig. 5.4. The FWHM of the preferred (222) orientation

peak is observed to decrease between 69 and 327 nm from to 0.702 to 0.559°. When the same experiment was performed between 654 and 1467 nm, the (611) peak dominated and its FWHM was taken. A somewhat smaller decrease is observed from 0.489 to 0.452°. These results suggest an overall and gradual improvement in crystallinity, larger grain size and lower residual stress as t increases.

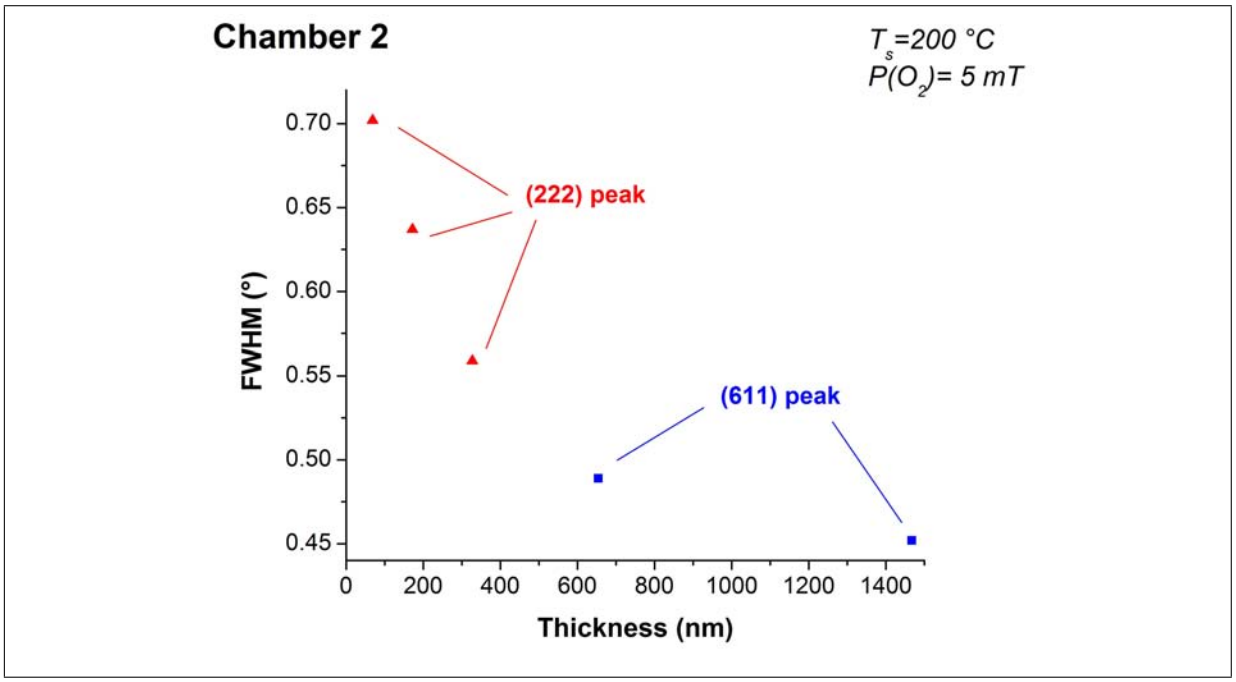

Figure 5.4 FWHM of preferred orientation peaks of ITO thin films deposited in chamber 2 and varying thickness from 47 to 1467 nm; Gaussian peak fitting (mot shown) was performed on the dominant peak to compute the FWHMs; other deposition parameters used are listed in Table 5.1.

Surface morphology was studied by AFM with 2×2 μm 3-dimensional AFM scans being performed on each sample grown at a different number of pulses. The results are shown in Fig. 5.5.

RMS roughness resulting from the above measurements is plotted in Fig. 5.6.

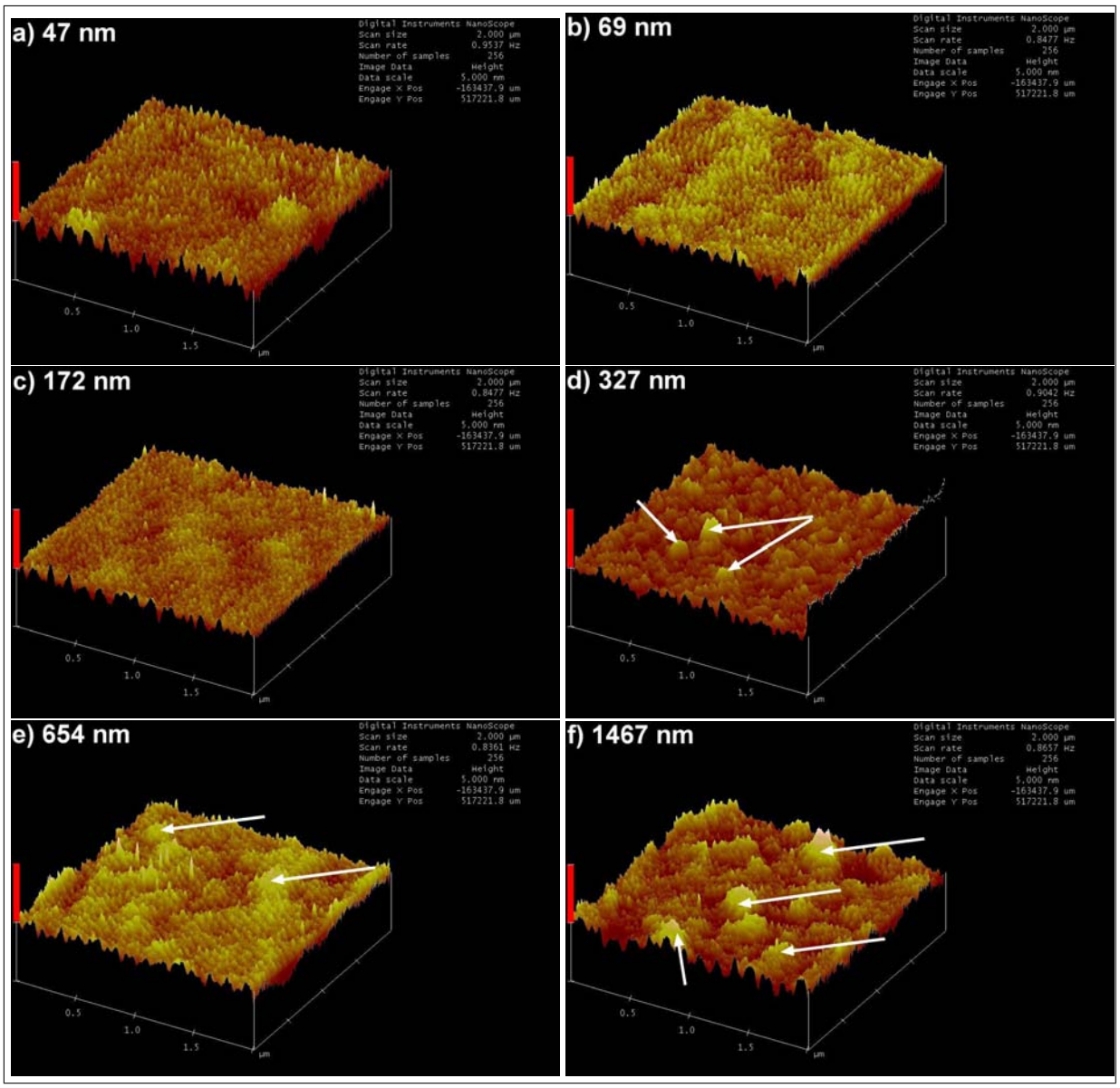

Figure 5.5 2×2 μm 3-dimensional AFM scans of ITO thin films deposited in chamber 2 by varying the film thickness from 47 to 1467 nm; other deposition parameters used are listed in Table 5.1.

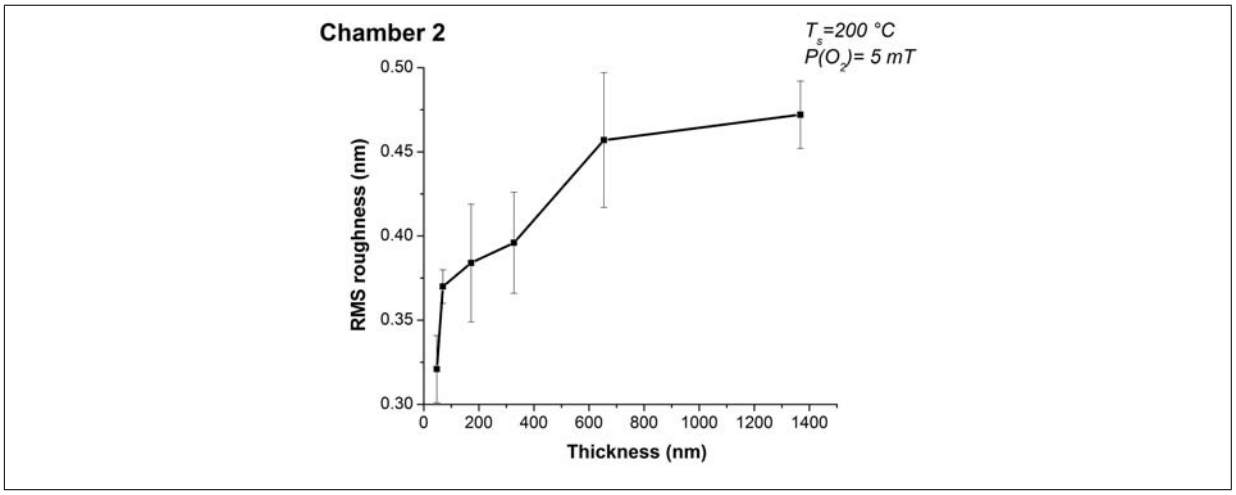

Figure 5.6 RMS roughness of ITO thin films deposited in chamber 2 with varying thickness from 47 to 1467 nm; other deposition parameters used are listed in Table 5.1. Errors were calculated as the standard error of the mean and represented by error bars.

The RMS roughness appears to increase with the thickness in steps, although this statement needs to be moderated when account is taken of the error bars. A rather strong increase between 47 and 69 nm is noticed while between 69 and 327 nm pulses, the increase is more moderate. Since only one set of samples was grown, one cannot be too conclusive about this effect. Finally, a stronger increase is noticed between 327 and 654 nm before a levelling-off takes place around 1467 nm. Unfortunately, it was not possible to fire more pulse to confirm this plateau. Overall, however, the roughness remains extremely low compared with those reported from other deposition techniques such as sputtering [25] or spray pyrolysis [45].

Finally, based on the AFM pictures presented in Fig. 5.5, some degree of grain growth is observed as the number of pulses increases. The features observed in Fig. 5.5 (see white arrows) were interpreted as grains showing different faces at the top surface. However, at thicknesses as low as 47 and 69 nm, one cannot make an accurate quantitative measure of the crystallite size (if any). Such an effect is also in agreeement with the improved crystallinity evidenced in Fig. 5.3 by a decrease of the FWHM of the preferred orientation peak.

5.1.2.2 Electrical properties of ITO films deposited by varying the thickness

Hall effect and four-point probe measurements were performed on the samples listed in Table 5.2. Results are given in Fig. 5.7 for N (carrier concentration) and μ (carrier mobility).

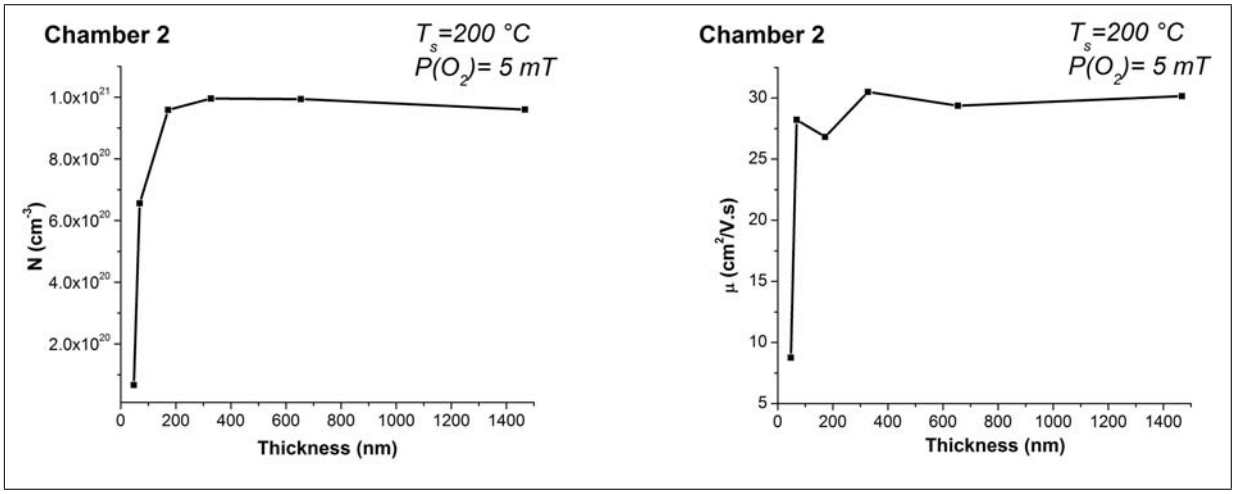

Figure 5.7 Variation of N (left) and μ (right) of ITO thin films deposited in chamber 2 by varying the thickness; it was varied from 47 to 1467 nm; other deposition parameters used are listed in Table 5.1.

Fig. 5.8 illustrates variation of ρ (resisitivty) with t.

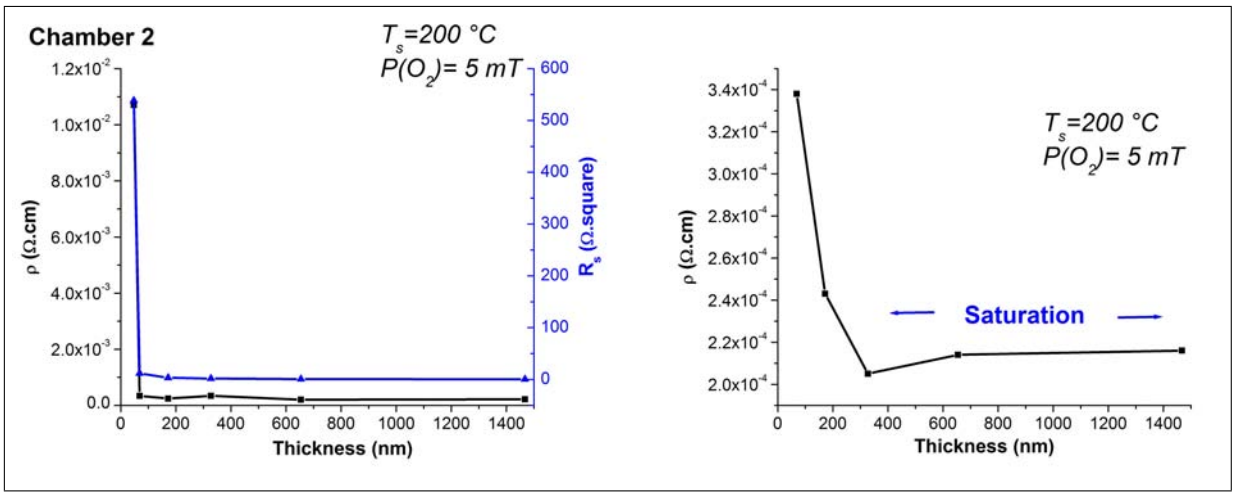

Figure 5.8 Variation of ρ of ITO thin films deposited in chamber 2 by varying the thickness from 47 to 1467 nm (left). On the right, the variation of ρ with thickness is shown in more detail by omitting the experimental point at t=47 nm; other deposition parameters used are listed in Table 5.1.

As shown in Fig. 5.7 and 5.8, values N, μ and ρ all saturate above a certain thickness value after a very sharp rise. Minor improvements are observed after 172 nm for N and, 327 nm for μ and ρ respectively. This value for ρ (327 nm) is slightly lower than the one reported in [8] for chamber 1 where saturation of ρ was observed above 654 nm. However, the chamber and the deposition rate are different as well (see section 4.1, Fig. 4.1). Both N and μ increase sharply with increasing thickness up to about 180 and 70 nm respectively, beyond which, both tend to saturate.

5.1.2.3 Optical properties of ITO films deposited for various thicknesses

Fig. 5.9 shows the optical properties from the near-UV (250 nm) to the near-IR range (1000 nm) as the film thickness is varied from 47 to 1467 nm.

For the sake of clarity, Fig. 5.10 shows how the average transparency over 400 - 1000 nm range varies with the film thickness. This range is chosen as transmittance values show smaller variations with wavelength (λ) than over the band gap region (250 - 350 nm).

At very low thickness (e.g. 47 nm), average optical transmittance for the 400 - 1000 nm range is strongly degraded as compared with those over the 69 - 327 nm range. At higher thicknesses (654 - 1467 nm), once again, average optical transmittance is strongly degraded. When the thickness reaches 1467 nm, average transmittance is only about 60%, despite the enhanced crystallinity of this film (see Figs. 5.3 - 5.4).

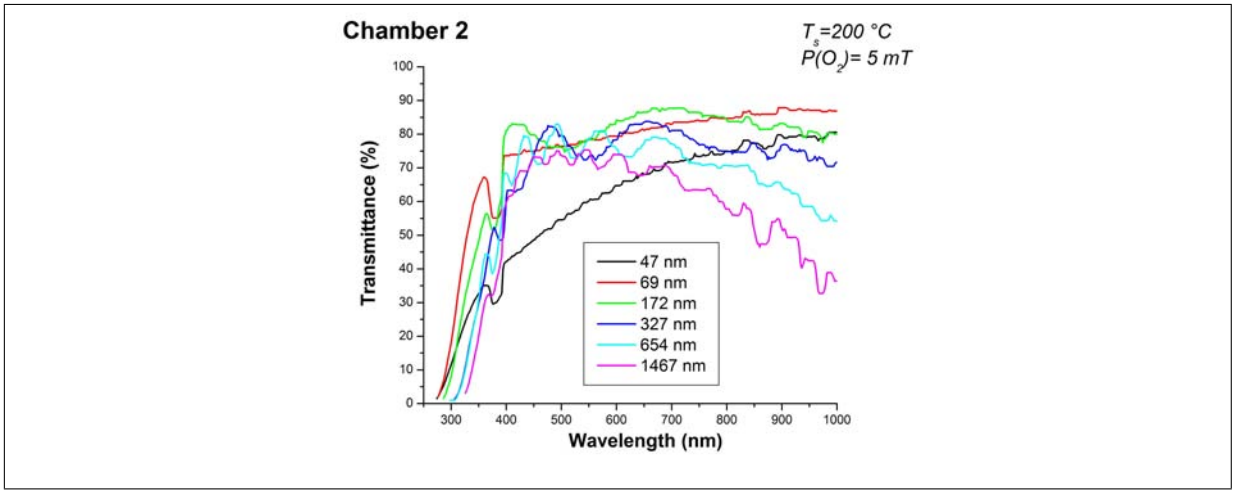

Figure 5.9 Optical properties of ITO thin films deposited for varying film thickness in chamber 2; the thickness varied from 47 to 1467 nm; other deposition parameters used are listed in Table 5.1.

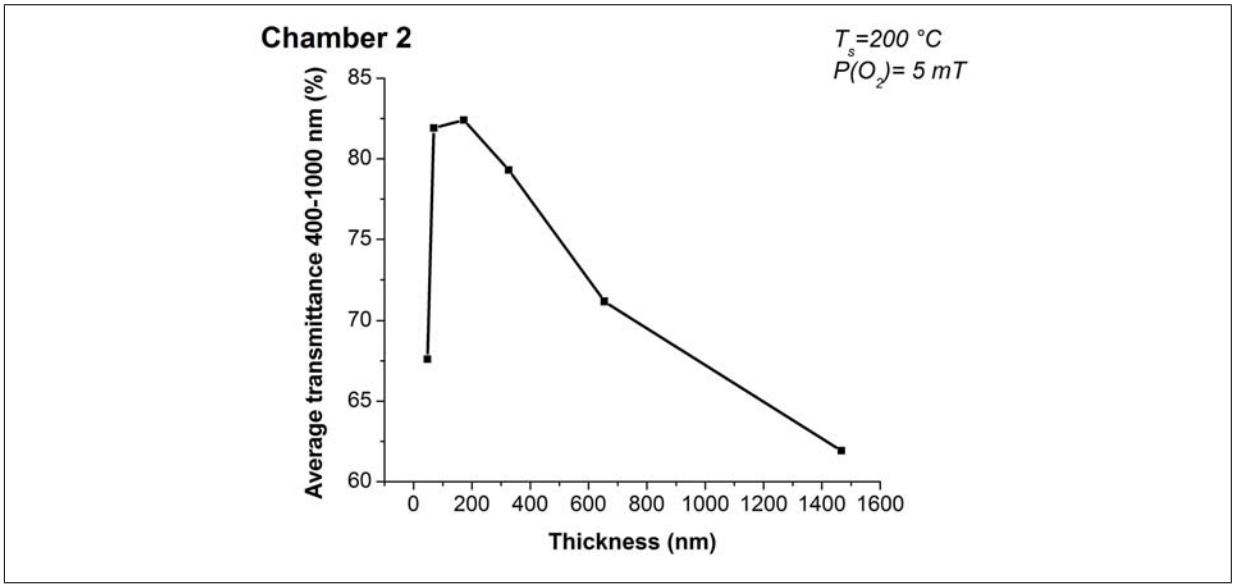

Figure 5.10 Average transmittance over the 400 - 1000 nm optical region of ITO thin films deposited with varioua thicknesses in chamber 2. The thickness varies from 47 to 1467 nm; other deposition parameters used are listed in Table 5.1.

5.1.3 Discussion

5.1.3.1 Structural properties

The growth orientation was affected as t increased (Fig. 5.3). This can explained on the basis of thermodynamics and kinetics. It is suggested that the occurence of a preferred (222) growth orientation up to ∼350 nm is related to the minimisation of the surface and interface free energies (see eq. 2.20) which makes the growth rate of such crystals higher than others (competitive growth). As the thickness increased over 350 nm, the importance of interface and surface free energies relative to the the total bulk free energy of the solid decreased. Since the orientation favouring a minimisation of bulk free

energy is not necessarily the same as the one minimising the interface and surface free energies, a (611) orientation seems to predominate at higher thicknesses (Fig. 5.3), once again because of the higher growth rate of such crystals as compared with other directions. Roughness was also found to be affected with thicker films being found to be rougher. This is explained on the basis of enhanced crystallinity and development of other orientations as the films become thicker.

5.1.3.2 Electrical properties

It has been observed that both the electron transport properties (N, μ and ρ) are thickness dependent before reaching a plateau. The latter occurs at different thickness values: 172 nm for N and 69 nm for μ and ρ. Based on Figs. 5.7 - 5.8, 100 nm is taken as the thickness value afterwhich N, μ and ρ show minor change: it is identified as a critical thickness. Therefore, the discussion will be divided between the following thickness ranges: below and above 100 nm. It is suggested that this value corresponds to a thickness at which a transition takes place from a film containing voids to a more continuous one.

During the initial growth stage, a rather stressed defective structure is likely to be formed at the interface with the substrate because the nucleation and coalescence processes that occur with thinner films are not continuous [170] [171] [172]. It is suggested that such processes do not favour the electrical activation of Sn resulting in films with lower N. Moreover, thinner films have a larger surface-to-volume ratio meaning that thin films contain more defects than thicker films [173]. More scattering of carriers is therefore expected in thinner films and hence a relatively low μ was observed.

Above 100 nm (critical thickness), it is suggested that the transition from a porous to a more continuous film takes place. The crystallinity still improves (lower FWHM, see Fig. 5.4) but at a much slower pace as the film formed is already continuous. This transition is also confirmed by a parallel improvement in μ. After a certain threshold ($\simeq$100 nm), increased μ results from increased grain size, possibly combined with a change in the preferred orientation of crystallites with film thickness as shown by XRD. In general, if the thickness of the layer is increased, the crystallites become larger in size [174] in agreement with thin film growth theory [175]. The lower FWHM is also an indication that the grain size of the films increases with growing film thickness. The growth orientation does not seem to play any significant role in determining μ as no large difference is observed between 69 and 327 nm while films retain a preferred (222) orientation.

We now discuss the scattering mechanism of free carriers. The observed mobility and its dependence on N can be explained in terms of scattering mechanisms such as ionized impurity scattering. The relationships between μ and N calculated from the ionised impurity scattering theory presented in eq. 2.3 of section 2.2.2.1.2 show that there is a linear negative correlation between μ_I (the mobility arising from a dominant ionised impurity scattering) and N. Fig. 5.11 illustrates the relation obtained between μ (experiemntal) and N.

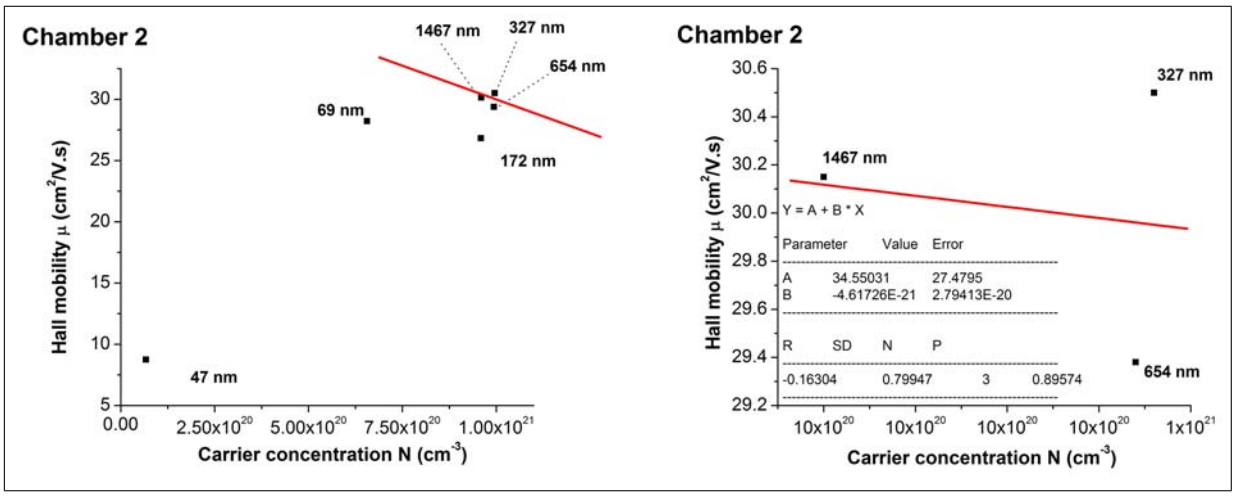

Figure 5.11 Mobility μ versus carrier concentration N of ITO thin films deposited for various film thicknesses. The thickness varies from 47 to 1467 nm; other deposition parameters used are listed in Table 5.1. A larger scale plot is shown on the right hand side in the region 327 - 1467 nm where a tentative linear fit (red line) is made.

Despite the obvious lack of data abd a very low correlation coefficient (R=-0.16), a tentative trend can be identified. Experimental points at 327, 654 and 1464 nm seem to fit a straight line with a negative slope. This would be in agreement with ionised impurity scattering being the dominant scattering mechanism. Thinner films do not fit this trend at all and the thinner the film is, the more it deviates from the straight line between 327 and 1467 nm. This suggests that the dominant scattering mechanism is different, especially at lower film thicknesses. This is perhaps not surprising as thinner films might be more discontinuous and those discontinuities might very well become the dominant scattering mechanism in combination with increased surface scattering.

It is now possible to explain the behaviour of ρ (see Fig. 5.8) since it depends on the variation of both N and μ. The larger grain size with increasing thickness results in a lower density of grain boundaries, which behave as traps for free carriers and barriers to carrier transport in the film (grain boundary trapping model [176]). Hence, an increase in the grain size can cause a decrease in grain boundary scattering, which leads to a

decrease in ρ. Thus, the initial decrease in ρ is due to an increase in both carrier density and carrier mobility of the films, which result from the increased grain size/crystallinity and better film continuity. For thicker films (t>100 nm), ρ remains constant because both N and μ become independent of film thickness (it is reasonable for ρ to become independent of the film thickness since thick films eventually behave like bulk materials).

Finally, below 100 nm, ρ was observed to increase with decreasing thickness. This increase in ρ can be related to the increase in carrier scattering due to a decrease in grain size or to other discontinuities in the film. The relatively rapid increase in ρ as the films get thinner is related to the percolative structure of the ITO film [177].

5.1.3.3 Optical properties

When t$\sim$50 nm, the transmittance is extremely low (down to about 67%) despite the low thickness of such films. This is attributed to the very small degree of crystallinity. Indeed, AFM does not really show a grainy surface morphology while XRD does not show any peaks and the absorption edge slope is lower than for thicker films. At higher thicknesses (>600 nm), the transmittance is once again degraded. This cannot be explained similarly by a lack of crystallinty, since the XRD and AFM results show fully crystallised films above 600 nm. Rather, it is suggested that the thickness is playing a dominant role via the simple Beer-Lambert Law:

$$T = \frac{I}{I_0} = e^{-\alpha t} \tag{5.1}$$

where α is the absorption coefficient, t the distance the light travels through the material and I and I_0 are the intensity of the incident and transmitted light. Thus, T decreases exponentially with t, and as t increases above a certain threshold (here 600 nm), t becomes the dominant parameter in determining the resulting transmittance. Grain size, which is observed to increase with increasing t no longer influences the transmittance. Another factor which might influence the optical properties is the surface roughness which increases as t increases. However, it is suggested that it plays a minor role because of the low roughness found between 47 and 1467 nm (<0.5 nm). Moreover, the RMS roughness does not vary to a great extent so that it does not affect the comparison in optical properties of the different films.

5.1.3.4 Optimal thickness

Based on the electro-optical properties reported previously, the best compromise between low resistivity and high transparency for chamber 2 was obtained for films of about 350 nm thickness (5000 pulses). An identical conclusion was reached for chamber 1 [8] but resulting thicknesses were about 250 nm. In consequence of these findings, 5000 pulses were fired for all the subsequent films deposited at various T_s and $P(O_2)$ reported in this study.

5.2 Influence of substrate temperature

This section investigates the changes in physical properties and microstructure as T_s is varied in chambers 1 and 2, starting with electrical property changes with Hall effect measurements presented first. Optical properties will be presented subsequently. These electro-optical property changes will be explained and discussed on the basis of microstructural evidence. An attempt is also made to reconcile the physical properties of films grown in chambers 1 and 2 and discussed. As a reminder, it is noted that these two chambers and their different set-ups have already been described in section 4.1.

5.2.1 Electrical properties

Hall effect measurements were performed on samples deposited at constant $P(O_2)$ in the two chambers. $P(O_2)$ was set at 10 mT and 5 mT in chambers 1 and 2 respectively. In order to be as representative as possible of the "true" physical reality, the following method was adopted: five consecutive Hall effect measurements were performed for each particular sample. The averages of these five measurements were taken as the true values of the mobility (μ), carrier concentration (N) and resistivity (ρ). The same method was repeated on as many samples as possible (depending on how many were available during the time of measurement) grown under exactly the same conditions. Finally, the averages of these different samples were taken as the representative values of μ, N and ρ for each particular growth condition. Errors were calculated as the standard error of the mean and represented by error bars. Where error bars are not visible on the plots, it is either because they were very small or simply because only one sample was measured.

Since thickness (t) affects electrical properties [80][39], the variation of t with T_s was studied first for chambers 1 and 2. t could vary because a crystalline phase is likely to be denser than an amorphous one. Moreover, sticking coefficients could change significantly

when T_s is varied from RT to 400°C. t was calculated through direct (cross-sectional SEM or TEM) and indirect (ellipsometry) measurements. Tables 5.3 - 5.4 sums up fitted (ellipsometry) and measured (SEM or TEM) thicknesses. Fitted thicknesses were derived from the Cauchy model (see section 4.7.2.1).

Table 5.3 Summary of fitted and measured thicknesses for samples deposited in chamber 1 between RT and 400°C. 5000 pulses were fired.

T_s (°C)	Fitted t (nm)	Measured t (nm)
RT	242	221 (TEM)
	313	227 (SEM)
50	246	no data
100	251	214 (SEM)
	241	286 (SEM)
175	256	no data
	292	no data
200	287	245 (TEM)
	233	no data
300	301	282 (SEM)
400	252	246 (TEM)
Average t (nm)	264.91	245.86
Standard deviation	27.84	28.60

Table 5.4 Summary of fitted and measured thicknesses for samples deposited in chamber 2 between RT and 400°C. 5000 pulses were fired.

T_s (°C)	Fitted t (nm)	Measured t (nm)
RT	327	374 (TEM)
	337	no data
100	352	no data
200	365	349 (SEM)
	347	383 (TEM)
400	317	376 (SEM)
Average t (nm)	340.83	370.5
Standard deviation	17.44	14.84

In both chambers, fitted thicknesses (derived from ellipsometric measurements over a 1.2 mm^2 area) and measured ones do not differ to a great extent over the temperature range investigated (RT - 400°C), indicating that the approach of using a Cauchy model to approximate film thicknesses is sufficiently good in the visible spectrum for our purposes. Film thicknesses in chamber 2 are larger than in chamber 1 due to the different working oxygen pressures in chamber 1 (10 mT) and 2 (5 mT). A higher $P(O_2)$ induces more scattering of ejected species reducing the amount of material reaching the thin film surface [72] [73]. Fitted thicknesses shown in Tables 5.3 and 5.4 are plotted in Fig. 5.12 for the sake of clarity.

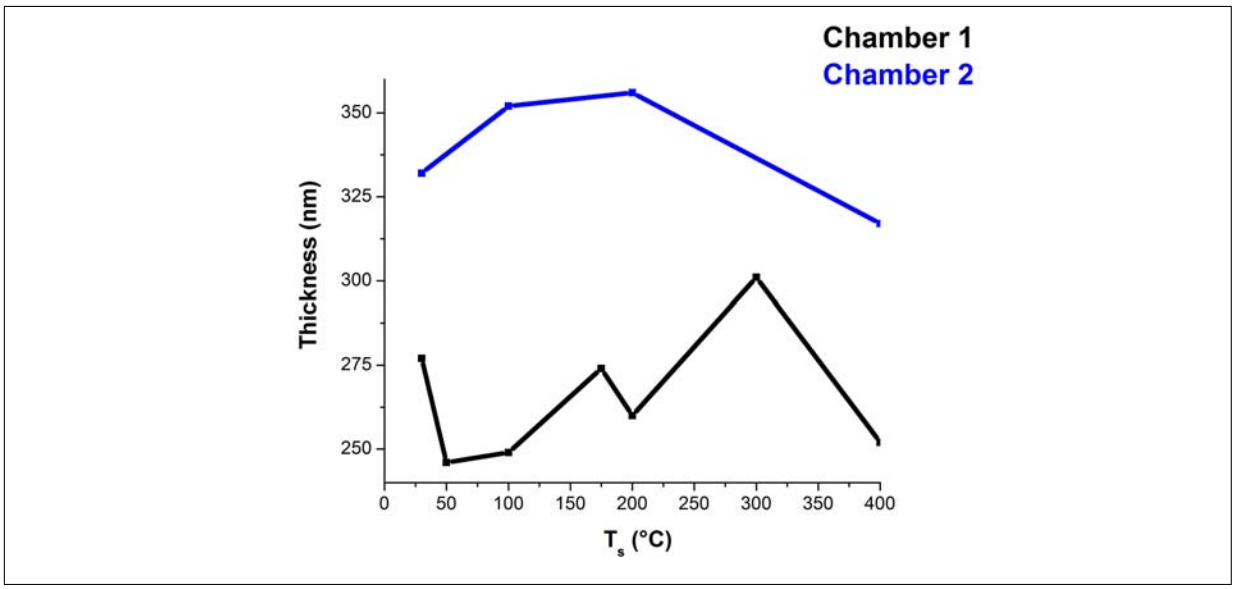

Figure 5.12 Variation of thickness (t) with T_s in chamber 1 (black curve) and 2 (blue curve). T_s was varied from RT to 400°C.

It is observed that t is not a strong function of T_s in the RT - 400°C range for either chamber for the sets of samples studied, while no particular shrinkage (in terms of densification) is observed at low or high T_s. It is expected that these samples are representative of the average thickness over the T_s range from RT to 400°C. When the thickness was not known for a particular sample in chambers 1 or 2, the average value (see Tables 5.3 and 5.4) in the corresponding chamber was taken.

5.2.1.1 Film microstructure

XRD measurements were performed in both chambers and the evolution of XRD patterns with T_s is illustrated in Figs. 5.13 - 5.14 for chambers 1 and 2 respectively.

The following observations are made: a reproducible small "bump" between 2θ=25 and 32° is observed in both chambers and originates entirely from the glass substrate since an X-Ray scan from a bare glass substrate shows exactly the same feature (Fig. 5.15).

Films are (nearly) amorphous below 150°C in chamber 1 which is the reported onset of crystallisation temperature for ITO thin films [77]. A longer counting time (from 1 to 10 s) in the 25 - 40° region did not improve the visibility of any peak in that region as shown in Fig. 5.16.

In chamber 2, evidence of crystallisation is observed at RT with a low intensity (400) peak. In addition, the growth orientation is affected by T_s in chamber 2 where a change from a (400) to a (222) preferred orientation takes place at T_s=150°C (see the red

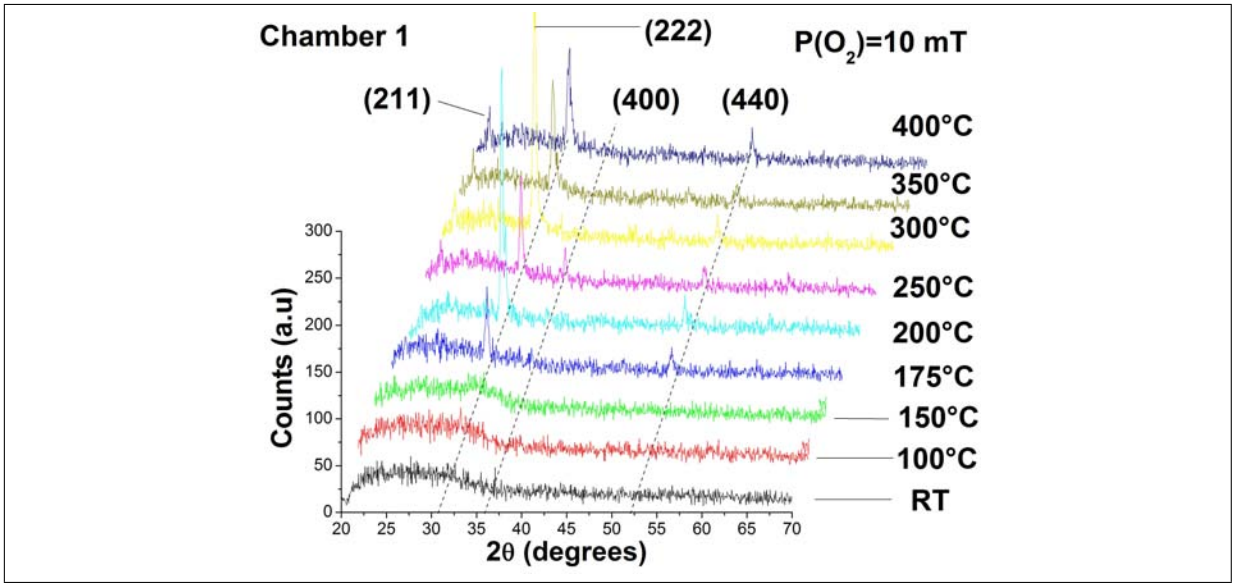

Figure 5.13 XRD patterns of the ITO films deposited at different substrate temperatures in chamber 1. A constant pressure of $P(O_2)=10$ mT was maintained. Data were shifted to the right for the sake of clarity.

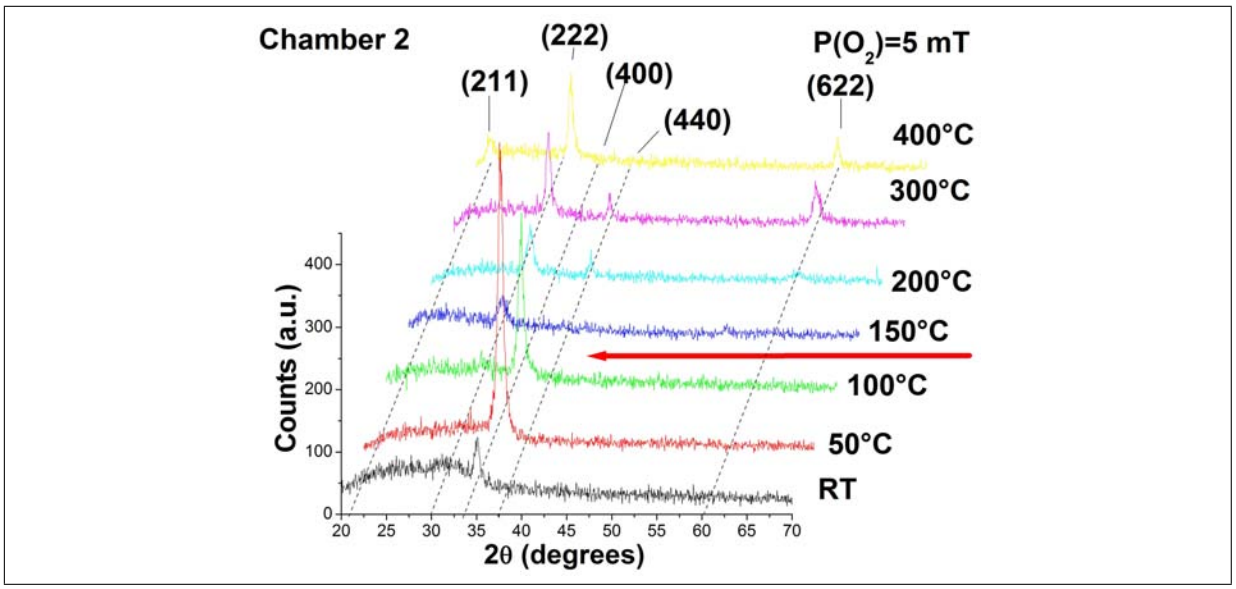

Figure 5.14 XRD patterns of the ITO films deposited at different substrate temperatures in chamber 2. A constant pressure of $P(O_2)=5$ mT was maintained. Data were shifted to the right for the sake of clarity. A red arrow shows where the orientation change is taking place.

arrow in Fig. 5.14). In chamber 1, no such orientation growth change is observed. Films conserved a (222) texture from 150 to 400°C. The Full Width at Half Maximum (FWHM) of preferred orientation peaks versus T_s is also investigated and plotted in Fig. 5.17.

The FWHM in chamber 2 appears relatively stable except at $T_s=150$°C where a growth orientation change takes place (see XRD patterns in Fig. 5.14). In chamber 1, the FWHM increases linearly with T_s between $T_s=175$ and 400°C. In addition, the texture quality in the present thin films was qualitatively evaluated by calculating the texture coefficient

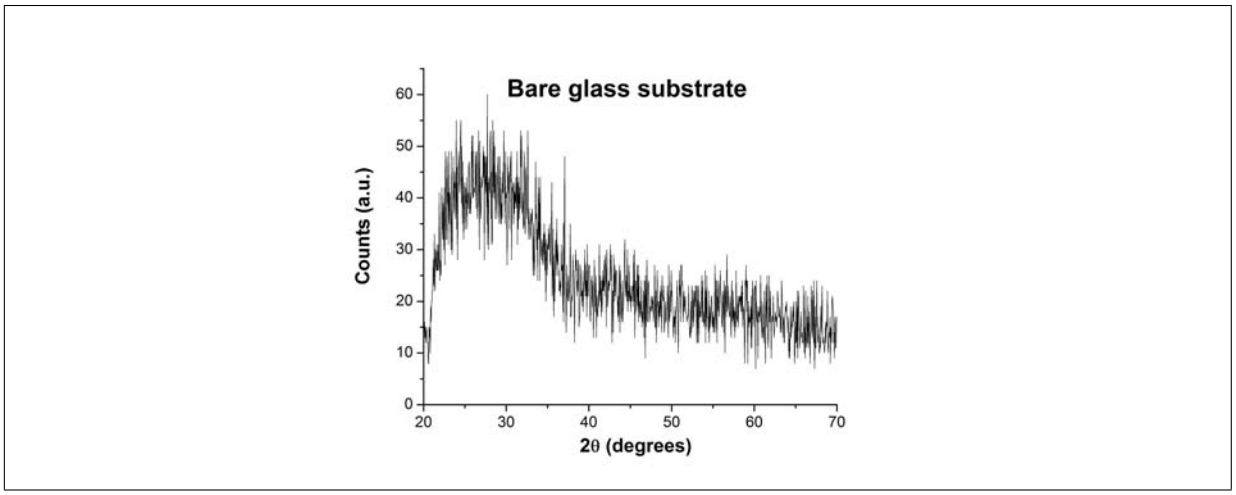

Figure 5.15 XRD pattern of a bare glass substrate between 2θ=20 and 70°.

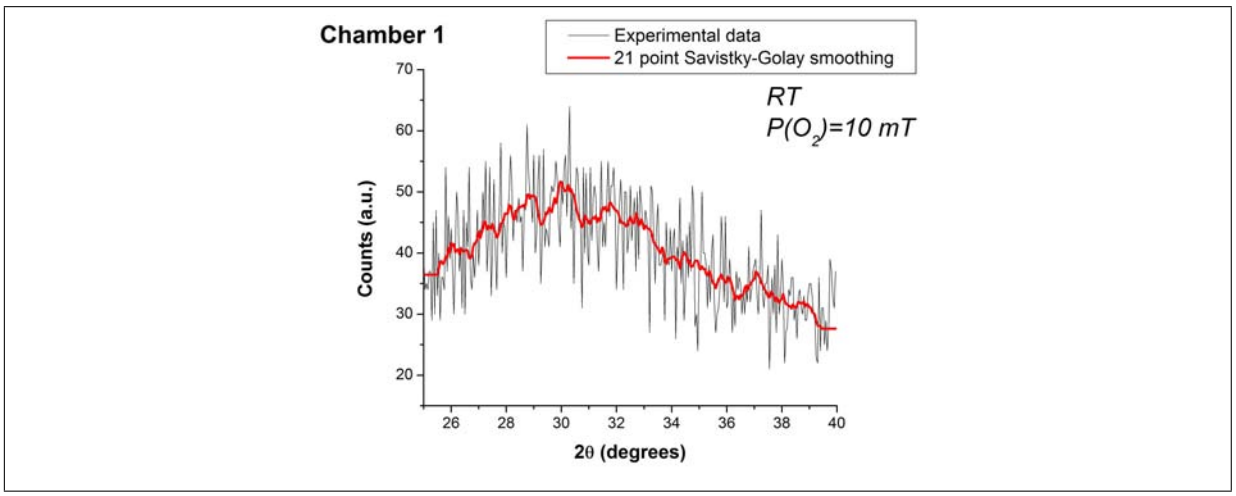

Figure 5.16 XRD pattern in the 25 - 40° region of a sample grown at RT in chamber 1. Noise was filtered out with a 21 point Savitsky-Golay smoothing [169] (red curve).

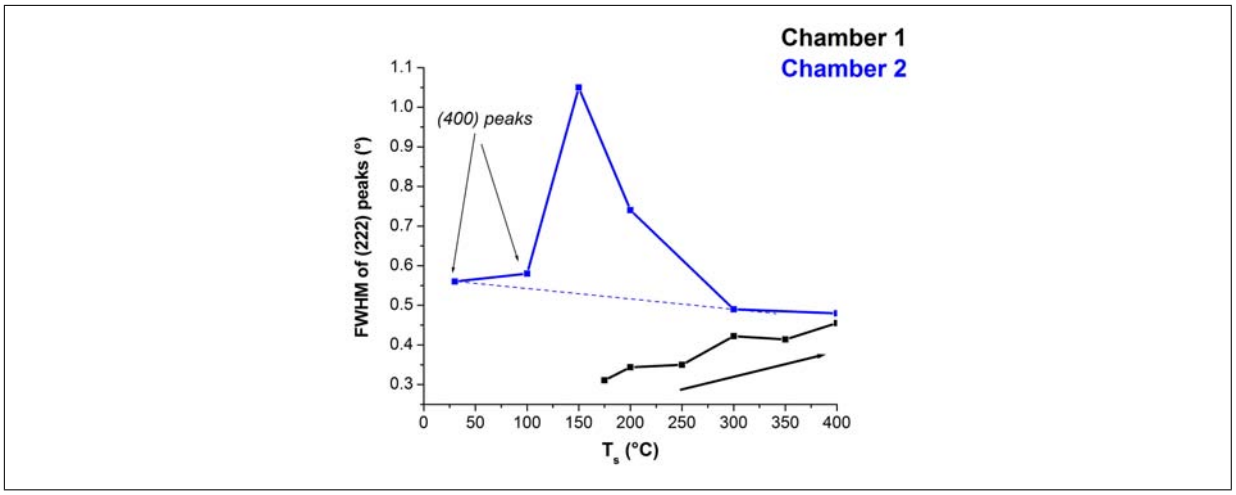

Figure 5.17 Corresponding FWHM of preferred orientation peaks of XRD patterns presented in Figs. 5.13 - 5.14. Unless stated otherwise, FWHMs were measured on (222) peaks.

($TC_{(hkl)}$) as described in section 4.2.1. A linear correlation between mobility and $TC_{(222)}$ or $TC_{(400)}$ was evidenced in both chambers (Fig. 5.18) between RT and 400°C.

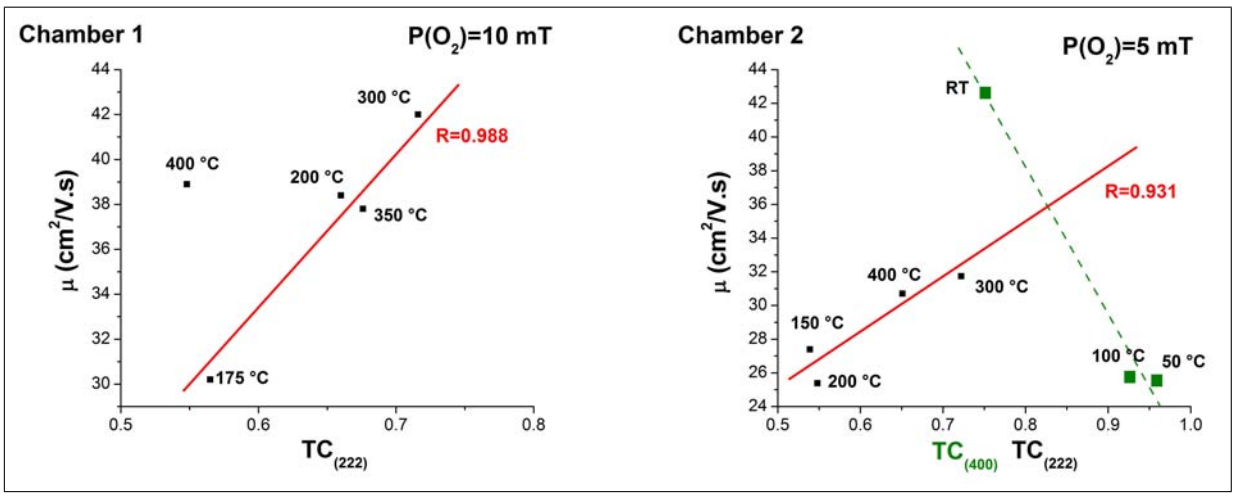

Figure 5.18 Relation between mobility μ and texture quality of ITO thin films grown in chamber 1 (left) and 2 (right). Chamber 1, $P(O_2)$=10 mT; chamber 2: $P(O_2)$=5 mT. In chamber 1, the 400°C data was not included in the calculation of R. The mobility values are taken from the samples corresponding to the X-Ray diffractograms presented in Figs. 5.13 and 5.14.

The following observations can be made:

- In chamber 1, a positive linear relation between $TC_{(222)}$ and μ is observed between T_s=175 and 300°C, although the experimental point at 400°C does not fit the general trend.
- In chamber 2, a positive linear relation between $TC_{(222)}$ and μ is observed between T_s=150 and 400°C.
- Experimental points at RT, 50 and 100°C do not fit the trend from T_s=150 to 400°C for chamber 2. Rather linear relation possibly governs the behaviour in this temperature range (shown in Fig. 5.18 with green dashes and points) although more experimental points are needed to confirm such a conclusion.

A preferred growth orientation change was also observed within the layers themselves. For example, glancing angle XRD (GAXRD) was performed on a sample deposited in chamber 2 at T_s=200°C and $P(O_2)$=5 mT and the results are presented in Fig. 5.19. The incidence angle Ψ was varied from 0.5 to 20° to probe the whole film thickness and beyond (glass substrate). The right hand side of Fig. 5.19 shows a plot of the attenuation length in microns versus the glancing angle (°). The attenuation length is defined as the length at which the X-Ray intensity in the material has fallen by a factor e^{-1} and was obtained from the Centre for X-Ray Optics (CXRO) [158]. The sample was 350 nm thick.

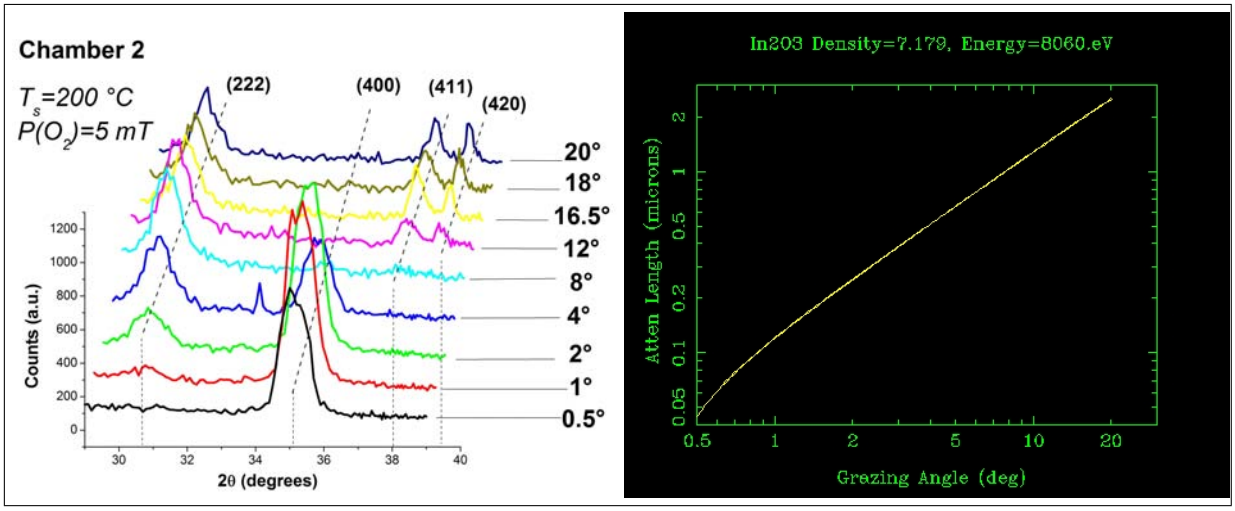

Figure 5.19 GAXRD patterns of a sample deposited in chamber 2 at T_s=200°C and $P(O_2)$=5 mT (left) by varying the incidence angle Ψ from 0.5 to 20°. The patterns were superimposed and shifted to the right for the sake of clarity. The correspondence between incidence angles and attenuation lengths is shown (right).

At low Ψ (0.5°), which corresponds to the top part of the film (the first few tens of nanometres), a preferred <100> growth direction is identified. But, from Ψ=2° - 4° onward, which corresponds approximately to the second half of the film (next to the substrate), the (400) preferred orientation vanishes and the film tends to become more polycrystalline with a (222), (411) and (420) orientations gradually appearing.

Mobility can be strongly affected by grain size effects [178][25] and other related aspects like surface roughness [39]. These constitute crystallographically disturbed regions which lead to defect electronic levels in the bandgap of ITO. Surface morphologies were investigated in both chambers by SEM, AFM and TEM. Low and high magnification SEM micrographs are presented in Fig. 5.20 and 5.21 respectively for samples grown in chamber 1. The corresponding AFM pictures are presented in Fig. 5.22.

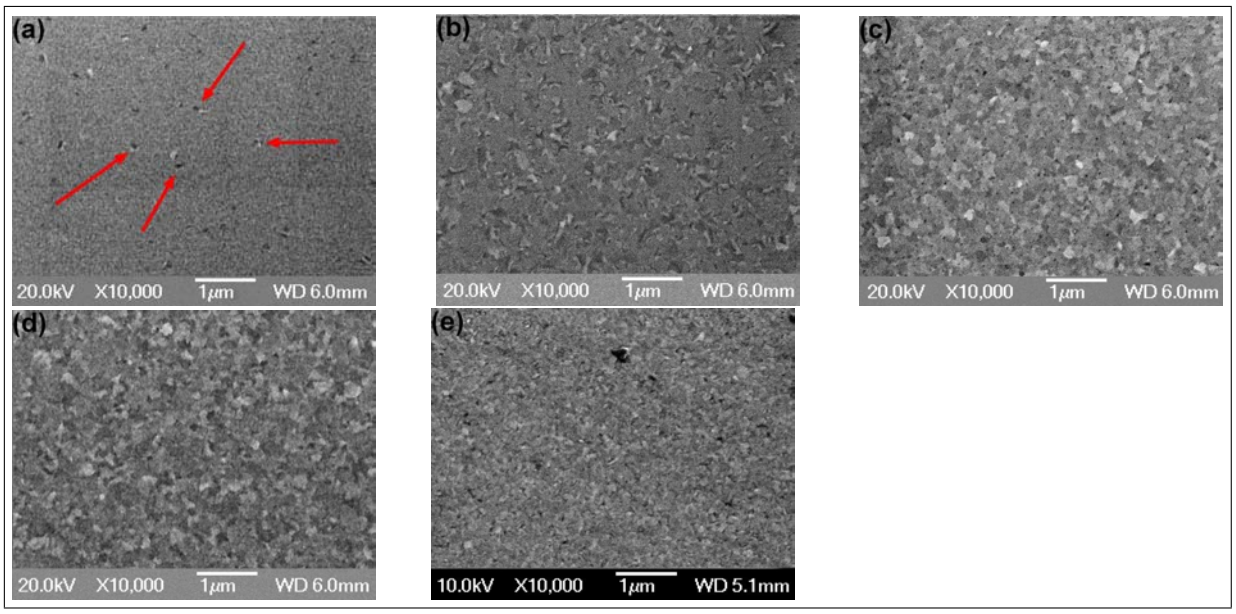

Figure 5.20 Evolution of surface microstructure in chamber 1 observed via low magnification SEM micrographs. The samples were grown at (a) T_s=150°C , (b) 175°C, (c) 200°C, (d) 300°C and (e) 400°C at P(O_2)=10 mT. Crystallites at T_s=150°C (a) are shown with red arrows.

Higher magnification sections of the SEM micrographs presented above are shown in Fig. 5.21.

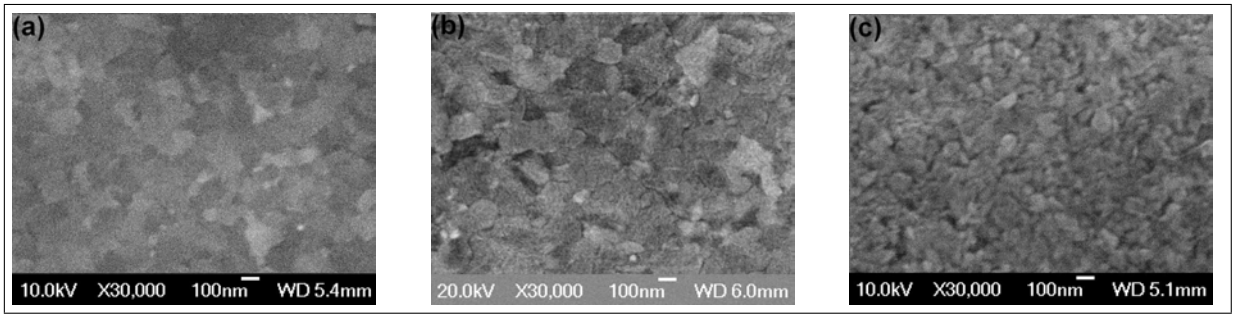

Figure 5.21 Evolution of surface microstructure in chamber 1 observed by high magnification SEM. The samples were grown at (a) T_s=200°C , (b) 300°C and (c) 400°C at P(O_2)=10 mT.

The corresponding AFM micrographs for chamber 1 are presented in Fig. 5.22.

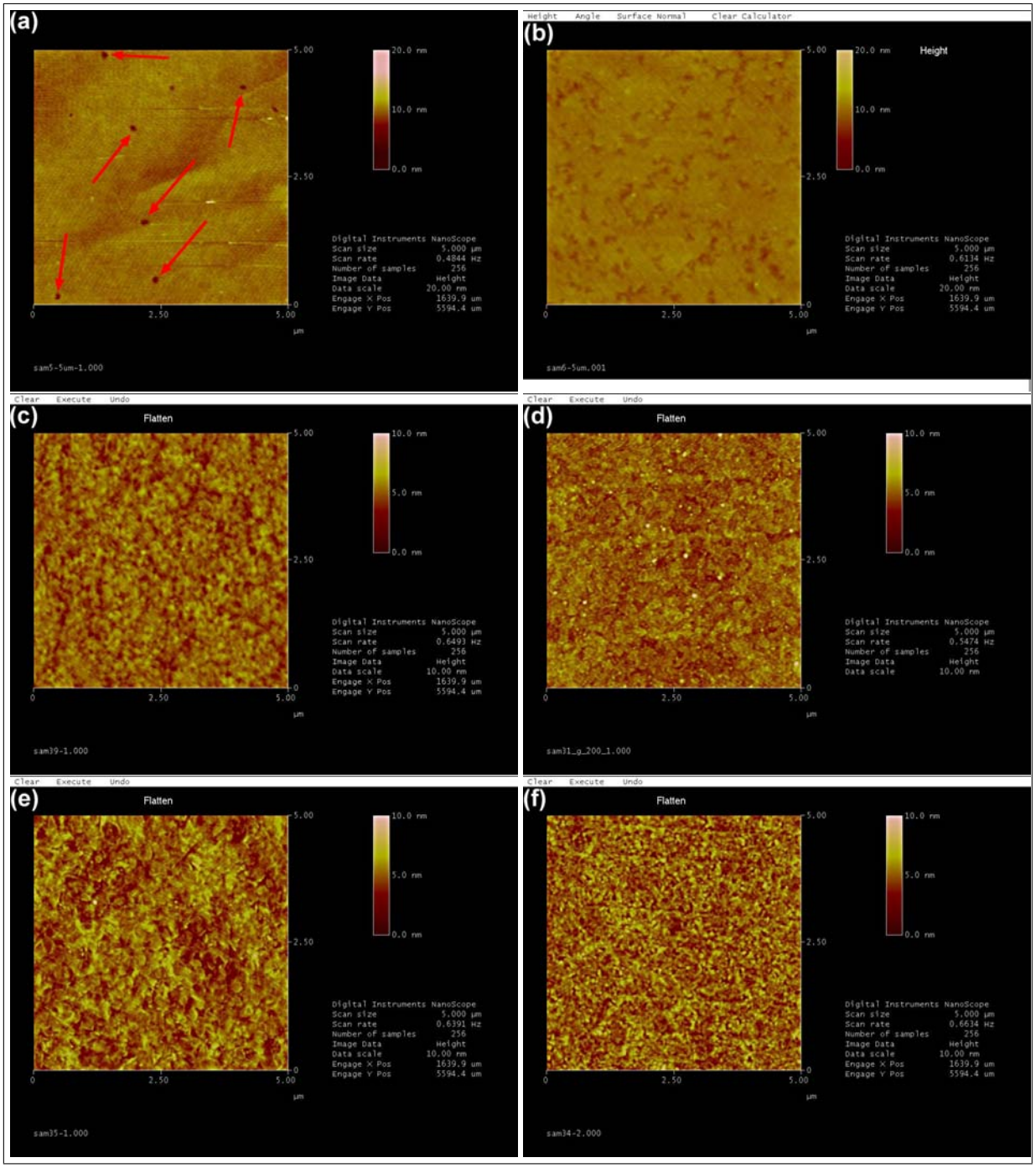

Figure 5.22 5×5 μm AFM scans of samples grown at (a) RT, (b) T_s=150°C, (c) 175°C, (d) 200°C, (e) 300°C and (f) 400°C at P(O_2)=10 mT in chamber 1. Red arrows in a) show the round shaped crystallites and the dip they induce.

The exact same work was repeated in chamber 2. Low and high magnification SEM micrographs are presented in Fig. 5.23 and 5.24 respectively. The corresponding AFM pictures are presented in Fig. 5.25.

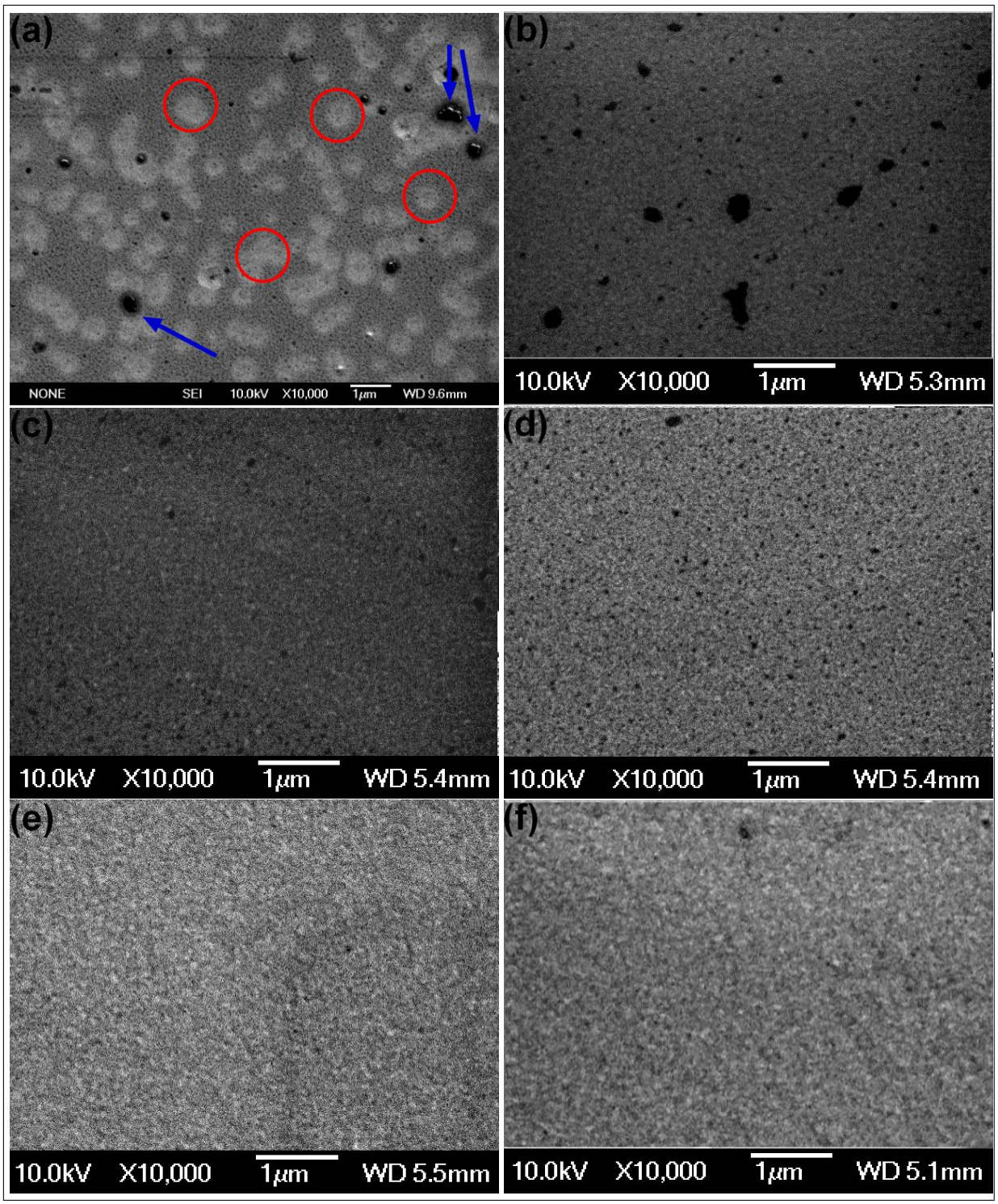

Figure 5.23 Evolution of surface microstructure in chamber 2 observed by low magnification SEM. The samples were grown at (a) RT, (b) T_s=100°C, (c) 150°C, (d) 200°C, (e) 300°C and (f) 400°C at $P(O_2)$=10 mT. The crystallites at RT (a) are encircled in red while blue arrows point to some carbon contamination.

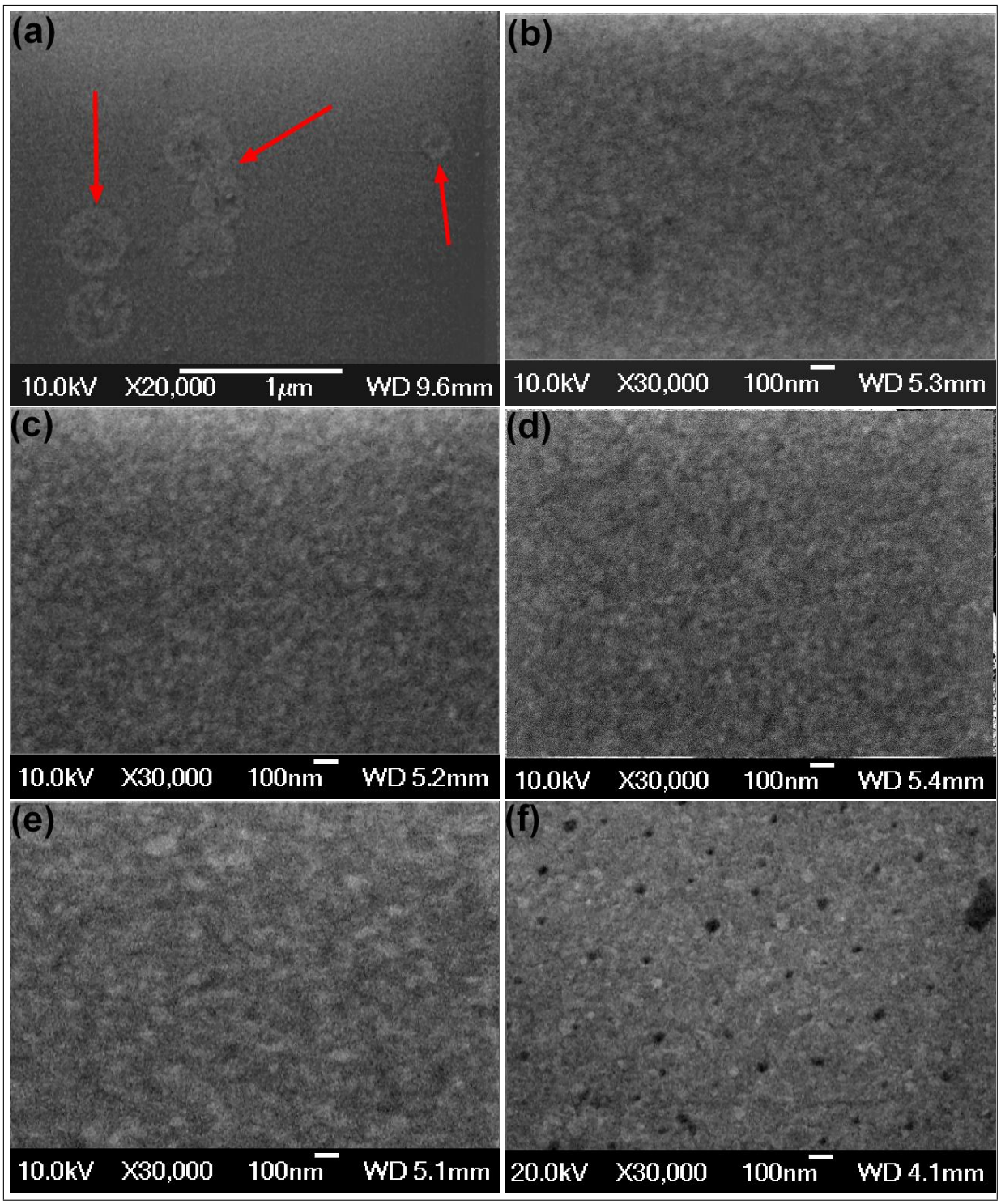

Figure 5.24 Evolution of surface microstructure in chamber 2 observed by high magnification SEM. The samples were grown at (a) RT, (b) T_s=50°C, (c) 150°C, (d) 200°C, (e) 300°C and (f) 400°C at $P(O_2)$=10 mT. The crystallites at RT (a) are shown with red arrows.

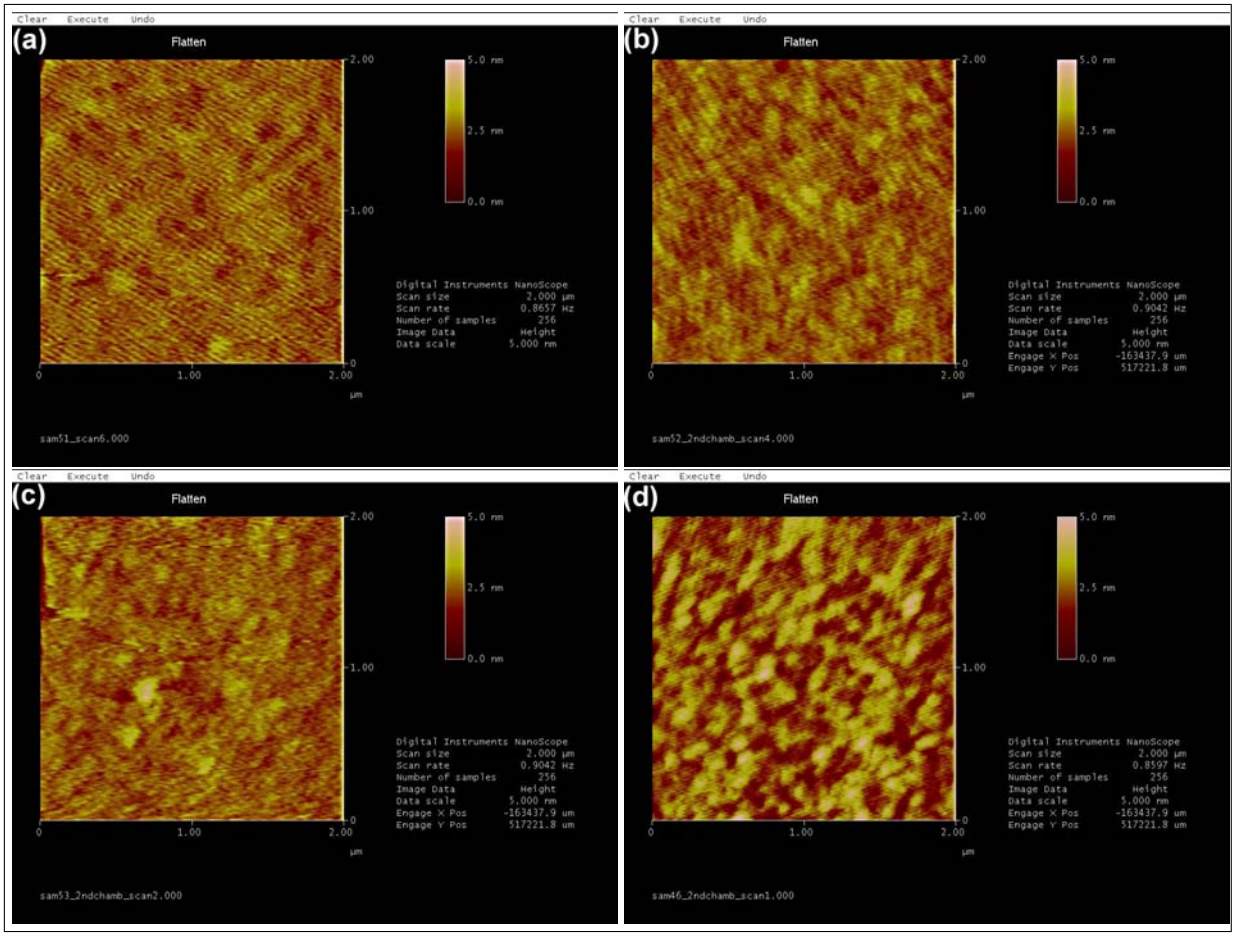

Figure 5.25 2×2 μm AFM scans of samples grown at (a) RT, (b) T_s=200°C, (c) 300°C and (d) 400°C at P(O_2)=5 mT in chamber 2.

Difficulties were encountered in obtaining good quality SEM pictures for samples from chamber 2. This is attributed to the extremely low surface roughness of the ITO thin films grown in this chamber (∼0.4 nm). The surface roughness of samples grown in chambers 1 and 2 between RT and 400°C is illustrated for comparison purposes in Fig. 5.26. It is seen that surface roughness in chamber 1 is typically double that of samples from chamber 2 and almost triple at 400°C. It is suggested that higher adatomic mobilities in chamber 2 gives rise to such behaviour.

Several observations based on the previous SEM and AFM micrographs can be made in terms of hole density, crystallites and grain size:

- No dramatic change of grain size with T_s is observed in either chamber.
- The lateral growth of grains seems to be more inhibited in chamber 2 than in chamber 1 resulting in a smaller average grain size.
- Holes are present regardless of T_s and tend to be more numerous in chamber 2.
- Films become rougher at high temperature (400°C) in both chambers.

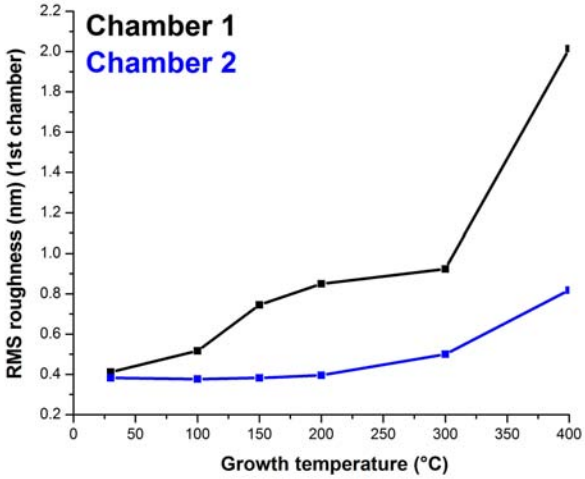

Figure 5.26 RMS roughness comparison between chamber 1 (black curve) and 2 (blue curve). RMS roughness is calculated on the basis of 5×5 and 2×2 μm scans in chambers 1 and 2 respectively. Holes were avoided so as to reflect the true roughness of the film surface.

- Round crystallites (200 to 300 nm diameter) are visible in RT samples from chamber 2 at a calculated density of 2.38×10^8/cm^2.
- Much smaller round crystallites (50 to 100 nm diameter) are visible on samples grown in chamber 1 at T_s=150°C. At T_s=175°C, the matrix is almost fully crystalline and becomes totally so at T_s=200°C.
- Crystallites are visible on AFM micrographs as a small dip on the surface (less than 5 nm).

The particular contrast shown by the crystallites on the SEM micrographs in chambers 1 (Fig. 5.20 (a)) and 2 (Fig. 5.23 (a)) is due to topography (as confirmed by AFM images with small dip on AFM images in chamber 1, Fig. 5.22) and also to density: a crystalline area is always denser than an amorphous one.

Grain size and crystallites were further investigated via bright field TEM plan view (Figs. 5.27 - 5.28) and cross sectional (Fig. 5.29) micrographs for samples from both chambers.

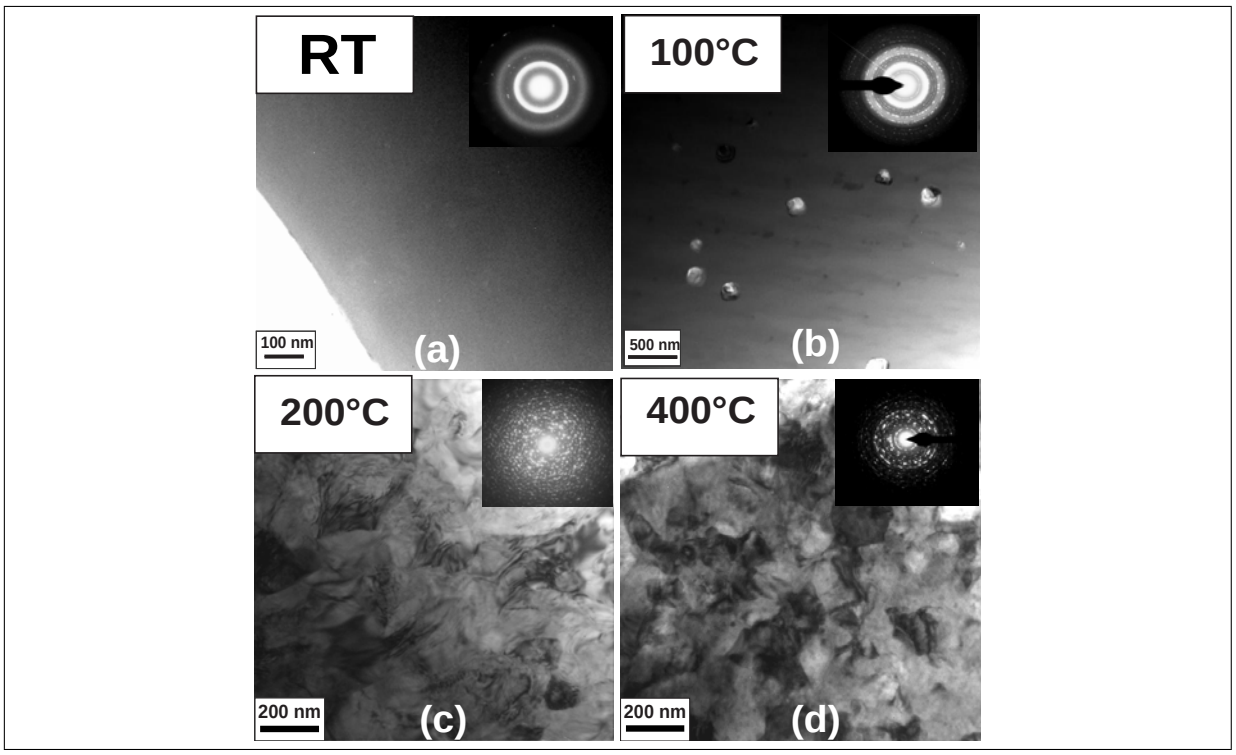

Figure 5.27 TEM bright-field plan view microgprahs of films grown in chamber 1 at (a) T_s=RT, (b) 100°C, (c) 200°C and (d) 400°C. The oxygen pressure was kept constant at $P(O_2)$=10 mT.

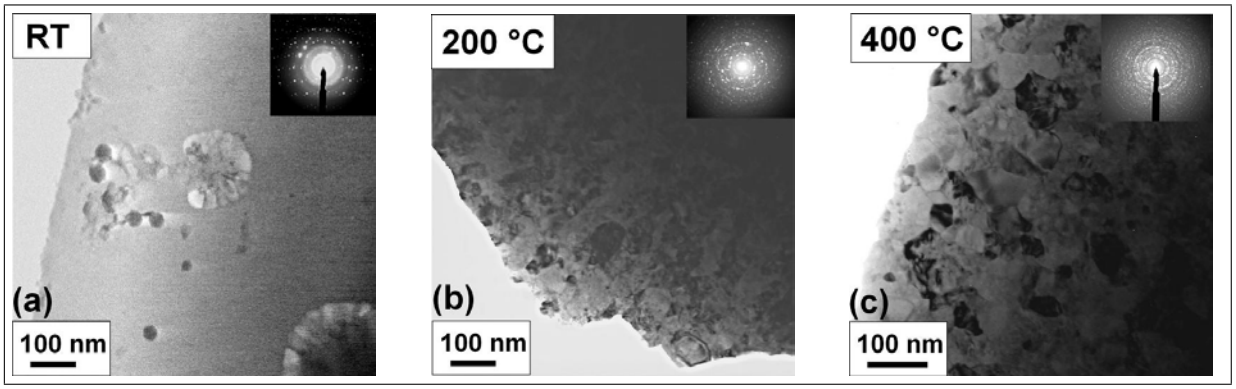

Figure 5.28 TEM bright-field plan view micrographs of films grown in chamber 2 at (a) T_s=RT, (b) T_s=200°C and (c) 400°C. The oxygen pressure was kept constant at $P(O_2)$=5 mT.

Bright field cross sectional micrographs at T_s=200°C confirm a smaller average grain size in chamber 1 as compared with chamber 2 (Fig. 5.29).

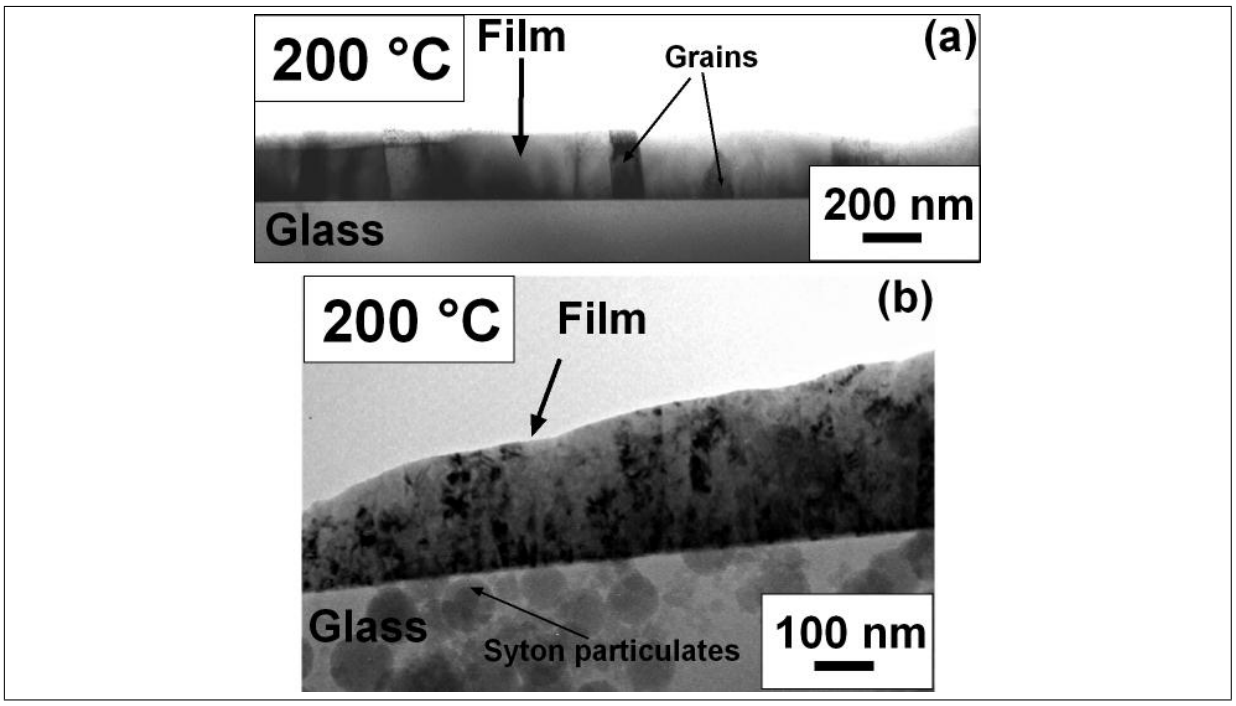

Figure 5.29 TEM bright-field cross sectional micrographs of films grown in (a) chambers 1 and (b) 2 at T_s=200°C. The oxygen pressure was kept constant at P(O_2)=10 and 5 mT in chambers 1 and 2 respectively. Syton particulates were visible in (b) and indicated with a black arrow.

The large round shaped crystallites visible in chamber 2 samples at RT were also observed on cross sectional TEM micrographs (Fig. 5.30).

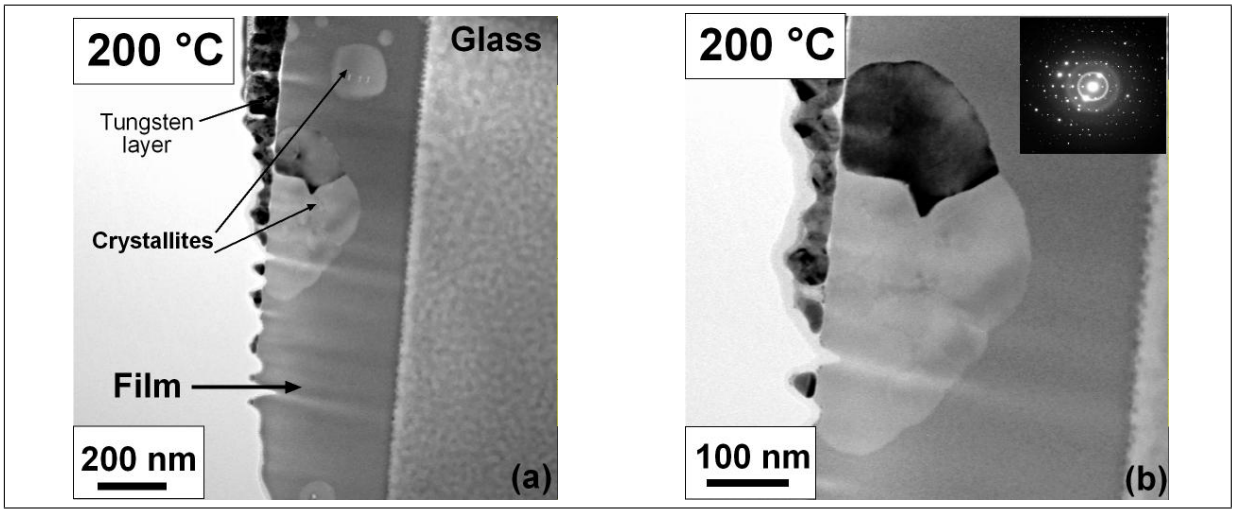

Figure 5.30 TEM bright-field cross sectional micrographs of a film grown at RT in chamber 2. The oxygen pressure was kept constant at P(O_2)=5 mT.

Crystalites observed at RT in chamber 2 look like “flowers” where the “petals” constitute large crystals consuming/advancing through the amorphous matrix while the inner part contains smaller grains and has a more complicated structure. The “petals” are separated by still amorphous regions. Such an observation has been previously reported

for amorphous metal oxide films [179] and will be discussed further in section 5.2.1.7. Unwanted syton contamination is visible as black round shaped spots on the brigh-field micrographs.

The grain size derived from previous SEM and TEM micrographs are summarised in Table 5.5.

Table 5.5 Average grain size (nm) at T_s= RT, 100°C, 200°C, 300°C and 400°C in chambers 1 and 2.

	Average grain size (nm)		
Substrate temperature (°C)	Chamber 1	Chamber 2	Technique used
RT	n.a.	n.a	/
100	n.a.	90	SEM
200	200	90	TEM
300	200	100	SEM
400	150	90	TEM

5.2.1.2 Mobility

The mobility (μ) variation with T_s is presented for chambers 1 and 2 in Fig. 5.31.

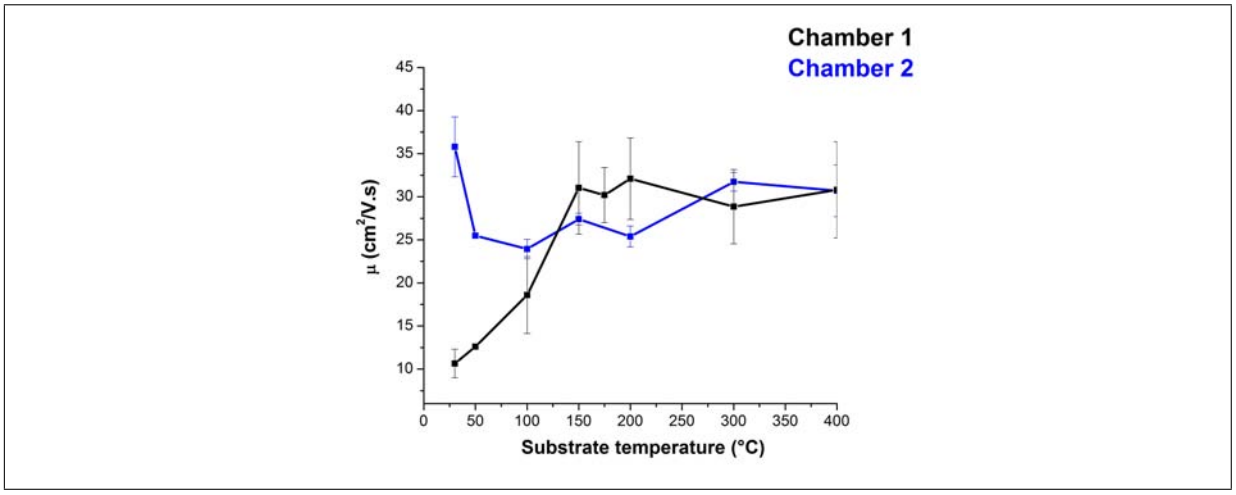

Figure 5.31 Variation of μ with T_s. T_s is varied from RT to 400°C. The black curve is for chamber 1 while the blue one is for chamber 2.

The mobility measurements show a similar behaviour for both chambers in the 150 - 400°C range: μ improves slightly. This is typical for a semi-metal or degenerate semiconductor. Below 150°C, there is a significant disagreement in the mobility values between the two chambers: in chamber 1, μ increases almost linearly from RT to 150°C while in chamber 2, μ is constant except at RT where it rises. This disagreement at lower T_s is statistically confirmed.

5.2.1.3 Calculations

To assess the grain boundary scattering impact on μ, the free carrier mean free path (L) in ITO was calculated using a highly degenerate free electron gas model [4]:

$$L = (3\pi^2)^{1/3}(h/e^2)\rho^{-1}N^{-2/3} \tag{5.2}$$

where h is Planck's constant, e is the electron charge, ρ is the resistivity and N is the carrier concentration. L versus T_s using values of ρ and N obtained by previous Hall effect measurements is plotted in Fig. 5.32 for samples from chambers 1 and 2.

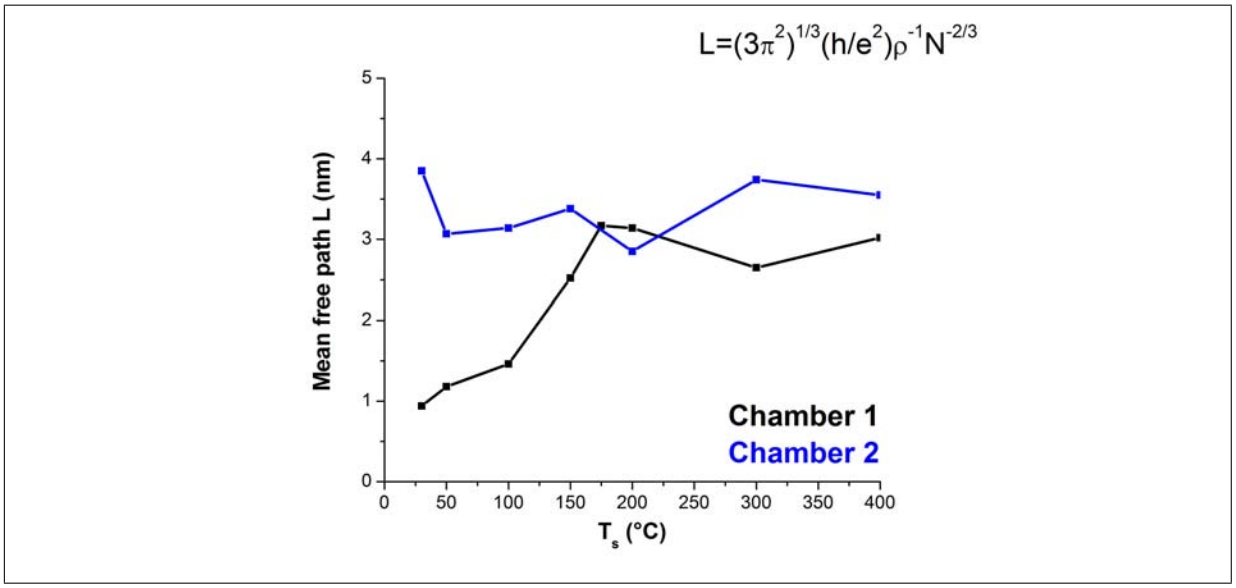

Figure 5.32 Calculated mean free path L for ITO thin films grown in chambers 1 (black curve) and 2 (blue curve). P(O_2) was maintained at 10 mT and 5 mT in chambers 1 and 2 respectively.

The calculated mean free paths are about the same in both chambers. Moreover, all the L values are much smaller than the average grain size for both chambers as derived by AFM (Figs. 5.22 - 5.25), SEM (Figs. 5.21 - 5.24) and TEM (Figs. 5.27 - 5.28) micrographs when T_s >200°C. It is deduced, therefore, that electron scattering at grain boundaries (GBs) is negligible in both chambers when the matrix is fully crystalline.

At lower T_s, where isolated crystallites are embedded in an amorphous matrix, the situation is somewhat different (Figs. 5.27 (b) - 5.28 (a)). For example, μ is found to be thermally activated in chamber 1 between RT and 200°C where an excellent linear regression between log(μ) and 1/T_s (R=0.989) is obtained for experimental points within this temperature range. This is not the case in chamber 2 as illustrated in Fig. 5.33 where the experimental points are more widely scattered.

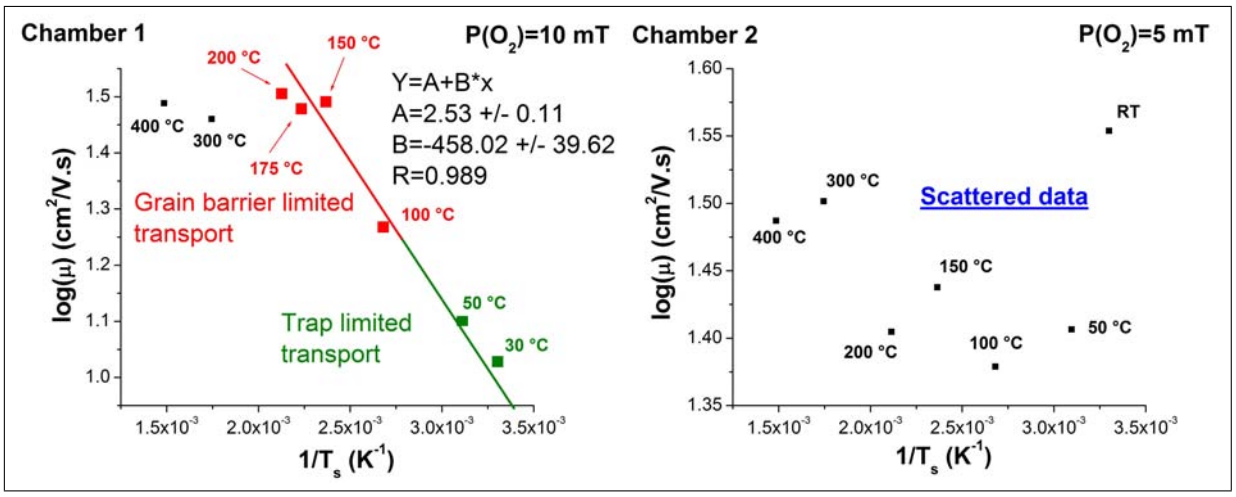

Figure 5.33 Plot of log(μ) versus 1/T_s for chambers 1 (left) and 2 (right). In chamber 1, a good linear regression is obtained for the experimental points coloured in green and red.

The behaviour observed in chamber 1 between 100 and 200°C is in excellent agreement with the model developed by Petritz [180]. He considered the case where carrier transport occurred by thermionic emission across intergrain barriers. This model yields an effective mobility μ_{eff} dominated by thermionic emission across the grain barriers with an energy E_b:

$$\mu_{eff} = \mu_0 \times e^{-\frac{E_b}{kT}} \tag{5.3}$$

where

$$\mu_0 = \frac{L_g q}{\sqrt{2\pi m^* kT}} \tag{5.4}$$

E_b is the energy barrier at the grain surface, T the sample temperature (which is set equal to the substrate temperature T_s), L_g is the grain size, q is the charge of the trap, m^* is the effective mass of the charge carriers and k is Boltzmann's constant. Based on the slope of the linear regression obtained in chamber 1, it is estimated that E_b=39.46 meV. This activation energy is smaller than the grain boundary activation energies for a semiconductor such as Si and is consistent with the fact that grain boundary effects are not very strong in crystalline ITO. Below 100°C, μ is more likely to be trap-limited [181]. For chamber 2 samples, the data was too scattered for a log(μ) versus 1/T_s for a Petritz relation.

5.2.1.4 Carrier concentration

The carrier concentration of the thin films was measured via Hall effect measurements using the Van Der Pauw method, presented in section 4.6.2. Results obtained for films from chambers 1 and 2 are presented in Fig. 5.34.

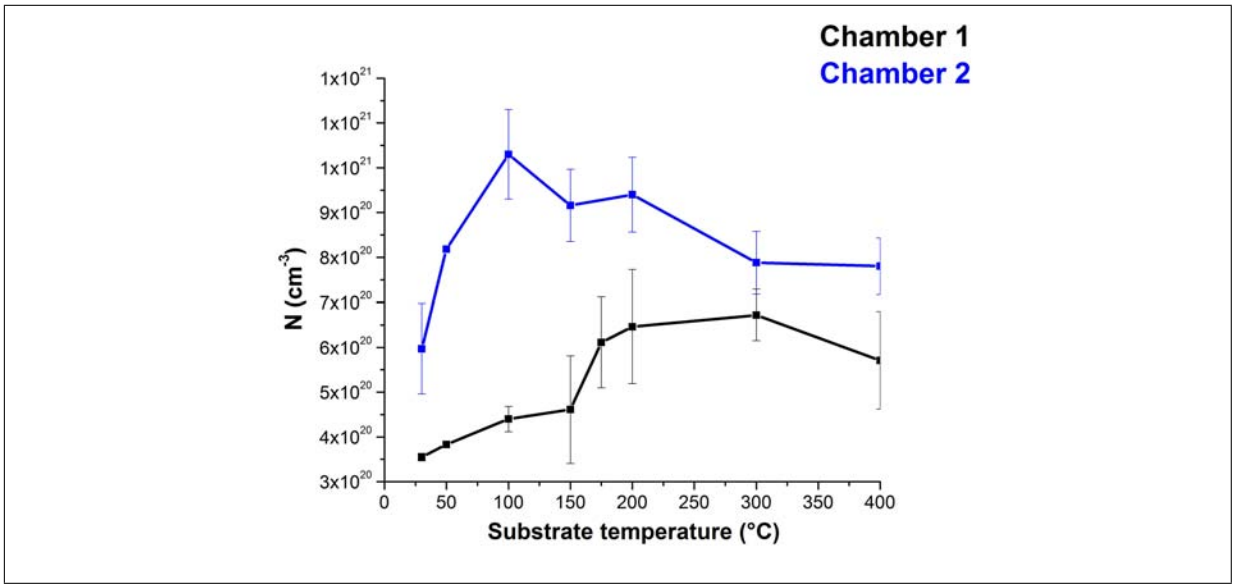

Figure 5.34 Variation of N with T_s when T_s is varied from RT to 400°C. The black curve is for chamber 1 while the blue one is for chamber 2.

Based on Fig. 5.34, the following observations can be made: in the RT - 400°C range, N is statistically larger for chamber 2 than for 1. A slight decrease in N was observed to take place at high temperature (400°C) in chamber 1, while this effect occurs much earlier in chamber 2 (200°C). It is reminded that there are two contributions to ITO thin film conduction:

1. oxygen vacancies.
2. "electrically active" Sn (effective substitution of an In atom by a Sn atom).

In chamber 1, the matrix is fully crystalline from 200°C (Fig. 5.27). As for chamber 2, it can be considered that 100°C is the temperature at which the matrix is fully crystalline (Fig. 5.24). In crystals, all the Sn is electically active, i.e., each Sn effectively substitutes for one In. This is a reasonable approximation since the Sn concentration used (3.65 at.%) is well below its solubility limit in In_2O_3 (∼5 at.% [182]). This also implies that there are no particular complexes/precipitates/phases "extinguishing" Sn (i.e. preventing it from donating one free carrier to the matrix), a situation confirmed by XRD and TEM measurements (Figs. 5.13 - 5.14 - 5.27 - 5.28). Below 200°C for chamber 1 and 100°C for chamber 2, where there is a mix of amorphous and crystalline phases, it is assumed that

a combination of oxygen vacancies and a gradual Sn activation governs the generation of free carriers. Table 5.6 sums up how free carriers are generated in each temperature range.

Table 5.6 Generation of free carriers for ITO thin films grown in chambers 1 and 2.

Chamber number	Temperature range (°C)	Generation of free carriers
Chamber 1	RT - 150	Oxygen vacancies
	150 - 400	Oxygen vacancies + Sn
Chamber 2	RT - 200	Oxygen vacancies + Sn
	200 -400	Oxygen vacancies

The variation of oxygen content as T_s changes was studied by SEM EDX peformed at 7 kV. This yields the average composition of an interaction volume which comprises the whole film from top surface to substrate/film interface (see Monte carlo simulations in section 4.3.2.2). The In/Sn and (In+Sn)/O atomic ratio evolutions with T_s in both chambers are presented in Fig. 5.35.

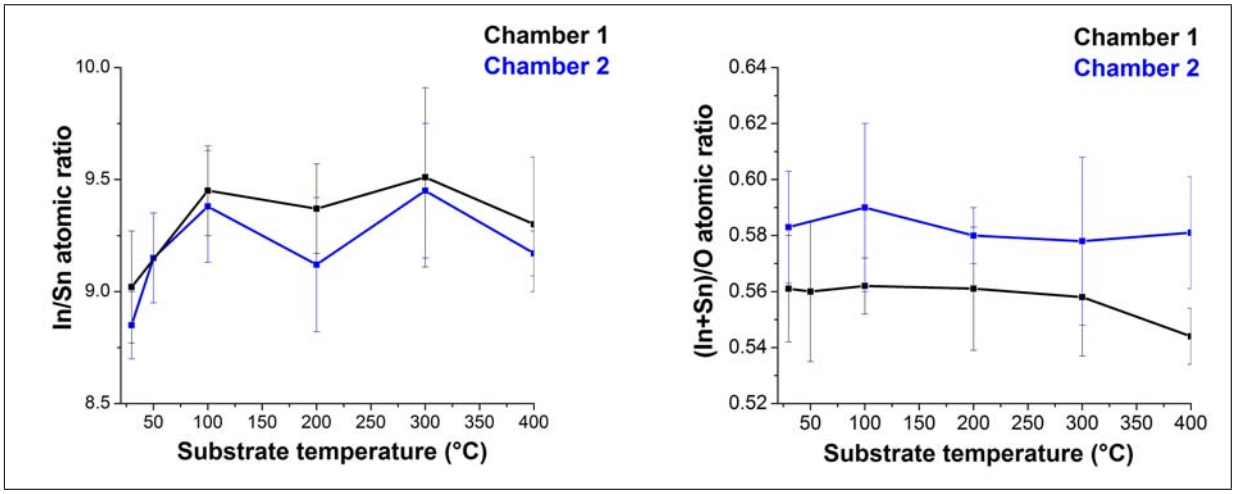

Figure 5.35 Variation of In/Sn and (In+Sn)/O atomic ratios for chambers 1 and 2 when T_s varies from RT to 400°C. O K, In L and Sn L lines were used for quantification.

Three main observations can be made:

- the (In+Sn)/O atomic ratio seems to decrease slightly with T_s in chamber 1 while no change is observed in chamber 2.
- the (In+Sn)/O atomic ratio in chamber 2 is slightly higher than that in chamber 1 in the RT - 400°C range.
- the In/Sn atomic ratio is stable and close to the nominal ratio in both chambers.

The stability of the In/Sn atomic ratio suggests that the variation of the (In+Sn)/O atomic ratio is solely due to a change in oxygen concentration. As noted in[], as the oxygen content changes, there are changes in the density of the film, the efficiency of X-ray production in the sample and the degree of absorption the X -Rays suffer as they exit the specimen. However, no correction for the oxygen absorption (typically by changing the density of the film) was made because of the large uncertainty in the magnitude of the change in the film density.

Profiles of Sn segregation to the film surface were obtained from STEM EDX (in the Tecnai F20) to complement the SEM EDX study. An electron probe was used and moved accross the whole film layer. A sample grown in chamber 2 at T_s=200°C and P(O_2)=5 mT kindly prepared by FIB by Dr. Chu. Drift affected the measurements but not to the extent of impacting on precision: under INCA software, a spatial drift of 1 to 3% as compared with the initial "locked" area was observed for a 200 seconds acquisition time. X-Ray absorption and specimen thickness were taken into account to yield results as accurate as possible (see section 4.3.1.2 for the k-factor determination for In, Sn and O). Three five-point line scans (noted as a, b and c) across the film were carried out as illustrated in Fig. 5.36.

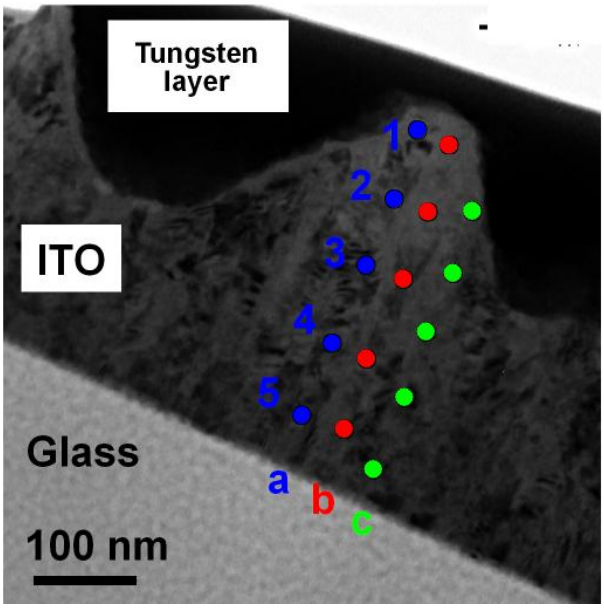

Figure 5.36 STEM EDX linescans. The sample was prepared by FIB and grown at T_s=200°C and P(O_2)=5 mT in chamber 2. The coloured dots illustrate from which area compositional data were acquired.

The STEM EDX results obtained are summarised in Table 5.7.

Table 5.7 Summary of In/Sn and (In+Sn)/O atomic ratios obtained from the three five point line scans shown in Fig. 5.36). The sample was prepared by FIB and grown at T_s=200°C and P(O_2)=5 mT in chamber 2.

Line scan	Position in Fig. 5.36	In/Sn	(In+Sn)/O
a	1	9.82	0.52
	2	9.67	0.56
	3	10.12	0.58
	4	9.42	0.54
	5	10.38	0.57
Average		9.88	0.55
Standard deviation		0.38	0.02
b	1	9.52	0.58
	2	9.27	0.54
	3	9.78	0.57
	4	9.49	0.57
	5	9.23	0.53
Average		9.70	0.56
Standard deviation		0.43	0.02
c	1	9.23	0.59
	2	9.56	0.54
	3	10.21	0.52
	4	9.43	0.62
	5	10.09	0.57
Average		9.68	0.57
Standard deviation		0.37	0.04
Total average		9.75	0.56
Total standard deviation		0.48	0.03

No clear trend can be discerned for both the In/Sn or (In+Sn)/O atomic ratios, indicating that no significant Sn segregation to the film surface took place even at high T_s where the mobility of Sn atoms is enhanced. The atomic ratios agree rather well with those obtained by SEM EDX for chamber 2 (see Fig. 5.35).

5.2.1.5 Resistivity - Surface resistance

The resistivity ρ was calculated from the values of μ and N previously determined by Hall effect measurements and using the Van Der Pauw technique (as indicated previously ρ=1/Neμ). It is observed that ρ of films grown in chamber 2 does not change appreciably between RT and 400°C because μ and N variations cancel each other. A totally different behaviour is observed in chamber 1 where the resistivity decreases linearly up to $175/200$°C before reaching a plateau. The results are illustrated in Fig. 5.37.

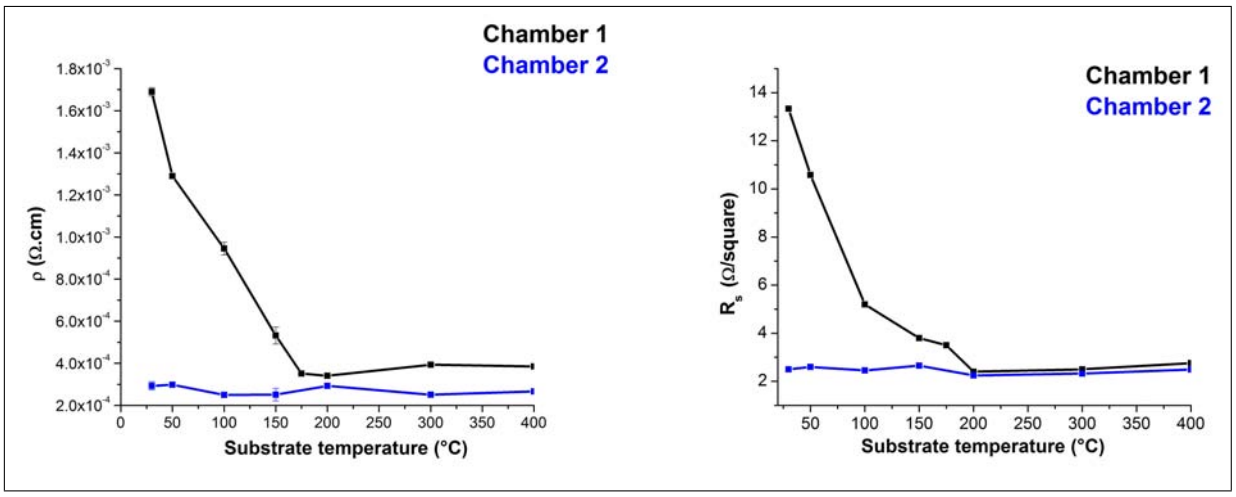

Figure 5.37 Variation of ρ (left) and R_s (right) with T_s as T_s is varied from RT to 400°C. The black curve is for chamber 1 while the blue one is for chamber 2.

This linear behaviour is remarkable and worth investigating further. An *in-situ* study could not be performed here, and, all subsequent characterisations made in this study were performed *ex-situ*. Nonetheless, the true microstructure at a given temperature might not be accurately represented by that after cooling the sample since they could differ at low and high T_s. That is the reason why a low cooling rate was chosen (3°C/min) so as to limit any possible change in microstructure during cooling down. In that case, the resistivity measured after cooling down is representative of the resistivity at higher T_s.

ρ was found to show a temperature activated behaviour as illustrated by an Arrhenius type plot of $\log(\sigma)$ versus $1/T_s$ (Fig. 5.38).

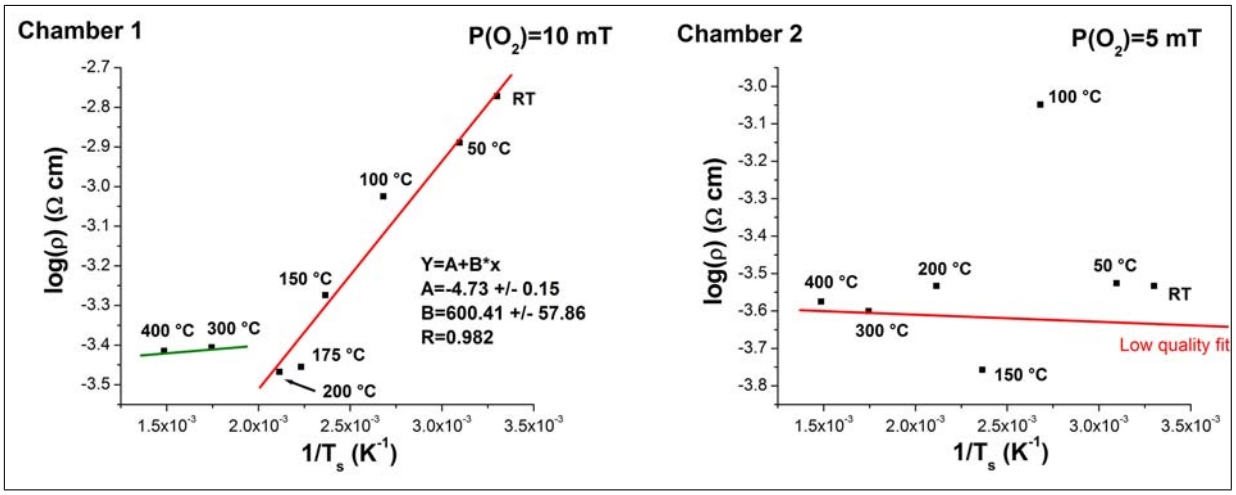

Figure 5.38 Arrhenius plot of $\log(\rho)$ versus $1/T_s$ for chambers 1 and 2. T_s was varied from RT to 400°C and $P(O_2)$ was kept constant at 10 and 5 mT in chambers 1 and 2 respectively.

If a straight line is obtained in a log(ρ) versus 1/T_s plot, ρ can be assumed to obey an Arrhenius type law:

$$\rho = \rho_0 e^{-\frac{E_a}{kT}} \tag{5.5}$$

where E_a is an activation energy. Since the fall of resistivity may be associated with the rearrangement and removal of point defect clusters and recombination centres along with crystallization, E_a is the overall activation energy of these processes. The slope was used to determine the activation energy E_a of the reaction described above. The linear fit performed for chamber 1 gave a slope of: -600 yielding E_a=0.52 eV, taking k=8.62$\times 10^{-5}$ eV/K. This value is close to the one found by Bhatti et al. [183] (0.49 eV) for ITO films deposited by r.f. sputtering. Another fitting region was identified (green curve in Fig. 5.38, chamber 1) which yielded E_a=0.03 eV. While further experimental points at these temperatures are needed to confirm this value, it can be assumed that ρ does not show any temperature dependence in that range. A very low activation energy seems to hold true for films grown in chamber 2 between RT and 400°C. However, no calculation of this activation energy was performed owing to random nature of the experimental log(ρ) - 1/T_s plot.

5.2.1.6 Summary of the results

ITO thin films were deposited in chambers 1 and 2 by varying T_s from RT to 400°C. The oxygen pressure was kept constant and set at 10 and 5 mT in chambers 1 and 2 respectively. The number of pulses fired was indentical in both chambers, but films in chamber 2 were thicker than in 1 while T_s was not found to significantly affect thickness. The microstructure was strongly impacted. At RT, a nearly amorphous matrix was obtained in chamber 1, yet the crystallisation process was already well underway in chamber 2. Full crystallisation was achieved at 200°C and 100°C in chambers 1 and 2 respectively. In both chambers, the average grain size did not vary much with increasing T_s, although it was smaller in chamber 2 than in 1. The electrical properties were influenced in both chambers by microstructure changes even though the impact was less marked in chamber 2. Finally, thin film composition varied only moderately with T_s.

5.2.1.7 Discussion

5.2.1.7.1 Structural properties In chamber 2, the growth orientation was affected by the substrate temperature T_s (Fig. 5.14): films were orientated along the <100>

direction up to 100°C. Above this temperature, the films increasingly developed a preferred (222) orientation. No such change could be observed in chamber 1 (Fig. 5.13), because no evidence of crystallinity could be seen below T_s=150°C. At high temperature (T_s=400°C), films tended to become more and more polycrystalline in both chambers with the gradual development of (211) and (440) orientations.

The choice of a particular preferred growth orientation is determined primarly via the minimisation of the surface and interface free energies of the thin film. Indeed, glass is amorphous in nature so that the growth of ITO films on such substrates is not principally determined by the lattice mismtach between the film and substrate as it is for crystalline substrates. Hence, in chamber 1, the preferred (222) orientation is suggested to be the one minimising both the surface and interface free energies. In chamber 2, a texture change arose between 100 and 150°C. It is suggested that such a change is connected with adatomic mobilities which vary with T_s. A lower adatomic mobility at low T_s might result in a structure under more stress. The preferred (100) orientation would be the one minimising such stress. As it relaxes at higher T_s, the growth orientation would be once again controlled by the minimisation of the surface and interface free energies, leading to the (222) texture, which was also observed in chamber 1.

The difference in microstructure at low T_s between chamber 1 and 2 was explained with variations in adatomic mobilities with the laser energy density falling on the target (E_d) and $P(O_2)$. Since a higher E_d and a lower $P(O_2)$ were used in chamber 2 (see section 4.1), the kinetic energies of species impacted onto the growing surface in chamber 2 was greater than in chamber 1. This explains why RT films were more crystalline in chamber 2. In chamber 1, clear evidence of crystallisation by XRD was only observed above T_s=150°C (Fig. 5.13), although, a very small amount of crystallites were already present at RT in chamber 1, as witnessed by TEM micrographs (Fig. 5.28 a)) along with DPs (diffuse rings with spots). As a consequence, RT grown films in chamber 1 are not fully amorphous. Complete crystallisation of the matrix was observed at 200 and 100°C in chambers 1 and 2 respectively, following an initial stage whereby round crystallites were embedded in the amorphous matrix (Figs. 5.27 - 5.28).

Cross-section (Fig. 5.30) TEM micrographs for samples from chamber 2 showed that the layer adjacent to the substrate tended to be amorphous whereas the top layer was crystalline. After nucleation, grains are observed to grow as very narrow 10 - 50 nm wide parallel-sided columns perpendicular to the substrate (Fig. 5.29). A very different behaviour is observed in chamber 1, where a large lateral growth from the substrate is

observed. This larger lateral growth results in a higher average grain size observed at the surfaces of samples grown in chamber 1 (Fig. 5.21) as compared with those grown in chamber 2 (Fig. 5.24). The lower average grain size observed in chamber 2 compared to chamber 1 is attributed to a different density of pre-existing nuclei within the matrix. The latter is in turn attributed to the higher energy density E_d falling on the target in chamber 2, thus evaporating a larger number of ions and other reactive species, with larger kinetic energies, eventually forming more nuclei.

GAXRD profiles (Fig. 5.19) demonstrated that the degree of texture tended to evolve during thin film growth in chamber 2, at $P(O_2)$=5 mT and T_s=200°C. The film originally grows with no preferred orientation during the first 100/150 nm, with (222), (411) and (420) peaks visible. Afterwards, a (400) preferred orientation was increasingly favoured indicating that more pronounced textures are obtained after the film has achieved a certain crtitical thickness, estimated to be around 200 nm. This observation may be explained in terms of energetic considerations, since during the first stages of the growth, the thin film has to minimise both its interface and surface free energies. In addition, the amorphous nature of the substrate does not favour any specific growth orientation. Hence, several growth orientations could meet the requirements of minimising both the surface and interface free energies.

The change of the preferred growth orientation in chamber 2 was found to affect the FWHMs of the preferred oriention peaks. The FWHMs gradually decreased with T_s except at 150°C where a significant maximum (1.05°) was observed (Fig. 5.17). This can be explained in terms of an intermediate/transition state if the matrix undergoes the change in texture change as demonstrated by the XRD measurements (Fig. 5.14). This maximum did not show a strong impact on the electron mean free path (L), as illustrated in Fig. 5.32, which remains of the order of a few nanometres. This is not contradictory since L is defined as: $L = (3\pi^2)^{1/3}(h/e^2)\rho^{-1}N^{-2/3}$.

Since ρ is found to be almost constant in the RT - 400°C range (Fig. 5.37), variations of L are solely due to changes in N, which shows a maximum at 100°C, but not significant to impact on L. The fact that L remains almost unchanged as the matrix undergoes a texture change and some loss of crystallinity combined with increased internal stress (FWHM increase) is related to L being of a few nanometres. The possible structural disorder implied by a texture change occurs on a much smaller scale than L so that it is not strongly affected by such a disorder.

The impact of the texture strength was connected to μ in chambers 1 and 2 (Fig. 5.18). A positive linear relation between $TC_{(222)}$ and μ was found in chamber 1 except at T_s=400°C due to possible oxygen absorption effects as shown by SEM-EDX measurements (Fig. 5.35). Therefore, a more textured film tends to have a higher mobility on account of crystallisation enhancement with higher T_s. In chamber 2, two different temperature ranges were identified where a correlation between the orientation and μ occured: between RT and 150°C, a negative linear correlation between $TC_{(400)}$ and μ is observed, while between 150 and 400°C, there is a positive linear correlation between $TC_{(400)}$ and μ. In the range 150 - 400°C, and likewise for chamber 1, the positive linear corrrelation is attributed to thermally induced crystallisation. The negative linear correlation in the low temperature range is not believed to be related to any physical phenomenon taking place in the films.

In chamber 1, the situation is somewhat simpler but opposite to that in chamber 2. FWHMs were found to increase steadily with T_s (Fig. 5.17). While it is often explained that a higher T_s enhances adatomic migration improving overall crystallinity, it is argued that at high T_s, oxidation can take place more easily (Fig. 5.35). The enhanced diffusion of oxygen within the layer would impact on the crystallinity as oxidation could result in oxygen atoms going into interstices (in addition to those filling in oxygen vacancies) distorting the structure and increase its stress level. This hypothesis is confirmed by the noticeable decrease of the (222) peak amplitude at T_s=400°C (Fig. 5.13) along with a FWHM increase (Fig. 5.17).

On a final note, the average FWHM for films from chamber 2 is higher than that for chamber 1. This is attributed to a higher deposition rate in chamber 2 due to the higher laser energy density used. This also implies that a larger amount of material is evaporated from the target in chamber 2 as compared with chamber 1 as partially confirmed by the higher film thicknesses obtained in chamber 2 (Fig. 5.12).

5.2.1.7.2 Chemistry Oxygen can be easily incorporated/desorbed into/from the lattice via the surface owing to the unique crystal-defect structure of bixbyite based materials which includes a high concentration of vacancies. The higher the T_s, the higher the oxygen diffusion rate since the latter is thermally activated. It has been proposed [10] that O_2 gas can be adsorbed as O^{2-}, O^- and/or O_2^-. Such an oxygen intake was not significant for films grown in either chambers as demonstrated by SEM-EDX (Fig. 5.35): both film types showed a relative stability of the In/Sn and (In+Sn)/O atomic ratios. A slight decline of the (In+Sn)/O atomic ratio was however noticed at 400°C in chamber

1. This is in line with previous carrier concentration measurements (Fig. 5.34) where a significant decline in N (chamber 1) was observed. This was accounted for by the filling of oxygen vacancies, which was less significant in chamber 2. Oxygen intake at high T_s was also reported in [184] [48].

Such a low level of interaction with the oxygen atmosphere might be explained by the fact that for T_s <450°C, the vacancy concentration is frozen in [185]. Hence, it is argued that the level of oxygen vacancy concentration encountered in the films at T_s <400°C (for both chambers) is not sufficiently high to enable significant oxygen absorption and desorption.

5.2.1.7.3 Carrier concentration, mobility and resistivity As the crystallization improved with increasing T_s, the carrier concentration in the ITO films increased in both chambers (Fig. 5.34). It is suggested that 2 independent carrier generating mechanisms take place. Initially, a structural rearrangement or relaxation of the amorphous phase [186] led to ordering of the oxygen vacancies. As the crystallisation proceeds further, larger crystallites are formed. Within each of these crystallites, Sn can effectively substitute for In atoms (a thermally activated process), further releasing free carriers. In chamber 1, this hypothesis and the chronological order of these two mechanisms is reinforced by the carrier concentration results presented in Fig. 5.34 which showed at first a steady and linear rise in N between RT and 150°C (structural rearrangement of the amorphous phase). This is followed by a much sharper increase between 150 and 200°C (Sn substitution for In atoms). The matrix is then fully crystallised as observed in SEM and plan view TEM micrographs.

In chamber 2, a rapid rise of N is observed between RT and 100°C where a maximum is observed. At that temperature, complete crystallisation of the matrix is also achieved as witnessed by SEM micrographs showing a grainy surface morphology at a T_s as low as 100°C (Fig. 5.24 (b)). Nonetheless, the occurrence of a strong (400) preferred orientation (see Fig. 5.14) could also be considered as another factor to enhance the carrier concentration (N), although further investigations are needed to be carried out to find out the relation between the (400) preferred orientation and why such a maximum is not observed for μ (Fig. 5.31).

Saturation occurs after 200 and 150°C in chambers 1 and 2 respectively. It is suggested that this takes place when the majority of Sn has effectively substituted for In atoms for a given concentration of oxygen vacancies depending on the oxygen pressure during growth. A slight decrease in N is observed above 300 and 200°C in chambers 1 and 2

respectively due to oxygen absorption as explained above.

The difference in microstructure between samples from chambers 1 and 2 at low T_s had a dramatic impact not only on N, but also on μ. μ was shown to be almost independent on T_s in chamber 1 above 200°C and over the whole temperature range investigated in chamber 2 (Fig. 5.31), suggesting that degenerate conduction behaviour, as in (semi-)metals, takes place. In chamber 1, below 200°C, μ and ρ exhibit thermally activated behaviour between RT and 200°C (Figs. 5.33 and 5.38) with energy barriers of 39.46 meV and 0.52 eV respectively. For ρ, this activation energy was attributed to the crystallisation process occurring over this temperature range, while for μ, such a barrier is suggested to result from the formation of trapping states due to the inherent atomic disorder (incomplete atomic bonding) at grain boundaries (grain boundary trapping theory [176]) in the 100 - 200°C range and in the amorphous matrix (RT - 100°C) [181]. Above 200°C, this activation energy is close to zero since no strong variations with T_s are observed (Fig. 5.34). This reduction of activation energy in the transition to a polycrystalline matrix seems to be related to the transition from trap/grain barrier limited conduction to quasi-impurity band conduction. In addition, the increase in N between RT and 200°C (for reasons stated in the above paragraph) might impact on the gradual diminishing action of energy barriers on the conduction.

On the other hand, μ does not appear to be thermally activated in chamber 2 and values do not vary to a great extent between RT and T_s = 400°C. This would imply a very low or non-existent activation energy of the mobility with free carriers flowing freely across grain surfaces. This might be due to the difference in N between films from the two chambers: a higher carrier density N would screen energy barriers set by grain boundaries and amorphous/crystalline interfaces. While the highest μ observed in chamber 2 is at RT, this result is to be taken with caution. Such a discepreny might result from crystallites being of much lower resistivity than the intercrystalline barriers. Therefore, the measured Hall mobility μ_H (noted μ in this work) would be the mobility within crystallites/grains without accounting for the effects of intercrystalline barriers, hence the much higher mobility observed at low temperature. This affects the validity of the measurements and makes r in eq. 4.6 different from unity. As the matrix becomes fully crystalline at T_s=100°C, the effect of energy barriers on carrier flow becomes less predominant via grain growth and/or less disordered grain boundaries so that the measured mobility reflects the true nature of the sample under investigation. Segregation of impurity (particularly Sn) at grain boundaries cannot be totally ruled out either based on our experimental results in explaining grain interiors having lower resistance than

grain boundaries (segregation model [187]). The reason why this is not happening in chamber 1 is puzzling and requires further work to confirm whether this trend is true or not.

The derivation of μ and N enable the calculation of ρ. In chamber 1, ρ was found to decrease from RT to 200°C. Over this range, and a similar manner to μ, the ρ exhibited a thermally actived behaviour between RT and 200°C so that:

$$\rho = \rho_0 e^{-\frac{E_a}{kT}} \tag{5.6}$$

The thermally activated behaviour of ρ is related directly to that of μ (and possibly N, although, more experimental points are needed). The lowest resistivity was obtained for ITO films deposited at T_s >200°C in chamber 1 (Fig. 5.37). ρ reaches a plateau above this temperature. This plateau is seemingly reached when crystallinity is at a maximum and no more free carriers can be generated by oxygen vacancy creation and Sn activation. The overall decrease in ρ in chamber 1 was explained by thermally induced crystallisation generating carriers and a mobility increase. Meanwhile, log(ρ) versus $\frac{1}{T_s}$ in chamber 2 (Fig. 5.38) showed a linear dependence, but the fit was so poor that no reliable calculations were possible using this fit. The resistivity is almost constant in the RT - 400°C range owing to the inverse relationship between μ and N.

5.2.1.7.4 Scattering mechanisms The different microstructures observed in chambers 1 and 2 as T_s was varied impacted on the dominant scattering mechanisms operating in our films. The large surface roughness observed at 400°C in chamber 1 is not believed to cause strong surface scattering as only the very top surface (∼1.5 nm) was affected, as compared with a total layer thickness of about 250 nm. In chamber 2, films were even smoother, so surface scattering was not considered to be significant in either chamber. Neutral defect scattering was not considered either as TCO materials are highly ionised semiconductors showing very low ionisation energies. For example, in In_2O_3, the ionisation energy of the donors is only about 0.01 eV [188]. Consequently, the concentration of neutral donors at RT is very low meaning that ionised impurity scattering (oxygen vacancies and Sn ions) is not expected to operate. Ionised impurity scattering is the most likely mechanism remaining. It is demonstrated by plotting μ versus N (see Fig. 5.39).

Fig. 5.39 shows that μ depends strongly on N in chamber 1 (between T_s=150 and 400°C) and in chamber 2 (RT - 400°C). This behaviour is compatible with the ionised

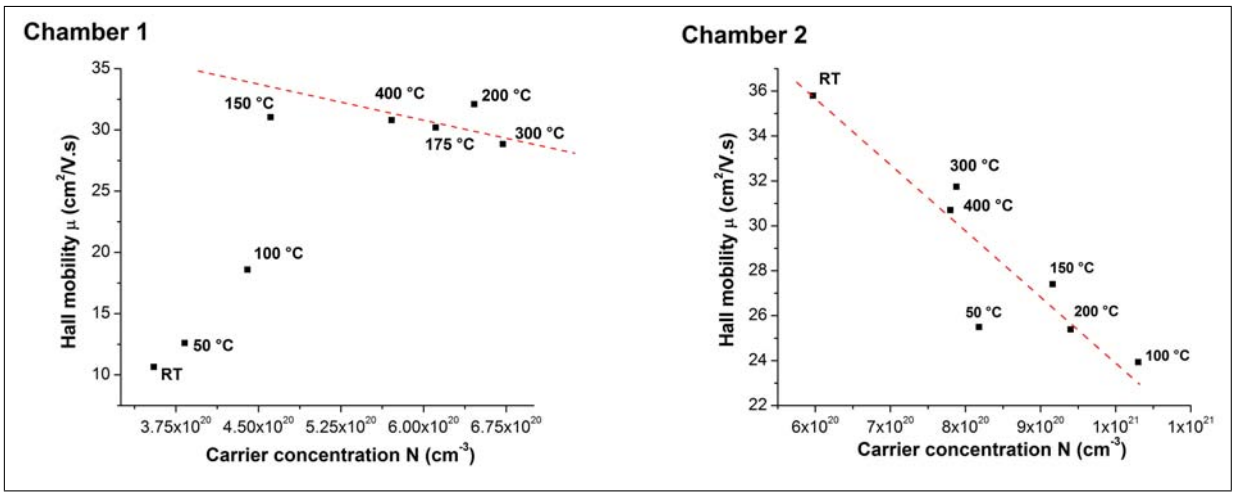

Figure 5.39 Relationship between the carrier concentration N and the mobility μ of ITO thin films when T_s varies from RT to 400°C. Left: chamber 1; right: chamber 2.

impurity scattering theory developed by Dingle et al. [6] (chapter 2/section 2.2.2.1.2).

The experimental μ - N plots in chambers 1 and 2 are compared with this model (see Fig. 5.40) assuming either scattering at Sn ions (red curve) and scattering at oxygen vacancies (green curve).

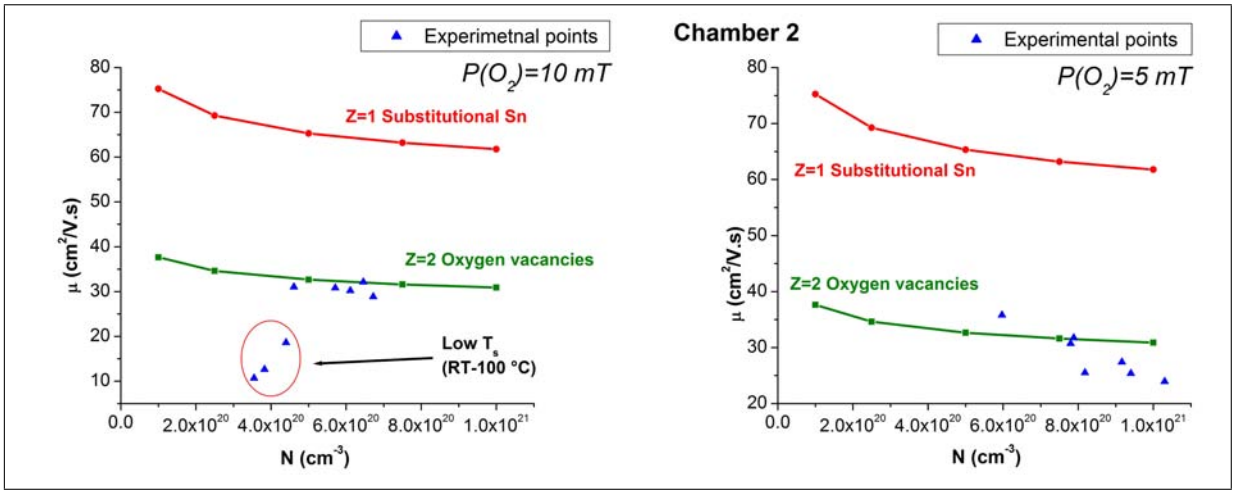

Figure 5.40 Hall mobility μ versus carrier density N for chambers 1 (left) and 2 (right). Experimental data are shown as blue triangles. Also shown are the calculated μ based on charged impurity scattering assuming that all carriers are substitutional Sn ($[Sn_{In}]$, Z=1, red curve) or doubly charged oxygen vacancies ($[V_{O^{\cdot\cdot}}]$, Z=2, green curve).

The value of ε_r=9 [72] and m^*=0.35m_0 [28] (where m_0 is the stationary mass of an electron) is taken from the literature. The scattering at doubly charged oxygen vacancies is obviously larger than at singly charged Sn for a given donor density. The values of N_i are postulated to be N/2 for Z=2 ions (half of oxygen sites are vacancies) and N for Z=1 ions (all substitutional Sn are ionised) as explained in [38]. This model assumes no temperature dependence of μ which is reasonably well observed in both chambers for

the higher temperature range ($> 200°$C) (see Fig. 5.31).

Ionised impurity scattering is observed to be dominant between 150 and 400°C in chamber 1 and over the whole temperature range in chamber 2. This scattering is also shown to be mainly due to oxygen vacancies since the curve representing scattering by oxygen vacancies gives a better fit with the experimental data. The departure from the modelled to the experimental data in chamber 1 at low T_s means that ionised impurity scattering is not predominant within this temperature range. It was indeed shown that trap and grain boundary limited conductions were taking place at these T_s's which is the reason why μ was found to be thermally activated (Fig. 5.33). Moreover, at RT, Sn atoms are believed to form neutral complexes with the oxygen anions [13]. They are said to be "deactivated" and no longer constitute ionised impurities making the conduction mechanism depart further from the ionised impurity model.

In chamber 2, the dominance of ionised impurity scattering between RT and 400°C was justified by the larger N as compared with chamber 1, suggesting that an equally large number of oxygen-vacancy-like electron-donating defects are present and that degenerate ionised impurity scattering remains dominant over the whole temperature range studied. The relatively low mobility variation with T_s combined with a more or less constant electron density N point to a highly degenerate semiconductor-type behaviour where the films behave like a semi metals [189]. Finally, and in both chambers, the electron mean free path was found to be only a few nanometres. Hence, grain boundary scattering was not considered as strongly affecting electrical conduction through the films.

5.2.2 Optical properties

As mentioned in section 5.2, the film thickness in both chambers did not show any dependence on T_s. As a consequence, it is assumed that the film thickness parameter does not play any significant role in optical property changes with T_s.

5.2.2.1 Transmittance and ellipsometric measurements

Transmittance measurements in the UV-visible-near infra red range (250 - 1000 nm) were performed. Fig. 5.41 shows the results.

The fluctuations in the spectra of chamber 2 (see blue arrows in Fig. 5.41) are connected

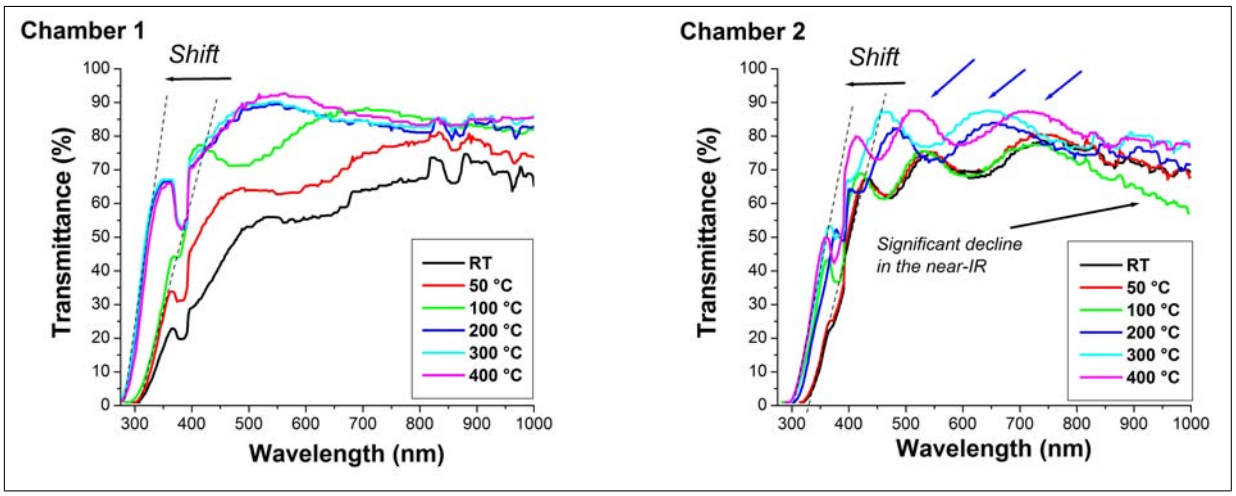

Figure 5.41 Transparency in the 400 - 1000 nm region of ITO thin films deposited at varying T_s in chambers 1 and 2. T_s was varied from RT to 400°C and $P(O_2)$ was kept constant at 10 and 5 mT in chambers 1 and 2 respectively.

with the film thickness, resulting in interference between light reflected from the top surface and the film/substrate interface. A "zoom" over the 250 - 500 nm range is provided in Fig. 5.42 to emphasise the band gap shift taking place.

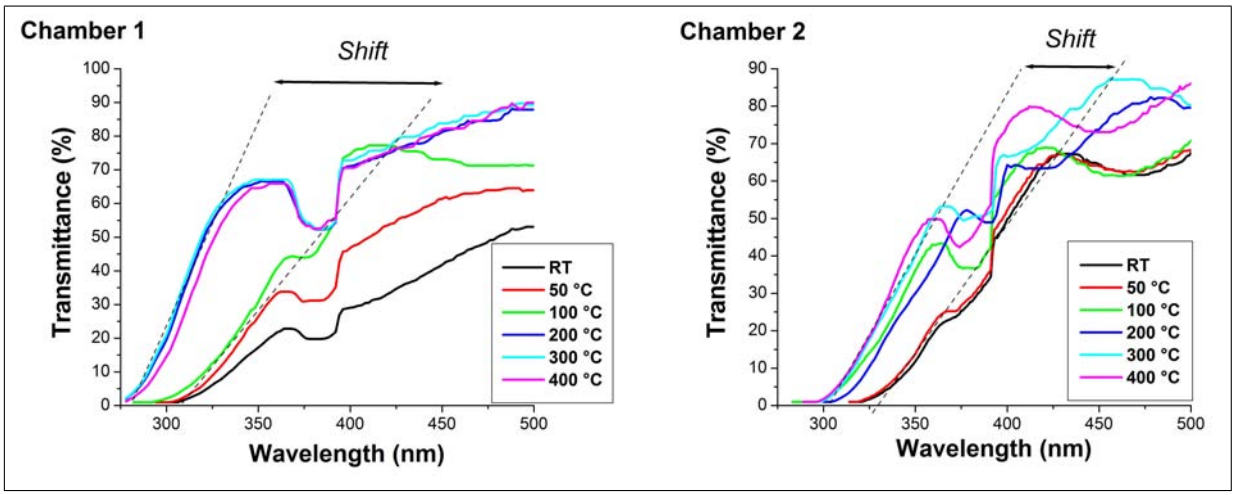

Figure 5.42 Transparency in the 275 - 500 nm region for ITO thin films deposited at varying T_s in chambers 1 and 2. T_s was varied from RT to 400°C and $P(O_2)$ was kept constant at 10 and 5 mT in chambers 1 and 2 respectively.

For the sake of clarity, the average transmittance over the 400 - 1000 nm range is plotted in Fig. 5.43. This range was chosen since the data vary somewhat less in that region than in the band gap region 250 - 400 nm meaning that a better comparison can be achieved. The variation of the bandgap E_g with T_s is also shown in the same figure (right). The latter is calculated by plotting α^2 (α=absorption coefficient) versus the photon energy E=hν (Tauc plot [190]).

Several observations can be made. Based on Figs. 5.41 and 5.42, a shift of the bandgap towards lower wavelengths takes place as T_s increases. This shift is observed in both

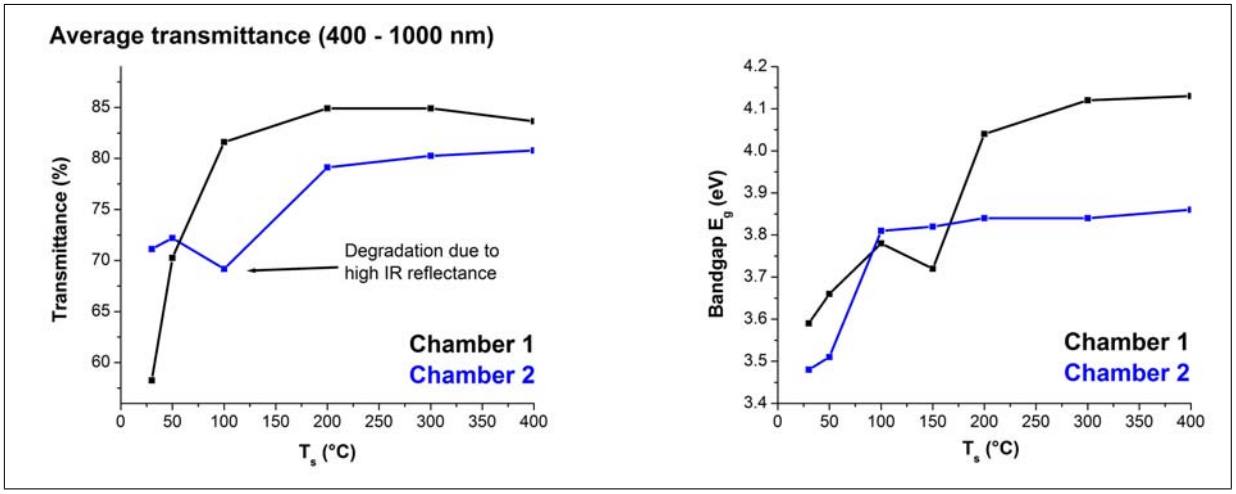

Figure 5.43 Left: average transparency in the 400 - 1000 nm region of ITO thin films deposited at $T_s's$ from RT to 400°C in chambers 1 and 2. Right: variation of bandgap E_g with T_s. T_s was varied from RT to 400°C and P(O_2) was kept constant at 10 and 5 mT in chambers 1 and 2 respectively.

chambers but its magnitude is different: it is more pronounced in chamber 1 than in 2. In addition, saturation can be identified in both chambers. Whereas in chamber 2, no appreciable shift is visible after 100°C, in chamber 1 this occured at the higher temperature of 200°C. This agrees well with carrier concentration measurements (N) (see Fig. 5.34) which showed a relative stability of N after 100 and 200°C in chambers 2 and 1 respectively. Hence the link between N and the bandgap shift known as the Burstein-Moss effect (see earlier explanation section 2.2.1).

Based on Fig. 5.43, the average transmittance in the 400 - 1000 nm region improves with T_s in both chambers. In chamber 1, at RT, the ITO films were dark brown in colour with an average transmission of less than 60% over the 400 - 1000 nm range. Transmittance at that same temperature and over the same range was significantly higher in films from chamber 2 with an average transparency of 75%. A further increase in temperature (200°C in chamber 1 and 300°C in chamber 2) does not lead to an increase in transmittance over the wavelength region studied, indeed transmittance seems to degrade slightly at 400°C in chamber 1. It was previously shown that the electrical properties degraded slightly over this range, illustrating once again the interdependence of electrical and optical properties. AFM showed (Fig. 5.44) that the roughness increases strongly with T_s in chamber 1 up to about 2 nm at 400°C. A strong increase is also observed in chamber 2: RMS roughness doubled between 200 and 400°C in chamber 1 while in chamber 2, even at 400°C, films remained extremely smooth with only 0.6 nm RMS roughness.

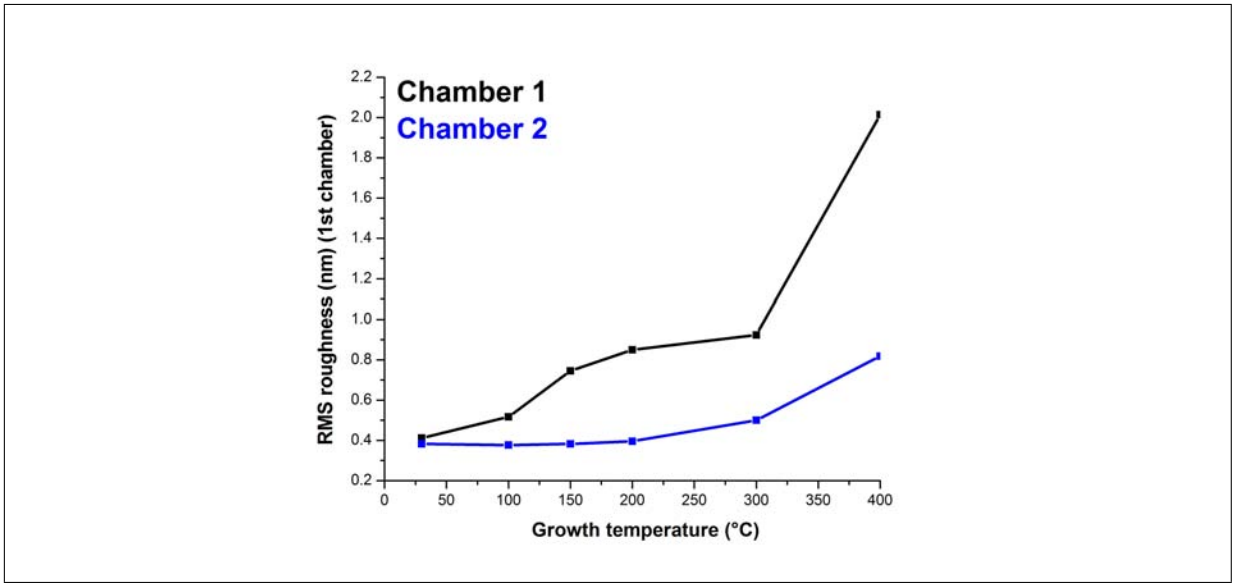

Figure 5.44 RMS roughness comparison for chambers 1 and 2. RMS roughness is calculated on the basis of 2×2 μm scans. Holes are avoided to reflect the "true" roughness of the film surface.

Another effect is worth noting in Fig. 5.42 is the gradual increase in steepness of the absorption edge as T_s increases. The steepness of an absorption edge is related to the degree of crystallinity of the volume probed by the transmittance measurements [46]. The more crystalline is the specimen, the sharper is the edge. This increase in steepness of the absorption edge can be related directly to the TEM plan view micrographs shown in Figs. 5.27 and 5.28. These show the gradual disappearance of the amorphous phase at the expense of the crystalline one. This gradual steepness increase is definitely less marked in chamber 2 and, once again, this can be related to the SEM and TEM micrographs which show that, even at RT, the crystalline phase represents a significant fraction of the ITO thin films in chamber 2 so that sharp edges are obtained at temperatures as low as RT.

In chamber 1, $N^{2/3}$ is found to be linearly related to E_g while in chamber 2, no such link is obvious as shown in Fig. 5.45.

From the slope, B, of the linear E_g versus $N^{2/3}$ plot in chamber 1 (Fig. 5.82), the derivation of the electron reduced effective mass in the material is possible using the formula:

$$B = \frac{\hbar^2}{2m^*_{VC}}(3\pi^2)^{2/3} \tag{5.7}$$

With linear regression, it is found that m^*_{VC}(chamber 1)=8.93×10^{-30} kg. Since m_0=9.11×10^{-31}

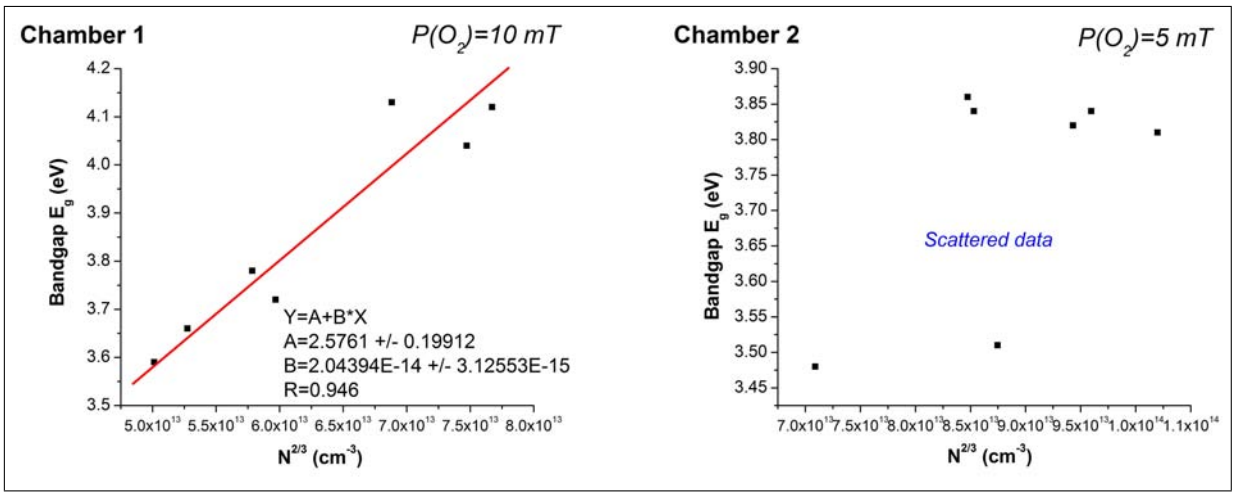

Figure 5.45 Variation in the optical bandgap E_g with $N^{2/3}$ in chambers 1 (left) and 2 (right). T_s was varied from RT to 400°C and $P(O_2)$ was kept constant at 10 and 5 mT in chambers 1 and 2 respectively.

kg, m^*_{VC}(chamber 1)=0.98m_0. Agreement with the literature is not satisfactory since Vainshtein et al. [191] obtained m^*_{VC}=0.50m_0 while Kostlin et al. [28] calculated m^*_{VC}=0.54m_0. It is concluded that the band gap shift is not solely due to carrier concentration variation (especially in chamber 2 where no linear relation is evidenced) and hence the Burstein-Moss shift is not fully obeyed. Other effects competing with this shift (resulting in band-gap shrinkage) will be discussed in section 5.2.2.3.

Finally, ellipsometric measurements are presented in Fig. 5.46 which enable the derivation of the refractive index n and the extinction coefficient k.

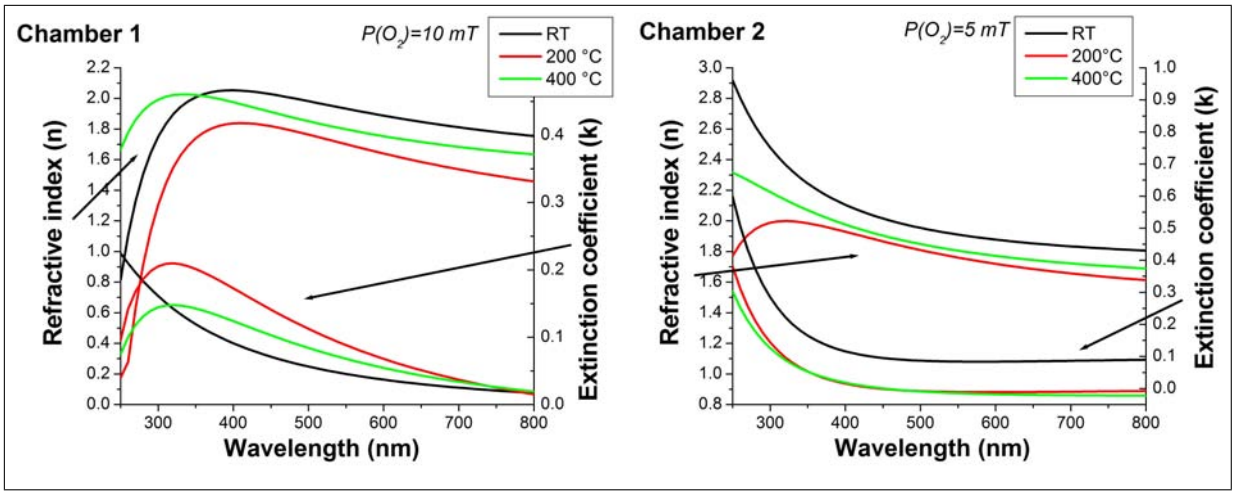

Figure 5.46 Real part of the complex refractive index (n) and extinction coefficient (k) derived from ellipsometric results for ITO films grown at RT, 200 and 400°C in chambers 1 (left) and 2 (right). The Cauchy model was used.

The refractive index n is observed to decrease with T_s increasing from RT to 200/400°C. Meanwhile, the extinction coefficient k was also found to decrease over this same

temperature range which is compatible with an increase in transmittance with increasing T_s (see Fig. 5.43). The variations of (n,k) is much more pronounced in the band gap region (250 - 350 nm).

5.2.2.2 Summary of the results

ITO thin films were deposited at various T_s (RT - 400°C) in both chambers. Films with similar thicknesses were compared and the optical transmittances were found to be impacted in two different ways:

- the (average) transmittance improved over the visible range with increasing T_s.
- absorption edges shifted towards lower wavelenghts with increasing T_s.

The complex refractive index was also found to be affected. In chamber 1, the absorption edge shift with increasing T_s permitted the calculation of the electron reduced effective masse via the Burstein-Moss relation (eq. 2.13). This was not the case in chamber 2 because of other effects at play.

5.2.2.3 Discussion

The transmittance was found to be affected by T_s in both chambers but to a different degree (Fig. 5.41). In chamber 1, the transmittance spectra showed significant changes in values, absorption edge shifts and shapes. These changes were more moderate in chamber 2, this being attributed to the lower working oxygen pressure combined with the slightly higher energy density (E_d) used in this chamber. These 2 parameters result in higher surface mobilities of ejected species on the growing surface resulting in better crystallinity and optical properties at temperatures as low as RT. In chamber 1, however, the surface mobilities are lower than those in chamber 2 - significantly lower to the extent that T_s is suggested to be the dominant parameter in determining these surface mobilities. Hence, the larger spread of features (band gap shifts, transmittance values in the visible range) observed for transmittance spectra chamber 1.

In chamber 1, for films prepared at RT, the transmittance was less than 60% over the visible range while for T_s over 100°C gave films with an average transmittance of 85%. The low transmittance at RT was attributed to an amorphous structure, which by definition is composed of a higher level of structural defects than a crystalline one, giving rise to numerous impurity or trap energy levels within the band gap. Since non oxidised particulates and other non stoichiometric compounds, such as InO and SnO [192], sitting

on the surface, were not observed by SEM measurments (Fig. 5.20), these could not account for the loss of transparency.

The increased transmittance with increasing T_s was attributed to crystallisation. Films grown in chamber 2 also showed an improving transmittance with increasing T_s with a 10% improvement between RT and 400°C. At RT, films grown in chamber 2 were significantly more transparent than those grown in chamber 1 due to higher crystallisation as a result of surface mobilities. Therefore, the degree of matrix crystallisation has an important effect on resulting transmittance over the visible range. An interesting feature was observed on the films grown at T_s=100°C, namely a decline in transmittance in the near-IR region ($\sim$900 nm). This was attributed to the very high carrier density (of the order of $10^{21}cm^{-3}$) as indicated by Hall effect measurements (Fig. 5.34) at T_s=100°C. The increasingly rough surfaces at higher T_s demonstrated by AFM measurements (Fig. 5.44) were not expected to cause any sort of light scattering as the RMS roughness remained around 1 - 2 nm, i.e., far less than the wavelength of the visible light (a few hundred nanometres).

The absorption edge shape was also found to depend on T_s. Its slope was observed to decrease at lower T_s in chamber 1, although, no such observations were made for chamber 2. This behaviour is consistent with the slope of the absorption edges being linked to the defect density. The latter is expected to be very high for the nearly-amorphous film grown at RT in chamber 1 compared with the one grown in chamber 2 where crystallisation was well underway, effectively reducing the total defect concentration. These structural defects are believed to give rise to localised energy levels within the band gap so that an electron is less and less likely to make a direct transtion from the valence to the conduction band, blurring the band gap.

A plot of band gap E_g versus $N^{2/3}$ (Fig. 5.45) showed good agreement between the Burstein-Moss shift theory (see section 2.2.2.2.2) and experiment in chamber 1 but not in chamber 2 (Fig. 5.45). There is however another competing mechanism to fully take into account for the overall band-gap widening (see eq. 2.13): a band-gap narrowing (or band-gap renormalisation) which is a consequence of electron-electon and electro-impurity scattering [193] [194]. Electron-electron scattering is expected to play a more important role at high N and this might be the reason why data in chamber 2 are not in good agreement with the theory, since films grown in chamber 2 showed a higher N. The further departure of the Burstein-Moss shift theory in chamber 2 might

be due to a stronger electron-impurity scattering mechanism since these films contain a higher number of oxygen vacancies (which is also a consequence of a high N). Finally, it has to be noted that no dependency between effective mass and carrier concentration N as postulated in [195] was taken into account in this study, perhaps explaining some scattering in our data.

Transmittance spectra (Fig. 5.41) demonstrated a saturation in the shift above 200°C and 100°C in chambers 1 and 2 respectively which is in excellent agreement again with previous Hall effect measurements (Fig. 5.34). Hence, the electro-optical properties observed in our study are self-consistent. This shift towards lower wavelengths with increasing T_s is equivalent to band gap widening.

Finally, the spectroscopic ellipsometry measurements presented in Fig. 5.46 showed that the refractive indexes n in the visible range (400 - 800 nm) were quite close to the reference values previously reported [196][197] for high quality ITO films and that the extinction coefficients k of the deposited films were below 0.1 in the visible region. This is characteristic of very transparent films, as is also demonstrated with transparency measurements. k was found to decrease with increasing T_s which is compatible with an increase in transmittance with increasing T_s (Fig. 5.41). In the band gap region (250 - 350 nm), the variations of (n,k) were more marked. n and k vary together because they are interdependent since they are derived from the real and imaginary parts of a single parameter, namely, the complex refractive index. (The reader is reminded that the general relationships between n and k are given by the Kramers-Kronig equations (eq. 2.11 and 2.12)). N is varying modestly in both chambers (Fig. 5.34), while the matrix density is not expected to vary greatly as T_s changes, even though direct measurements could not be performed. Therefore, the decrease of n might be related to electron concentration.

5.2.2.4 Optimal substrate temperature

From the result presented in sections 5.2 and 5.2.2, it is deduced that the optimal temperature leading to the highest [Transparency over the visible range]/[resistivity] ratio in both chamber 1 and chamber 2 is 200°C. Therefore, subsequent variations of oxygen pressure is performed at T_s = 200°C.

5.2.3 Reconciling results from chambers 1 and 2

An attempt is made to correlate the electrical and optical data of ITO thin films grown for chambers 1 and 2 since the transposition of the growth parameters from chamber 1 to chamber 2 resulted in films an order of magnitude more resistive than those in chamber 1. Then, it was noticed that at given growth conditions, thin films grown in chamber 2 had a resistivity ρ very close to the films grown in chamber 1 (under exactly the same conditions) provided a static atmosphere is used in chamber 2. Here "static" means that no pumping took place in the chamber after the introduction of a certain amount of pure O_2 gas. Consequently, a comparison between chamber 1, where a dynamic atmosphere (i.e. pumping plus continuous introduction of O_2 gas) was used, and chamber 2, under a static atmosphere, is made. (The differences in set-up between the two chambers was illustrated in section 4.1, Fig. 4.1). All other parameters used in chamber 2 were set to be exactly the same as those used in chamber 1, i.e. 10 mT of pure oxygen was introduced to the chamber and then pumping was stopped. It was found necessary to inject regulary some oxygen inside the chamber as gas was consumed by the thin film during its growth. Table 5.8 summarises the growth conditions used in chamber 2.

Table 5.8 Summary of ITO growth parameters in chamber 2. P(O_2) was kept at 10 mT. The parameters were unchanged as compared with chamber 1, although the atmosphere was static.

Temperature	RT - 400°C
T-S distance	63 mm
Laser fluence	7.5 J/cm^2
Laser frequency	10 Hz
Oxygen pressure	10 mT

Electro-optical and structural properties are studied and compared.

5.2.3.1 Electrical properties

Fig. 5.47 shows Hall effect measurements where the mobility μ, the carrier concentration N and the resistivity ρ are plotted versus T_s.

The resistivities are similar over the range RT to 400°C. Here the carrier concentration, agreement is satisfactory (less than 25% difference) up to 200°C, after which the curves diverge increasingly. Conversely, the agreement in mobility is not good except above 300°C.

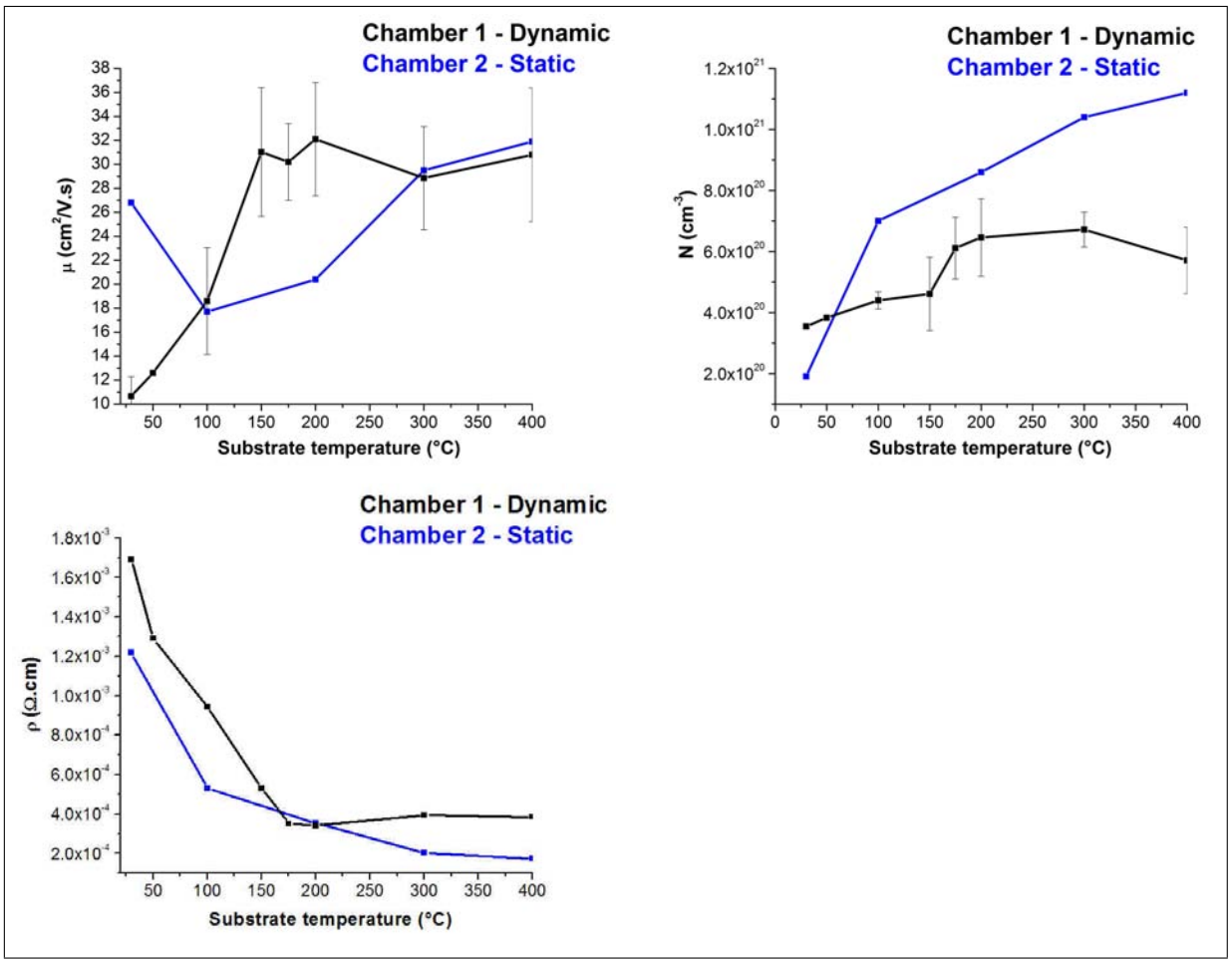

Figure 5.47 Comparison of electrical properties between chambers 1 and 2 in terms. T_s is varied from RT to 400°C.

5.2.3.2 Structural properties

XRD patterns are presented and compared at RT, 200°C, 300°C and 400°C (see Fig. 5.48).

It is interesting to observe that the agreement between the mobility measurements is best (at 300°C and 400°C) when both films are textured along the <111> direction.

5.2.3.3 Optical properties

Fig. 5.49 shows a comparison of optical properties in transmission between specimens grown at RT, 200, 300 and 400°C in chambers 1 and 2.

Films grown in chamber 1 show a systematic absorption edge shift towards higher wavelengths as compared with chamber 2. Since the thickness of the films compared is similar, this shift was explained on the basis of free carrier concentration. Indeed, carrier concentration measurements (Fig. 5.47) showed that films grown at RT, 200, 300 and

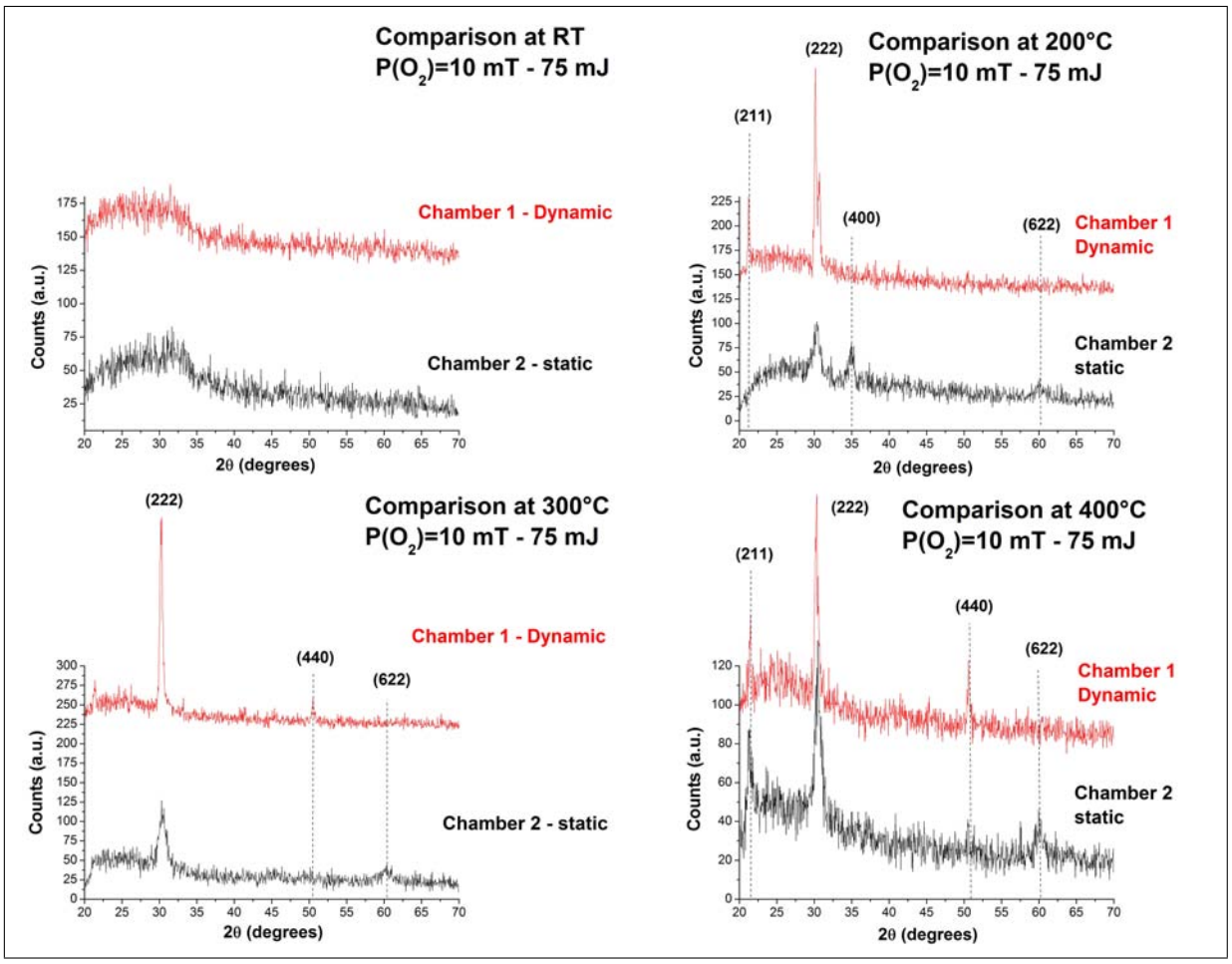

Figure 5.48 Comparison between XRD patterns of films grown in chamber 1 (dynamic atmosphere) and 2 (static atmosphere) at four different T_s: RT, 200, 300 and 400°C.

400°C in chamber 1 contain a lower amount of free carriers than those grown in chamber 2 in a static atmosphere. The change in carrier concentration is particularly large at 400°C, which seems to induce the slightly larger shift observed at this temperature (Fig. 5.49). At RT, the shift is reversed owing to the higher carrier density in chamber 1. Hence, electro-optical measurements are self-consistent. It is also interesting to note that the absorption edge slope at RT is much less steep than at higher T_s due to the lower crystallinity. Both absorption edges are similar in both shape and slope showing that the crystallinity might be about the same in both chambers.

5.2.3.4 Summary

Reconciling results from chambers 1 and 2 comes down to reconcile with static and dynamic pumping. Comparing films grown at different T_s in chamber 2 under a static atmosphere with those grown initially in chamber 1 under a dynamic atmosphere yielded mixed results. As regards the electrical properties, μ and N do not compare particulary well showing opposite behaviour in the two chambers, although ρ does compare well, a

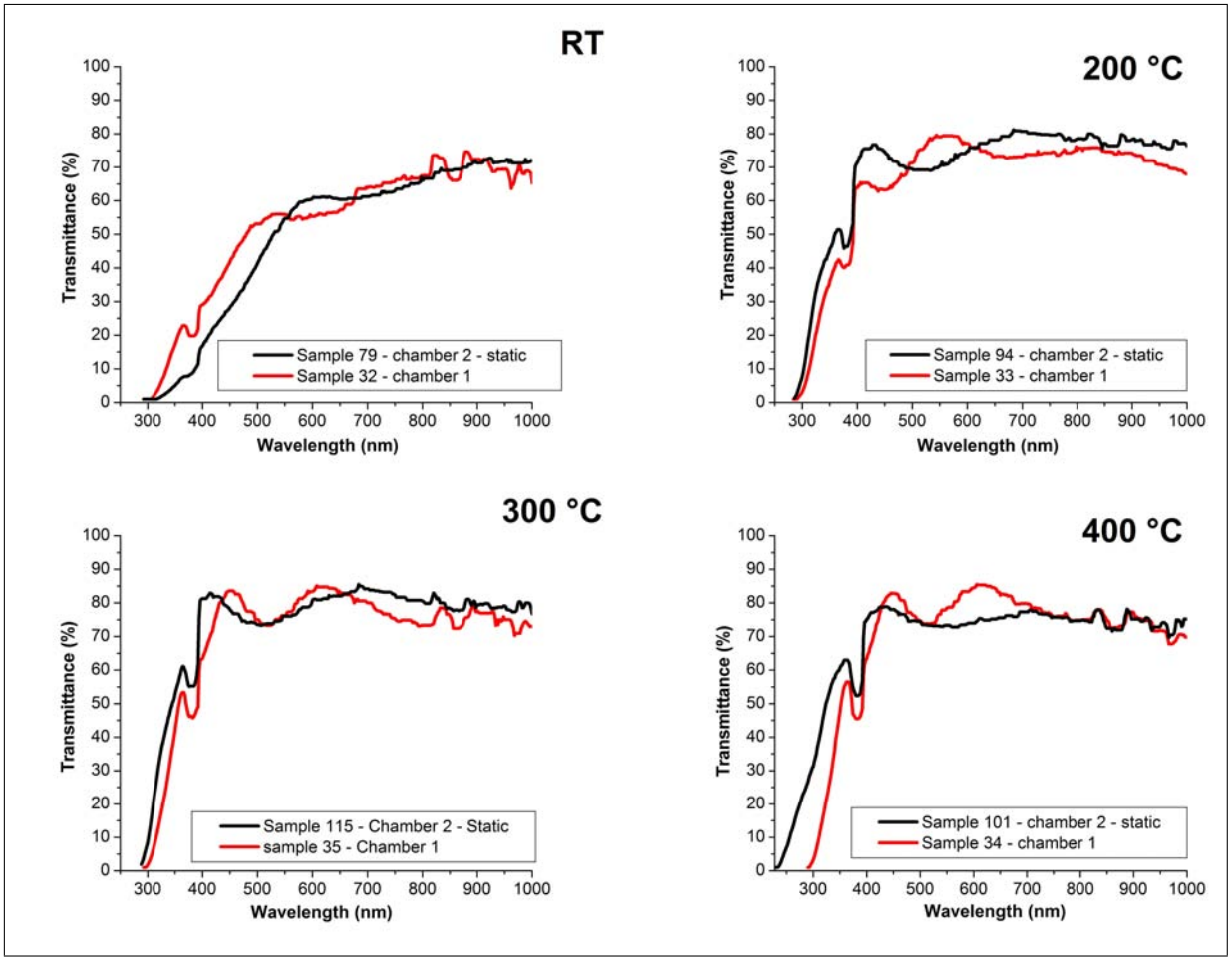

Figure 5.49 Comparison between chambers 1 and 2 for transmittance over the 300 -1000 nm wavelength range. A static atmosphere was used in chamber 2 where $P(O_2)$ was kept at 5 mT. In chamber 1, there was a constant pressure of $P(O_2)$=10 mT in a dynamic atmosphere (pumping system operating). T_s was varied from RT to 400°C.

fact that had initially lead us to make the present comparisons. The XRD results compare relatively well with an observed (222) preferred orientation, although at T_s=200°C, the agreement is not so good since films in chamber 2 do not show any preferred orientation. Optical properties agree very well, especially at RT where the slope of the absorption edge was reproduced in chamber 2. A systematic absorption edge shift towards lower wavelength is also noticed between chambers 1 and 2 and is attributed to the previously discussed Burstein-Moss effect due to the difference in N. The fact that using a static atmosphere in chamber 2 makes it possible to grow ITO thin films with similar physical properties to those initially grown in chamber 1 demonstrates the very strong impact of oxygen flow and the resulting gas dynamics in a PLD chamber during growth. Very few studies have been undertaken regarding that matter. One of the most detailed study coming from Spencer et al. [198] for a magnetron sputtering system. They monitored the film and pump consumption of oxygen and showed that the best way to obtain a stable deposition system (i.e. a constant $P(O_2)$ on the substrate surface so that the arrival

rate of different species and the stoichiometry stay constant) is to ensure that most of the oxygen gas is removed by the vacuum pumps and not by consumption by the growing film. This process is likely to take place in chamber 2 where the oxygen nozzle on top of the chamber directly points at the growing film before being pumped down at the bottom. The oxygen nozzle, the substrate and the pumping system all sit on a straight line. In chamber 1, the oxygen is both introduced and pumped down at the bottom of the chamber. This might result in a more static flow of the oxygen molecules over the entire surface of the growing film as the ambient gas would tend to accumulate on top of the chamber. The fact that μ and N could not be reproduced exactly indicate that some other parameters are at play. Such oxygen accumulation may not occur in chamber 2 due to the different oxygen introduction/pumping configuration. The location of the oxygen nozzle directly pointing at the growing film might also facilitate more efficient incorporation of oxygen into the film hence the lower P(O_2) needed to obtain high quality thin films. The higher energy density needed in chamber 2 might be due to the fact that oxygen moleclues are likely to be less uniformly distributed (since they are mainly concentrated in the vicinity of the growing thin film) as compared with the situation in chamber 1. Therefore, dissociation/ionisation of oxygen molecules leading to reactive oxygen species in the ambient gas is not favoured in chamber 2 hence the use of a higher energy density (also enhancing formation of such reactive species).

5.3 Influence of Oxygen pressure

ITO films that exhibit optimum values of conductivity and transparency require an oxygen partial pressure in the PLD ambient to be kept within very narrow limits. Good process control and reproducible starting conditions for every PLD run are required to obtain films of constant quality. This section investigates the change in physical properties and micrsostructure as the oxygen pressure (P(O_2)) is varied in chambers 1 and 2 (with the growth temperature (T_s) is kept at 200°C for reasons stated in section 5.2.2.4). Discussion of how the electrical properties are presented first, with optical properties presented in a later section (5.3.2.1). As in section 5.2, an attempt to correlate results from chambers 1 and 2 is made, while the section ends with a discussion.

5.3.1 Electrical properties

A similar approach to the one taken when T_s was varied (section 5.2.1) was followed regarding the data processing of μ, N and ρ.

The first parameter to take into account is the film thickness (t) since films need to be of constant thickness to be compared correctly with each other. Indeed, it has been reported [86] [199] that TCOs tend to have a large dependence of carrier concentration on film thickness, (similar to the results presented in section 5.1). In chamber 1, when the oxygen pressure was set above 30 mT, 8000 instead of 5000 pulses were fired to counteract additional scattering by the oxygen atmosphere at 30, 40 and 50 mT $P((O_2)$ resulting in a film thickness of about 260 nm. Such an adjustment was found to be unnecessary in chamber 2, as illustrated in Fig. 5.50 where films grown at $P((O_2)$=0.5 and 50 mT in chamber 2 are compared showing no strong impact of $P((O_2)$ on t.

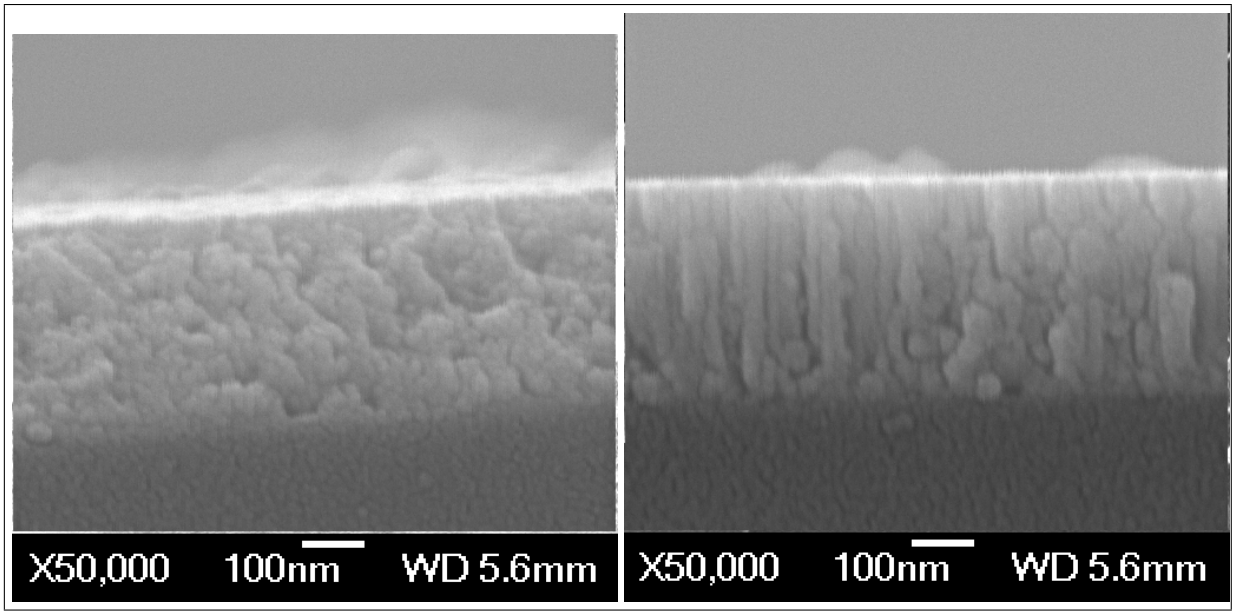

Figure 5.50 Comparison via SEM cross sectional micrographs of the thicknesses of films deposited at P(O_2)=0.5 (left) and 50 mT (right) in chamber 2. The temperature was kept at T_s=200°C.

Table 5.9 sums up the growth conditions used in the two chambers.

Table 5.9 Summary of ITO growth parameters when varying P(O_2).

Parameter	Chamber 1	Chamber 2
Temperature	200°C	200°C
T-S distance	63 mm	63 mm
Laser fluence	7.5 J/cm^2	10 J/cm^2
Laser frequency	10 Hz	10 Hz
Oxygen pressure	1 - 50 mT	0.2 - 70 mT

5.3.1.1 Film microstructure

XRD patterns for chambers 1 and 2 are presented in Figs. 5.51 and 5.52.

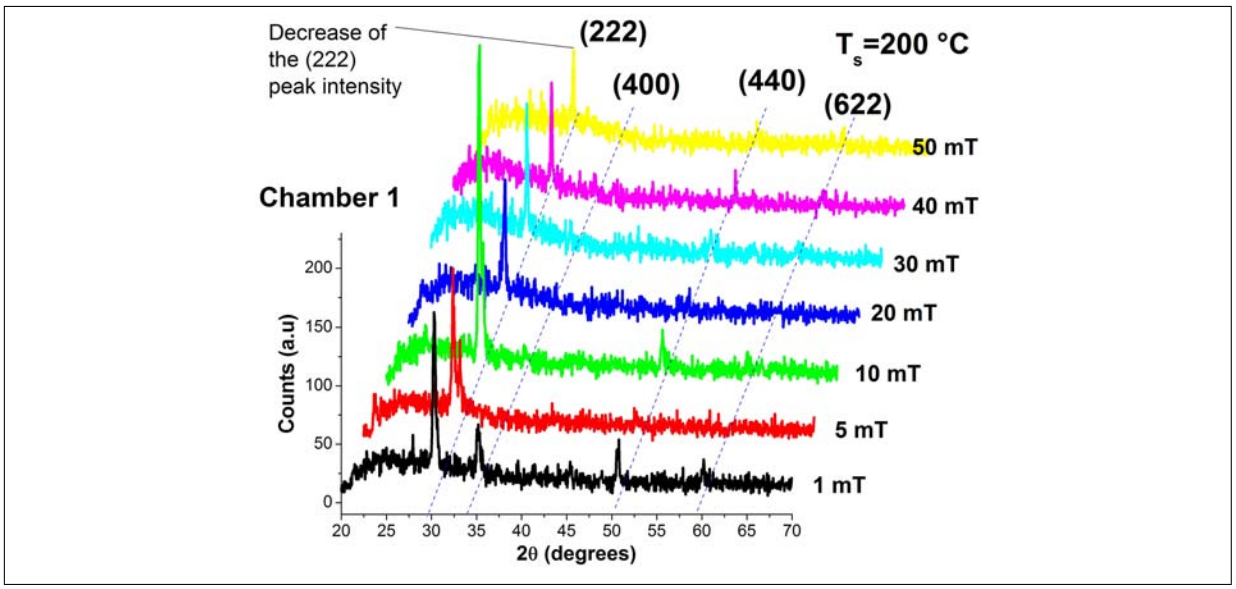

Figure 5.51 XRD patterns of ITO films deposited at different oxygen pressures in chamber 1. $P(O_2)$ was varied from 1 to 50 mT. Patterns were shifted to the right in order not to mask any features. Other process conditions are listed in Table 5.9.

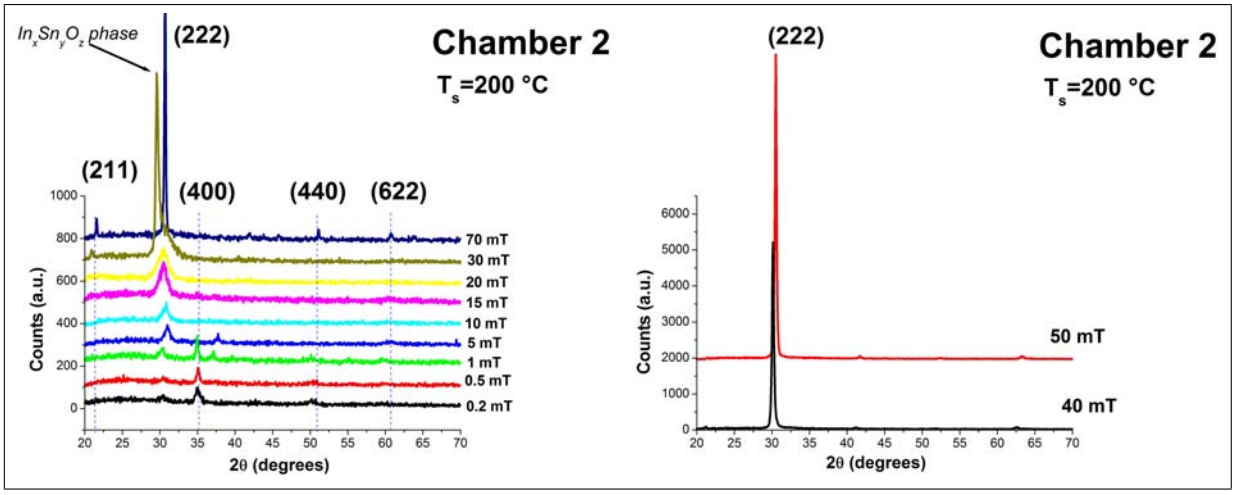

Figure 5.52 XRD patterns of ITO films deposited at different oxygen pressures in chamber 2. $P(O_2)$ was varied from 0.2 to 70 mT (left). For the sake of clarity, the high intensity XRD peaks obtained at $P(O_2)$=40 and 50 mT are reproduced on the right hand side. Other process conditions are listed in Table 5.9.

Fig. 5.53 shows a plot of the corresponding FWHMs of (222) or (400) (preferred orientation) peaks versus $P(O_2)$.

In chamber 2, the preferred orientation of the film is strongly affected by $P(O_2)$. In chamber 1, ITO films increasingly developed a (222) preferred orientation (Fig. 5.51) with higher $P(O_2)$. The (222) peak intensity decreases at 50 mT while the FWHM stays constant (see Fig. 5.53). For chamber 2, an orientation change (from (400) to (222)) takes place between 1 and 5 mT (Fig. 5.52). At high $P(O_2)$, the (222) peak intensity decreases in both chambers, with no major change in the FWHM. It is observed that μ in

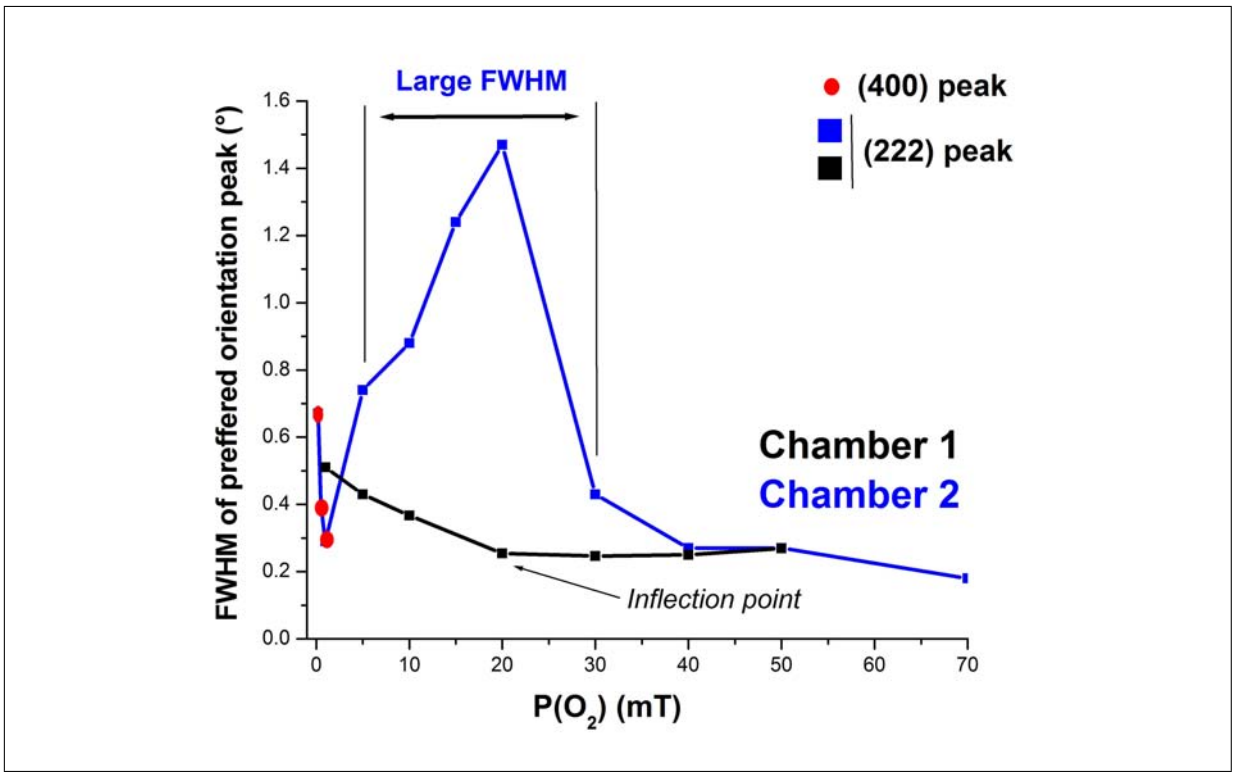

Figure 5.53 FWHM of preferred orientation (222) (except for red experimental points) peaks as $P(O_2)$ is varied. $P(O_2)$ varies from 1 to 50 mT in chamber 1 and from 0.2 to 70 mT in chamber 2.

chambers 1 and 2 shows a negative linear correlation with the FWHMs (presented in Fig. 5.53) of both the preferred (222) and the (400) peaks (Fig. 5.54).

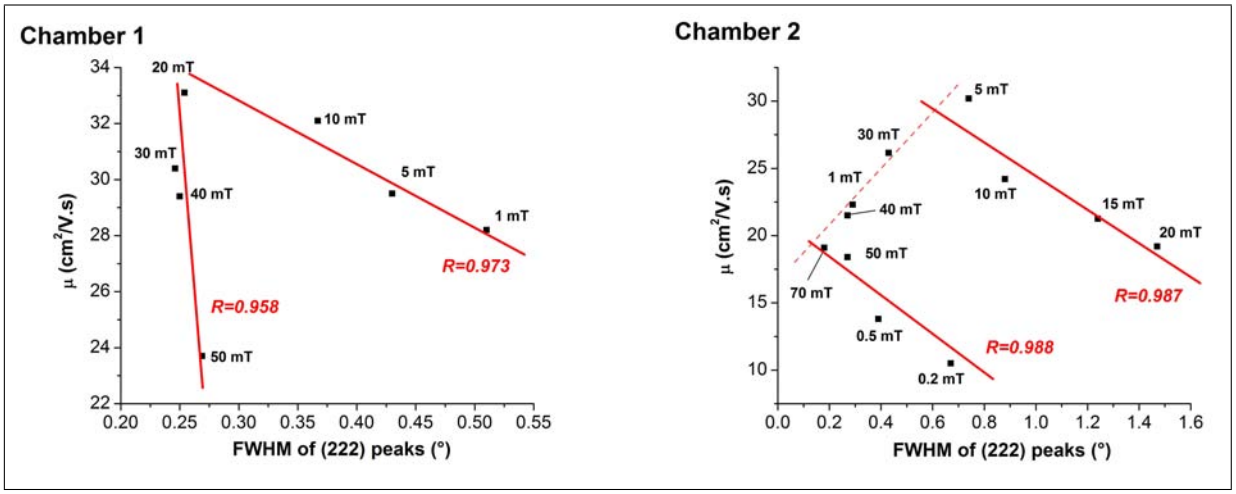

Figure 5.54 Correlation between FWHM and the mobility μ in chambers 1 (left) and 2 (right). T_s was kept at 200°C. The mobility values are taken from the samples corresponding to the X-Ray diffractograms presented in in Figs. 5.51 and 5.52.

The texture quality (noted as $TC_{(222)}$ or $TC_{(400)}$) also affected μ as illustrated in Fig. 5.55.

In chamber 2, the large FWHM obtained in the intermediate 10 - 30 mT range (see Fig. 5.53) was not attributed to the amorphous glass substrate (see the amorphous “bump”

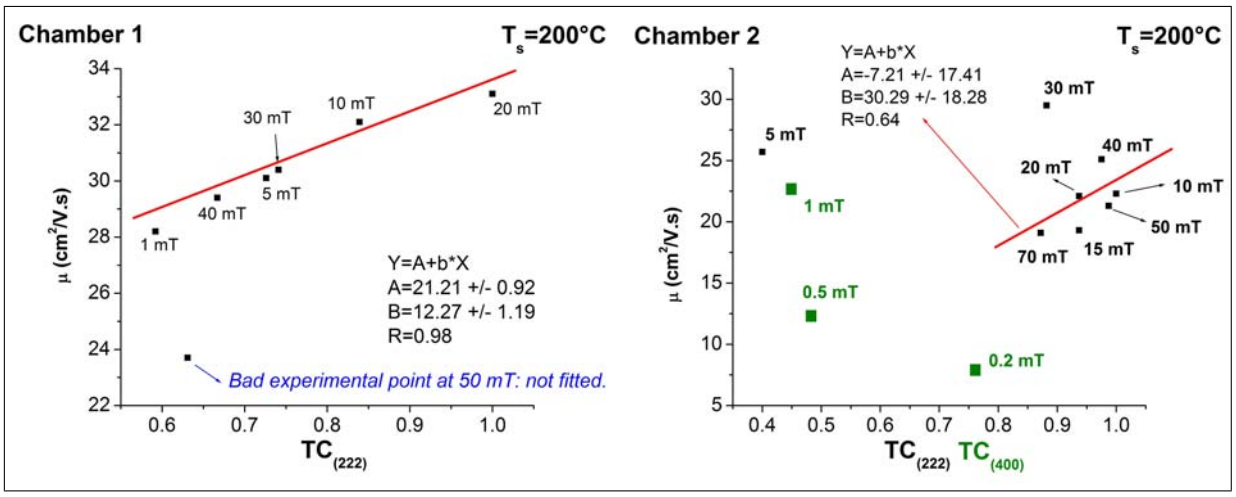

Figure 5.55 Relation between μ and $TC_{(222)}$ - $TC_{(400)}$ in chambers 1 (left) and 2 (right). $P(O_2)$ was varied from 1 to 50 mT in chamber 1 and from 0.2 to 70 mT in chamber 2. The mobility values are taken from the samples corresponding to the X-Ray diffractograms presented in Figs. 5.51 and 5.52.

originating from the glass substrate in Fig. 5.15) since this large FWHM vanishes both at low and high $P(O_2)$ (and the films are of about the same thickness). Instead, it is argued that the large FWHM peak obtained in the 10 - 30 mT range originates from a gradual phase development. At $P(O_2)$=30 mT, a shoulder on the right hand side of the peak is clearly distinguishible and found to be reproducible (Fig. 5.56).

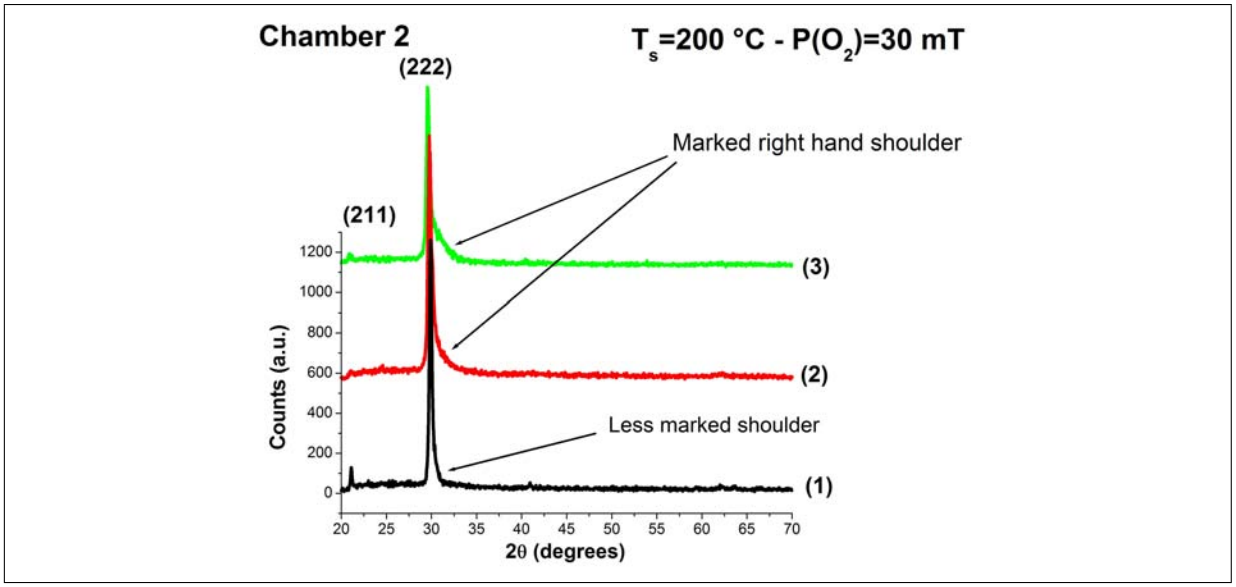

Figure 5.56 Reproducibility of the (222) peak asymmetry for three different samples grown under exact the same conditions. Deposition was performed in chamber 2 at T_s=200°C and $P(O_2)$=30 mT.

These particular features were studied in greater detail with glancing-angle XRD (GAXRD) by varying the incidence angle from Ψ=1 to 16°, so that the peak shapes and position could be studied as a function of film thickness. Fig. 5.58 shows how the shape and position of the (222) diffraction peaks evolve at these different incident angles (Ψ). The

approximate thickness probed is also indicated for information.

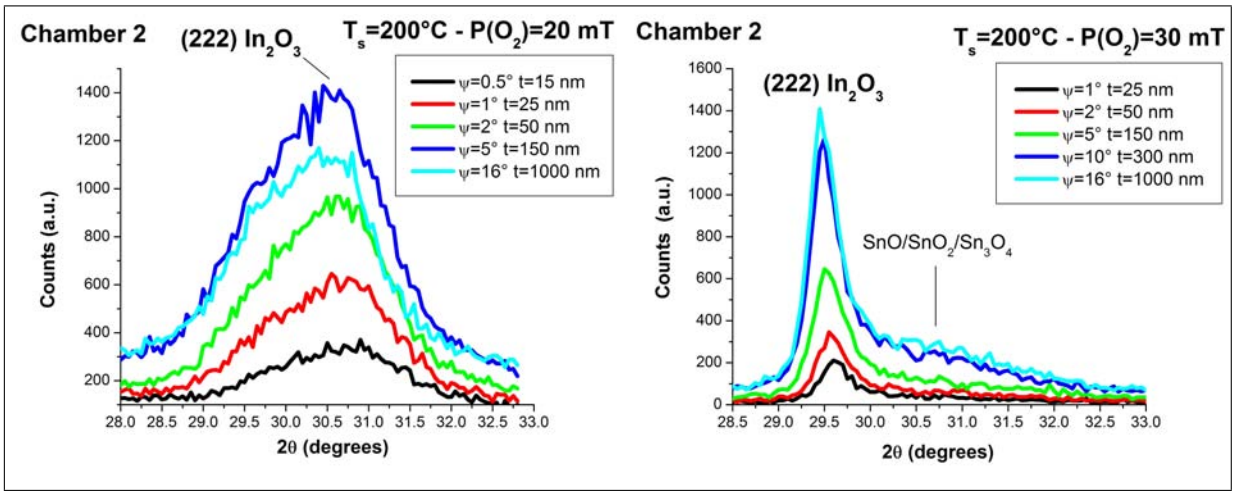

Figure 5.57 GAXRD patterns performed on a film grown at P(O_2)=20 (left) and 30 mT (right). Ψ was varied from 0.5/1 to 16°. Other growth conditions are listed in Table 5.9.

Fig. 5.58 illustrates the necessary double peak fittings to fit the asymmetry. The incidence angle was chosen to be Ψ=16° to ensure the maximum intensity signal (whole thickness probed).

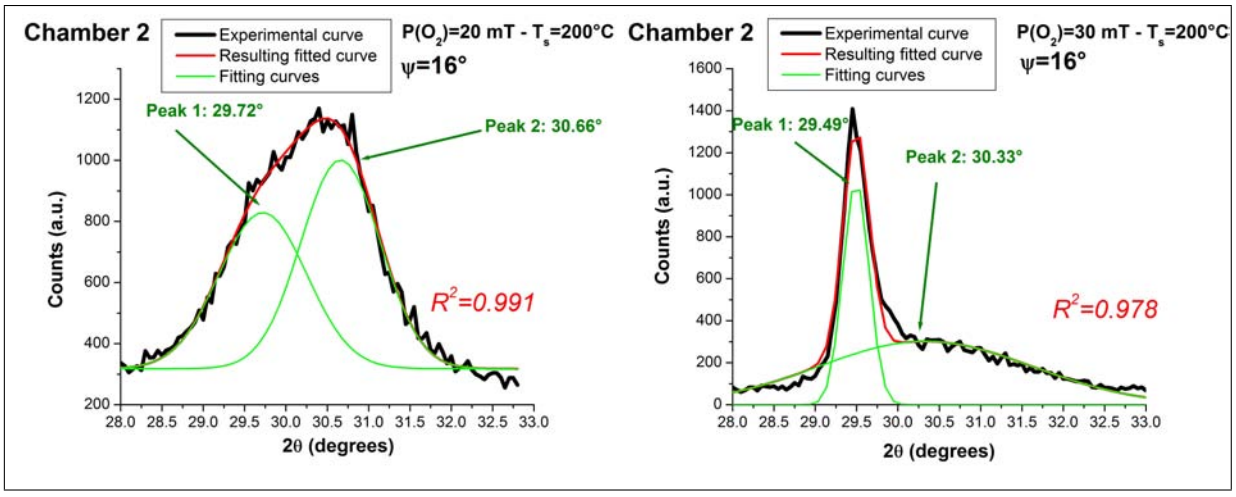

Figure 5.58 Multi peak fitting of the GAXRD peak asymmetry for films grown at P(O_2)=20 mT and T_s=200°C in chamber 2. The incident angle was set at Ψ=16°.

Fig. 5.58 shows that this effect is not a "simple" peak splitting, rather at P(O_2)=20 mT, the large (222) peak is composed of two subpeaks: "Peak 1" at $29.72°$ and a "peak 2" at $30.66°$. "Peak 1" at 2θ=29.49° (d=3.13$\AA$) is attributed to the host matrix cubic phase In_2O_3 ((222) reflection) (JCPDS 44-1087). "Peak 2" is more difficult to account for. Its large FWHM at P(O_2)=30 mT makes an overlap of SnO (JCPDS 01-072-2324), SnO_2 (JCPDS 01-071-5329) and possibly Sn_3O_4 (JCPDS 00-020-1293) peaks likely so that indivudual identification remains difficult. Although other metastable $In_xSn_yO_z$ compounds have not been reported in the literature, they remain a possibility on the basis

of our diffraction data. It is also observed that at P(O_2)=20 and 30 mT, the shapes of the peaks are conserved through the whole specimen thickness, which is strong evidence that the phases mentioned previously is a bulk one rather than a surface or substrate interface effect. As regards the position of "peak 1", a significant peak shift (1°) towards lower 2θ as compared with JCPDS data (JCPDS 00-006-0416) is observed indicating a relatively high level of stress within the thin film, at least under these growth parameters. The coexistence of several oxides might explain such an observation.

Surface morphology was investigated by SEM and AFM imaging. Figs. 5.59 - 5.60 present low magnification SEM micrographs of the surfaces of samples grown in chambers 1 and 2 at different P(O_2).

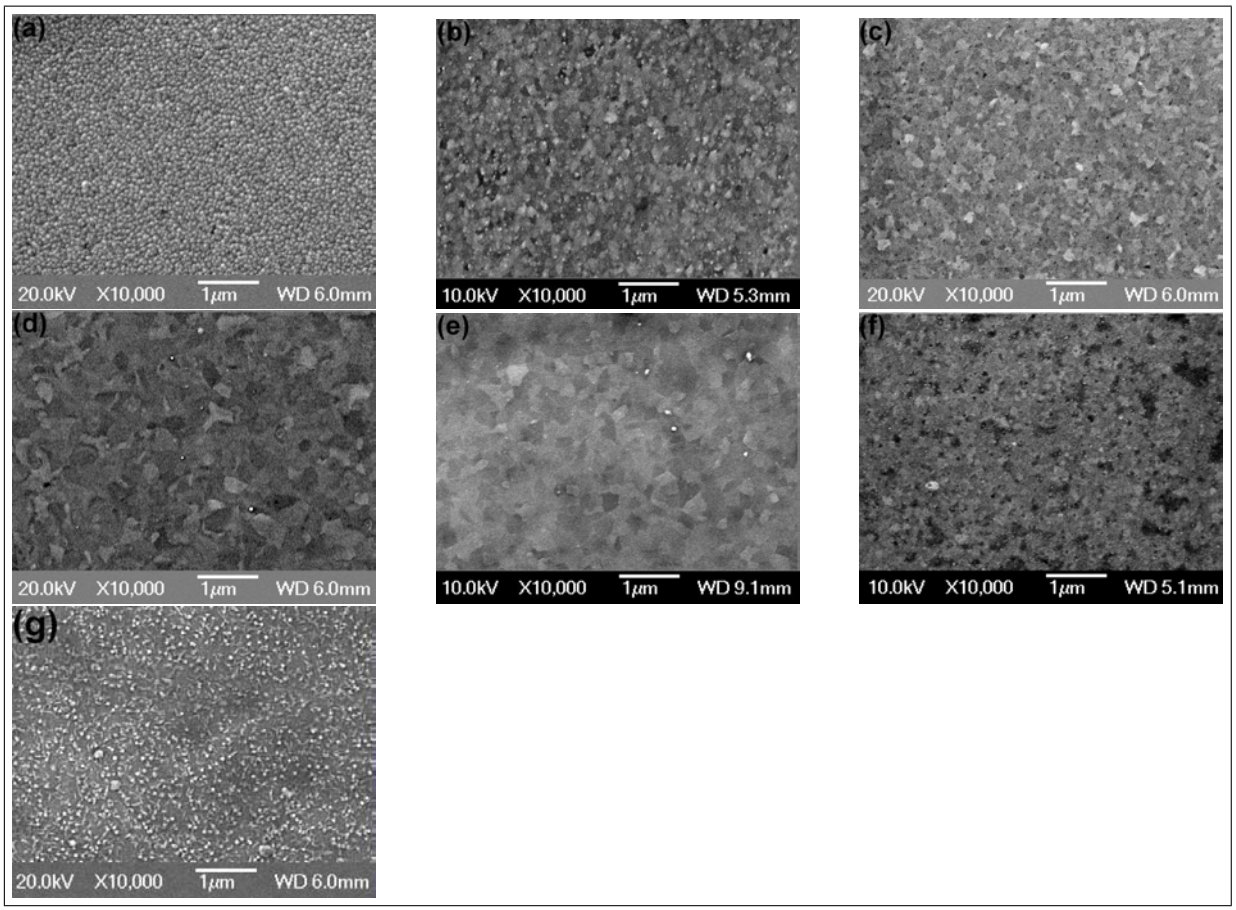

Figure 5.59 Low magnification SEM micrographs of samples grown at (a) P(O_2)=1 mT, (b) 5 mT, (c) 10 mT, (d) 20 mT, (e) 30 mT, (f) 40 mT and (g) 50 mT in chamber 1. Holes are observed and attributed to highly energetic ejected species impacting the growing surface.

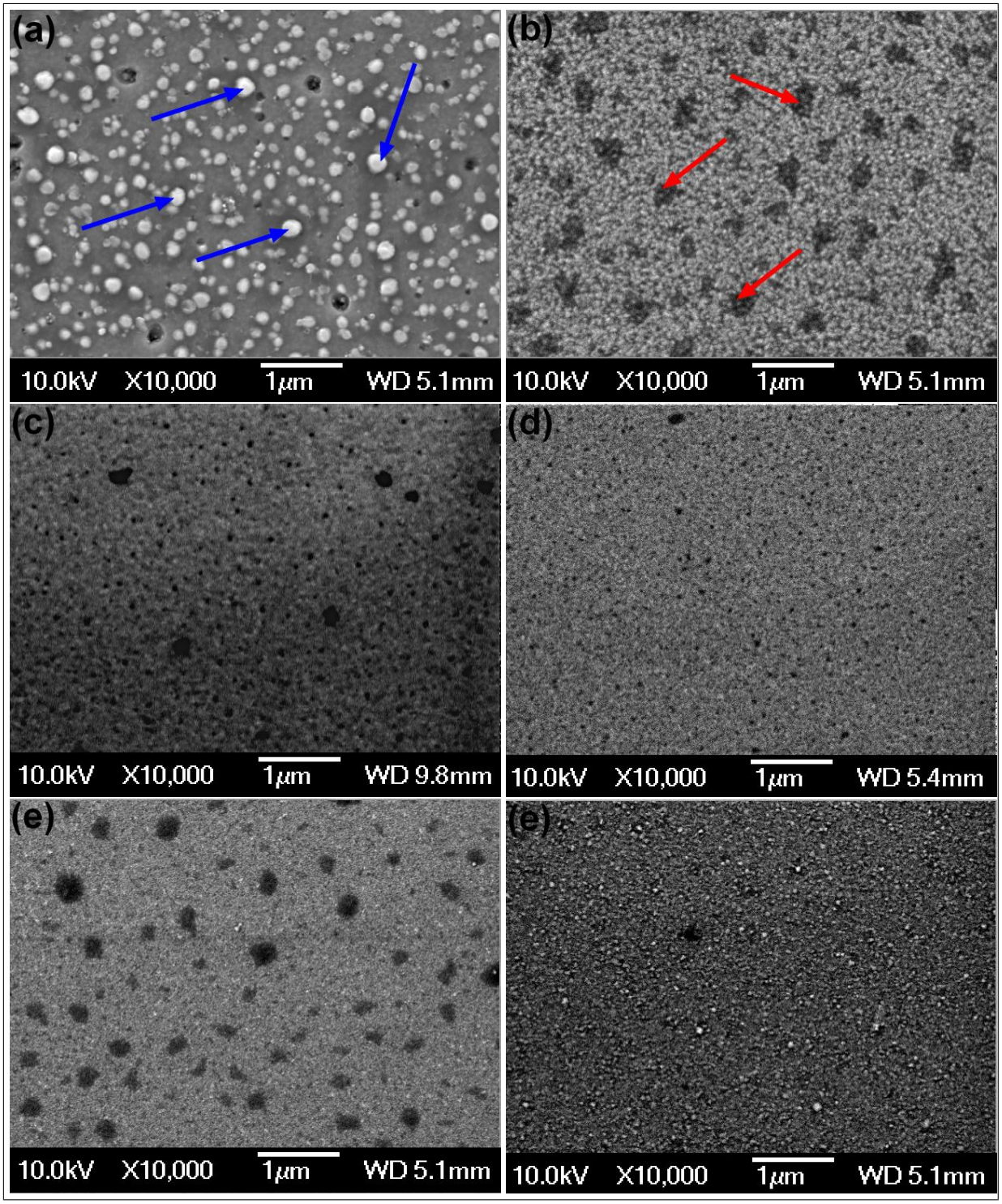

Figure 5.60 Low magnification SEM micrographs of samples grown at (a) $P(O_2)$=0.2 mT, (b) 0.5 mT, (c) 1 mT, (d) 5 mT, (e) 50 mT and (f) 70 mT in chamber 2. Holes are observed and attributed to highly energetic ejected species impacting the growing surface (see red arrows). Round particulates are also observed scattered homogeneously over the surface of the sample grown at 0.2 mT (see blue arrows in (a)).

Holes are observed at low $P(O_2)$ for samples grown in chambers 1 and 2, while surface particles with an average diameter of 100 nm are also identified in chamber 2 at $P(O_2)$=0.2 mT. Because PLD is a very energetic deposition process (with kinetic energies of ejected species up to 1000 eV as compared a few hundreds eV at most [61] with

sputtering or a few tens eV [200] for evaporation), thin film surface/bulk structure can be badly damaged. This is particularly the case at low $P(O_2)$, so control of the atmosphere pressure used is of utmost importance. Unfortunately, quantitative SEM EDX could not be performed on the particles observed at $P(O_2)=0.2$ mT due to spatial resolution constraints.

Higher magnification SEM micrographs were acquired to study in more detail the average grain size. Figs. 5.61 - 5.62 present high magnification SEM images of the surface morphology of samples grown in chambers 1 and 2 at different $P(O_2)$.

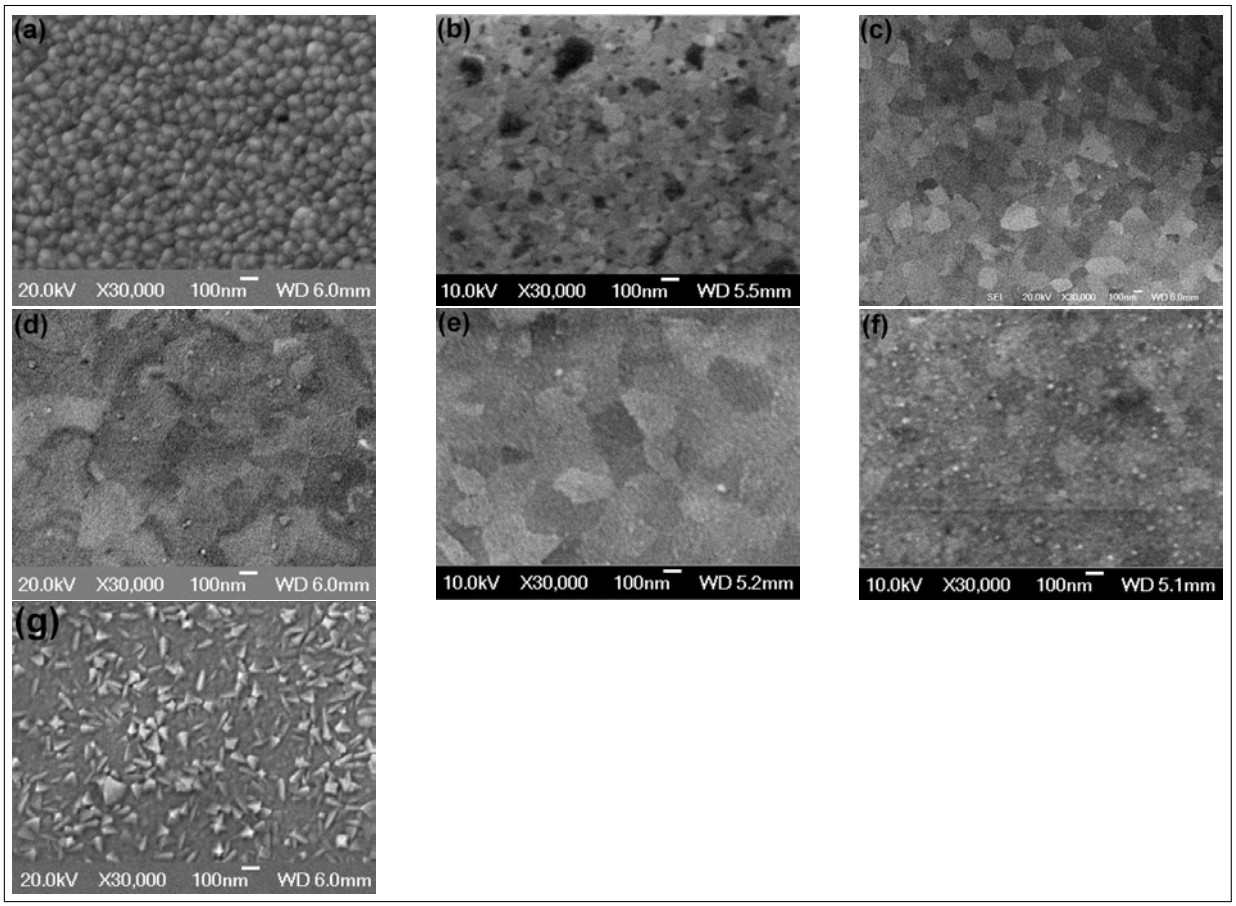

Figure 5.61 High magnification SEM micrographs showing the change of surface microstructure at (a) $P(O_2)=1$ mT, (b) 5 mT, (c) 10 mT, (d) 20 mT, (e) 30 mT, (f) 40 mT and (g) 50 mT. Films were grown in chamber 1 at $T_s=200°C$. Surface particles are visible in (g).

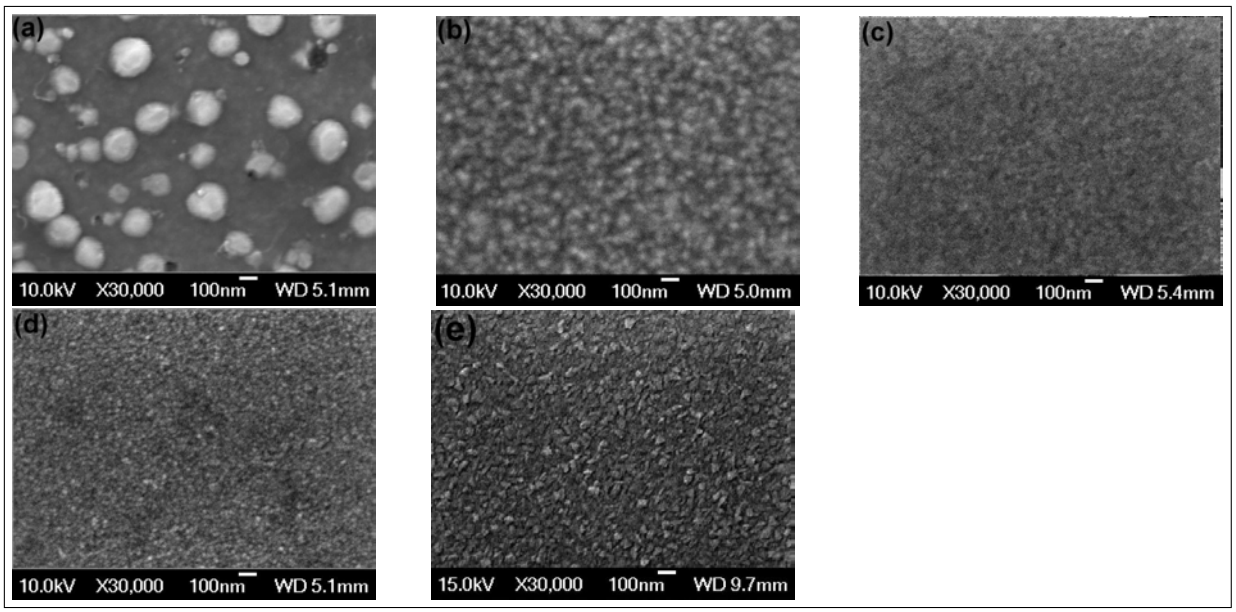

Figure 5.62 High magnification SEM micrographs showing the surface microstructure evolution at (a) $P(O_2)$=0.2 mT, (b) 0.5 mT, (c) 5 mT, (d) 50 mT and 70 mT (f). Films were grown in chamber 2 at T_s=200°C.

AFM images of samples grown at different $P(O_2)$ in chambers 1 and 2 are shown in Figs. 5.63 - 5.64.

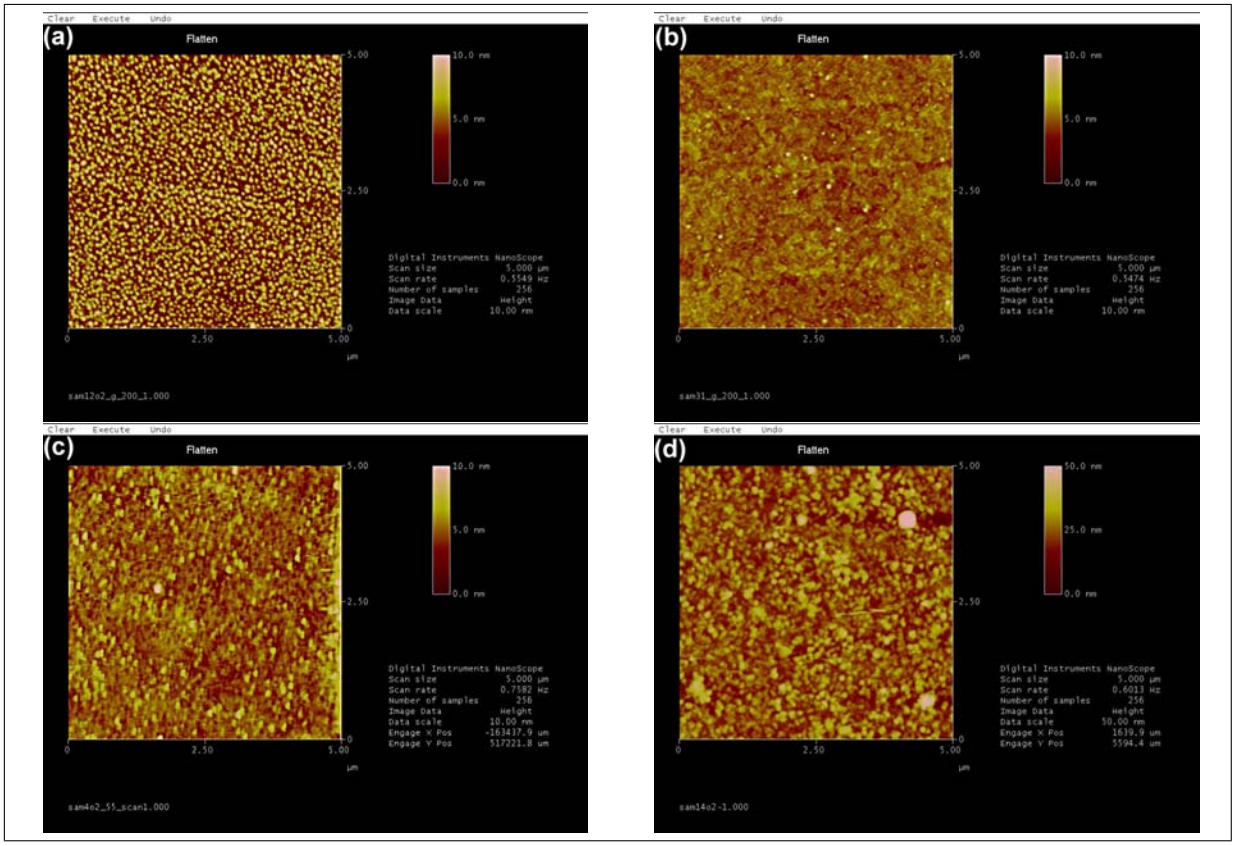

Figure 5.63 AFM images showing the surface microstructure evolution at (a) $P(O_2)$=1 mT, (b) 10 mT, (c) 30 mT and (d) 50 mT. Films were grown in chamber 1 at T_s=200°C.

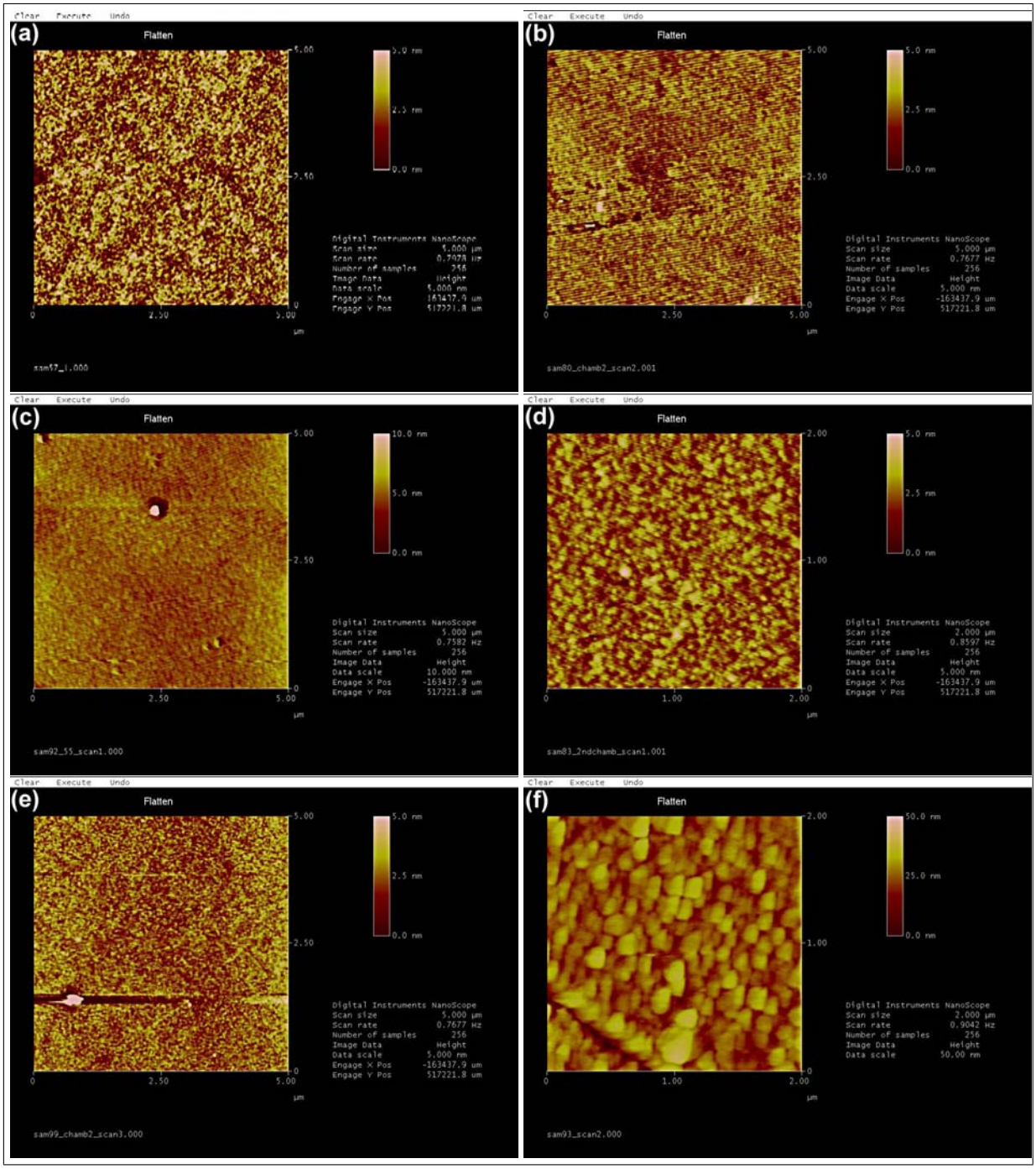

Figure 5.64 AFM images showing the change of surface microstructure evolution at (a) $P(O_2)$=0.2 mT, (b) 5 mT, (c) 20 mT, (d) 30 mT, (f) 50 mT and (g) 70 mT. Films were grown in chamber 2 at T_s=200°C. In (e), an artefact is present due to a particulate sitting on the surface.

The AFM images presented above enabled the derivation of surface roughnesses. Fig. 5.65 illustrates graphically the variation of surface roughnesses with $P(O_2)$ in chambers 1 and 2.

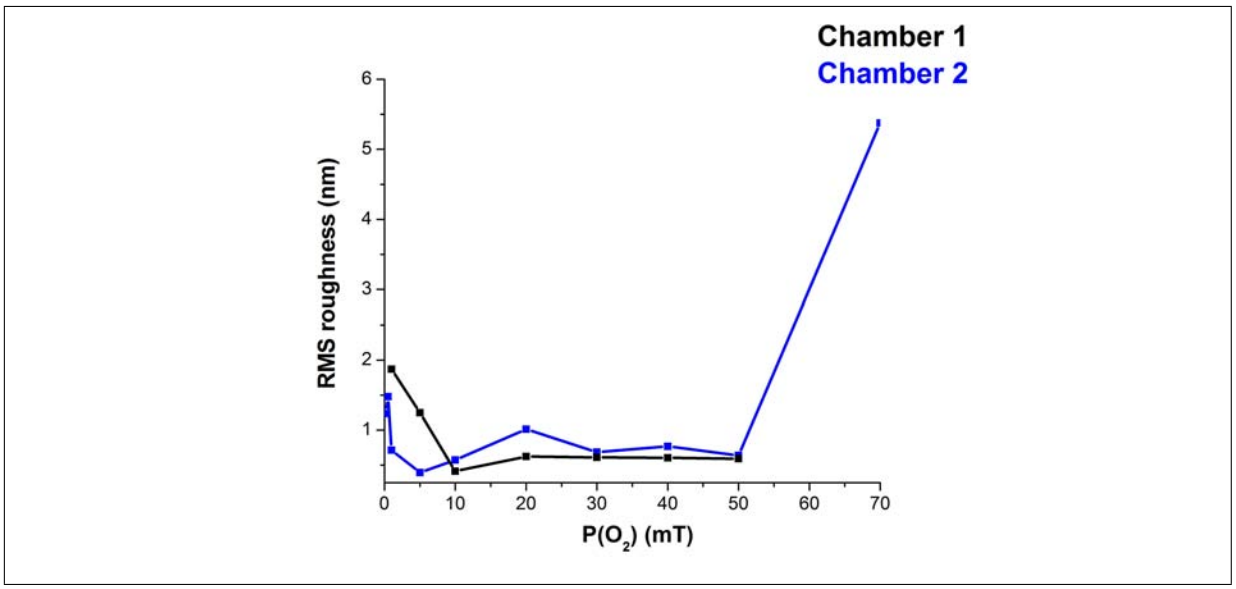

Figure 5.65 RMS roughness of ITO thin films deposited at various oxygen pressures in chambers 1 (black curve) and 2 (blue curve). $P(O_2)$ was varied from 1 to 50 mT for chamber 1 and 0.2 to 70 mT for chamber 2. T_s was kept constant at 200°C.

At low $P(O_2)$, the surfaces are rough due to the presence of particles. The roughness also increases at very high $P(O_2)$ (70 mT) and significant grain growth seems to take place. At intermediate $P(O_2)$ the films appear relatively smooth.

The grain size derived from previous AFM and SEM micrographs are summarised in Table 5.10.

Table 5.10 Average grain size as $P(O_2)$ is varied from 1 to 50 mT and from 0.2 to 70 mT in chambers 1 and 2 respectively.

	Average grain size (nm)		
Oxygen pressure (mT)	Chamber 1	Chamber 2	Technique(s) used
0.2	n.a.	n.a	/
0.5	n.a.	25	SEM
1	90	50	AFM/SEM
5	100	90	AFM/SEM
10	200	no data	AFM/SEM
15	no data	no data	/
20	250	90	SEM
30	200	120	AFM/SEM
40	150	no data	AFM/SEM
50	n.a.	50	AFM/SEM
70	no data	100	AFM/SEM

5.3.1.2 Mobility

Mobility measurements for both chambers are presented in Fig. 5.66.

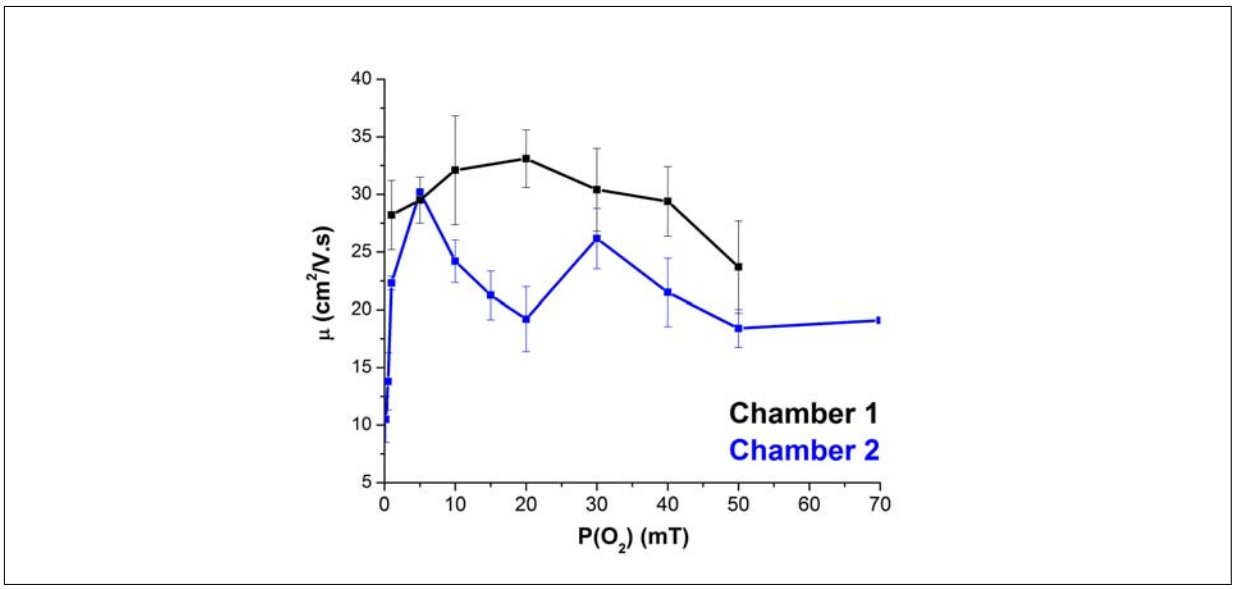

Figure 5.66 Mobility (μ) variation for films grown in chambers 1 and 2 versus $P(O_2)$. The growth conditions used are listed in Table 5.9.

Fig. 5.66 shows one maximum for mobility values in chamber 1 at 20 mT, while two maxima are observed at 5 and 30 mT in chamber 2.

5.3.1.3 Calculations

As with the substrate temperature study (see sections 2.2.2.1.2 and 5.2.1.3), grain boundary scattering is not expected to be the dominant conduction mechanism since the average grain size, calculated using AFM and SEM imaging, is much greater than the calculated electron mean free paths (MFP) L as shown in Fig. 5.67 at different $P(O_2)$. L was calculated using eq. 5.2.

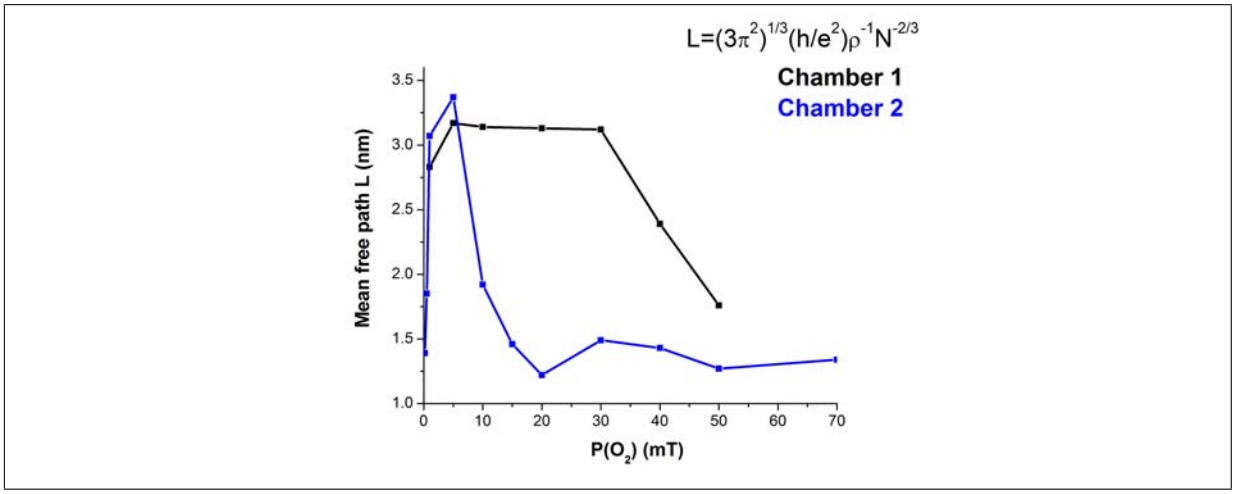

Figure 5.67 Calculated mean free paths of free carriers for films grown at various $P(O_2)$ in chambers 1 and 2 based on a highly degenerate free electron gas model [4].

The same overall trend for MFP versus pressure is observed for both chambers, i.e. the

MFP decreases drastically at low or high P(O_2) in both chambers leaving a pressure window where the MFP is a few nanometres. This window is relatively large for chamber 1 (5 - 30 mT), while it is much narrower for chamber 2 with a maximum MFP of 3.4 nm at P(O_2)=5 mT. Hence, it can be stated that the best quality films in terms of MFP are grown at 5 - 30 mT and 5 mT in chambers 1 and 2 respectively.

To investigate the occurence of surface holes observed in micrographs presented in section 5.3.1.1, an empirical formula estimating the mean free path of ejected particulates from the target proposed by Mergel et al. [5] was used:

$$P\lambda = 0.63 \tag{5.8}$$

where P is the deposition pressure expressed in Pa. λ is the mean free path expressed in cm. This curve is plotted in Fig. 5.68 with the pressure converted to mT.

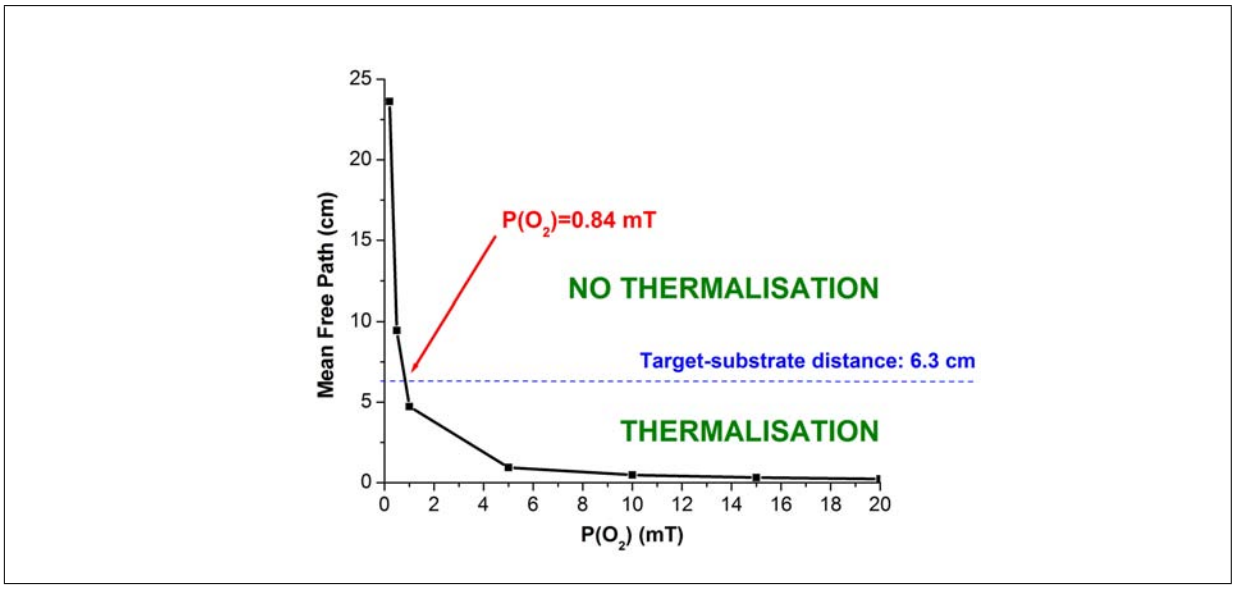

Figure 5.68 Mean free path versus P(O_2) according to the empirical formula proposed by Mergel et al. [5].

For a target-substrate distance of 6.3 cm, no thermalisation (the process whereby particles lose energy through mutual interaction, eventually reaching thermal equilibrium) occurs below P(O_2)=0.84 mT and hence more surface/bulk damage is to be expected. These seem to correspond well with observations in chamber 1, although no films were grown below 1 mT. However, in chamber 2, the threshold is much higher with damage still being observed at oxygen pressures as high as 50 mT (Fig. 5.60).

5.3.1.4 Carrier concentration

The carrier concentration was derived from Hall effect measurements using the Van Der Pauw technique (see section 4.6.2). Carrier concentrations (N) versus $P(O_2)$ for chambers 1 and 2 are illustrated in Fig. 5.69

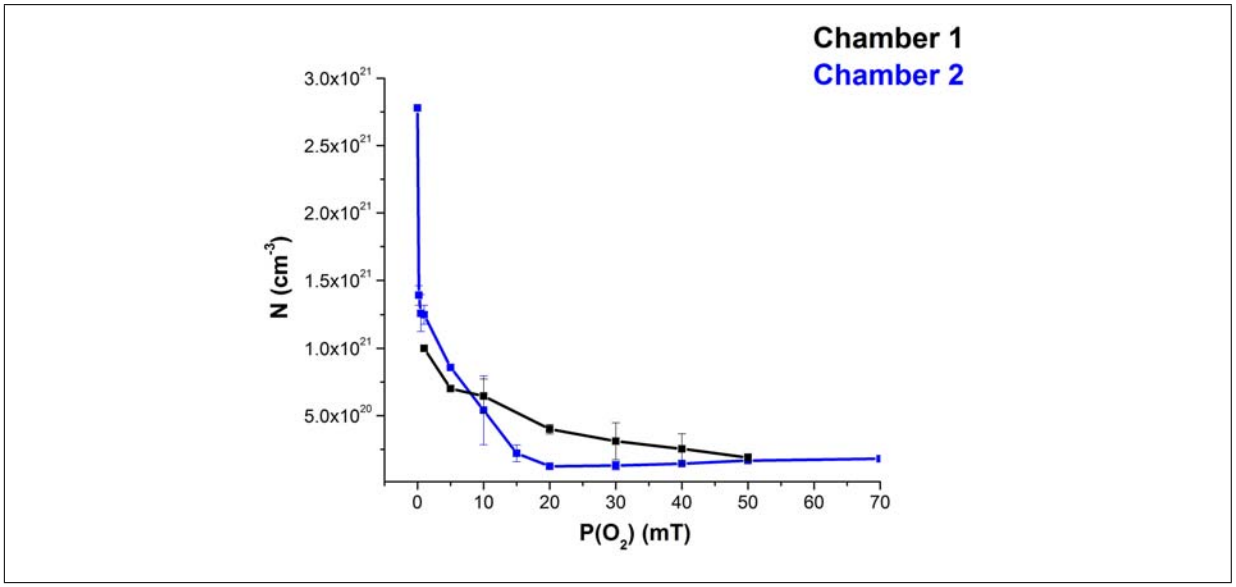

Figure 5.69 Carrier concentration (N) variation for chambers 1 and 2 with $P(O_2)$. The growth conditions used are listed in Table 5.9.

The N curves show the same trend in both chambers and show a far less complex behaviour than the mobilities, especially in chamber 2: an overall decrease in N as $P(O_2)$ increases is observed in both chambers. A steeper decline is observed in chamber 2 between 0.2 and 10 mT. In both chambers, N reaches about the same value of 50 mT. A plateau is clearly visible in chamber 2, although the data for chamber 1 is missing above 50 mT so a similar trend cannot be confirmed. Data for both chambers were fitted over the 1 - 50 mT range with a first order exponential curve as illustrated in Fig. 5.70. The first order exponential is $y = y_0 + A_1 e^{-(x/t_1)}$ with y_0, A_1 and t_1 as fitting parameters.

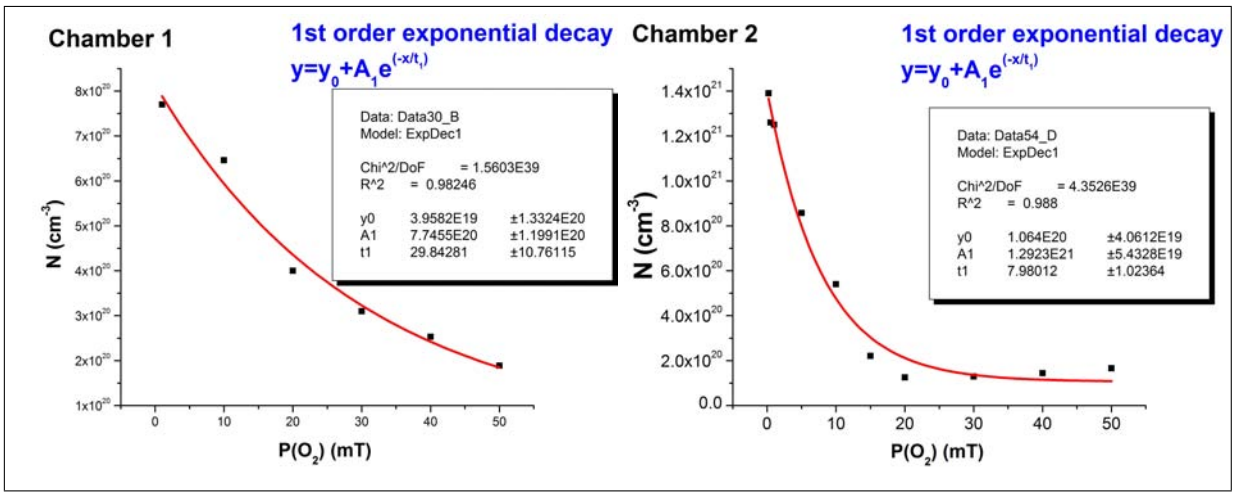

Figure 5.70 Dependence on $P(O_2)$ of N. Films were grown in chambers 1 (left) and 2 (right) at a constant T_s=200°C in the 1 - 50 mT range.

The fits obtained are of very good quality with R^2 of 0.982 and 0.988 respectively in chambers 1 and 2 so that the following relationships can be established: $N(chamb1) = 3.96 \times 10^{19} + 7.74 \times 10^{20} \times e^{-\frac{P(O_2)}{29.84}}$ and $N(chamb2) = 1.06 \times 10^{20} + 1.29 \times 10^{21} \times e^{-\frac{P(O_2)}{7.98}}$.

The following two observations suggest that changes in carrier concentration N with $P(O_2)$ are solely due to changes in oxygen vacancy concentration: (1) at T_s=200°C, previous TEM micrographs (Figs. 5.27 and 5.28) showed a fully crystalline matrix with no particular precipitates for either chamber. (2) XRD showed no peak other than that from the In_2O_3 phase at 5 mT in chamber 2 (see Fig. 5.52). These observations suggest that Sn is in solid solution in the In_2O_3 matrix, effectively substituting for In atom and releasing one free carrier to the matrix per atom [24]: Sn is said to be fully "activated" (thermally and electronically speaking).

SEM EDX results illustrated in Fig. 5.71 indicate incorporation of oxygen in both chambers as the oxygen pressure increases. Fig. 5.71 shows how the (In+Sn)/O and In/Sn atomic ratios vary with $P(O_2)$ during growth in chamber 2.

Recall that the experimental atomic ratios for the target were: In/Sn=9.65±0.2 and (In+Sn)/O=0.61±0.03. Fig. 5.71 shows that the In/Sn atomic ratio is fairly constant over the oxygen pressure range investigated, while the (In+Sn)/O ratio decreases overall with $P(O_2)$ suggesting that the bulk structure is absorbing some oxygen, resulting in changes in vacancy concentration.

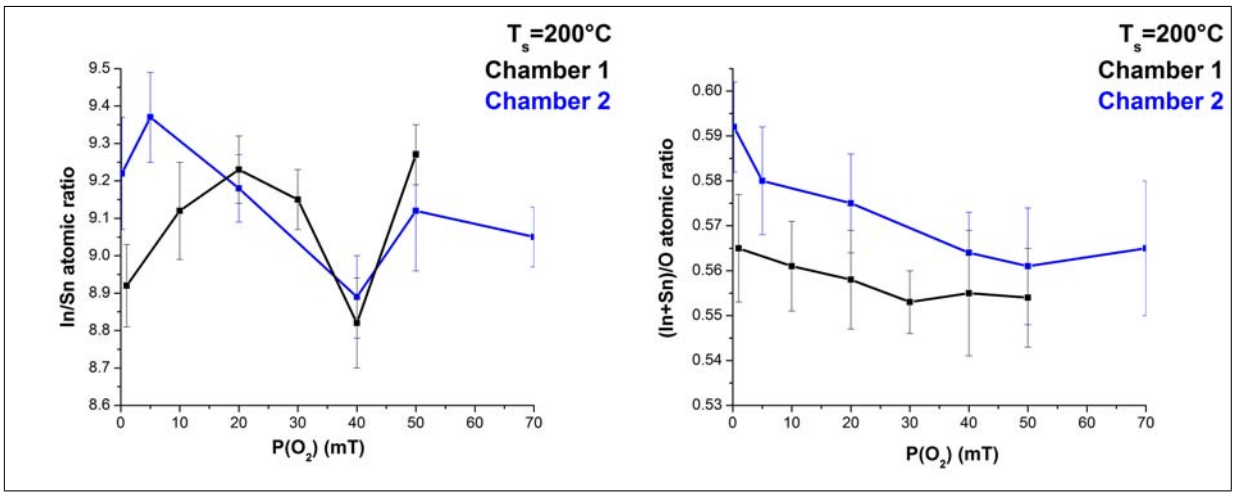

Figure 5.71 In/Sn (left) and (In+Sn)/O (right) atomic ratios for chambers 1 and 2 obtained by EDX SEM as $P(O_2)$ is varied from 1 to 50 mT (chamber 1) and 0.2 to 70 mT (chamber 2). Films were grown in chambers 1 and 2 at a constant temperature of T_s=200°C. O K , In L and Sn L lines were used for quantification.

An XPS survey was undertaken to investigate the role of the top surface in the oxygen intake since the latter represents by definition an interface. The evolution of the In, Sn and O XPS peaks with increasing $P(O_2)$ is presented in Fig. 5.72.

There is a small but reproducible binding energy shift in the same direction for all core levels (In 3d, Sn 3d and O 1s). With regard to the peaks, the In 3d ones are Gaussian, indicating single state oxidation. The binding energy of In 3d is around 445 eV corresponding to In^{3+} in agreement with an In_2O_3 host matrix [201]. The In 3d peaks are insensitive to the loss/gain of oxygen as peak shapes show no appreciable differences. This indicates that the electronic environment of In^{3+} ions is not strongly modified as $P(O_2)$ increases.

However, the Sn and O 1s peaks show more complex structures, particularly at very low $P(O_2)$ (0.2 mT) where asymmetries in the higher energy part of the peaks are observed. These asymmetries require a multipeak fitting to account for exact peak positions: single and double Gaussian peak fits were performed using Origin 6.1. depending on whether such an asymmetry was observed. Particular attention was paid to the sample grown at $P(O_2)$=0.2 mT where the asymmetries are more marked and relatively large particles were observed on the surface by SEM (Figs. 5.60 - 5.62). Fig. 5.73 presents the In, Sn and O peaks of the sample grown at 0.2 mT with their various fitted curves.

The main Sn 3d peak position (subpeak 1) is at 487.7 eV and corresponds to the binding energy of SnO_2 [201]. This indicates that the main component of Sn in ITO is Sn^{4+}, even at the top surface. The “electrically active” Sn atoms (Sn^{4+}) are thought to be bound

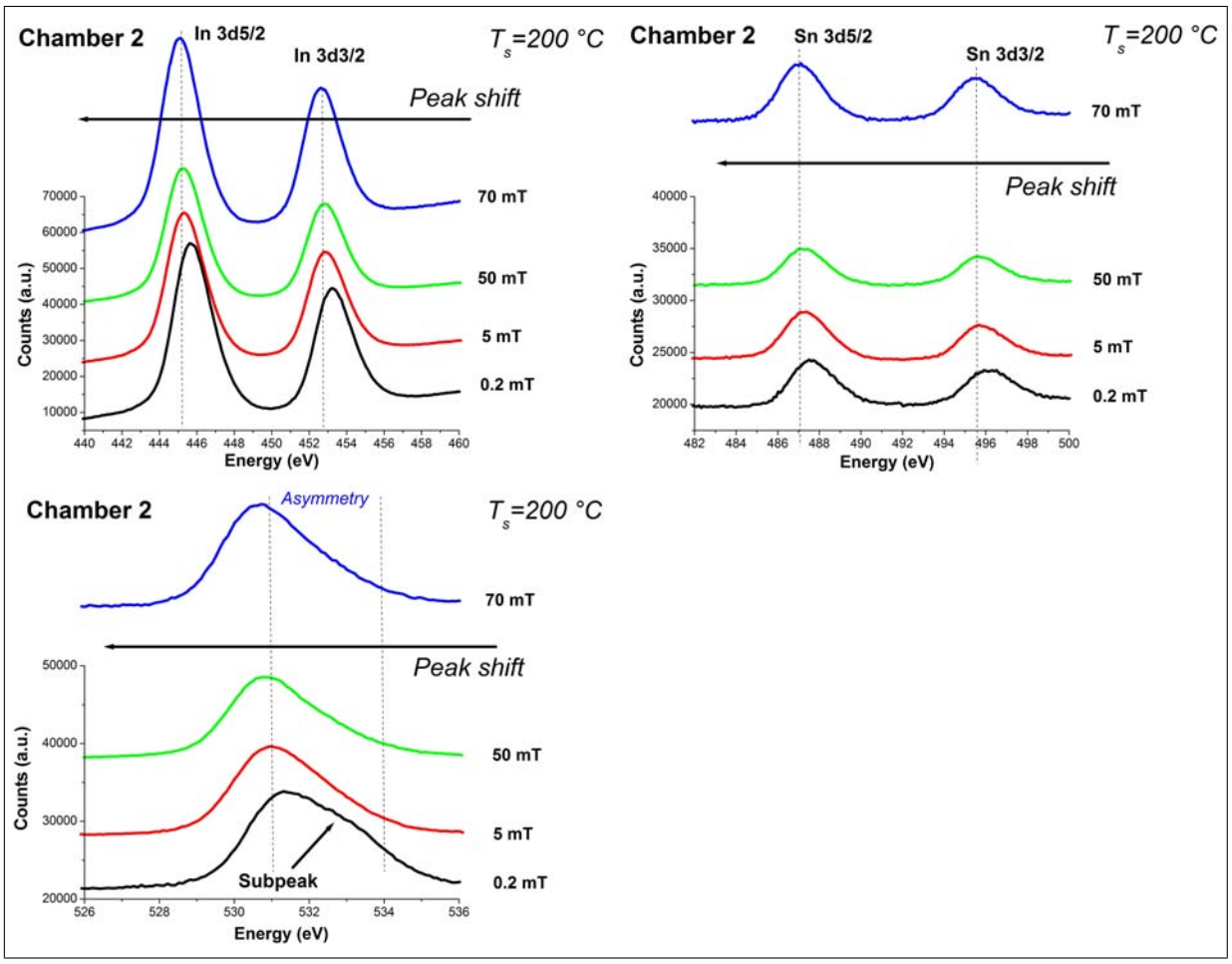

Figure 5.72 XPS survey of the In, Sn and O peaks for ITO thin films grown in chamber 2. Spectra are compared at P(O_2)=0.2, 5, 50 and 70 mT. T_s was 200°C.

to three lattice O atoms and to donate one electron to the conduction band: they are said to be “activated”. Although the same behaviour cannot be extrapolated to the whole thin film based on the XPS experimental results since only the first 10 nm were probed, it is suggested that Sn remains in the same oxidation state, i.e “activated”, through the whole thin film. The subpeak 2 at 489.1 eV points to Sn ions within another electronic environment.

The peak at 530.9 eV (subpeak 1) corresponds to O^{2-} ions [201]. Such ions have neighbouring In atoms with a full complement of six nearest-neighboring O^{2-} ions. This corresponds well to the ionic structure of In_2O_3. However, the other peak at 532.5 eV (subpeak 2) indicates another type of O with a much more complex environment. It is assigned to a suboxide forming at the surface which is held to be responsible for the low transparency in the visible range and for the presence of the particles witnessed by SEM imaging (Figs. 5.60 - 5.62). It is possible that it is an electrically inactive complex involving interstitial oxygen and neighbouring Sn atoms.

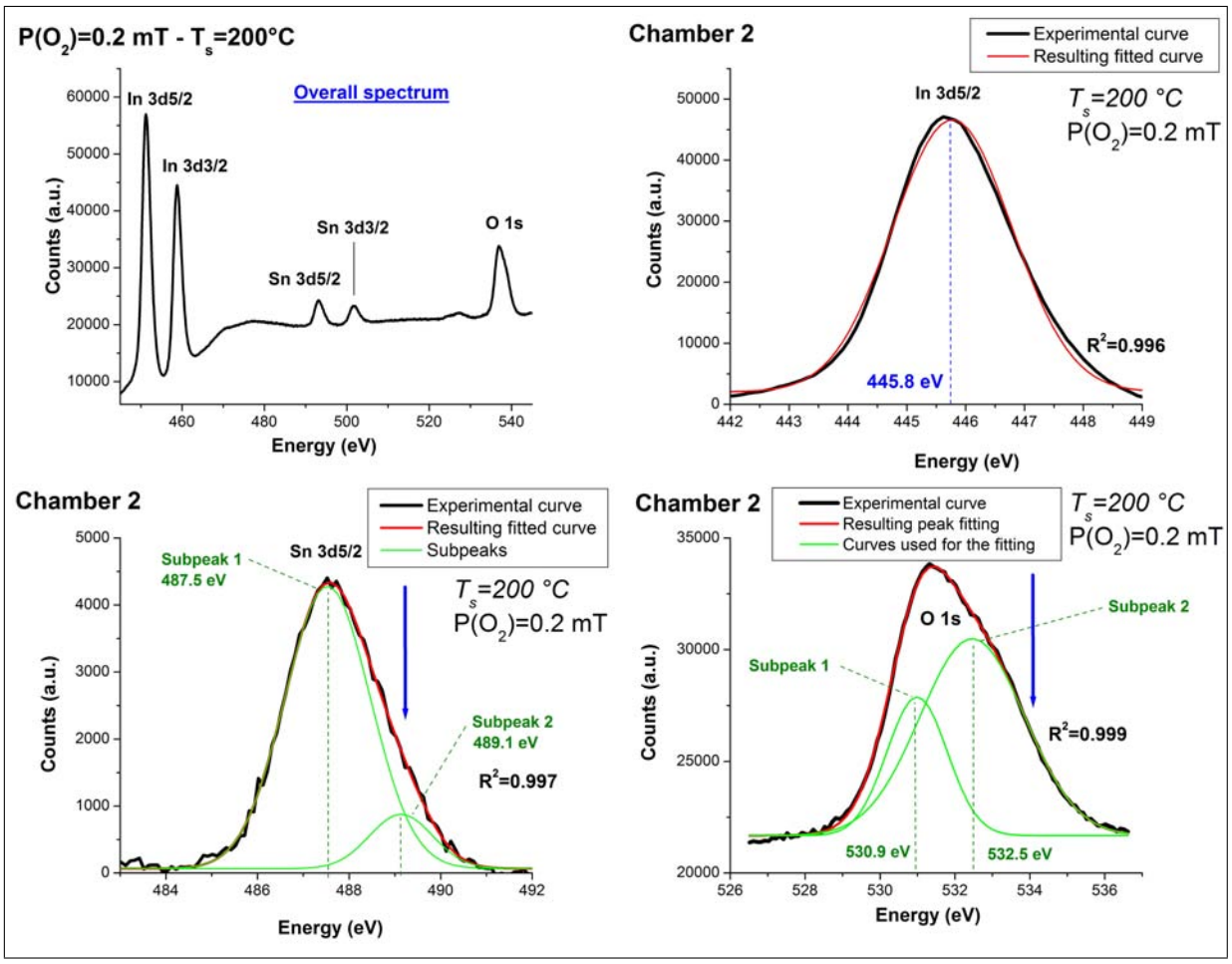

Figure 5.73 XPS of a sample grown in chamber 2 at $P(O_2)$=0.2 mT. Background corrected In 3d5/2 Sn 3d5/2 peaks are shown along with double Gaussian curve fitting to derive accurate peak positions. Sn 3d and O 1s peaks show asymmetries on their right hand side as shown by blue arrows.

Table 5.11 presents In/Sn and (In+Sn)/O atomic ratios computed from XPS measurements. They were derived from peak area ratios which were computed with the XPS Peak Fit 4.1 software [202] after a linear background subtraction. Individual peak areas were corrected by their respective atomic sensitivity factor (ASF) taken from Evans et. al [203]. These values are semi-quantitative at best as the photoionisation cross section in the 100 - 1500 eV range are difficult to measure reliably.

Table 5.11 Variation with $P(O_2)$ in chamber 2 of the In/Sn and (In+Sn)/O atomic ratios given by XPS.

Oxygen pressure	In/Sn	(In+Sn)/O
0.2 mT	9.96	0.56
5 mT	9.81	0.71
50 mT	10.99	0.61
70 mT	9.61	0.72

The EDX SEM and XPS results agree well as far as the In/Sn atomic ratio is concerned,

again demonstrating that there is no Sn segregation at the top surface, as previously shown with STEM EDX (Fig. 5.36) in section 5.2 when T_s was varied. However, whereas the EDX results in Fig. 5.71 showed a noticeable decrease in the (In+Sn)/O atomic ratio as $P(O_2)$ increased, the XPS results do not show any clear trend. The (In+Sn)/O surface atomic ratio is close from the nominal value at $P(O_2)$=0.2 mT, while higher oxygen pressure seems to result in an oxygen deficient environment at the surface.

The change in the oxygen content suggested by SEM EDX is accompanied by a change in film stress and density as demonstrated by the accurate monitoring with GAXRD of the (222) peak position of samples grown between $P(O_2)$= 0.2 and 7.5 mT in chamber 2 (see Fig. 5.74).

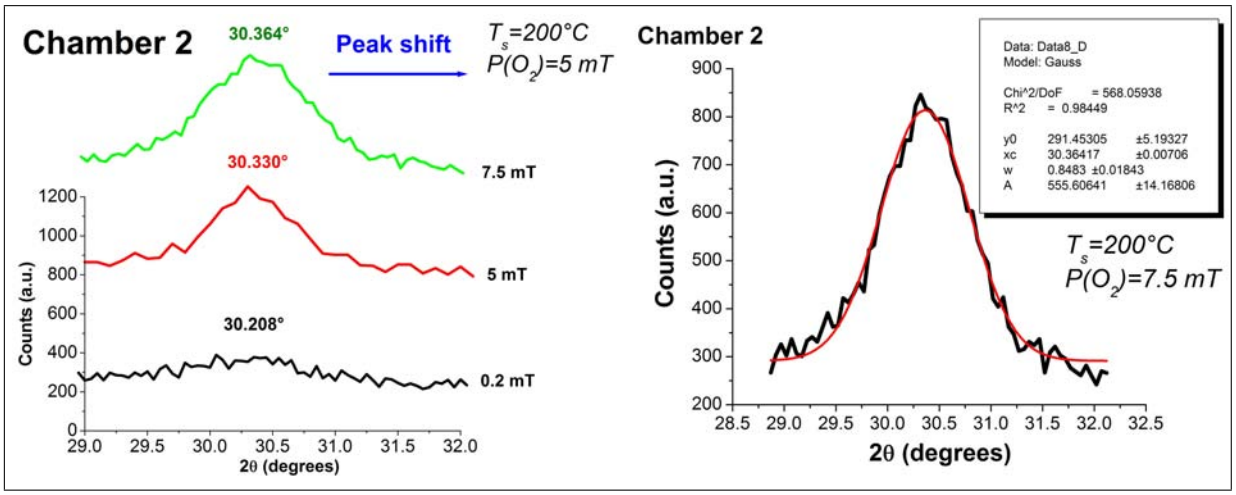

Figure 5.74 Evolution of the position of the (222) peak as $P(O_2)$ varies from 0.2 to 7.5 mT (left). Peak positions were computed with Gaussian fitting as shown with an example on the right at $P(O_2)$=7.5 mT. Films were grown in chamber 2 at a constant temperature of T_s=200°C. The incidence angle was kept identical at Ψ=16° for comparison purposes.

Data is rather limited here because it was acquired on selected samples grown in chamber 2 using the GAXRD diffractometer set-up in another department. The much higher precision level of peak position attainable compared with the conventional $\theta/2\theta$ Bragg-Brentano geometry diffractometer used for most of this study makes it a particularly good choice to study such tiny shifts. It is observed that a steady shift in the (222) diffraction peak position towards higher 2θ angles with increasing $P(O_2)$ is taking place, or, put another way, the (222) interplanar spacing parallel to the substrate is steadily decreasing. However, the shape of the peaks does not change substantially.

5.3.1.5 Resistivity - Surface resistance

The resistivity (ρ) was calculated via the relation: ρ=1/Neμ where N and μ are the carrier concentration and mobility derived from Hall effect measurements (see section 4.6.2). The resistivity ρ the and surface resistance R_s measurements are presented in Fig. 5.75

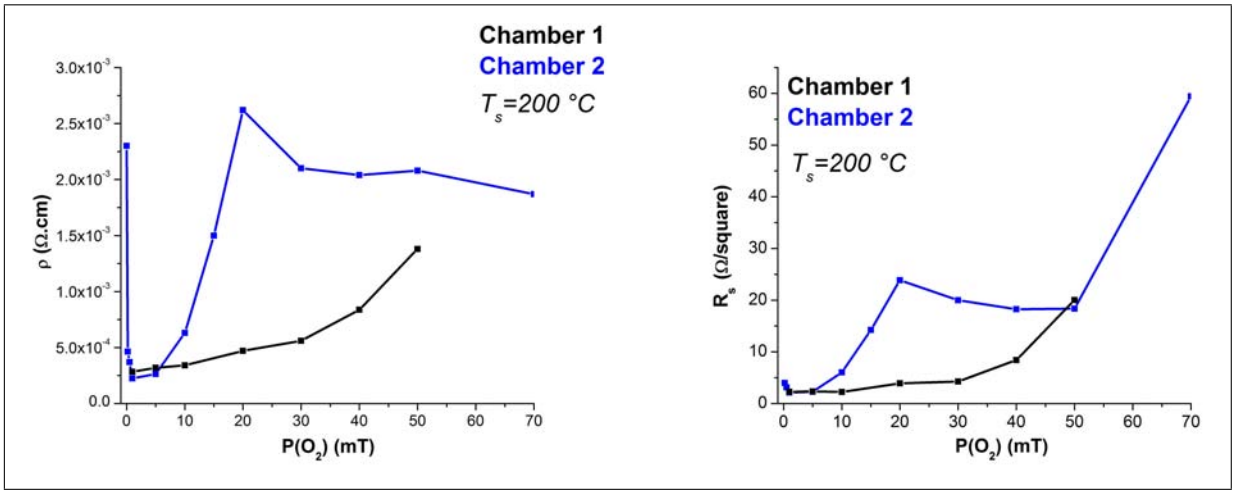

Figure 5.75 Resistivity (ρ) (left) and surface resistance (R_s) (right) versus P(O_2) for chambers 1 and 2. The growth conditions used are listed in Table 5.9.

It is observed that in both chambers, the resistivity increases with P(O_2). The resistivity maximum observed in chamber 2 at 20 mT is mainly due to the low mobility of free carriers (see Fig. 5.66). It saturates at $P(O_2)$ >20 mT. The lowest resistivity in chamber 1 was obtained for ITO films deposited between P(O_2)=1 and 10 mT. A narrower range is identified for chamber 2 (1 - 5 mT). In both chambers, ρ increases due to the combined effect of carrier concentration and mobility decline, although the former dominates since its variations are more important than the resistivity ones.

5.3.1.6 Summary of the results

ITO thin films were deposited by varying P(O_2) from 1 to 50 mT and from 0.2 to 70 mT in chambers 1 and 2 respectively. While the number of pulses had to be adjusted in chamber 1 at high P(O_2) in order to obtain films of similar thicknesses, such an adjustement was found unecessary in chamber 2. The microstructure was strongly impacted: the films deposited at low P(O_2) were composed of very small packed grains and their surfaces showed extended damage in chamber 2. These effects were more significant in chamber 2 than chamber 1 and were visible at P(O_2) as high as 50 mT. In addition, surface particles were observed at low P(O_2). Higher P(O_2) resulted in films with larger grains in chamber 2 while in chamber 1 this was less evident. These

microstructural changes impacted on electrical properties, compounded by the bulk and surface chemistry variations of the films with increasing $P(O_2)$.

5.3.1.7 Discussion

5.3.1.7.1 Thickness In both chambers, electrical properties were found to show a strong dependence on $P(O_2)$, while the film thickness was also affected in chamber 1 and had to be adjusted by varying the number of pulses fired. Surprisingly, as shown in Fig. 5.50, the thickness for chamber 2 was not affected when $P(O_2)$ was varied from 0.5 to 70 mT meaning that the deposition rate was identical between 0.2 and 70 mT. This is attributed to the different growth/pumping configurations between the chambers (as stressed in section 4.1 - Fig. 4.1) and reinforces the findings of section 5.2.3.4 that the O_2 gas interacts "less" with the plume in chamber 2 as compared with that in chamber 1, i.e., less scattering of the oxygen molecules occurs from the atmosphere by the energetic species ejected from the target and the deposition rate remains about constant. It also implies that the kinetic energy of the species impacting the growing film surface is greater overall in chamber 2 than in chamber 1 as confirmed by a higher surface hole density from chamber 2 films as observed up to 50 mT. High-energy particles from the plasma are expected to have sufficient energy to create defect centres in the films; indeed such defect centres include holes are observed at a very high density for samples grown below 1 mT in chamber 2.

5.3.1.7.2 Structural properties XRD results suggested a texture change as $P(O_2)$ was increased in chamber 2 (Fig. 5.52). This took place between $P(O_2)=1$ and 5 mT when the texture changed from (400) to (222). Such a change was not observed in chamber 1 (Fig. 5.51), probably because no samples were grown below 1 mT. A similar texture change was also noticed for chamber 2 as T_s was varied (as explained in section 5.2) where energetic considerations were used to explain such changes. It is believed that the same explanation holds true here: the minimisation of the surface and interface free energies gives rise to a preferred (222) growth orientation. In addition, it is believed [48] that films with a preferred <111> growth direction can accommodate more oxygen into their lattice, meaning that films grown at high $P(O_2)$ would see this orientation favoured and the growth can be explained by reduced oxygen vacancies.

However, at low $P(O_2)$ (<5 mT), a stress growth is suggested to take place: the films contains a high density of oxygen vacancies so that the structure is under more stress. Larger stress would favour <100> aligned grains to be preferentially nucleated and

grown, as reported in [204]. In addition, it is further reported [205] that the (400) plane has more resistance to the bombardment of energetic neutral atoms than the (222) planes, possibly reinforcing growth along the <100> direction. Overall, the change in preferred crystal orientation appears to be related to film oxidation, although this hypothesis could not be fully confirmed since no films were grown in chamber 1 below $P(O_2)$=1 mT.

XRD peak intensities were also affected by $P(O_2)$. In both chambers, a decrease in the (222) orientation peak intensity at high $P(O_2)$ was observed (50 and 70 mT in chambers 1 and 2 respectively). A similar observation was made by Dietrich et al. [206] although no explanation was advanced. It is proposed that under a high oxygen pressure, crystal growth of ITO resembles the bulk growth mechanism with decreased oxygen vacancy conditions. Under these circumstances, less effective tin doping can be observed due to an oxygen rich environment in which oxygen is likely to form complexes and precipitates with Sn, which would degrade the crystal structure causing the (222) peak intensity to decrease. However, the FWHMs do not vary much (Fig. 5.53) as compared with lower $P(O_2)$. The low FWHMs observed at high $P(O_2)$ were attributed to enhanced crystallisation of the In_2O_3 matrix with increasing $P(O_2)$, although the formation of precipitates/secondary phases (possibly increasing the internal stress level resulting in peak broadening) is likely to be a competing mechanism.

5.3.1.7.3 Bulk and surface chemistry The enhanced crystallisation with increasing $P(O_2)$ could be a direct result of the increasing oxygen flow leading to restoration of the stoichiometry of the crystalline phase. This is indicated by SEM EDX measurements (Fig. 5.71) which show that the ITO matrix actually incorporates oxygen from the atmosphere, since the In/Sn atomic ratio remains stable while (In+Sn)/O decreases. However, the decline is not particularly significant if the error bars are taken into account showing that the actual Oxygen intake by the bulk structure is rather small. Even at low $P(O_2)$, the inner part of ITO remained oxidised since the EDX SEM atomic (In+Sn)/O ratios obtained were close to the nominal value. This in agreement with what was observed in section 5.2 where even at T_s values as high as 400°C (which favours oxygen bulk diffusion), the interaction of the oxygen atmosphere with the bulk material was relatively moderate (Fig. 5.35).

XPS gave further insight into the intake of oxygen and related phenomena at the film/air interface. The surface was slightly oxygen deficient at higher (>5 mT) than at lower

$P(O_2)$ ($\sim$0.2 mT). This might indicate some degree of oxygen adsorption on the top surface at very low $P(O_2)$. This process may be favoured via the larger amount of oxygen vacancies and holes populating the top surface at such pressure. This oxygen deficient environment was responsible for Sn 3d and O 1s peak asymmetries (Fig. 5.73). The formation at the surface of a new phase incorporating Sn and O atoms is not ruled out either. This possible phase would disappear gradually as $P(O_2)$ increases, this being attributed to the restored stoichiometry (as regards to the bulk) of the structure.

Based solely on the XPS results presented in this study, these possible other phase(s) could not be identified with any certainty. The involvement of Sn and O atoms seems very likely as their respective peak profiles were modified at low $P(O_2)$. Nonetheless, the presence of a suboxide like In_2O (a non-transparent and highly resistive material [207]) cannot be totally ruled out since the samples obtained at low $P(O_2)$ were darkish. SEM imaging (Fig. 5.60) did show particles sitting on the top surface. Their true nature could not be quantified owing to SEM EDX spatial resolution constraints, but they are expected to be of metallic and/or suboxidic in nature. Therefore, changes to the shape of the core-levels with oxygen content in the chamber were attributed to the formation of intermediate compound(s), combined with possible surface suboxide/metallic particle formation favoured by a very poor oxygen environment at $P(O_2)$=0.2 mT.

In addition to the O 1s asymmetry, systematic changes with $P(O_2)$ of binding energies towards lower energies were observed for the In 3d, Sn 3d and O 1s spectra. Such a shift in the whole spectrum was interpreted as a change in the surface Fermi level E_F. A shift towards lower binding energy as $P(O_2)$ increases is compatible with an increase in the surface work function, which corresponds to the energy needed to move an electron from the surface Fermi level into vacuum. This observation is in agreement with the increased surface work function observed after oxidative surface treatments [208]. Interest in the ITO surface potentials was generated by the observation that an increase of the ITO work function leads to a desired lower injection barrier for holes at the interface with organic conductors. This increase in work function is typically achieved by oxidative treatments such as oxygen plasma, UV ozone, or chemical treatments. However, in solar cells, the ITO electrodes are used as electron collectors which requires a low work function. The change in E_F was attributed to changes in surface coverage by O_2.

The film textures were quantitatively evaluated via the texture coefficients $TC_{(400)}$ or $TC_{(222)}$ (see section 4.2.1 for more details) and related to the mobility μ as measured by

Hall-effect measurements. Excellent linear agreement (R=0.98) in chamber 1 is found between $TC_{(222)}$ and μ (Fig. 5.55), although the experimental point at 50 mT was not taken into account as it showed very poor agreement with the rest of the data. This is attributed to oxygen accumulating in the structure and forming complexes/precipitates. In addition, this linear relation means that the maximum in μ observed previously (Fig. 5.66) at 10/20 mT in chamber 1 also corresponds to the film with the strongest (222) preferred orientation.

No particular strong linear regression (R=0.64) was found for chamber 2, especially in the low pressure range (0.2 - 5 mT), where the crystal damage dominates the mobility behaviour. Therefore, μ appears to be more independent of the texture than in chamber 1. No other explanations could be found for the discrepencies between chambers 1 and 2 since films in both chambers showed about the same carrier density, so, any argument based on defect screening by a high carrier density does not hold. The mixed findings in this study reflect the situation in the literature, where orientation is sometimes believed to affect the mobility of free carriers [209] [210] [211], while other authors suggest no influence whatsoever [29][212].

The mobility μ was found to be linearly related to the FWHMs of preferred oriention peaks in both chambers (Fig. 5.54), which gives an indication of the degree of crystallinity of a certain film (of no or negligible crystallite size and strain broadening). Linear relations were identified for both chambers. One is between $P(O_2)$=1 and 20 mT and $P(O_2)$=20 and 50 mT in chamber 1. At $P(O_2)$=20 mT, the proportionality changes corresponding to the maximum observed mobility (Fig. 5.66). After $P(O_2)$=20 mT, μ degrades much faster than in the 1 - 20 mT range as witnessed by the steeper slope of μ versus the FWHM of the (222) peaks. As for chamber 2, linear relations between μ and the FWHMs were found for all the pressure ranges investigated (0.2 - 70 mT) except at $P(O_2)$=1, 30 and 40 mT. It is concluded that the higher the FWHM, the lower the mobility.

The particularly marked discrepancy in chamber 2 near $P(O_2)$=30 mT in terms of FWHMs and μ is explained on the basis of a structure argument. The (222) preferred orientation peak showed a systematic and reproducible asymmetry at larger 2θ (Fig. 5.56): this broad peak (shoulder) was attributed to a combination of SnO (JCPDS 01-072-2324), SnO_2 (JCPDS 01-071-5329) and possibly Sn_3O_4 (JCPDS 00-020-1293) phases. These were not stable at $P(O_2)$ >30 mT. The sharper and more intense peak at 2θ=29.49° was still attributed to the cubic In_2O_3 phase despite a significant 1° shift of the main (222) XRD peak as compared with JCPDS data (JCPDS 00-006-0416). Moreover, the

ever larger FWHM(222) between P(O_2)=5 and 20 mT is suggested to arise from this particular phase development, which also has a large (positive) impact on μ (Fig. 5.66), while no effect whatsoever was noticed on the carrier concentration N (Fig. 5.69). Hence, these phases appear to be more conductive than In_2O_3.

GAXRD confirmed that these phases are present across the whole layer since the peak shape is conserved as the incident angle is varied (i.e. as different thicknesses were probed) as observed in Fig. 5.58. Such a behaviour was not observed in chamber 1, at least between P(O_2)=1 and 50 mT. At $P(O_2)$ >30 mT, the asymmetry disappears. In addition, when working under a static atmosphere (and also a lower energy density), it also vanishes. This points to the fact that gas dynamics might play a central role in the formation of secondary phases during PLD growth. It is worth mentioning that very few reports of asymmetry in the (222) peak have been published to date [30]. The non-thermal nature of PLD favours the formation of such metastable phases which could explain why such effects are not systematically reported. It is suggested that the high energy density used in chamber 2 might favour such formation since it results in a plume containing a larger amount of reactive species facilitating metastable phase formation.

GAXRD also showed a slight change in film density as P(O_2) was increased. A shift towards higher 2θ was observed as P(O_2) was changed from 0.2 to 7.5 mT (Fig. 5.74). This shift is explained in terms of oxygen vacancy filling and bombardment by energetic particles during growth. As P(O_2) increased, more oxygen vacancies are filled and the molar volume of the film increases. This moderate intake was evidenced by EDX SEM (Fig. 5.71) and probably explains the observed moderate shift of the (222) peaks. Since the film is attached to a rigid substrate (glass), this shift is expected to result in some compressive stress. In addition, bombardment by energetic particles of the film surface could also play a role in this peak position shift as it is also known [5] to additional compressive stress via compaction and distortion of the surface.

5.3.1.7.4 Mobility, carrier concentration and resistivity At low P(O_2), μ was clearly affected in both chambers. In chamber 2, at very low P(O_2), SEM micrographs (Figs. 5.60 (a) - 5.62 (a)) showed porous films with pore sizes with an average diameter of 100 nm and high uniformity. It appears that when the flux of bombardment becomes too high, the growth of larger grains is suppressed and the film tends to become microcrystalline. Similar results were found by Kim et al. [87]. The large number of voids is held responsible for the dramatic decrease in μ observed at P(O_2)=0.2 mT in chamber 2. This

effect is compounded by a decline in oxygen atoms (leaving oxygen vacancies) which degrades the crystal structure and increases the level of concentration of defects, thus increasing μ. If the increase in the concentration of oxygen vacancies (as demonstrated by the strong rise of carrier density in the low pressure range, Fig. 5.69) at lower $P(O_2)$ is responsible for the decrease of μ during this "over-reduction", this would indicate strong scattering by these defects. This degardation in crystallinity at low $P(O_2)$ (below 1 mT) in chamber 2 seems to be confirmed by a decrease in the FWHM of the main (400) orientation peak (Fig. 5.53). The same mechanism is likely to operate in chamber 1 where at $P(O_2)=1$ mT the first significant decrease in μ is observed.

The addition of low amounts of oxygen leads to very fine grained films in chamber 2. This fine grained and nearly featureless film morphology prevails in chamber 2 from 1 to 50 mT oxygen (Figs. 5.60 - 5.62). At $P(O_2)=70$ mT, a much rougher surface ($\sim$5 nm RMS roughness) and a larger grain size ($\sim$100 nm) is observed. At high $P(O_2)$, the mobility shows a plateau (except at 30 mT as a result of the phase development described above).

In chamber 1, an average grain size increase is also noticed between 1 and 20 mT before decreasing again. The surface morphology is markedly different at $P(O_2)=50$ mT, perhaps indicative of a new growth mode leading to rougher surfaces at higher $P(O_2)$. Meanwhile, in the 1 - 20 mT range, μ increased. A lower density of grain boundaries and a better texture might have a positive impact on μ. As with chamber 2, the mobility showed a steady decline possibly before reaching a plateau.

Although no direct evidence could be found in this work, it is believed [13] that neutral and charged complexes ($SnOO_i/Sn_{In}O_i$) with excess interstitial oxygen form at grain boundaries. This has the effect of "deactivating" donors, further decreasing the overall carrier concentration in the film. Excess oxygen would accumulate at grain boundaries acting as trapping centres for free carriers [115] and setting grain boundary energy barriers, thus impacting on the mobility. In that case, the mobility would be temperature activated but because no experiment involving deposition of films at different T_s in a high oxygen pressure atmosphere were carried out, this hypothesis could not be verified. Finally, the hypothesis that excess oxygen would accumulate in the structure (and typically at interstices) is reinforced since SnO_2 is in solid solution in In_2O_3 for the SnO_2 concentration used in this work [213]. This is in accordance with XRD measurements (Figs. 5.51 - 5.52) showing no secondary phases formation at high $P(O_2)$. The formation of complex/precipitates eventually reaches a plateau, when no more excess oxygen can

be incorporated in the structure. This would explain the nearly constant μ observed in chamber 2 at $P(O_2)$ >30 mT, although insufficient experimental points are available in chamber 1 to confirm such a trend.

The carrier concentration was also affected when P(O_2) was varied (Fig. 5.69). The filling of oxygen vacancies decreases the carrier concentration as evidenced by Hall effect measurements. However, saturation is observed at 20 mT in chamber 2 while the decline is more gradual in chamber 1. This plateau can be attributed to the total filling of oxygen vacancies. More experimental points would be needed here to confirm the reaching of a plateau in chamber 1.

In both chambers, the decrease in N with P(O_2) was mathematically described by a first order exponential decay when P(O_2) was varied from 1 to 50 mT by:

$N = 3.96 \times 10^{19} + 7.74 \times 10^{20} \times e^{-\frac{P(O_2)}{29.84}}$ (chamber 1) and $N = 1.06 \times 10^{20} + 1.29 \times 10^{21} \times e^{-\frac{P(O_2)}{7.98}}$ (chamber 2). The closeness of these two relations is remarkable and points to the fact that a similar mechanism is taking place regarding the filling of oxygen vacancies.

A strong dependence of the resistivity on the partial oxygen pressure for laser ablated films has already been observed by Zheng and Kwok [74][73] and Jia et al. [214]. In this work, optimum oxygen pressure ranges were identified for growing low resistivity thin films in the chambers: 5 - 20 mT and 5 - 10 mT in chambers 1 and 2 respectively. Such a narrow range was attributed to the behaviour of the carrier concentration (Fig. 5.69) and the mobility (Fig. 5.66). High carrier density can only be realised at low P(O_2) while higher mobility can only be achieved at high P(O_2). As these two mechanisms cause opposite effects, the resistivity showed a minimum value at a certain P(O_2). In chamber 2, in the 20 - 70 mT range, N decreased with increasing P(O_2), but μ increased and compensated for the charge carrier concentration, so that the films show a constant resisitvity over this range (Fig. 5.75).

5.3.1.7.5 Scattering mechanisms The dominant scattering mechanism operating for films grown in both chambers was investigated, employing a similar approach to that used in section 5.2.1.3. Calculations (Fig. 5.67) showed that electron mean free paths were about equivalent (a few nanometres) and followed the same trend in both chambers. In chamber 2, at P(O_2)=0.2 mT, the MFP is barely above 1 nm. The same general trend is seen in chamber 1, although no film could be grown below 1 mT. It is suggested that electron scattering at the holes and pores observed by SEM (Figs. 5.59 -

5.60) is a major obstacle for good electrical conduction in these ITO films. The decrease in MFP at low $P(O_2)$ is related to an increase in FWHM (Fig. 5.53) demonstrating a strong crystal degradation. Even though grain sizes could not be derived accurately for some samples (especially in chamber 2 at very low $P(O_2)$), it was higher than a few nanometres. Therefore, grain boundary scattering is not expected to impact strongly on μ.

Similarly to section 5.2, ionised impurity scattering is shown to operate up to a certain oxygen pressure threshold. Since μ seem to be linearly correlated (in a specific oxygen range) as shown in Fig. 5.76, Eq. 2.3 proposed by Ding et al. [6] was used to model the theroretical mobility when ionised impurity scattering due to Sn or oxygen vacancies predominates over other scattering mechanisms (see Fig. 5.77).

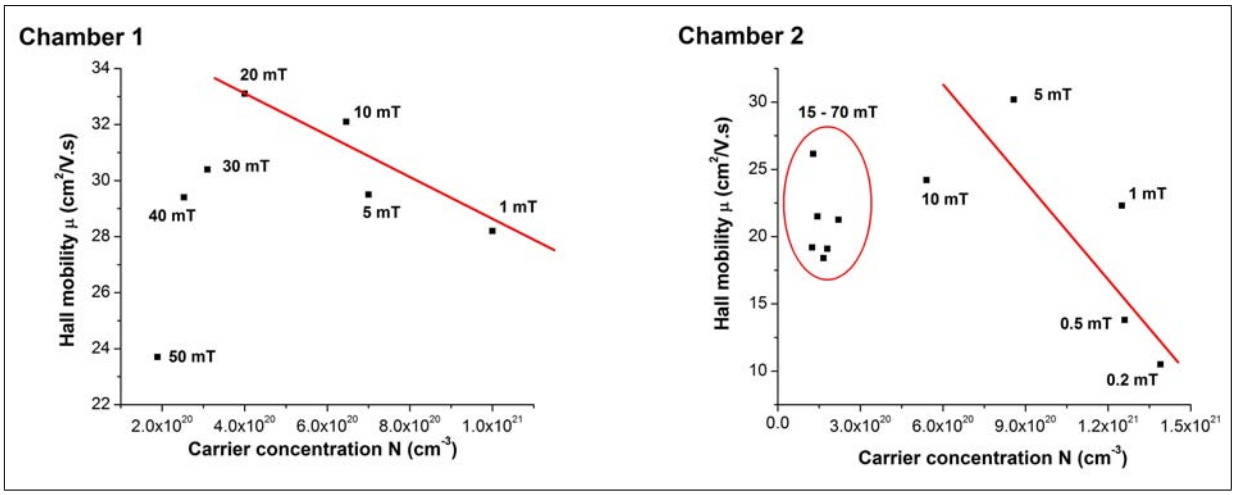

Figure 5.76 Relation between the mobility μ and the carrier concentration N in chambers 1 (left) and 2 (right).

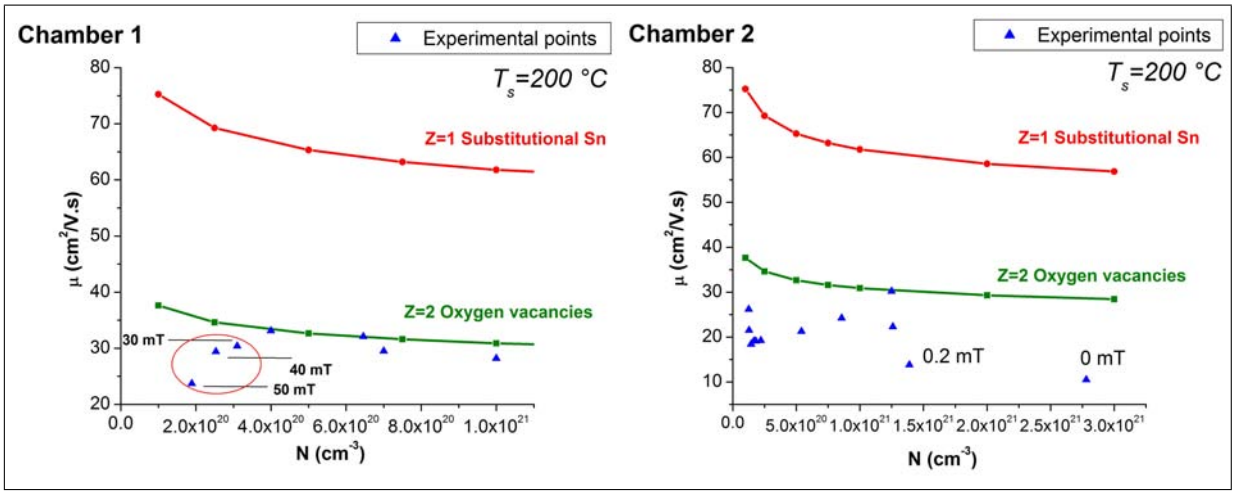

Figure 5.77 Ionised impurity scattering model developed by Dingle et al. [6] (red and green curves) and comparison with experimental data (blue triangles) in chambers 1 (left) and 2 (right).

Ionised impurity scattering is shown to dominate within certain P(O_2) ranges (Fig. 5.77): 1 - 20 mT and 0.2 - 10 mT in chambers 1 and 2 respectively. As the oxygen pressure increases up to 20 mT in chamber 1, the experimental points are closer to the theoretical mobility curve where the oxygen vacancies are the dominant ionised scattering impurities than the case where only singly charged tin impurities are considered. Above the 20 mT threshold (30 mT in chamber 2), the experimental values significantly depart from the theoretical mobility curves. It is suggested that above these pressures, most oxygen vacancies were filled leaving fewer ionised impurities hence switching the dominant ionised impurity scattering mechanism to a new one. The conduction mechanism at high P(O_2) could not be positively indentified in this work. It is suggested that the increasing probability of precipitate and complex formation(s) at higher oxygen pressures makes neutral impurity scattering likely to operate. In chamber 2, the fitting of the theoretical model to the experimental data is of less quality at $P(O_2)$ <0.2 mT, possibly due to scattering at discontinuities becoming predominant.

5.3.2 Optical properties

As mentioned in section 5.3.1 for electrical properties, the thickness of the films was found to show a strong dependence on P(O_2) in chamber 1 but not in chamber 2. As a consequence, the number of pulses was adjusted accordingly in order to produce films with comparable thickness as P(O_2) changed. Therefore, it is assumed that the thickness parameter did not play a significant role in any optical property change with P(O_2) reported in this section.

5.3.2.1 Transmittance and ellipsometric measurements

Transmittance measurements were performed in the 250 - 1000 nm range (Fig. 5.78) for chambers 1 and 2.

The variation of the interference structure in the visible range is believed to arise from interference between beams reflected from the top of the film and the interface of the substrate/film [96]. The effect is more pronounced for films grown in chamber 2 because they were thicker than those in chamber 1. In the near-IR region, the free carrier absorption becomes important for the transmittance and reflectance of the ITO films. The optical phenomena in this region can be explained on the basis of classical Drude theory, which states that the transition from high transmittance to high reflectance will occur at shorter wavelength for films with high carrier concentration. This is what is observed for

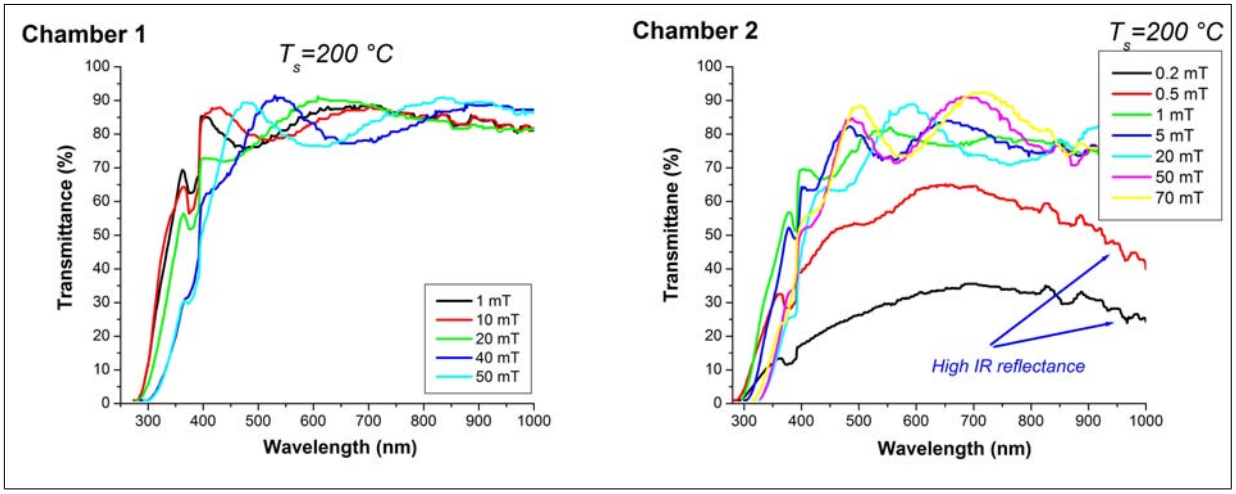

Figure 5.78 Transparency of ITO thin films deposited with varying $P(O_2)$ in chambers 1 (left) and 2 (right). $P(O_2)$ was varied from respectively 1 to 50 mT and 0.2 to 70 mT in chambers 1 and 2. T_s was kept constant at 200°C.

chamber 2 with $P(O_2)$=0.2 and 0.5 mT where a significant decline in transmittance (due to an increase in reflectance) is noticed in the near-IR region (∼900 nm). In chamber 1, in the $P(O_2)$ range investigated (1 - 50 mT), no significant differences are observed between the different spectra apart from a shift towards higher wavelengths as $P(O_2)$ increases. However, in chamber 2, where a larger oxygen range is studied, significant differences are observed, namely a strong improvement in transmittance in the visible range as $P(O_2)$ increases from 0.2 to 1 mT, although above this pressure, transparency improvements are minor.

Fig. 5.78 shows a shift in the absorption edge toward longer wavelengths with increasing $P(O_2)$ (consistent with a decrease in carrier concentration according to the Burstein-Moss effect) for both chambers. In chamber 1 the shift is gradual up to 50 mT (see Fig. 5.79). However, in chamber 2, no significant shift of the absorption edge is observed after 20 mT. The magnitude of these shifts versus different $P(O_2)$ are in accordance with the carrier concentration measurements presented earlier (Fig. 5.69).

It is observed that at very low $P(O_2)$ in chamber 2, the absorption edge steepness is strongly affected. Above 1 mT, no significant difference is evident despite the large FWHM obtained at $P(O_2)$=20 mT (Fig. 5.53) and the decrease of the (222) peak intensity at $P(O_2)$=70 mT (Fig. 5.52). In chamber 1, no films were grown below $P(O_2)$=1 mT, hence the impact of the absorption edge steepness is unknown. However, at $P(O_2)$ >40 mT, the absorption edge slope is found to decrease contrary to the behaviour in chamber 2. This could be related to the decrease of the (222) peak intensity observed by XRD (Fig. 5.51) and the slight increase of the FWHM of the (222) peak (Fig. 5.53) which

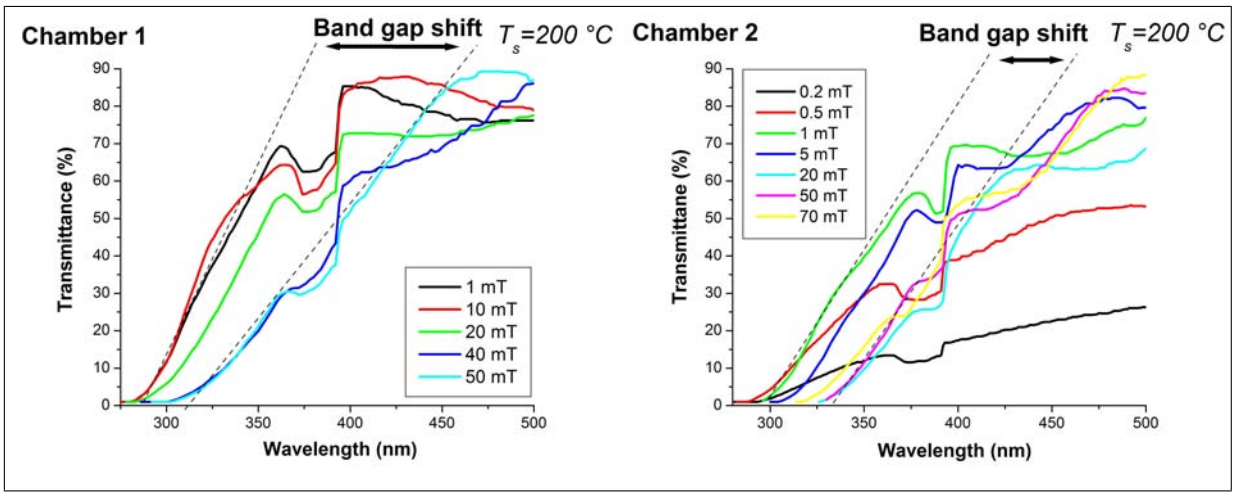

Figure 5.79 Variation of the absorption edge in chambers (left) 1 and 2 (right) with $P(O_2)$. $P(O_2)$ was varied from 1 to 50 mT and 0.2 to 70 mT respectively in chambers 1 and 2. T_s was kept constant at 200°C.

point to a degradation in crystallinity combined with a higher residual stress level.

For the sake of clarity, the average transmittance in the 400 - 1000 nm range is also plotted in Fig. 5.80 for both chambers.

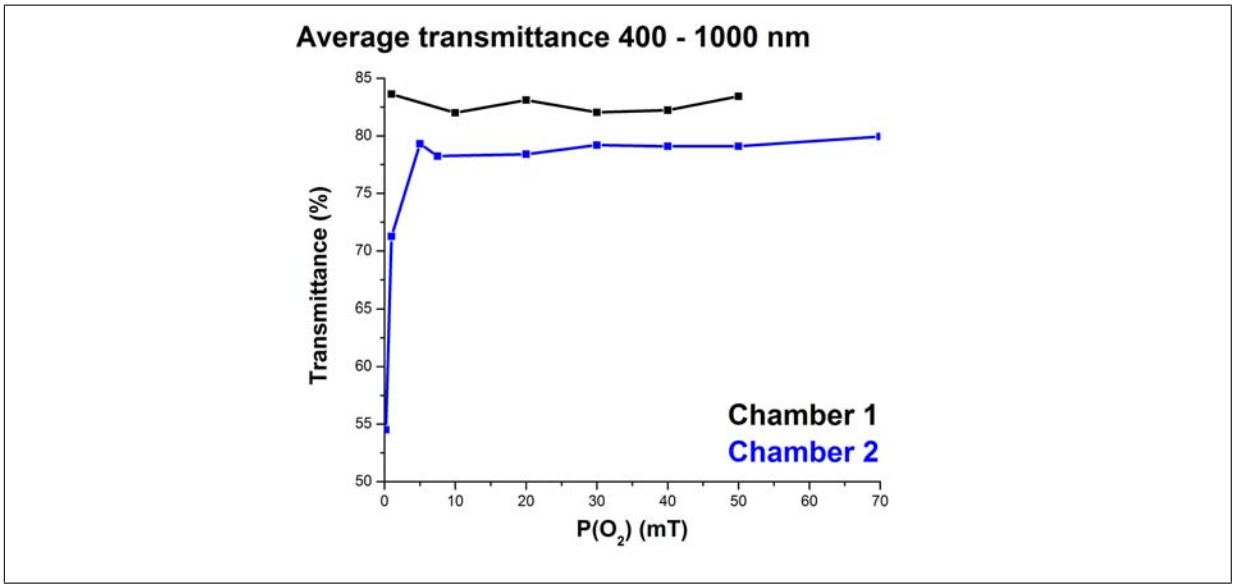

Figure 5.80 Average transmittance over the 400 - 1000 nm range of ITO thin films deposited at various oxygen pressures in chamber 1 and 2. $P(O_2)$ was varied from 1 to 50 mT and 0.2 to 70 mT respectively in chambers 1 and 2. T_s was kept constant at 200°C.

In the present work, the surface roughness was not found to be a significant parameter determining final optical properties. Indeed, the film grown in chamber 2 at $P(O_2)$=70 mT is by far the roughest (∼5 nm) of all films grown, nonetheless it still showed an excellent transparency of about 80% in the visible range as compared with smoother films at lower pressures.

Fig. 5.81 shows more clearly the variation of the optical band gap energy of the ITO thin films with $P(O_2)$. Tauc plot were used to derive the optical band gap energy.

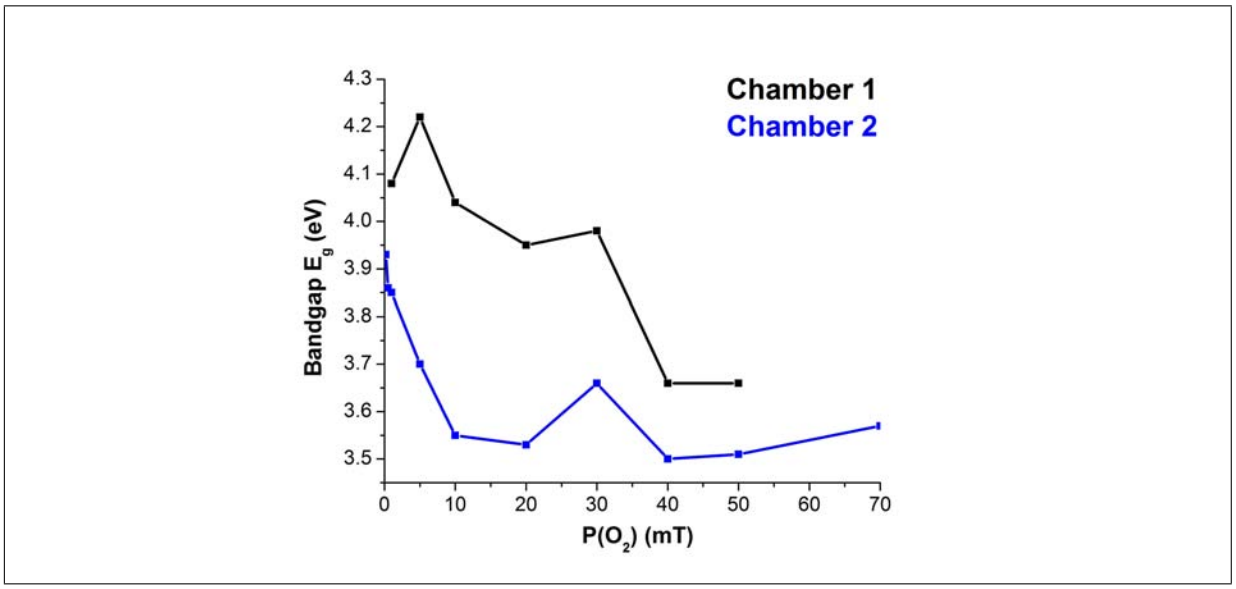

Figure 5.81 Optical bandgap variation of ITO thin films deposited at various oxygen pressures in chambers 1 (black curve) and 2 (blue curve).

Fig. 5.82 plots the relation between the band gap and $N^{2/3}$.

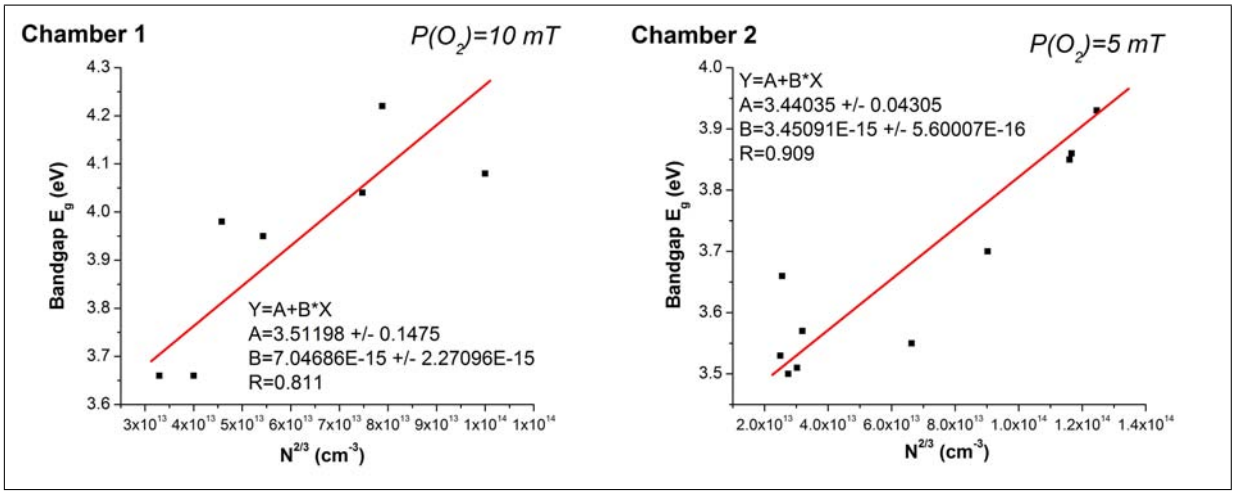

Figure 5.82 Variation in the optical band gap with carrier concentration $N^{2/3}$ in chambers 1 (left) and 2 (right), showing the Burstein-Moss shift in ITO thin films. $P(O_2)$ was varied from 1 to 50 mT and 0.2 to 70 mT in chambers 1 and 2 respectively. The oxygen pressure for each experimental point is added for information. T_s was kept constant at 200°C in both chambers.

The linear plot obtained show the proportionality between the bandgap E_g and $N^{2/3}$ in both chambers, verifying the Burstein-Moss shift relation. The intrinsic band gap E_{g0} (band gap of the undoped semiconductor) can be derived from the intersect with the y axis. It is calculated to be 3.51 eV in chamber 1 and 3.44 eV in chamber 2. These 2 values are lower than the ones reported generally in the literature: 3.99 eV [215], 3.83

eV [97] and 3.76 eV [216]. It is worth noting that these 2 values are relatively close to each other considering that the films were deposited in two different chambers, tending to confirm that the Burstein-Moss shift theory holds well for both chambers.

Using eq. 5.7, it is found that m^*_{VC}(chamber 1)=2.94×10^{-30} kg and m^*_{VC}(chamber 2)=6.01×10^{-30} kg. Since m_0=9.11×10^{-31} kg, m^*_{VC}(chamber 1)=0.31m_0 and m^*_{VC}(chamber 2)=0.64m_0. Agreement with the literature is satisfactory in chamber 2 since Vainshtein et al. [191] obtained m^*_{VC}=0.50m_0 while Kostlin et al. [28] calculated m^*_{VC}=0.54m_0. In chamber 1, this agreement is more moderated.

Ellipsometric results are presented to complement the transparency measurements presented above. The complex refractive index n_c=n+ik is derived, which includes its real part, the proper refractive index (n), and its imaginary part, the extinction coefficient (k). Only results from chamber 2 are presented. The Cauchy model (see section 4.7.2.1) was used to derive the optical and dielectric data presented here and Fig. 5.83 shows the results for ITO films grown at 0.2, 1, 5, 20, 50 and 70 mT.

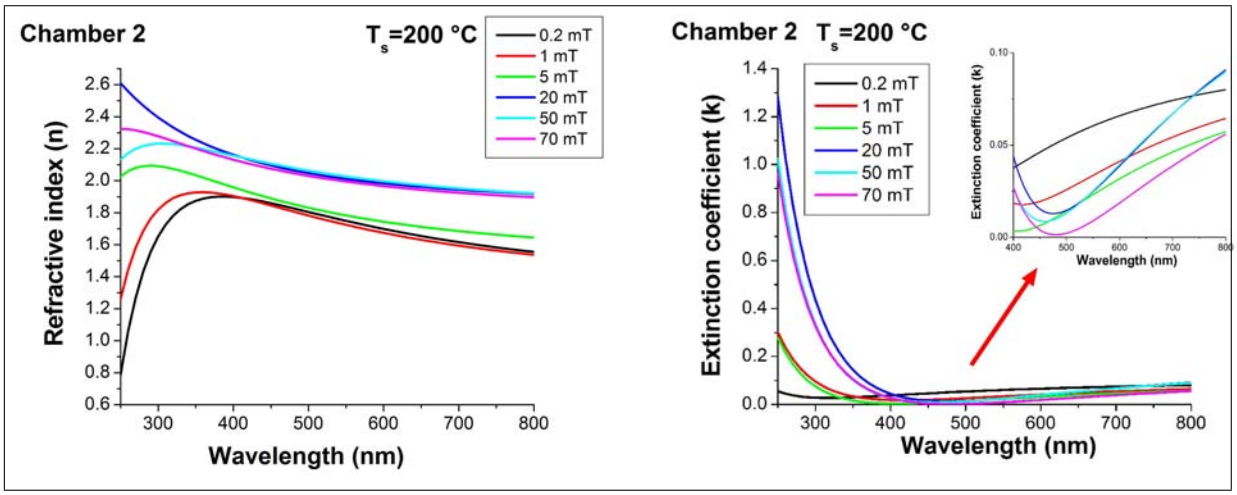

Figure 5.83 Refractive index n (left) and complex coefficient k (right) derived from ellipsometric measurements using a Cauchy model for ITO films grown at 0.2, 1, 5, 20, 50 and 70 mT. T_s was kept constant at 200°C in both chambers.

It is observed that the refractive index increases as $P(O_2)$ increases, while in the visible range (400 - 800 nm), the extinction coefficient is decreasing with increasing $P(O_2)$. This is in good agreement with transmittance measurements for chamber 2 presented in Fig. 5.78 where it was observed that overall transparency over the visible range improved as $P(O_2)$ increased. The variation of k (250 - 350 nm) in the band gap region is more dramatic, with k increasing exponentially in the near-UV range at high $P(O_2)$ (above 20 mT). As $P(O_2)$ goes up, the refractive index tends to have a more horizontal behaviour. Above 20 mT, no more improvement in the refractive index is observed except in the band gap energy range between 250 and 350 nm. Essentially, the same observation was

made in Fig. 5.79 regarding the absorption edge, which showed minor shift from 20 mT. This points to a relation between n and the carrier concentration N.

5.3.2.2 Summary of the results

ITO thin films were deposited by varying $P(O_2)$ from 1 to 50 mT and from 0.2 to 70 mT in chambers 1 and 2 respectively. Films with similar thicknesses were compared and the optical transmittance was found to be impacted in two ways:

- improving (average) transmittance over the visible range with increasing $P(O_2)$.
- absorption edge shift towards higher wavelenghts with increasing $P(O_2)$.

Meanwhile, the complex refractive index was also found to be affected. The absorption edge shift with increasing $P(O_2)$ enabled the calculation of the electron reduced effective masses in both chambers.

5.3.2.3 Discussion

The transmittance was found to be strongly affected by $P(O_2)$ in both chambers. In chamber 2, at low $P(O_2)$ (0.2 mT), the transmittance was less than 40% over the visible range while $P(O_2)$ over 1 mT gave an average transmittance of 80%. Such low transparency in the 0.2 - 1 mT range was accounted for by the observed strong blackening of the ITO thin films. Previous EDX SEM results (see Fig. 5.71) showed that ITO films become less oxygen rich as $P(O_2)$ decreases, leading to slightly non-stoichiometric films. However, at such low $P(O_2)$, the film surface was much more affected by the formation of surface intermediate phases and particles as discussed in section 5.3.1.4. These suboxide compounds forming at the surface are suggested to be responsible for the loss of transparency in the 0.2 - 1 mT range. In addition, at $P(O_2)=0.2$ mT, SEM microgaphs showed round particles about 100 nm in diameter and a few hundred nanometres apart sitting all over the surface: this is the scale of the wavelength of the light over the visible range. Therefore, these particulates are expected to cause strong light scattering, thereby reducing even more the transparency over the visible range at such low pressure.

Films grown at $P(O_2)=0.2$ mT also showed a plummeting transmittance in the near-IR region ($\sim$900 nm). This was attributed to the very high carrier density (of the order of $10^{21}cm^{-3}$) where free carriers screen the incoming electric field. The same was not observed in chamber 1 as no films were grown below $P(O_2)=1$ mT.

Moreover, bombardment by the high energy neutral or negatively charged ions (par-

ticularly in chamber 2) and deficiency of oxygen at such low $P(O_2)$ are likely to cause crystalline degradation resulting in the generation of structural defects and giving rise to deep localised impurity levels. Those can prevent electrons from making interband transitions from the valence to the conduction band so decreasing transmittance. The increasingly rough surface morphologies at low $P(O_2)$ were not found to cause any significant light scattering as even the roughest sample ($\sim$5 nm RMS roughness) did not show any degradation in terms of transmittance values. Roughness of a few nanometres, i.e. far less than the visible light wavelength scale (a few hundreds nanometres) explains such an observation.

In both chambers, as $P(O_2)$ increases, a clear absorption edge shift towards higher wavelengths is noticed. This effect is related to the density of free electrons: if the free carrier concentration N is so enlarged that the bottom of the conduction band is partly filled, then transition to these lowest levels is no longer allowed and the first transition now observable occurs at somewhat higher photon energy, i.e. lower wavelengths and higher energy gaps. As a consequence, a bandgap or absorption edge shift occurs which is known as the Burstein-Moss shift [21].

A good linear regression was obtained between 1 and 50 mT in chamber 1 and between 0.2 and 20 mT in chamber 2 (see Fig. 5.82) for the bandgap energy E_g versus $N^{2/3}$. The shift showed a plateau after 20 mT in chamber 2, while the effect was more gradual in chamber 1. It is perfectly in line with carrier concentration measurements showing a plateau after 20 mT in chamber 2 while N gradually declines between 1 and 50 mT in chamber 1 (see Fig. 5.69). Hence, the electro-optical properties observed in our study are self-consistent. The linear relation evidenced between E_g and $N^{2/3}$ enabled the calculation of the electron reduced effective mass (m^*_{VC}) of our films in chambers 1 (m^*_{VC}=0.31m_0) and 2 (m^*_{VC}=0.64m_0). Overall, these values were found to be in moderate agreement with the literature but similarly to section 5.2.2.3, no dependence between effective mass and carrier concentration was taken into account.

The slope of the absorption edges was linked to the concentration of defects in our films. It was found to be modified by $P(O_2)$ since its slope was observed to decrease at very low $P(O_2)$ for chamber 2 in agreement with larger FWHMs and low (400) XRD peak intensity. Films grown at low $P(O_2)$ showed a high defect concentration as mentioned above. This gave rise to localised energy levels within the band gap so that an electron is less and less likely to make a direct transtion from the valence to the conduction

band. At $P(O_2)$ >1 mT, the slope of the absorption edge was not found to vary despite the large FWHM obtained at P(O_2)=20 mT (Fig. 5.53) and the decrease of the (222) peak intensity at P(O_2)=70 mT (Fig. 5.52) which would suggest a loss in crystallinity. It was concluded that the large FWHM observed around 20 mT was due to a phase development rather than a proper loss of crystallinity. In addition, the FWHMs tended to decrease/increase with P(O_2) in chambers 2 and 1 respectively. The slight increase of the FWHMs in chamber 1 with P(O_2) were connected with a loss of crystallinty since no asymmetry of the (222) peak could be determined, hence the less steep absorption edge observed at higher P(O_2) in chamber 1. It is also suggested that films grown in chamber 1 at $P(O_2)$ <1 mT would probably have shown a similar impact on the transmittance spectra.

The refractive index n was found to increase with P(O_2), especially in the band gap region. This was related to the carrier concentration N, although crystallinity and material density variation effects (filling of oxygen vacancies) cannot be excluded. Both parameters were shown to increase sligthly with an increase in P(O_2), as evidenced by FWHM (Fig. 5.53) and GAXRD (Fig. 5.74) measurements respectively.

The extinction coefficient k tended to decrease over the visible range with increasing P(O_2). This is consistent with the observed increase in transmittance with increasing P(O_2) (Fig. 5.78), since k determines the absorption coefficient α (see eq. 2.8). This is attributed to a restored stoichiometry at high P(O_2). In the band gap region, larger variation were observed. Films grown at high P(O_2) were more opaque in the band gap region and this opacity extended to the visible range (>400 nm). This is in agreement with transparency measurements (Fig. 5.79) showing a shift towards higher wavelengths with increasing P(O_2) in accordance with the Burstein-Moss shift theory (Fig. 5.82).

In conclusion, the behaviour of n and k was connected to the absorption and desorption of oxygen in the film structure as P(O_2) is varied, as shown by previous EDX SEM and XPS measurements.

5.3.2.4 Optimal oxygen pressure

The results from sections 5.3.1 and 5.3.2 show that the optimal oxygen pressures leading to the largest [transparency over the visible range]/[resistivity] ratio are 10 mT and 5 mT in chambers 1 and 2 respectively.

5.3.3 Reconciling chambers 1 and 2

An attempt to reconcile results from the two chambers has already been made in section 5.2.3 for varying T_s. The same work is done here for the reasons stated in section 5.2.3. In this section, electrical (μ, carrier concentration N and ρ) and optical properties are compared and discussed in terms of $P(O_2)$. The reader is reminded that chamber 1 was used under a dynamic atmosphere, while in chamber 2, the atmosphere was static, i.e. no pumping took place after introduction of a certain amount of pure O_2 gas and deposition. The set-up difference between the two chambers was illustrated in section 4.1, Fig. 4.1. All other parameters used in chamber 2 are set to be exactly the same as for chamber 1. 10, 20, 30 and 50 mT of pure oxygen gas was introduced to chamber 2 and then pumping was stopped. To maintain pressure, it was found necessary to inject regulary some oxygen inside the chamber as it was consumed by the thin film during its growth. Table 5.12 summarises the growth conditions used in chambers 1 and 2.

Table 5.12 Summary of ITO growth parameters by varying $P(O_2)$ in chamber 2. T_s was kept at 200°C. The atmosphere was static.

Temperature	200°C
T-S distance	63 mm
Laser fluence	7.5 J/cm^2
Laser frequency	10 Hz
Oxygen pressure	1 - 50 mT

5.3.3.1 Electrical properties

Fig. 5.84 shows how μ, N and ρ vary when $P(O_2)$ is varied from 1 to 50 mT.

Reasonably good agreement is obtained concerning N, the trend being exactly the same with an inflextion point at 20 and 30 mT in chambers 1 and 2 respectively. The agreement not so good as far as the mobility is concerned, the two curves looking to be shifted relative to one another on the $P(O_2)$ axis by 10 mT. This is the value by which the inflection point in N is shifted in chamber 2. All in all, the resistivity comparison shows a mixed trend (Fig. 5.84). Fairly good agreement is obtained between 10 and 20 mT while above, the values increasingly diverge. The two curves can also be seen as shifted from one another along the $P(O_2)$ axis by 10 mT. Taking account of this shift, the comparison between N, μ and ρ would be reasonably satisfactory. Such a shift is due to the slightly different gas dynamics at play in the two chambers. The higher resistivity for films from chamber 2 under static O_2 pressure as compared with chamber 1 could demonstrate a

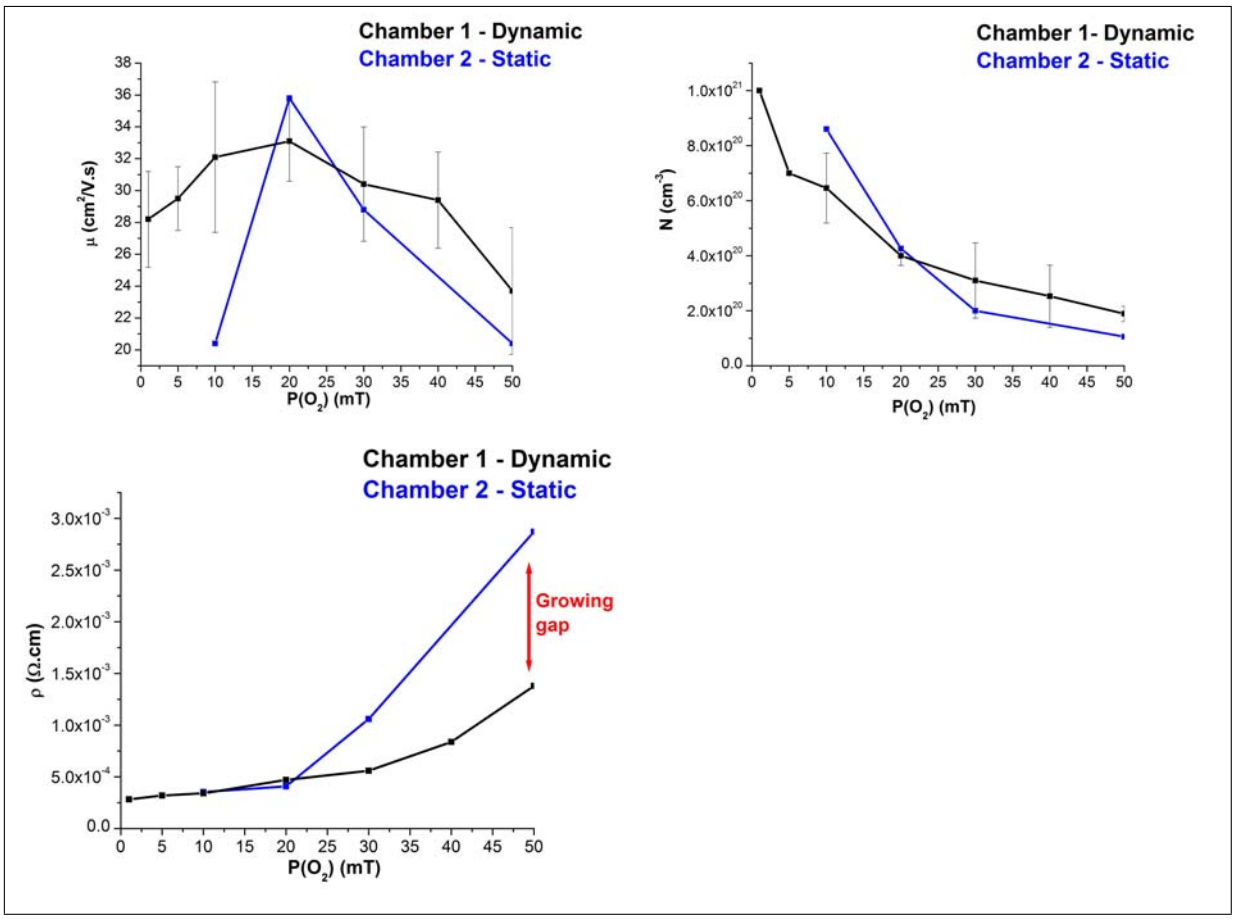

Figure 5.84 Comparison of the mobility μ , carrier concentration N and resistivity ρ for films from chambers 1 and 2. The temperature is set at 200°C. The pressure is varied from 10 to 50 mT in chamber 2 and from 1 to 50 mT in chamber 1.

capacity of the film to absorb more oxygen, thus filling in more oxygen vacancies. Only a rough trend can be established here however, as only one set of samples grown in chamber 2 under a static atmosphere was measured.

5.3.3.2 Structural properties

Structural properties were investigated by XRD. Fig. 5.85 compares XRD patterns at P(O_2)=10, 20, 30 and 50 mT between 2θ=20 and 70° for chamber 1 (dynamic) and 2 (static).

A (222) preferred orientation is observed in chamber 2. The agreement between the two chambers in terms of orientation is best at higher P(O_2) (30 and 50 mT). However, poorer agreement is found at 10 mT. Other orientations appear in chamber 1 and not in chamber 2 under a static atmosphere. This fact can be explained by the kinetic energy and velocity distribution of ejected species being slightly different between the two chambers. As a consequence, some differences in orientation are observed. As mentioned earlier, the asymmetric peak (Fig. 5.56) observed at 30 mT in chamber 2

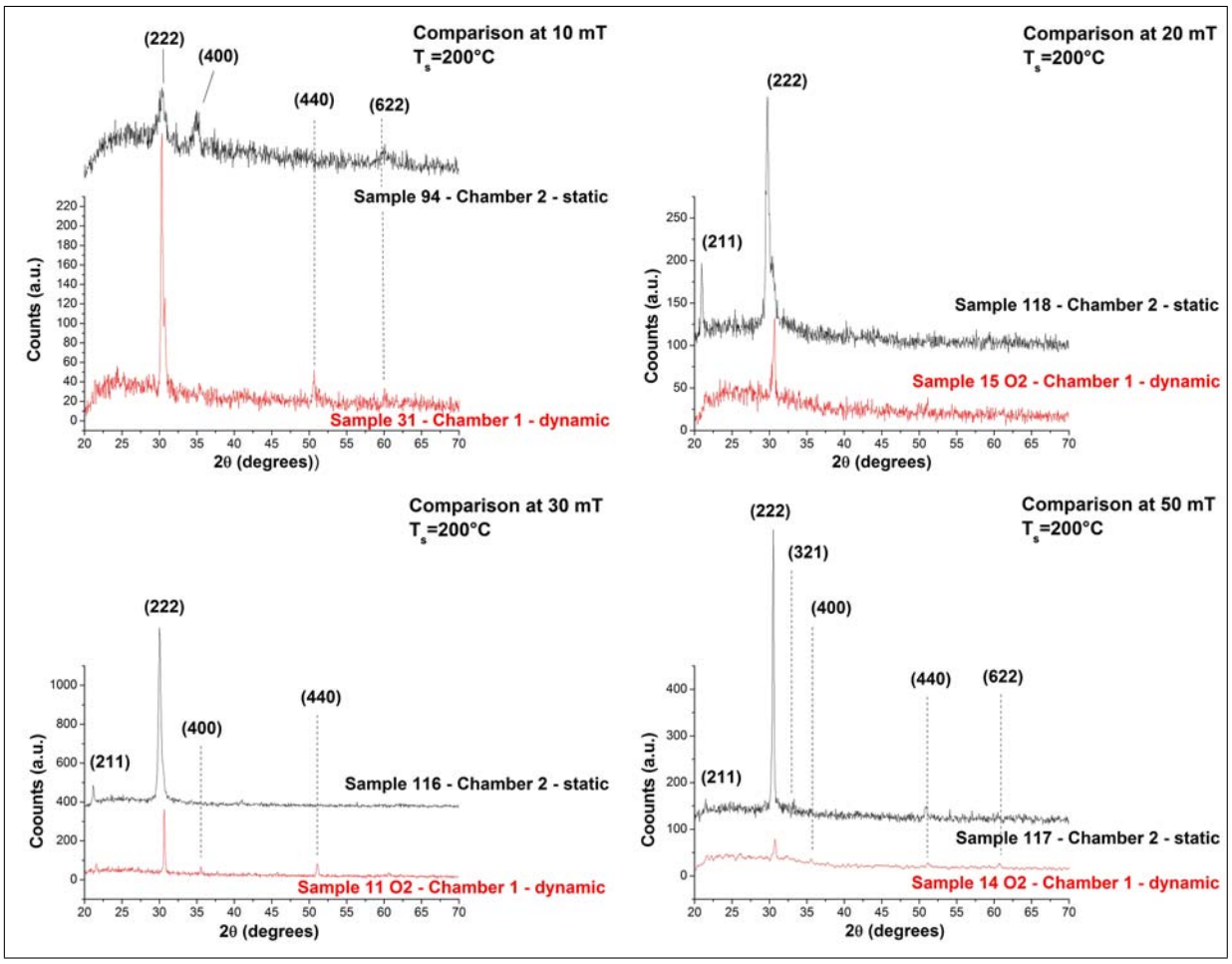

Figure 5.85 XRD pattern comparison for samples grown at T_s=200°C in chambers 1 and 2. Chamber 2 is operated under static atmosphere. P(O_2) was set to 10, 20 mT, 30 and 50 mT.

is not observed when operating under static atmosphere (albeit with a lower energy density used in chamber 1). This again shows that operating under static atmosphere in chamber 2 enables the operator to get closer to the orientation properties observed in chamber 1 and confirms the crucial role of gas dynamics in the resulting orientation of ITO thin films.

5.3.3.3 Optical properties

Transmittance in the UV/near-IR range is now compared for the two chambers. Fig. 5.86 shows how using a static atmosphere in chamber 2 affects the optical properties of the thin films.

As seen in section 5.2, when T_s was varied, films grown in chamber 1 showed a systematic shift of the absorption edge towards lower wavelengths when oxygen pressure was varied. Since the thickness of the films compared is similar, this shift can only be explained on the basis of free carrier concentration. Carrier concentration measurements presented

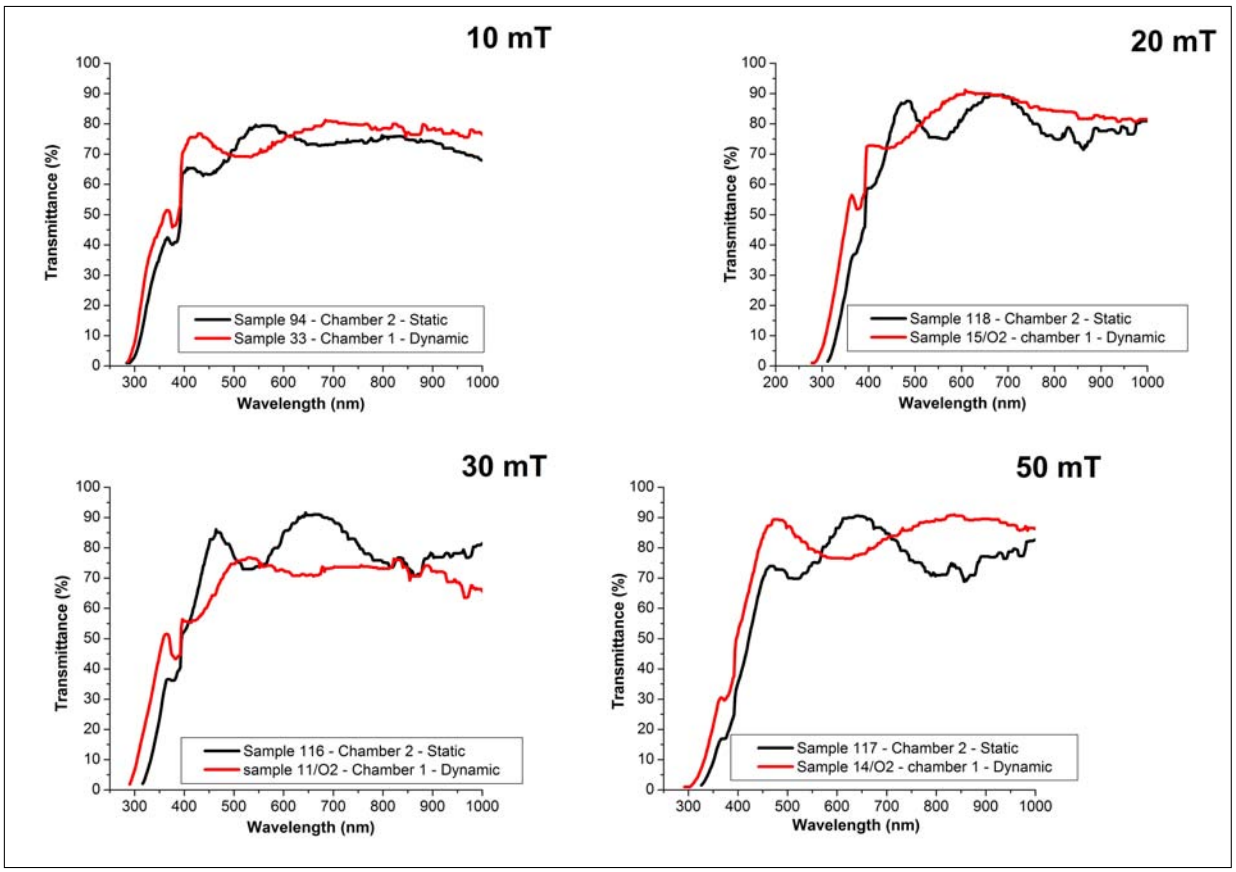

Figure 5.86 Optical properties comparison in the 250 - 1000 nm range of films grown in chamber 1 and 2 when chamber 2 is operated under a static atmosphere. The oxygen pressure was set to 10, 20, 30 and 50 mT. The substrate temperature was kept constant at T_s=200°C.

above (Fig. 5.84) show that films grown at $P(O_2)$=30 and 50 mT in chamber 1 indeed contain more free carriers than the corresponding films grown in chamber 2 under a static atmosphere, which is self-consistent with the Hall effect measurements (Fig. 5.84). At 20 mT, the values are similar, though, and the shift remains, even at 10 mT where the trend in carrier concentration is reversed. Therefore, it is still unclear if the absorption edge shift observed between a dynamic and a static atmosphere is solely due to carrier concentration effects or if another parameter is at play.

5.3.3.4 Summary

Comparing films grown at different $P(O_2)$ in chamber 2 under a static atmosphere with those grown initially in chamber 1 under a dynamic atmosphere yielded mixed results. In terms of electrical properties, μ and N do not compare particulary well, but ρ does compare well up to $P(O_2)$=20 mT. Similar observations were made in section 5.2.3 when T_s was varied. The very good agreement below $P(O_2)$=20 mT is due to the opposite behaviour of N and μ. Above that pressure, μ and N are constantly higher in chamber 1 than in chamber 2 hence the diverging behaviour. Both chambers showed a (222)

texture except at $P(O_2)=10$ mT in chamber 2 (in a static atmosphere) where the film tended to become more polycrystalline. Overall though, the structural agreement is satisfying.

Finally, optical properties were compared. A systematic absorption edge shift towards lower wavelengths is noticed between chamber 1 and 2, an observation that could not be solely attributed to the previously discussed Burstein-Moss effect (difference in carrier density N). Instabilities in the deposition system in chamber 1, resulting in different film properties at these pressures, might explain this behaviour. Once again, the fact that using a static atmosphere in chamber 2 makes it possible to grow ITO thin films with similar physical properties to those initially grown in chamber 1 shows the very strong impact of the oxygen flow and the resulting gas dynamics in a PLD chamber during growth; results can be influenced not only by varying T_s (section 5.2.3) but also $P(O_2)$. Therefore, the conclusion drawn in section 5.2.3.4 is also valid here: the O_2 gas in chamber 1 has a tendency to accumulate more around the growing film than in chamber 2 due to the different pumping configurations.

Chapter 6

Conclusions and future work

6.1 Summary

This study focused on pulsed laser deposited ITO thin films. On one hand, this project intended to study the relationship between microstructure and PLD growth parameters while on the other hand, it aimed to gain a greater understanding of the dependence between microstructure and physical properties. Such knowledge enabled the growth of high quality thin films which were integrated in solar cell devices.

Indium Tin oxide (ITO) thin films were deposited on borosilicate glass susbtrates by Pulse Laser Deposition (PLD). Two different chambers (chambers 1 and 2) were used during the course of the project with the deposition parameters of chamber 2 being chosen so that the film resistivity and transparency obtained matched the best obtained from chamber 1. The influence of three different deposition parameters were studied: the film thickness (t), the substrate temperature (T_s) and the oxygen pressure ($P(O_2)$). The microstructure was characterised using XRD, AFM, SEM and TEM. The electrical properties of the films (mobility, carrier density and resistivity) were characterised by four point probe and Hall effect measurements while the optical properties (transmittance, complex refractive index and dielectric data) were investigated using spectrophotometry, ellipsometry and EELS. The optimum film was defined in terms of low resistivity combined with high transparency. An attempt was made to reconcile results from chambers 1 and 2 in terms of electro-optical properties by varying T_s and $P(O_2)$ independently. For that purpose, exactly the same growth parameters used in chamber 1 were transfered to chamber 2 and depositions were made under a static oxygen atmosphere. Films obtained under these conditions in chamber 2 were comparable with those obtained in the initial chamber 1 in terms of their electro-optical properties.

Spectrophotometry, ellipsometry and EELS measurements were compared. A sample deposited at room temperature in chamber 2 was used as it contained a crystalline

phase embedded in an amorphous phase. Cauchy and Lorentz models were used to extract macroscopic dielectric data from ellipsometric measurements while a Kramers-Kronig procedure was used to extract nanaoscale dielectric data from low-loss EELS measurements. Two different microscopes operating in different modes were used to acquire low-loss EELS spectra within an amorphous and a crystalline phase to study possible electronic and optical differences.

The optimum film deposited on glass from chamber 2 was chosen to study the feasibility of using ITO thin films as a front and back transparent electrodes integrated in Dye Sensitized Solar Cells devices. A 1 μm thick porous layer, indispensible for the operation of such cells, was deposited on top of the optimum film using the same target and chamber. Two such devices were made and characterised in terms of their electrical current output; in addition, the optical transparency of the whole device was studied.

6.2 Conclusions

Three different growth parameters, i.e. the thickness, the substrate temperature and the oxygen pressure were varied independently in two different PLD chambers, although the thickness was only varied in chamber 2. The effects of each parameter on the structural and physical properties of the ITO films were studied and explained to enable the optimisation of physical properties.

6.2.1 Thickness

Film thickness was studied in chamber 2, where it was shown that a minimum critical thickness ($\sim$100 nm) was required to obtain combined low resisitivity and high transparency thin films. Identical behaviour was demonstrated in chamber 1 in previous work. The best trade-off was found at t$\sim$300 nm (5000 pulses) and thicknesses similar to this value were achieved in this study when T_s and $P(O_2)$ were subsequently varied. Below this critical thickness, the film appeared to be increasingly discontinuous, impacting on the mobility and carrier concentration and resulting in amorphous high resistivity thin films. Transparency over the visible range was adversely affected by crystallinty at very low thicknesses while the thickness values themselves affected it above about 1000 nm.

6.2.2 Substrate temperature

1) Initially, films were deposited in chamber 1. The lowest resistivity ($\sim 2.5\times10^{-4}\Omega$ cm) and highest transparency ($\sim$85%) were obtained for films deposited at T_s=200°C and $P(O_2)$=1 - 10 mT. In chamber 2, excellent electrical properties ($\sim 2\times10^{-4}\Omega$ cm) were already found in the low temperature range (RT - 200°C) as compared with chamber 1, although, optical properties were slightly degraded (75 - 80%). Therefore, the optimal [low resistivity]/[high transparency] ratio was found at T_s=200°C and $P(O_2)$=1 - 5 mT. These optimal growth conditions were relatively close to those found in chamber 1.

2) The discrepancies in electro-optical properties between the two chambers in the low-temperature range (RT - 200°C) were explained in terms of microstructural differences. In chamber 2, films were almost fully crystalline at RT. They achieved full crystallinity at T_s=100°C, well below the crystallisation temperature of ITO (~ 150°C) and showed a grainy morphology and a strong (400) preferred orientation. At RT, large (several hundred nanometre diameter) round shaped crystallites were observed, which took the form of "flowers" showing small grains in their centres from which large "petals" grew at the expense of the amorphous surrounding matrix.

3) On the contrary, films in chamber 1 in this temperature range, were found to crystallise in a more gradual way. At RT, films were nearly amorphous, while at T_s=100°C, round shaped crystallites were found scattered randomly within the amorphous matrix. The surface density of crystallites kept on increasing until at T_s=150°C, a very weak (222) XRD peak was observed. This became increasingly intense accompanying full crystallisation of the matrix, which was observed at T_s=200°C. This very different microstructural behaviour was explained on the basis of slightly different growth parameters and set-ups between chambers 1 and 2. In chamber 2, a higher energy density (10 J/cm^2 instead of 7.5 J/cm^2), a lower oxygen pressure (5 mT instead of 10 mT) combined with different gas dynamics as compared with chamber 1 (resulting from different pumping configurations), resulted in a higher surface mobility, making the film effectively crystalline at lower T_s. The surface morphology was impacted as well: smaller grains were obtained in chamber 2 owing to a higher nucleus/cluster density of the plasma. The grain size was not a strong function of T_s in either chamber.

4) As a result, electro-optical properties were found to be more heavily impacted in chamber 1 than in chamber 2. The gradual crystallisation of films in chamber 1 with increasing T_s from RT to 200°C led to a quasi-linear increase of carrier concentration

and linear increase mobility, resulting in a linear decrease of the resistivity over this temperature range. The mobility and the resistivity were found to be thermally activated because of the trap and grain boundary limited conduction mechanisms taking place within this temperature interval. Above 200°C, the conduction mechanism was found to become degenerate, (i.e. approximating to that of a semi-metal) while the mobility and the resistivity were very weak functions of T_s. The carrier concentration increased with the crystallisation, as explained by tin activation and gradual ordering of the matrix such that oxygen atoms and their associated vacancies formed an extensive array, effectively releasing free carriers to the matrix. Higher T_s resulted in slight thin film oxidation in chamber 1 although such an effect was not evident in chamber 2. No temperature-activated behaviour was observed in chamber 2 either. A higher carrier concentration and a fully crystallised matrix at low T_s resulted in degenerate conduction where the mobility and resistivity were found to be almost constant between RT and 400°C.

5) In neither chambers was grain size found to have a strong impact on electrical properties: ionised impurity scattering due to oxygen vacancies was dominant, except between RT and 150°C in chamber 1, where trap-limited conduction in the amorphous matrix was suggested to take place based on the observed temperature activated mobility.

6) The optical properties obtained in both chambers were similar, even though slightly more transparent films over the visible range were obtained in chamber 1 due to their higher oxygen content. This could also be due to less surface damage occurring in chamber 1 owing to a higher oxygen pressure and lower energy density used during deposition. The absorption edge position was found to obey the Burstein-Moss shift law (resulting in band gap widening) in chamber 1 as T_s varied, but not in chamber 2. This was accounted for competing band-gap narrowing from electron-electon and electro-impurity scattering. The refractive index n was shown to be connected with the carrier concentration N.

7) The preferred growth orientation was influenced by T_s in chamber 2 due to adatomic mobilities varying with T_s and the necessary minimisation of both surface and interface film/substrate free energies. The effect was not observed in chamber 1 due to the amorphous nature of the films in the low temperature range. Moreover, it was found that the stronger the texture, the higher the mobility, suggesting a positive relation between crystallinity and mobility.

6.2.3 Oxygen pressure

1) The oxygen pressure was also found to have a dramatic impact on the electro-optical properties of ITO thin films, which is not unexpected as the crystal structure of ITO accommodates oxygen vacancies facilitating the adsorption/absorption and desorption of oxygen. Low oxygen pressure (below 1 mT) was found to have a large effect on the crystal structure. An extensive pore network combined with surface particulates were observed, reducing resistivity and optical transparency via light scattering in the visible range (only 36% in chamber 2 at $P(O_2)$=0.2 mT).

Electron scattering at discontinuities dominated the electrical properties at low $P(O_2)$ in both chambers. At intermediate $P(O_2)$, ionised impurity scattering was found to be predominant. The ionised impurity scattering mechanism was no longer predominant at high $P(O_2)$ in either chamber as the oxygen vacancies gradually vanished. It was suggested that neutral impurity scattering due to the accumulation of excess oxygen at grain boundaries and interstices, became dominant resulting in neutral complex formations. However, no direct observation of such complexes were made in this work.

As $P(O_2)$ increased, the carrier concentration decreased due to the filling of oxygen vacancies (possibly combined with intermediate compound formation) while the mobility increased, although to a lesser extent. This was connected with the gradual removal of defects such as oxygen vacancies resulting in a decrease in the overall resistivity before reaching a plateau in chamber 2 at 30 mT. More experimental points are needed in chamber 1 to confirm such a trend.

2) The average grain size was found to increase with $P(O_2)$ in chamber 1 up to a certain threshold (20 mT) but was not observed to impact strongly on electrical conduction. The grain size did not vary to a great extent in chamber 2 except at very high $P(O_2)$ ($>$70 mT). The surface composition did not change dramatically in either chamber with $P(O_2)$ although the bulk composition was found to vary slightly with $P(O_2)$, with a moderate oxygen intake in both chambers observed using SEM EDX.

3) The optical transparency improved with increasing $P(O_2)$ over the visible range in both chambers due to improved crystallinity and restored stoichiometry from the bulk state. The absorption edge position was found to obey reasonably well the Burstein-Moss shift law in both chambers when $P(O_2)$ was varied, so that its position depended mainly on the carrier concentration N. The refractive index n was also shown to be related to

N. Both chambers showed similar electron reduced effective masses suggesting that the band structures of the films grown in chambers 1 and 2 were not too different. This might be especially so at high P(O_2) where the films tend to bulk behaviour.

4) The growth orientation was affected by P(O_2) in chamber 2. In this chamber, between 5 and 30 mT, an ever stronger asymmetry developed on the left hand side of the ITO (222) preferred orientation peak. This was due to a phase development (SnO/SnO_2/Sn_3O_4) which totally disappeared at higher P(O_2) (>30 mT). Moreover, it was shown that the stronger the texture, the higher the mobility, an effect related to crystallinity enhancement with increasing P(O_2). This was confirmed with the negative linear proportionality between the FWHM of the preferred oriented peak and μ and is in line with results gathered in both chambers at different T_s values: there is a link between the crystallinity and the mobility.

5) The best films, defined in terms of the highest average transparency over the visible range/resistivity ratio, were grown at T_s=200°C and P(O_2)=1 - 10 mT in chamber 1. In chamber 2, T_s and P(O_2) were found to lie in the 200°C - 400°C and 1 - 5 mT ranges.

6) An attempt was made to reconcile the electro-optical properties of both chambers when T_s and P(O_2) were varied independently. Similar resistivities were achieved when a static oxygen atmosphere was used in chamber 2 while keeping exactly the same growth parameters as for chamber 1. This stressed the very strong impact of different O_2 gas dynamics on thin film physical properties. The different gas dynamics were accounted for by the different pumping configurations between chambers 1 and 2. Similar resistivities were achieved because of the opposing behaviour of the mobility and carrier concentration under static and dynamic atmospheres. Similar optical properties were also achieved in terms of transparency over the visible range. However, the positions of the absorption edge varied slightly owing to the different carrier concentration achieved under static (chamber 2) and dynamic (chamber 1) atmospheres. This behaviour was accounted for by the Burstein-Moss shift effect, as already shown in the case of the oxygen pressure variation.

6.2.4 Achievements

This work demonstrated that it is possible to grow high quality thin films using the PLD technique. The laser energy density and the distance target substrate must first be determined, then, careful optimisation of the thickness, the substrate temperature and

the oxygen pressure is required. At that stage, the laser energy density and the distance target substrate can be refined. The gas dynamics in the deposition chamber play a very important role in the resulting electro-optical properties of the thin films.

Films with texture show slightly enhanced electro-optical properties, provided a certain critical thickness is reached. However, the grain size is not a critical parameter as long as it is not lower than 10/20 nanometres. The PLD growth parameters used in this work enabled the deposition of fully crystalline ITO thin films at substrate temperature as low as 100°C although higher temperatures (up to 200°C) are needed to achieve the best compromise between high conductivity and transparency. High temperature (> 400°C) must be avoided to prevent oxidation. The optimal oxygen pressure to achieve such a compromise lies in a narrow range.

Optical properties were measured on a conventional macroscale (ellipsometry, spectrophotometry) as well as at the nanoscale with STEM EELS (see appendix A). While these nanoscale measurements only constituted a prelimenary study, the results indicate the potential to derive optical properties of individual grain boundaries, amorphous/crystalline phases as well as nanowires as used in third generation solar technology such as Dye Sensitized Solar Cells (DSSCs).

This type of solar cell was made and despite the very low intensity generated current, an encouraging potential difference was detected (see appendix B). These solar cells were made using only one target: only the growth parameters were changed (live) to deposit the thin film electrode and the high aspect-surface ratio porous ITO layer on top of it. While more work needs to be done, the initial success of this process could be a first step towards an industrialisation of PLD deposited DSSCs.

6.3 Further work

The use of two different chambers in the project may have added some confusion in terms of electro-optical properties and microstructural comparisons and a complete understanding of the different gas dynamics in play in chambers 1 and 2 remains to be achieved. Additional oxygen gauges could be installed in both chambers to study in more detail oxygen gas flow within the whole chamber and particularly around the growing thin films. Gas scattering onto the walls and possible time/pressure dependent instabilities should be studied. The interaction of the oxygen gas flow with the plume

would also be interesting to study and understand in more detail. Computational Fluid Dynamics (CFD) modelling of oxygen gas flow might be particularly useful to account for such phenomena. It is suggested that optimal oxygen flow rate inputs and pumping speeds must exist in chambers 1 and 2 under which optimal thin films could be grown although independent variation of these two parameters and their impacts on the thin film properties remain to be investigated.

Hall effect measurements at different temperatures (10 K - 300 K range) on the ITO films grown in chambers 1 and 2 should be performed to study accurately carrier transport mechanisms and their relative proportions to each other. More understanding needs to be gained from samples where two phases of different conductivity are mixed (amorphous and crystalline) and the effect on the actual mobility and carrier concentration measurements.

Oxygen absorption was evidenced by SEM EDX, particularly when P(O_2) was varied. It would be useful to know whether this phenomenon takes place at grain boundaries and/or in the grains themselves. Variable-Angle XPS (VAXPS) experiments to probe different film thicknesses or Secondary Ion Mass Spectrometry (SIMS) are needed to study in much more detail how the In, Sn and O compositions vary throughout the whole film thickness. Analysing pure In_2O_3 and SnO_2 nanopowders prior to XPS measurements is also suggested to facilitate much of the interpretation of the In, Sn and O peaks observed for ITO thin films.

More films need to be prepared for TEM observations in the low temperature range to study in more detail crystallisation. Similarly, TEM plan view and cross sectional films need to be prepared when P(O_2) is varied. This would be particularly useful for studying any phase segregation at grain boundaries and the specific behaviour of films grown in chamber 2 at P(O_2)=30 mT where an XRD asymmetry was observed. It is possible that the second phase might be identifiable using TEM techniques.

A comparison of our pulsed laser deposited ITO thin films with other thin film materials such as doped-zinc oxide thin films needs to be made since Indium and Tin are becoming increasingly scarce and difficult to mine and hence more costly.

Appendix A

Ellipsometry and EELS: complex refractive index and dielectric function

A.1 Method

The optical data obtained by spectrophotometry and ellipsometry are compared with low-loss EELS measurements to evaluate the possible differences between nanoscale amd macroscale optical properties. Special emphasis is put on a sample grown at RT in chamber 2 since EELS measurements were performed on this sample both in the SuperSTEM at Daresbury Laboratory and in Birmingham.

A.2 Ellipsometric data

Measuring the dielectric properties of ITO thin films by ellipsometry is extremely challenging as ITO often has a graded microstructure and optical properties [217]. It was previously seen by glancing angle XRD (see Fig. 5.19) that a sample deposited at T_s=200°C and P(O_2)=5 mT evolved towards a more textured film as it grew thicker, which can introduce a thickness dependence of the optical constants such as the refractive index. Although, the Cauchy and the Lorentz models, presented back in section 4.7.2, assume structural homogeneity of the samples analysed, the thickness measurements derived using the Cauchy model (presented earlier in Tables 5.3 and 5.4 at the beginning of section 5.2.1) appeared to be in agreement with the measured thickness values. These thicknesses determined via the model were used as a "benchmark" or a measure of confidence in the dielectric data thus extracted.

Fig. A.1 shows how ε_1 and ε_2 vary with T_s in chambers 1 and 2.

For films from chamber 1, ε_1 and ε_2 are peaking between 3 and 4 eV. Such peaking behaviour can be seen as a resonance phenomenon within this energy range. A resonance of ε_2 is consistent with interband transitions (accross the band gap), i.e., the creation of excitons (electron-hole pairs). Surprisingly, for chamber 2 films, no such resonance

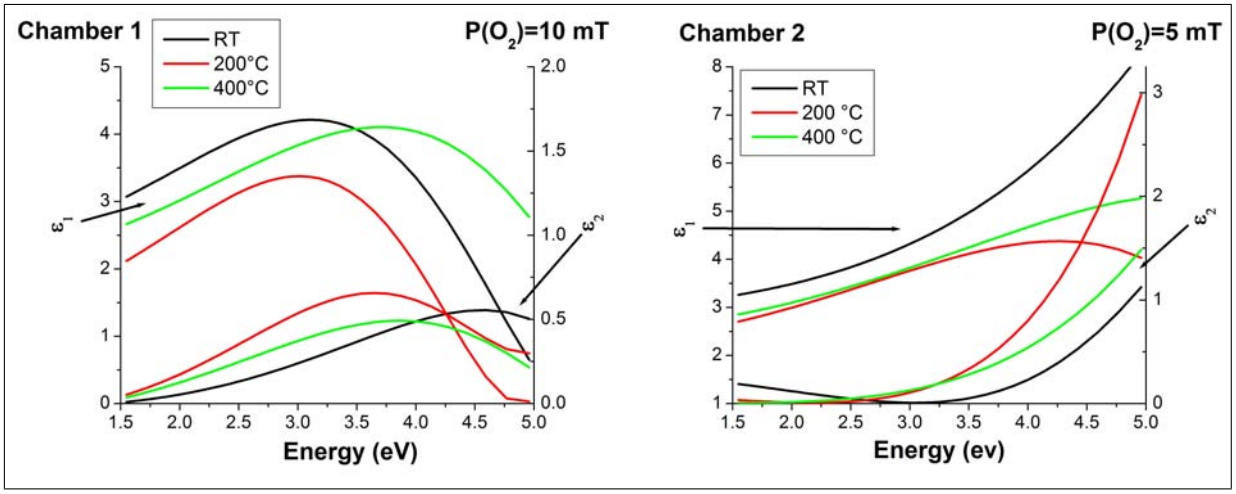

Figure A.1 The real (ε_1) and the imaginary (ε_2) parts of the dielectric function derived from ellipsometric results for ITO films grown at RT, 200 and 400°C in chambers 1 (left) and 2 (right). T_s was varied from RT to 400°C and $P(O_2)$ was kept constant at 10 and 5 mT in chambers 1 and 2 respectively. The Cauchy model was used for describing the complex refractive index of ITO.

could be seen in the band gap region. As a consequence, the ellipsometric Cauchy model was changed to a Lorentz model (presented back in section 4.7.2.2) since the latter gives a better account of free carrier absorption and interband transitions. This model splits the dielectric function into several contributions: free carriers (ε_{FC}), valence electrons (ε_{VE}) and other polarisation effects at low (ε_s) and high frequency (ε_∞). Each of these contributions is described by a Lorentz oscillator. The experimentally measured thickness was fed into the model and results on a RT deposited sample in chamber 2 are illustrated in Fig. A.2. This sample is used for the rest of this study for the reason stated in section A.1.

When using the Lorentz model, a clear resonance of ε_2 is identified in the direct band gap region at 3.8 eV which is in agreement with interband transitions as mentioned above. Another one around 2.5 eV might reveal the existence of an indirect band gap. Therefore, the Lorentz model outputs are considered to be more “consistent” than those for the Cauchy model ones for RT deposited films in chamber 2. The dielectric functions obtained at RT with both models will be used as a reference for the EELS measurements (with more emphasis on the Lorentz model) presented in the following two sections.

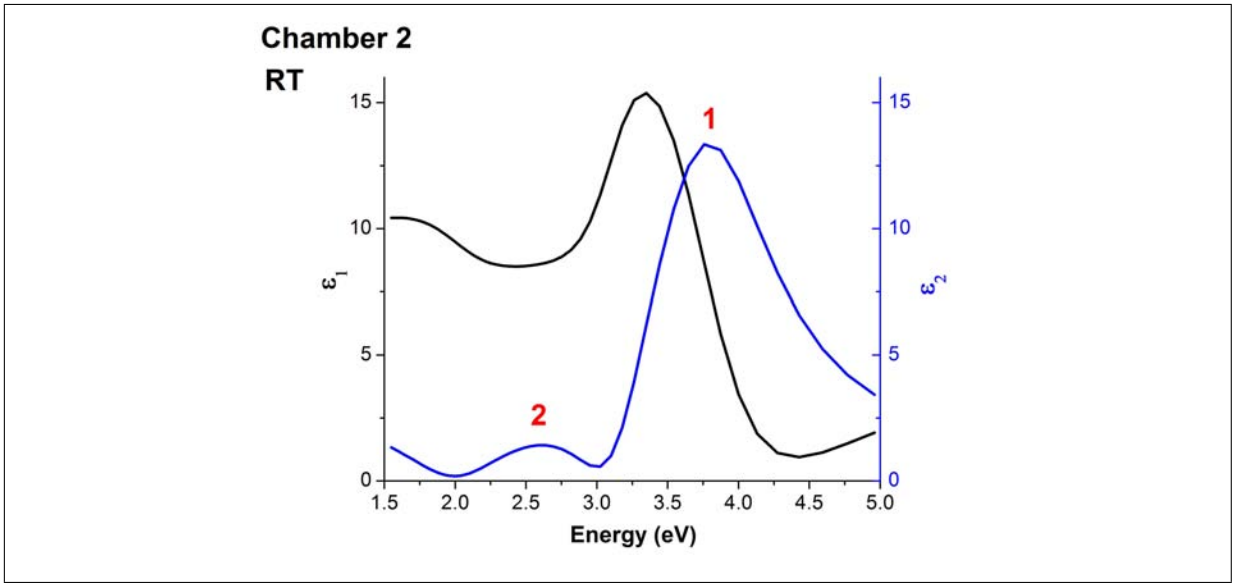

Figure A.2 The real (ε_1) and the imaginary (ε_2) parts of the dielectric function derived from ellipsometric results for ITO films grown at RT in chamber 2 using the Lorentz model. The two Lorentz oscillators (named 1 and 2) describing interband transitions are also shown in the ε_2 curve.

A.3 Low loss EELS data processing of spectra acquired on the SuperSTEM (Daresbury laboratory)

At very low losses (typically 0 - 5 eV), current deconvolution procedures for multiple inelastic scattering are not sufficiently accurate [218] (see section 3.3.2.5 on deconvolution procedures). Indeed, any differences between the experimental zero-loss peak (ZLP) and the modelled one can create large, random data spikes in the deconvoluted spectrum in the low-loss regime. These errors propagate during the data processing and in particular during Kramers-Kronig analysis to extract ε_1 and ε_2. As a consequence, only a background subtraction to remove the effect of the ZLP tail was performed meaning that the dielectric information is extracted from spectra in as raw a state as possible to reveal the true physical reality of the volume sampled. Sample stability can be an issue when acquiring position-resolved EELS linescans. In most cases, specimen drift originates from thermal difference between the stage and the holder itself: this type of drift is mostly linear and therefore straightforward to model and correct for post acquistions. Given time, it should disappear when the sample-stage assembly reaches thermal stability, although in the present case, even after baking, residual drift was still found. Linescans (series of spectra acquired serially along a given line) were performed within a crystalline or an amorphous area to avoid contamination build up around the electron beam. Care was taken to acquire spectra from a line parallel to the interface to prevent any significant thickness change during the scan. For crystallites, shorter

linescans (a few tens of nanometres) were used because of crystallite size constraints (more experimental details are given in section 4.3.2.3.2). Fig. A.3 shows HAADF micrographs illustrating where those line scans were taken.

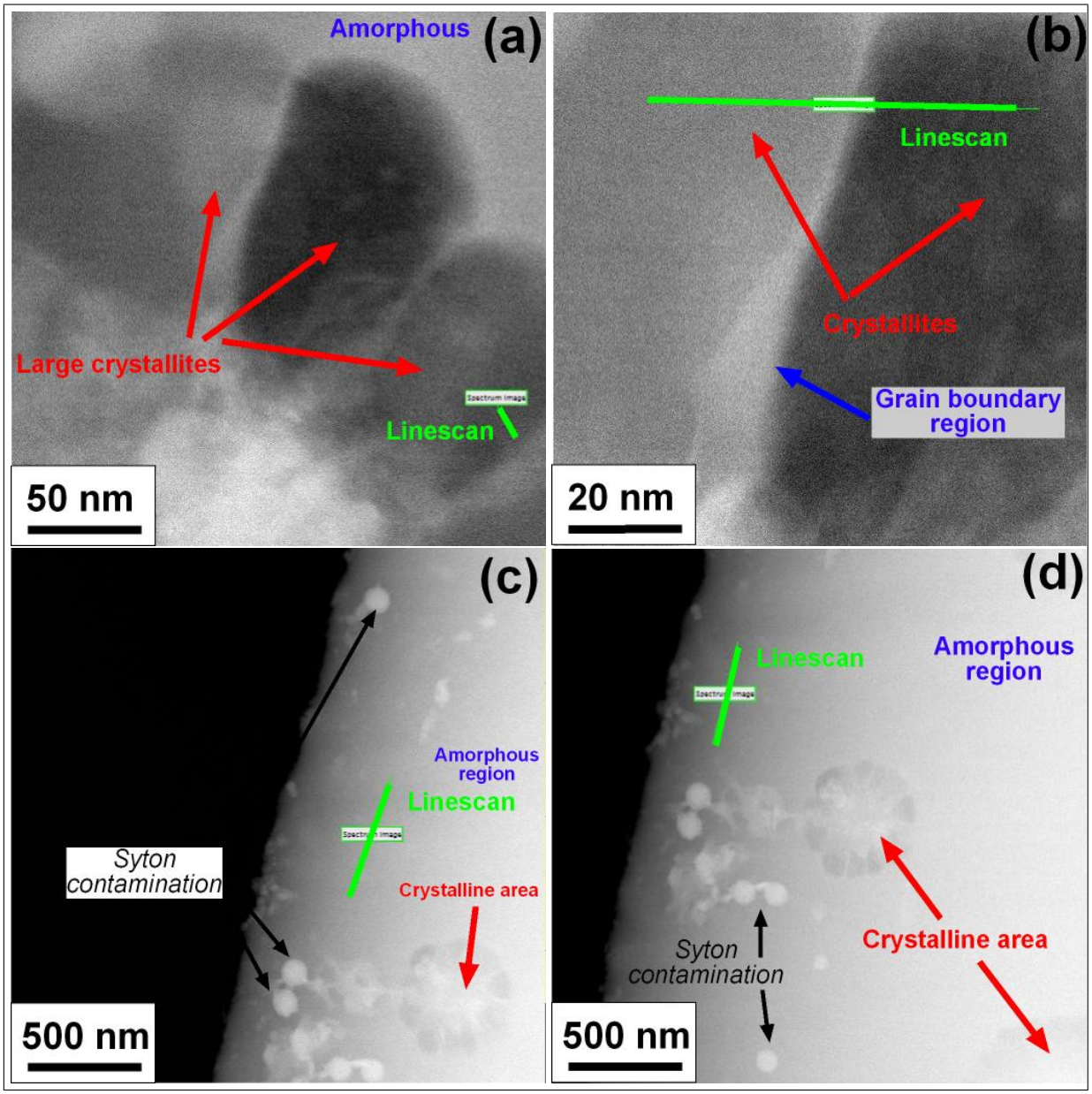

Figure A.3 HAADF micrographs showing where the line scans were taken from four different regions. Regions 1 (a) and 2 (b) are crystalline while regions 3 (c) and 4 (d) are amorphous. Line scan lengths vary from 70 to 500 nm. The acquisition time was set at 70 ms per spectrum. 100 to 500 spectra were accumulated and summed up to reduce noise and instabilities.

The most crucial and difficult step was the background subtraction as demonstrated below with "region 1". Depending on the characteristics of the electron source, the tails of the ZLP might spread up to 10 eV or more away from the nominal energy of the incident electrons, thus interfering with the bulk dielectric properties. Apart from finding the tail of the ZLP, the instrumental and the diffuse scattering background, on which the whole

spectrum sits, must also be determined. Inexact background extraction yields false results in any subsequent analysis. Furthermore, simple removal of the ZLP via deconvolution or subtraction of a theoretical, experimentally fitted or separately measured ZLP cannot achieve a fair comparison of spectra from differently diffracting regions due, again, to the lack of precision of the deconvolution procedures. Therefore, the single scattering distribution (SSD) was obtained by consistently subtracting the original spectrum with a power-law fitting of the tail performed using the Digital Micrograph software.

The next issue to address is how large should the fitting window be and over which energy range? The low-energy tail of the ZLP was fitted right in front of the first actual intensity onset using a power-law function, extrapolated to higher energies and subtracted from the experimental data. The very first signal after the ZLP was evaluated using the Origin 6.1 software in which the first derivative of the initial raw signal in the 2 - 10 eV range (see signal 1 Fig. A.4) was computed. Nonetheless, a 21-point Savitzky-Golay filter was used on the raw spectra prior to compute the first derivative so as not to add noise to the latter signal and make the best decision for the fitting window choice. The Savitzky-Golay algorithm [169] produces datasets with reduced noise, but attempt to preserve the height and width of peaks. It performs a least squares fit of a small set of consecutive data points (21 points in our case) to a polynomial and take the calculated central point of the fitted polynomial curve as the new smoothed data point. The main absorption features in the spectra were hardly affected by this filtering as can be seen from Fig. A.4, while residual noise is effectively removed. It is also observed that in the energy range between 5 and 9 eV, two weak features noted as “signal 2” and “signal 3” in Fig. A.4 are also present and these are attributed to single electron transitions from the valence band to the conduction bands (interband transitions). “Signal 1” could be the result of an indirect band gap. The spectrum presented here corresponds to “region 1”, which is a crystalline area.

The first feature was identified as the first significant crossing of zero counts of the first derivative. The energy to which this first crossing corresponds was taken as the upper limit of the fitting window. The lower limit was chosen to adjust finely the power law in order that the ZLP tail is correctly fitted.

Based on the first-derivative signal, the very beginning of the energy-gap signal is at 3.31 eV (in general agreement with the literature). A very weak signal is also visible around 2.80 eV with an onset at 2.65 eV which could result from an indirect band gap. However, this is also the region where retardation effects are abserved. As suggested

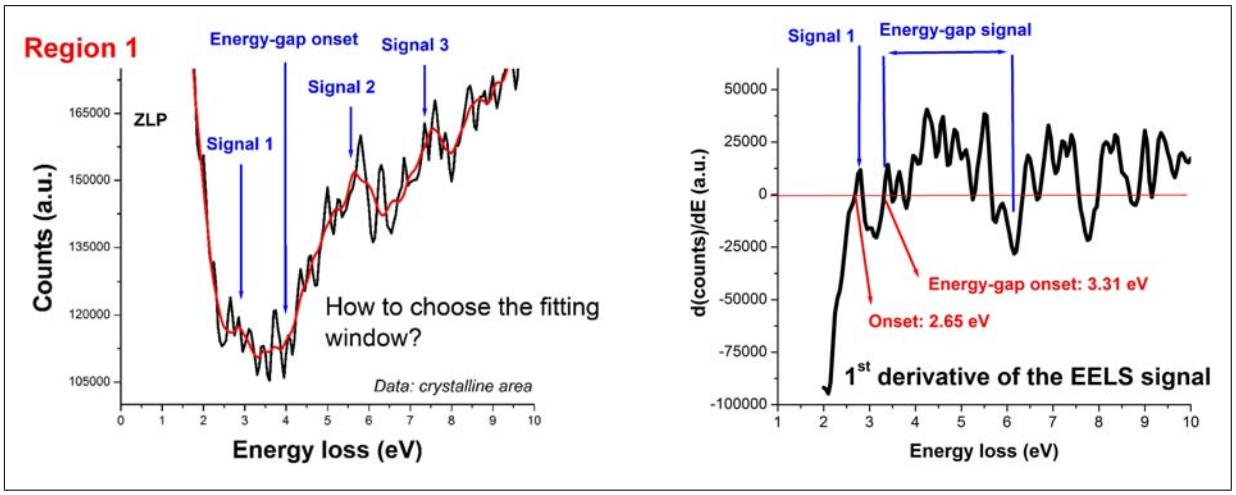

Figure A.4 Illustration of how to choose the fitting window for a spectrum acquired in region 1 (crystalline area). Left: plot of the raw (black curve) and 21 point Savistky-Golay fitered (red curve) signals. Right: first derivative of the previously filtered EELS signal.

by Erni et al. [136], the impact such effects on the spectra was estimated by analysing the probability of the emission of Cerenkov radiation. The number of Cerenkov photons emitted by a unit charge per unit path length in respect to the maximal emission rate in a bulk material is given by:

$$P_{Cerenkov} = 1 - \frac{c^2}{v^2 \varepsilon_1} \tag{A.1}$$

where c is the speed of light, v is the speed of the electrons and ε_1 is the real part of the dielectric function. Erni et al. [136] suggest that when $P_{Cerenkov}$ falls between 0 and 0.8, negligible or very weak retardation effects are expected provided the foil is thinner than 100 nm. ε_1 is taken to be 9 [72]. At 80 kV, v=1.42$\times 10^8$m/s giving $P_{Cerenkov}$=0.50. As a consequence, retardation effects are not expected to be a major cause of measurement artefacts, a factor that was essentially confirmed experimentally even if a weak signal noted as “signal 1” in Fig. A.4 in the 2 - 3 eV region was observed. This is attributed to weak Cerenkov radiation owing to a relative thickness close to 1 inelastic mean free path (IMFP) but the existence of an indirect band gap cannot be ruled out either. Such a feature was not observed on other spectra from other regions.

A small fitting energy window 0.20 eV wide extending from 2.45 to 2.65 eV (in front of the very first significant feature observed in the spectrum) was found to be adequate since:

- the fitted power low function must fit correctly the ZLP tail.
- negligible negative counts must be present within the extracted spectrum.

- Cerenkov losses can be modelled (“bump” around 2 - 3 eV).
- the energy band gap signal must be situated in the 3.5 - 4 eV region, as was found with previous experiments with the SuperSTEM, the spectrophotometer and in the literature.

This window and its width vary slightly from one spectrum to another since different parts of the sample yield different types of noise and energy-gap onset. As a consequence, the fitting window chosen will be specified each time. The ZLP removal procedure (left) and a resulting extracted signal (right) under Digital Micrograph are illustrated in Fig. A.5.

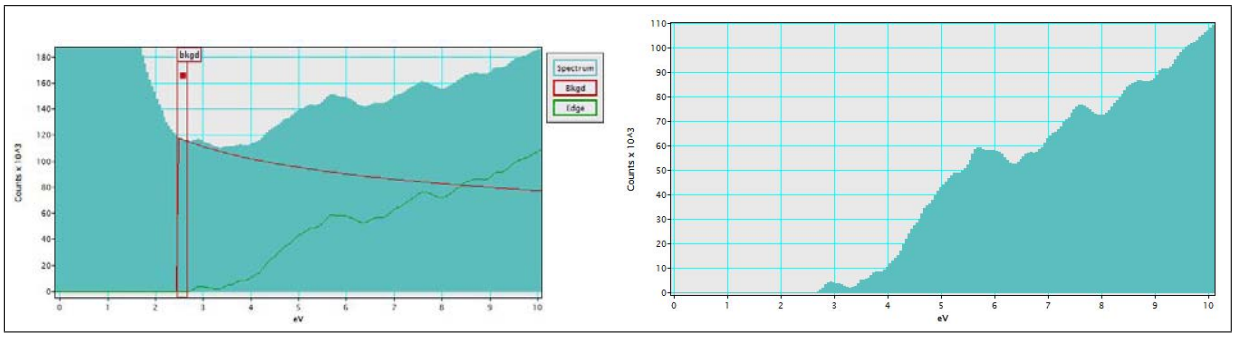

Figure A.5 Illustration of ZLP loss peak removal from a spectrum acquired from a crystalline area. Left: a power law is fitted over the 2.45 - 2.65 eV range to model the background (red curve) arising from instrumental noise and ZLP in the low loss range (here 0 - 10 eV). Right: the background thus extrapolated is subtracted from the original unprocessed spectrum to yield an SSD. The latter is shown over the 0 - 10 eV range.

Residual noise in experimental data can lead to large artefacts in subsequent Kramers-Kronig analysis, leading to large errors in the derivation of dielectric properties. Although the noise level obtained in this work at Daresbury could have been improved by simply choosing longer acquisition times, this could have also induced sample damage and recrystallisation of the amorphous matrix. In addition, since the focus was on recording low-loss spectra, the intense ZLP was systematically recorded meaning that the acquisitions are needed to be short so as not to burn the CCD camera. It is suggested that the best method would be to record a very large number of spectra and add them together in order to minimise instabilities and noise. While this was done in this study for some spectra, on other spectra, this would have had taken a few days so time constraints dictated that shorter acquisition times were chosen. In addition, since the Savitzky-Golay filter used earlier to compute the first derivative of the raw EELS signal was found to remove noise effectively, additional subsequent noise removal was not necessary. The resulting background subtracted signal was considered as a single scattering distribution (SSD) and used as input for the subsequent Kramers-Kronig analysis. While electrons

contributing to this signal may have undergone several elastic scattering events in addition to the energy loss they have sustained, we made sure to observe samples with thicknesses below one inelastic mean free path whenever possible. This ensures that the recorded signal is a good approximation to a single scattering distribution for the inelastic phenomena that we are interested in and the extracted spectra (such as that presented in Fig. A.5) will thereafter be referred to as SSDs.

Finally, Kramers-Kronig analysis (KKA) is applied to the SSD shown previously in Fig. A.5 (right), using a Fortran program, KRAKRO, written by Egerton [219] which employs the Fourier procedure for KKA. It also eliminates beam convergence, collection angle and the effect of thickness, but not possible surface losses. In this program, spectra are normalised using the method described by Egerton [137] which yields the energy loss function Im(-$\frac{1}{\varepsilon}$). Normalisation using the refractive index for visible light yields the absolute value of the dielectric function. The refractive index used was taken from ellipsometric measurements previously presented in Fig. 5.46 (right), i.e., n=2.1. This implies that n does not change significantly at the nanometre scale. The real and imaginary parts of the dielectric function could, therefore, finally be obtained. Inputs for the KRAKRO program are as follows: an SSD, the ZLP intensity, the beam energy (kV), the collection angle β (mrads) and the refractive index n. β was fixed at 6 mrads. All the results are saved in a file KRAKRO.dat and two spectra are created simultaneously: the real (ε_1) and imaginary (ε_2) parts of the dielectric function. The optical absorption α was also calculated separately according to:

$$\alpha(E) = (\frac{E}{\hbar c})[2(\varepsilon_1^2 + \varepsilon_2^2)^{1/2} - 2\varepsilon_1]^{1/2} \tag{A.2}$$

where E is the energy, ε_1 and ε_2 are the real and imaginary parts respectively of the dielectric function.

It was then converted into transmittance T (%) via the following equation:

$$T = 10^{-\alpha(E)} * 100 \tag{A.3}$$

to allow direct comparison with the spectra presented in section 5.2.2.1 Exactly the same data processing to yield dielectric data was applied to all EELS spectra presented in the next section.

A.4 Crystalline and amorphous areas

In order to study the different dielectric properties of the amorphous and crystalline phases, two line scans within amorphous (regions 1 and 2) and crystalline (regions 3 and 4) areas were acquired (Fig. A.3). Region 2 is a grain boundary (Fig. A.3 (b)). Although minute differences in the low loss spectra may arise at such grain boundaries, such detailed analysis was considered beyond the scope of this study (see future work). Therefore, the dataset was treated as one single crystalline region and the average of all the spectra taken on the linscan was considered as representative of of a crystalline area.

The corresponding raw EELS spectra and the first derivative of these signals are presented in Figs. A.6 - A.8 while efforts were made to be consistent regarding the width of the fitting window for the four different regions, this fitting window does vary slightly from one region to another. This work has already been performed on region 1 (Fig. A.4) and will not be repeated here.

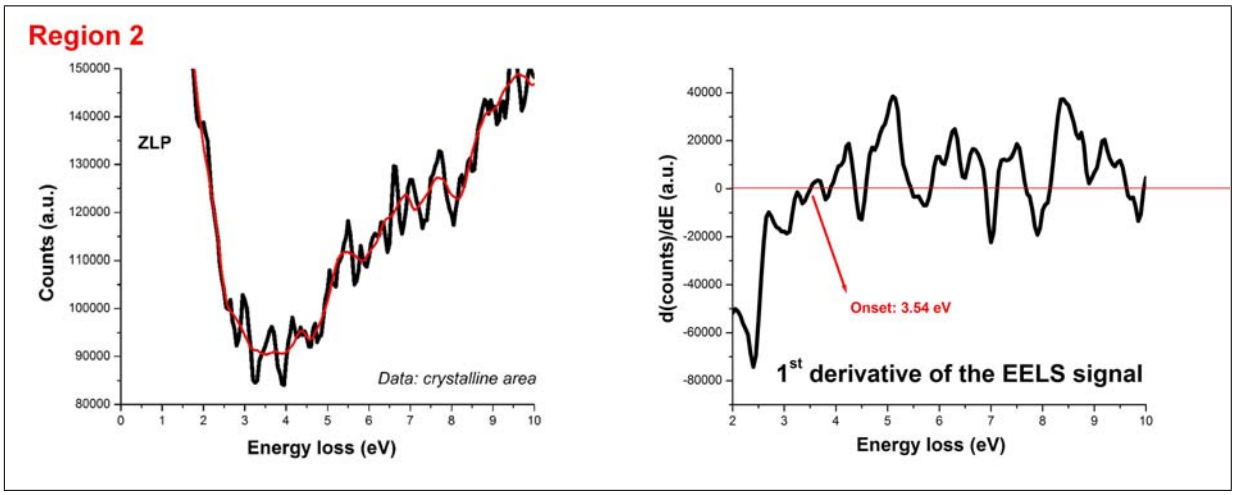

Figure A.6 Raw EELS signal corresponding to region 2 (crystalline) over the 0 - 10 eV range. A 21 point Savitsky-Golay filter of the raw EELS signal was applied and represented by the red curve (left). The first derivative of the filtered EELS signal over the 0 - 10 eV range was computed.

The fitting window for each region and its thickness (in terms of IMFP) are presented in Table A.1.

Finally, Kramers-Kronig analysis was performed on all the previous extracted SSD. Kramers-Kronig results are presented as dielectric data (ε_1, ε_2) and optical data (transmittance).

The real and imaginary parts of the dielectric function are shown in Fig. A.9 and compared with ellipsometric measurements.

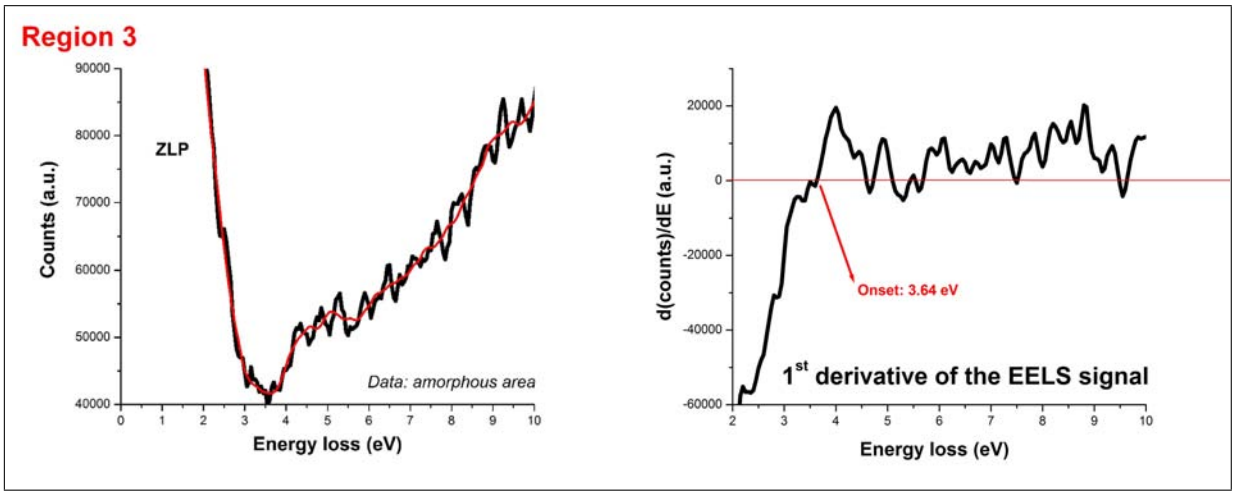

Figure A.7 Raw EELS signal corresponding to region 3 (amorphous) over the 0 - 10 eV range. A 21 point Savitsky-Golay filter of the raw EELS signal was applied and represented by the red curve (left). The first derivative of the filtered EELS signal over the 0 - 10 eV range was computed.

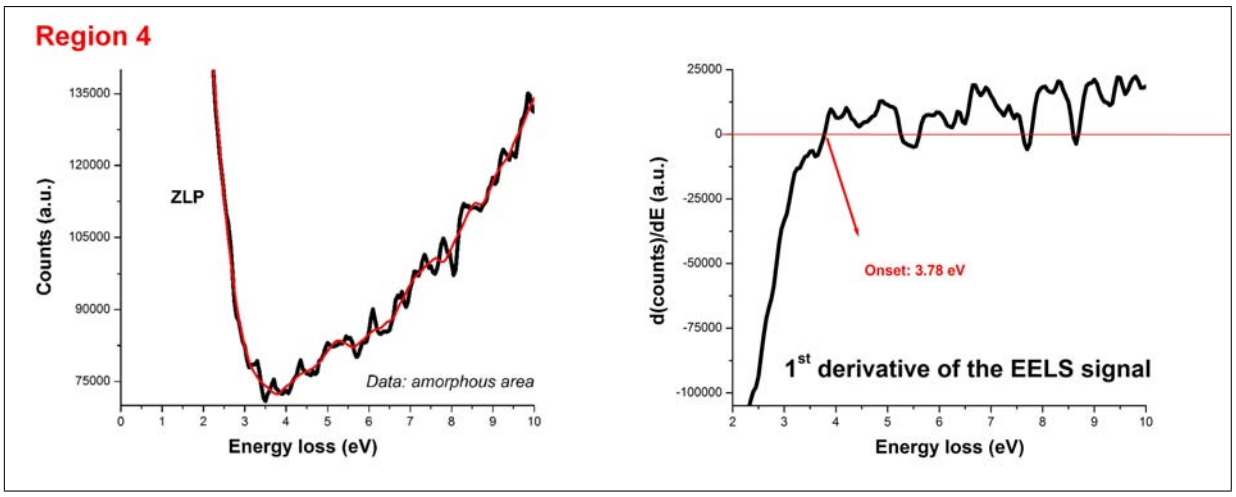

Figure A.8 Raw EELS signal corresponding to region 4 (amorphous) over the 0 - 10 eV range. A 21 point Savitsky-Golay filter of the raw EELS signal was applied and represented by the red curve (left). The first derivative of the filtered EELS signal over the 0 - 10 eV range was computed.

Table A.1 Summary of the chosen fitting windows from region 1 to 4. Relative and absolute thicknesses are specified. At 80 kV, IMFP is calculated to be 78 nm.

	Fitting window (eV)	Relative thickness (IMFP)	Absolute thickness (nm)
Region 1	2.45 - 2.65	1.49	116
Region 2	3.35 - 3.55	1.70	133
Region 3	3.54 - 3.65	0.76	59
Region 4	3.70 - 3.80	0.59	46

Finally, Fig. A.10 illustrates transmittance derived from EELS measurements from amorphous and crystalline areas and a comparison with measurements from the spectrophotometer.

Transmittance spectra obtained by KKA showed very good agreement with those obtained

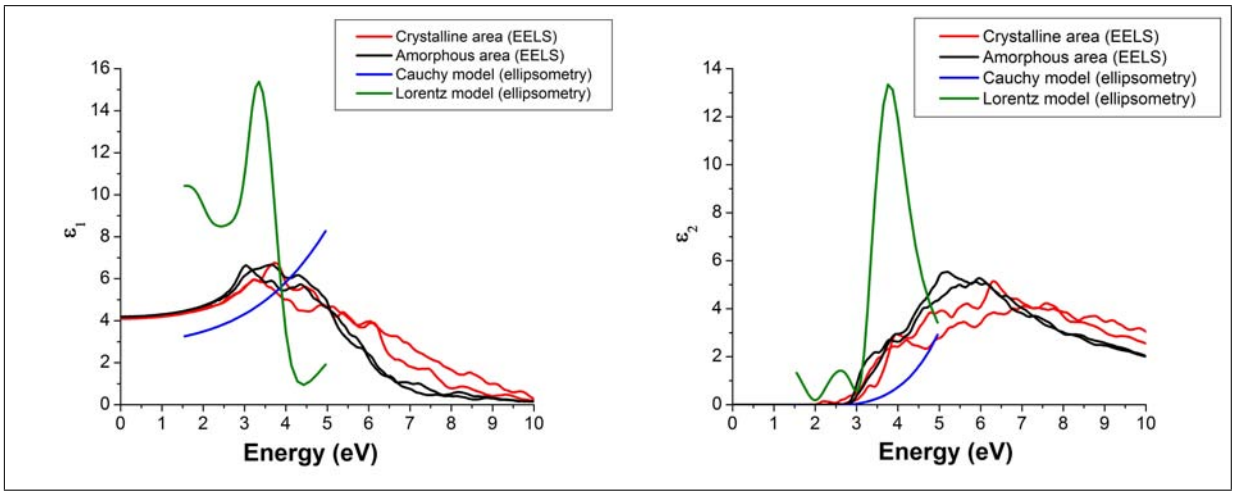

Figure A.9 Kramers-Kronig analysis results (ε_1 and ε_2) from spectra acquired from regions 1 and 2 (crystalline) and regions 3 and 4 (amorphous) and a comparison with the ellipsometric results (Cauchy and Lorentz models). The sample was grown at RT in chamber 2.

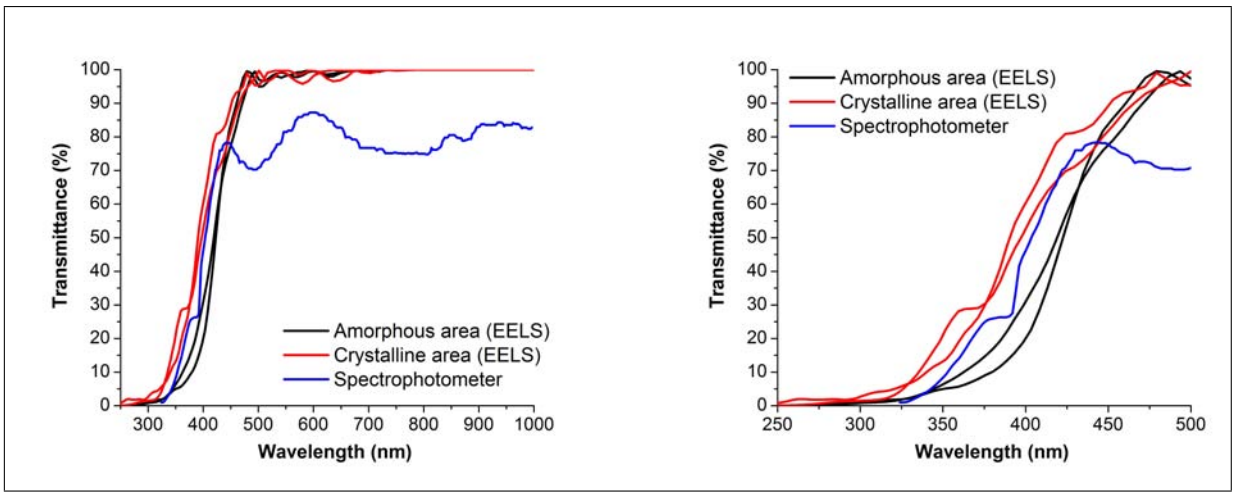

Figure A.10 Left: Kramers-Kronig analysis results (transmittance) from spectra acquired from regions 1 and 2 (crystalline) and regions 3 and 4 (amorphous) and a comparison with spectrophotometry results. The comparison is made in the 250 nm - 1000 nm range. Right: zoom of the bandgap region. The sample was grown at RT in chamber 2.

by spectrophotometry regarding the cut-off wavelength (or band gap). In the visible range, the 100% transmittance obtained with EELS measurements is due to the extreme difficulty in getting counts close to the ZLP which only stems from the material itself rather than from residual random noise. Data treatment, i.e. the residual signal extracted after power law fitting of the high energy ZLP tail, has a large impact in that region. Below the fitting window, counts cannot be recovered and are lost in the broad tail of the ZLP resulting in nil counts.

The agreement with the ellipsometric measurements is not wholly acceptable using the Cauchy model since the resonance behaviour of ε_2 in the energy gap region is not

modelled at all. This is attributed to the fact that the Cauchy model does not account for the different contributions of bound and unbound electrons. The Lorentz model, however, appears to account for the dielectric properties more satisfactorily. Three oscillators were used: a Drude term to account for free electrons and two others to account for interband transitions in the energy gap region. Moreover, low and high frequency polarisation effects were taken into account with the high frequency dielectric function ε_∞ and the static dielectric constant ε_s. The agreement between (ε_1, ε_2)(EELS) and (ε_1, ε_2)(Lorentz model, ellipsometry) is not yet satisfactory in terms of absolute values and peak position and width. The broadening of (ε_1, ε_2) peaks is related to damping effects taking place in the material, for example phonon generation (lattice vibrations). Hence, data processing and instrumental/specimen contributions aside, the fact that the ε_1 and ε_2 curves as given by EELS measurements are much broader than the ones given by ellipsometry indicates that a strong dampening is indeed taking place. The use of better energy resolution may also have resulted in narrower ε curves, although it may not account for the full broadening: dampening due to sample thickness would certainly be a major contributor too. It is also worth noting that on the EELS spectra, no deconvolution for multiple scattering was performed. Even though measurements are acquired from area less than 1 IMFP, multiple scattering events are still possible. In addition, crystalline areas were thicker than 1 IMFP which makes multiple scattering events unavoidable.

The fact that only very small differences were observed between EELS measurements from a crystalline and amorphous area is surprising at first. It is indeed expected that the band structure would be significantly altered upon crystallisation inducing different features in the resulting EELS spectra. Typically, more and/or stronger interband transitions are expected in the crystalline rather than in the amorphous material thus modifying the SSD and (ε_1, ε_2). More details are given in the discussion (section A.6).

A.5 Results from Birmingham

Data from the Tecnai F20 in Birmingham are also presented and compared with results from the SuperSTEM and the ellipsometric data. The experimental details for the acquisition of those spectra were presented in section 4.3.2.3.1. As a reminder, the largest difference for the EELS acquisition between these two microscopes is the accelerating voltage, which is 80 kV for the SuperSTEM and 200 kV for the Tecnai F20. Despite the advantage of decreasing the microscope accelerating voltage described above (less

sample damage and virtually no retardation effects), doing so on the Birmingham instrument was difficult in practise due to the extremely tedious alignments of the Gatan spectrometer necessitated by the voltage change.

As with previous measurements in the SuperSTEM, $P_{Cerenkov}$ was also computed for a 200 kV voltage and found to be 0.77. The criterion of Erni et al. [136] (i.e. $0< P_{Cerenkov} < 0.8$) is still respected, but at the limit. As a consequence, a thickness of only 0.5 IMFP was chosen whenever possible to counteract possible retardation effects. Thicknesses below 0.25 IMFP were not used as they increased the probability of surface effects that would interfere with the actual bulk dielectric losses.

Another major experimental difference was the energy resolution: 0.35 eV energy resolution was achieved on the SuperSTEM while 1 eV at best could be achieved on the Tecnai F20 microscope. With a 0.35 eV resolution, the tails of the ZLP are signficantly reduced with respect to the tails obtained in Birmingham. Even if the extraction of the ZLP presented exactly the same difficulties as encountered with the spectra from the SuperSTEM, they were compounded by this loss of energy resolution, making weaker features such as Cerenkov losses even more difficult to identify and assess. Some features next to the ZLP could simply not be recovered properly.

We now move on to the actual removal of the ZLP tails from the EELS signals where a similar approach to the one used for spectra acquired in SuperSTEM was used. Indeed, as in the previous section, deconvolution procedures yielded inconsistent results in the low energy range whatever collection angle was used. When present, very weak Cerenkov losses (and more generally non-relativistic effects) were seen “indirectly”, i.e., only after removal of the ZLP tails with a power law function to extrapolate and subtract them from the raw EELS signal. Owing to the loss of energy resolution when compared with superSTEM, no strong features could be identified when computing the first derivative of the raw EELS signals before the band gap signal. This is also likely to be due to the fact that retardation effects were relatively weak. While for superSTEM, the level of detail (energy resolution) enabled a power law function to be fitted right in front of the first feature in the spectrum, the same could not be done with the spectra acquired in Birmingham owing to the much lower energy resolution. Therefore, for the upper limit of the fitting window, an energy between 3.5 and 4 eV was chosen, assuming *de facto* that the band gap signal is the first significant signal of our EELS spectra and lies above 3.5/4 eV. As the lower limit, an energy of about 2 eV was chosen. These choices are not

arbitrary, but were made according to the four physical criteria presented in the previous section.

The procedure is illustrated by a raw spectrum acquired in diffraction mode with an acceptance angle of 4.2 mrads and shown in Fig. A.11 while the extracted signal is shown in Fig. A.12.

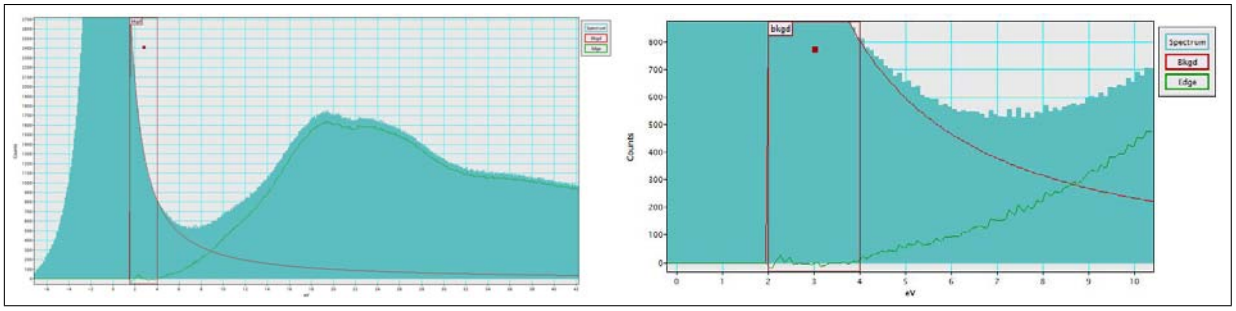

Figure A.11 ZLP loss peak removal from a spectrum acquired with an acceptance angle of 4.2 mrads. The thickness was calculated to be 0.53×IMFP. Left: a power law is fitted in the 2 - 4 eV range to model a background arising from instrumental noise and the ZLP tail in the low loss range and to extract the residual signal (green curve). Right: zoom of the 0 - 10 eV region.

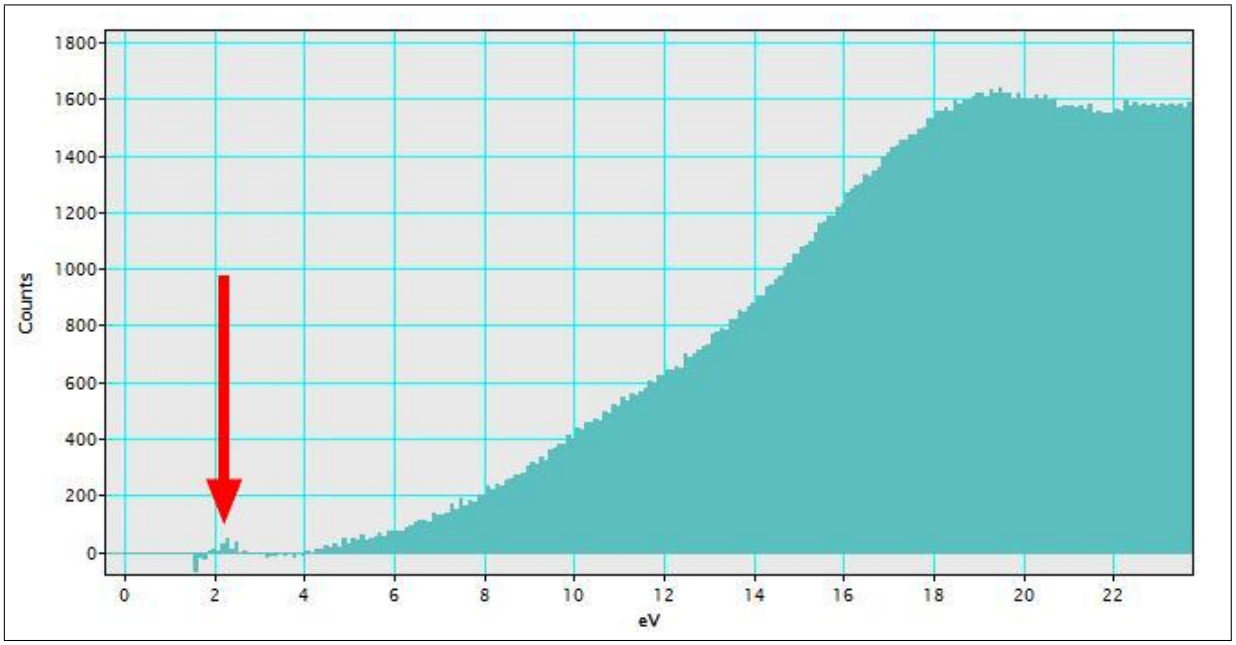

Figure A.12 Signal extracted after removal of the ZLP tail of the spectra presented in Fig. A.11. A weak singal was observed around 2 eV, as indicated with a red arrow.

A very weak signal (see red arrow in Fig. A.12) around 2 eV is identified. Indeed, non zero counts were sometimes observed within the background fitting window after subtraction. These subtraction errors may possibly be attributed to the presence of Cerenkov losses within this window; as explained above, however, those were too difficult to take into account given the extended ZLP tails. The assignment of such features to Cerenkov radiation is therefore tentative and should not be used for any

quantitative analysis. As a consequence, this spectrum is taken as an SSD ready to be fed into a Kramers-Kronig analysis program. It has to be stressed that when negative counts were encountered, they were manually set to nil due to the program's high sensitivity to negative values and difficulty in dealing with noisy backgrounds. It is argued that this is justified as negative counts do not make sense physically and most likely arise from noise in the data or errors in the background removal.

Since Cerenkov radiation does not stem from the material itself, it spoils the data in precisely the low-loss region that we are interested in. However, it arises at a much lower intensity than the overall low-loss EELS signal; it was, therefore considered negligible and as having no impact on the dielectric data. Before proceeding to Kramers-Kronig analysis, a major concern was the reproducibility of the results. To that end, several spectra from different regions were acquired and compared. They are all presented in Fig. A.19.

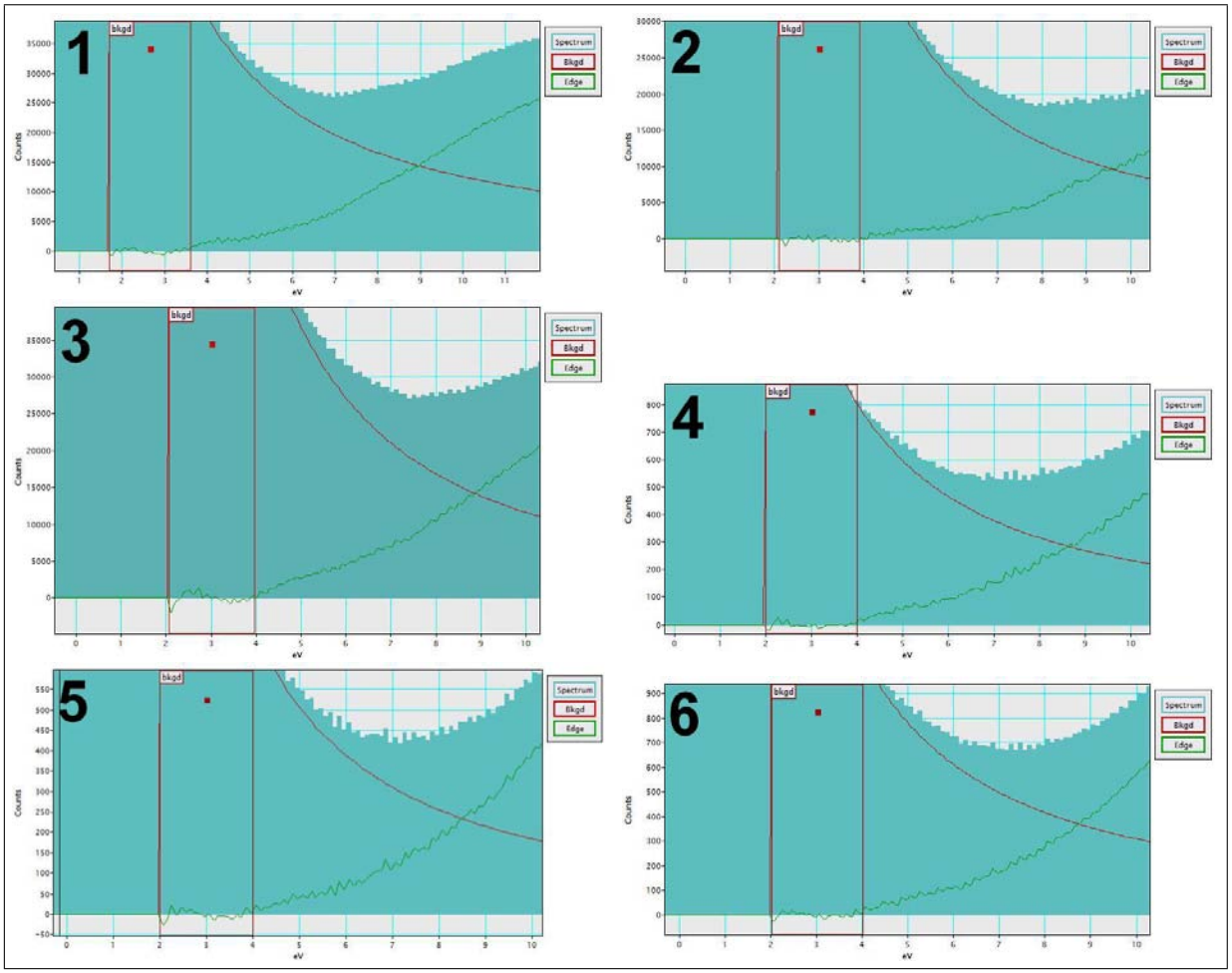

Figure A.19 Reproducibility of the EELS removal procedure illustrated over the 0 - 10 eV region for 6 spectra taken from 6 different regions (1...6).

Table A.2 sums up the fitting windows used for each spectrum as well as the thickness of

the area they originated from.

Table A.2 Fitting windows used to derive the spectra presented in Fig. A.19. Relative and absolute thicknesses are mentioned. At 200 kV, IMFP was calculated to be 160 nm. The spectrum number is indicated in the first column.

	Fitting window (eV)	Relative thickness (IMFP)	Absolute thickness (nm)
1	2.1 - 3.9	0.27	43.2
2	2.2 - 4	0.53	84.8
3	1.8 - 3.8	0.55	88
4	2.1 - 3.8	0.47	75.2
5	1.9 - 3.6	0.35	56
6	1.9 - 3.8	0.46	73.6

The SSD extracted are plotted in Fig. A.20, normalised with respect to the bulk plasmon peak to give a reference point for comparison.

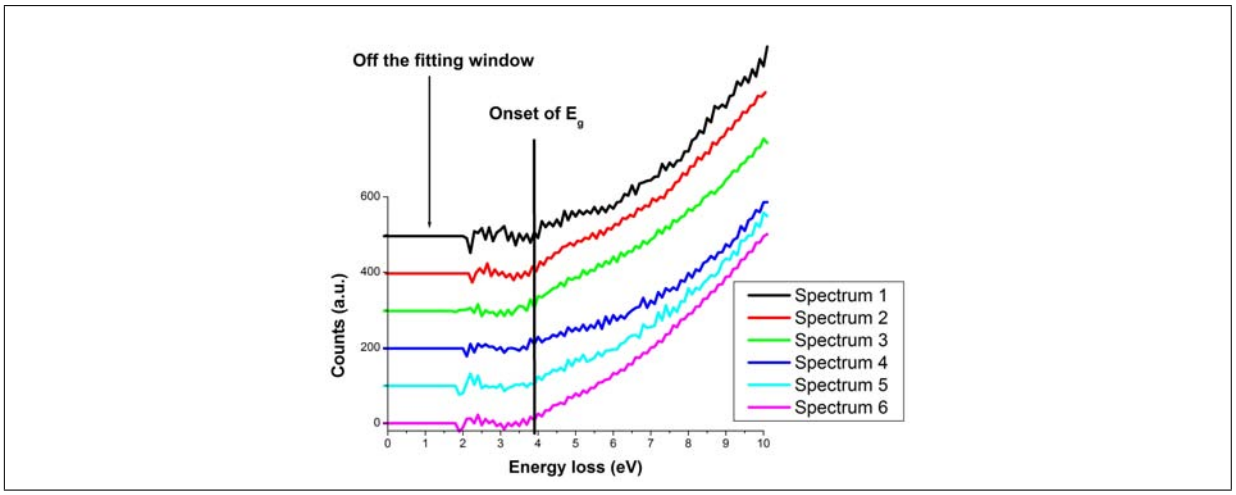

Figure A.20 Summary of the SSD obtained after extrapolation and removal of the ZLP tails from the low-loss EELS signal via a power-law function.

The data are seen to be reproducible with an energy gap onset around 4 eV. Features at higher energy are difficult to distinguish. Spectrum 4 also shows a slightly different behaviour, with an EELS signal taking off more rapidly than the other spectra. This is attributed to surface losses interfering with the bulk dielectric losses. Those are not removed with the Kramers-Kronig procedure as proposed by Egerton [219]. On all the spectra, there is some residual intensity over the 2 - 3 eV region, but the latter is part of the noise and does not significantly affect the spectrum shapes. It is likely that some weak retardation effects are responsible for these residual intensities since the emission probability $P_{Cerenkov}$ as defined by Erni et al. [136] is close to 0.8.

KKA was finally performed on the SSD shown in Fig. A.19. Its outputs are illustrated in Fig. A.21, in terms of dielectric data (ε_1, ε_2). The resulting transmittance using eq. A.2

and A.3 is also shown in Fig. A.22.

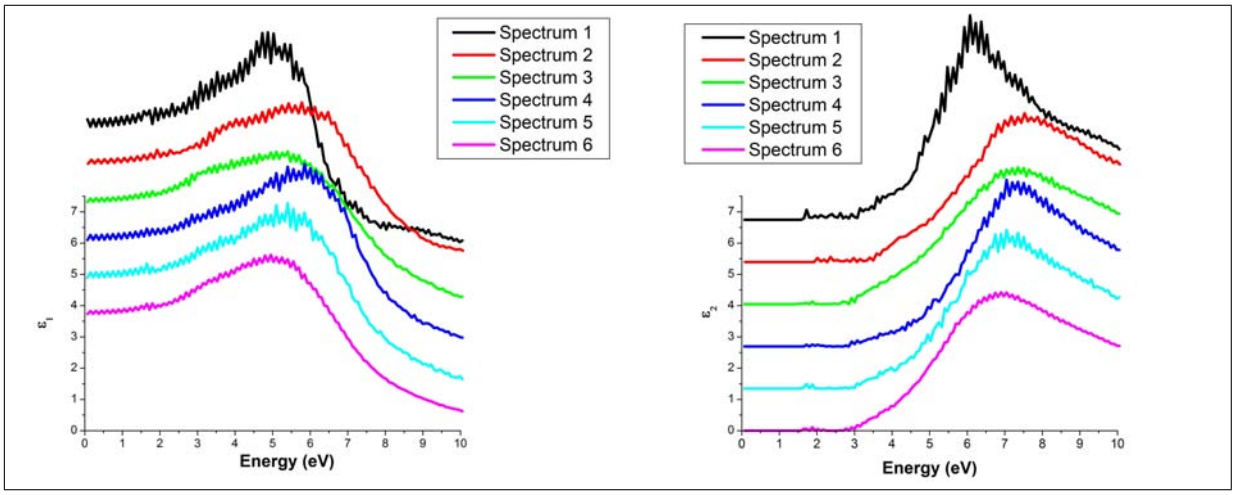

Figure A.21 KKA analysis results in terms of dielectric data (ε_1, ε_2) for the 6 SSD spectra presented in Fig. A.20.

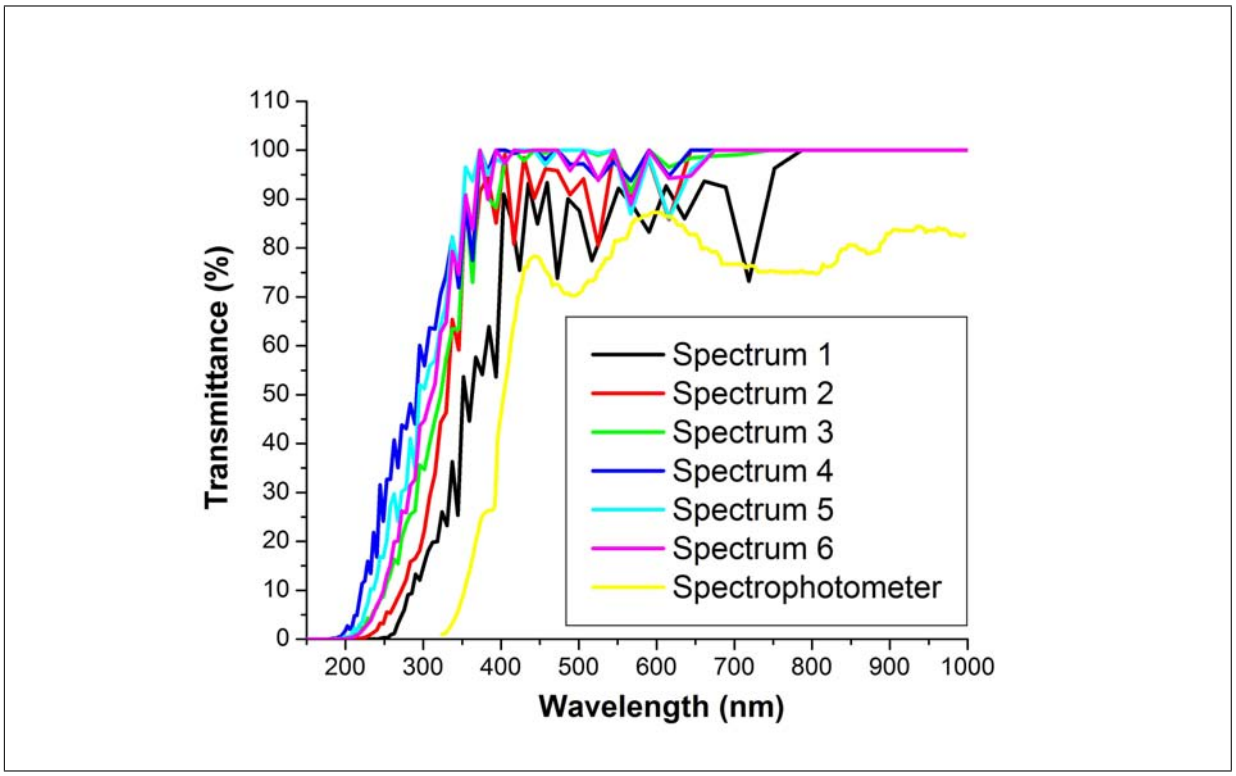

Figure A.22 KKA analysis results in terms of optical data (transmittance) of the 6 spectra presented in Fig. A.19.

The results are now compared with the previous ellipsometric measurements using the Cauchy and Lorentz models as shown in Fig. A.23. For the EELS measurements, the average of the 6 spectra presented in Fig. A.20 was taken.

The agreement between the EELS and the ellipsometric measurements is slightly better using the Cauchy model as compared with the EELS measurements in Daresbury (see Fig. A.9). This is due to the different positions of the ε_1 and ε_2 peaks as given by

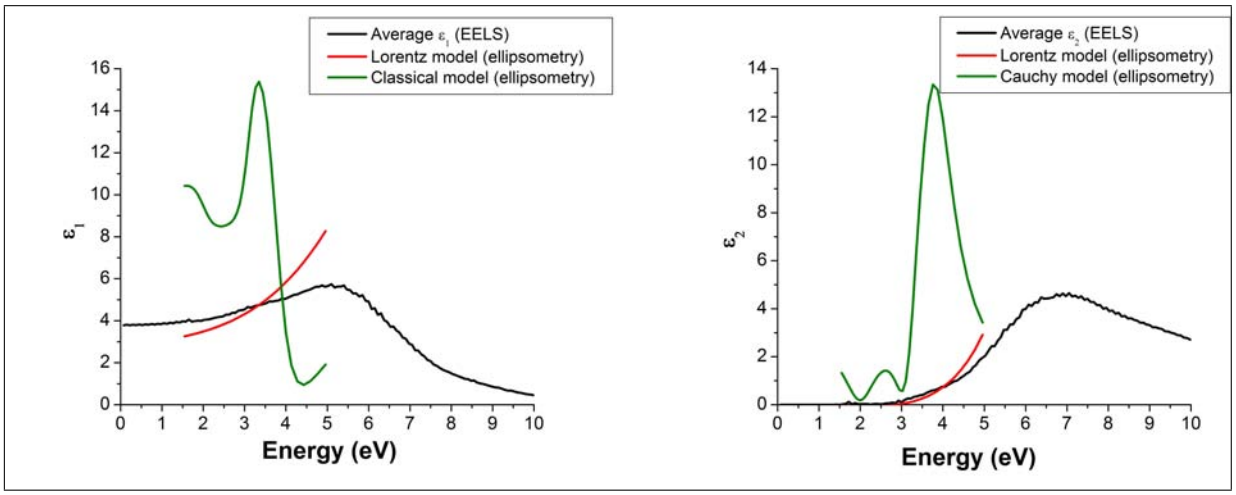

Figure A.23 Comparison of EELS and ellipsometric measurements (Cauchy and Lorentz models) over the 1-10 eV range for ε_1 (left) and ε_2 (right).

Kramers-Kronig analysis of SSD spectra acquired in Daresbury and Birmingham (see below Fig. A.24). However, the resonance behaviour in the energy gap region is still not modelled at all for the same reasons mentioned in section A.2. As a result of the different positions of the ε_1 and ε_2 peaks between Daresbury and Birmingham measurements, the agreement with the Lorentz model is still not satisfactory enough. Exactly the same effect occurs with the transmittance spectra, where the onset of the band gap is systematically modelled at lower wavelengths than the spectrum given with the spectrophotometer (and taken as reference).

Finally, a comparison between the EELS measurements in Daresbury and Birmingham is also shown in Fig. A.24.

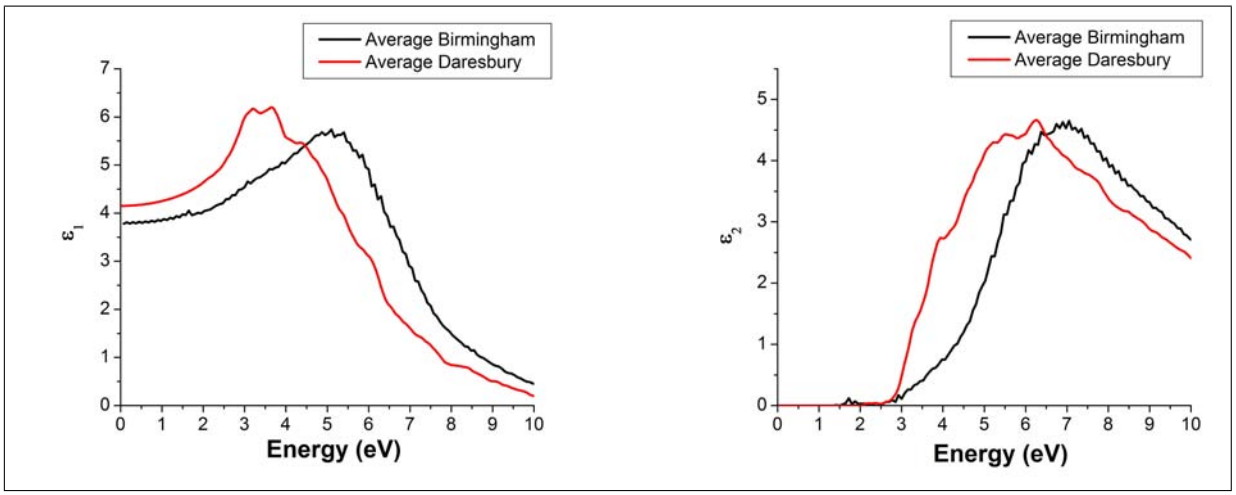

Figure A.24 Comparison between ε_1 (left) and ε_2 (right) obtained after Kramers-Kronig analysis of SSD acquired in Birmingham and in Daresbury.

While the different microscopes give the same trend and shape for the behaviour of ε_1 and ε_2 versus energy, the (ε_1, ε_2) peaks are shifted from one another by about 1 eV. The

absolute values remain very similar though, while the onset of the ε_2 signal is almost identical in both configurations.

It is observed that the (ε_1, ε_2) peaks have the same width (much larger than those given by the Lorentz model for ellipsometric measurements). This reinforces the previous assumption that such broad (ε_1, ε_2) peaks might stem from the fact that no multiple scattering deconvolution was performed on any of the SSD presented in this study even though it was ensured (whenever possible) that areas of interest were less than 1 IMFP.

A.6 Discussion

In this section, dielectric/optical data computed from EELS and ellipsometry measurements from a RT grown sample in chamber 2 were compared. Spectrophotometry results (i.e. transparency measurements) were also compared with the two former techniques. The Cauchy and Lorentz models were found to predict different dielectric responses, especially for films in chamber 2. This is was attributed to the fact that account was taken of the free carriers and interband transitions in the Lorentz model, while the Cauchy model only consists of parametric equations. Dielectric data showed maxima in both ε_1 and ε_2 in chamber 1 (consistent with interband transitions in the band gap region) while the latter was off-scale or even non-existent (RT) in chamber 2. This behaviour was not considered to be physically consistent and was attributed to the different behaviour of bound electrons for RT deposited chamber 2 films (Fig. 5.34), for which the mathematical form is too complex to be described adequately by the relatively simple Cauchy model. The width of the (ε_1, ε_2) peaks was modelled to be narrower for ellipsometric (Lorentz model) than for EELS measurements. This was connected with the EELS spectra processing: no multiple inelastic scattering deconvolution was performed owing to their inadequacy to process data in the low-energy range. In addition, emphasis were put on obtaining spectra that were processed as little as possible so that the SSD reflects as much as possible the interactions between electrons and the material. Moreover, the crystalline regions investigated in Daresbury were thicker than 1 IMFP contrary to the amorphous areas. This makes multiple scattering events unavoidable in the crystalline phase so that multiple inealstic scattering no longer plays a marginal role for IMFP$>$1 and is likely to mask additional features in the SSD of crystalline areas as compared with the amorphous phase.

Despite the two different microscopes and modes used, the EELS measurements at

SuperSTEM (Daresbury laboratory) and in Birmingham agree in terms of peak position (although a 1 eV shift occurs between the ε_1 and ε_2 maxima) and absolute intensities.

The difference observed in terms of peak position is attributed to (1) the lower energy resolution attainable in Birmingham, which leads to a loss of spectrum information, particularly in the low-loss range (0 - 10 eV); (2) significantly less material was probed in SuperSTEM since the STEM mode was used. This had the advantage that the surface analysed can be considered as homogeneous in terms of thickness contrary to measurements performed in conventional diffraction mode in Birmingham; (3) at Daresbury, despite efforts to obtain a scattering vector $\overrightarrow{q}$ as parallel as possible by choising the lowest objective aperture diameter, the latter still has a convergence of 20 mrads, which may give rise to a different scattering distribution; (4) the choice of the fitting window can impact on the SSD since a few tens of eV difference in the fitting window can result in a slightly different band gap energy onset, thus affecting the (ε_1, ε_2) peaks positions. This is connected with the loss of energy resolution in Birmingham which makes it more difficult to choose accurately the optimum fitting window.

No strong differences in the EELS spectra were noticed between the crystalline and amorphous areas, which is rather surprising as the band structures of the amorphous and crystalline material are expected to be significantly different. However, a lot more experiments are needed to check the statistics and derive any trend. Moreover, there is a significant thickness difference between crystalline (t>1 IMFP) and amorphous (t<1 IMFP) regions, That could result in fine features being masked in the SSD from crystalline areas. Hence, thinner samples are needed as well.

Regarding the cut-off wavelength (band gap energy), the EELS and spectrophotometry measurements were in good agreement in the SuperSTEM case. Interestingly, the cut-off wavelength modelled measured by spectrophotometric measurements falls roughly in between the ones modelled for the amorphous and crystalline areas via Kramers-Kronig analysis. This was attributed to the scale of the volumes probed with the two techniques since the spectrophotometric measurements result from the interaction of light with a few square millimetres of surface on the sample, while the STEM measurements only probed a volume of a few nm^3. Therefore, the dielectric responses obtained from spectrophotometric measurements represent an average from a large number of crystallites and from amorphous material. A trend in the transmittance measurements seems to emerge in that the band gap for the crystalline area is smaller than for the amorphous one, although more measurements are needed to refine this trend. Transparency in the visible range

did not match that obtained by spectrophotometry. This is attributed to the fact that collecting counts close to the ZLP and dissociating them from possible retardation effects is extremely challenging and there is bound to be some information loss, especially at such low energy loss. Regarding measurements in Birmingham, modelled optical data were not in good agreement with spectrophotometric data.

A.7 Further work on EELS measurements

A more complex ellipsometric modelling, taking into account possible thickness variations of the optical constants, would possibly result in a much better match with EELS. As for the EELS measurements themselves, different fit functions such as a Pearson VII function or a combination of different functions might reproduce much better the ZLP contribution than the power-law used in this study. A different approach to the Kramers-Kronig analysis using a normalisation of the SSD by the plasmon mean free path (as suggested by Stoger-Pollach et al. [220]) rather than the refractive index alone, might also yield a closer match with ellipsometric measurements. Finally, finding amorphous and crystalline regions of exactly the same thickness (t) would help to ensure that multiple scattering events do not spoil the data provided, t$<$IMFP.

Studying electronic structures at the crystalline/amorphous phase interface as well as at grain boundaries, together with their impact on optical properties, remains to be carried on to get a deeper understanding of their effects on macroscopic physical properties. Such knowledge would enable an accurate prediction of optical properties (transparency, refractive index, reflectance etc.) solely based on the grain size of the thin film grown.

It would have been helpful to perform low-loss EELS measurements on films grown at different T_s and $P(O_2)$ values to study in more detail the effects of these two parameters on the thin film optical and electronic properties. The use of a microscope equiped with a monochromator and hence capable to go down in resolution to 0.050 eV should be suitable for this type of study.

Appendix B

One application: Dye-Sensitized Solar Cells

B.1 Context and challenges

Every day, our planet receives from the sun an energy equivalent to the electric consumption of 5.9 billions of persons during 27 years. Human beings are only harvesting a very small amount of it, agriculture aside. Technologies developed during the twentieth century make it possible to harvest a significant amount of this energy to power our industrial civilisation.

There are two types of solar cells: inorganic and organic. Most of the inorganic solar cells are based on silicon (amorphous or single crystalline). This is the dominant technology (wafer technology) in the commercial production of solar cells. The manufacturing of silicon single crystal solar cells requires a massive amount of energy since the silicon has to be ultra-pure to prevent unwanted electron-hole recombinations. Hence, manufacturing such cells involves complex and energy intensive equipment. Therefore, the Energy Returned Over Energy Invested (EROEI) and energy payback are not always attractive. As for thin-film solar cells, their efficiencies are still lower than those of silicon (wafer-based) solar cells, but manufacturing costs are also lower, so that a lower cost per watt can be achieved. They also use less material. These types of solar cell also rely on a traditional p-n junction to separate photogenerated charge carriers.

On the contrary, organic solar cells are not based on a p-n junction. In general, over recent years, there has been growing interest in organic-based electronics, electrochemical systems, and cheap chemically synthesized inorganic semiconductors to replace traditional microelectronic technologies mainly based on silicon. Among organic solar cells, Dye Sensitized Solar Cells (DSSCs) are regarded as potential inexpensive alternatives to conventional solid-state devices.

Discovered in 1991 [221], their yield is nearly equivalent to that of standard amorphous silicon solar cells and they also enable very low cost production which makes them attractive. Moreover, organic solar cells also make possible the fabrication on flexible substrates such as plastic sheets. Nonetheless, DSSCs suffer from a lower lifetime than standard silicon solar cells, mainly because of the liquid electrolyte, even though solid-state electrolytes are being developed [222]. ITO is still used as an anode (top front electrode), but cheaper alternative materials like doped-ZnO are being investigated so as to achieve greater efficiency as well as cost savings.

B.2 Principle

The principle of a DSSC closely imitates the photosynthesis process used by plants. It is composed of the following main elements:

- Two electrodes: one is platinum coated, the other one has to be nanoporous.
- An electrolyte.
- A coloured dye.

The organisation of these elements in the cell is illustrated in Fig. B.1.

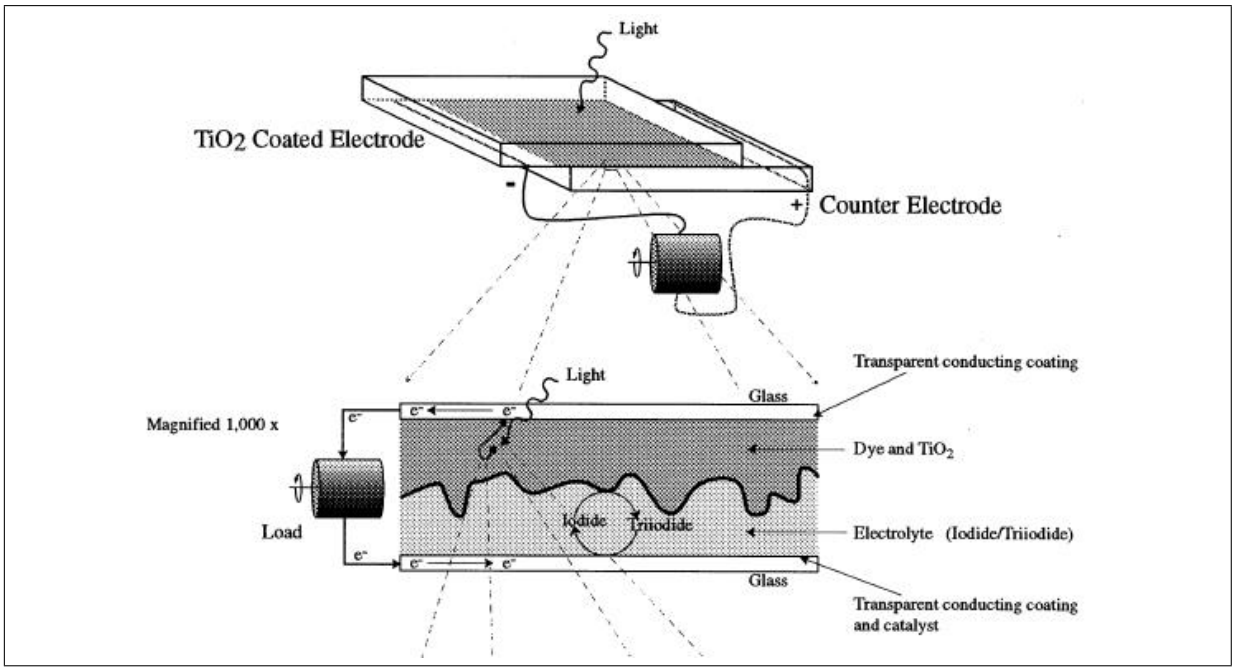

Figure B.1 Schematic of dye sensitized solar cell. Taken from Smestad [7]. In this work, the TiO_2 porous layer was replaced with an ITO porous one.

The light absorption, electron injection and regeneration reaction is illustrated in more detail in Fig. B.2.

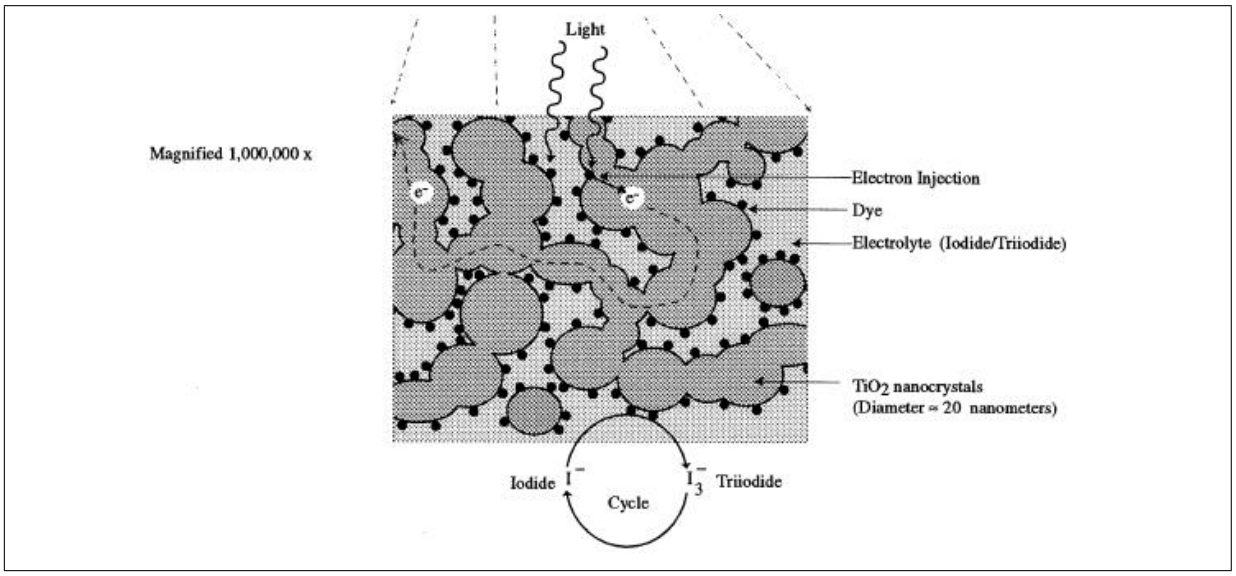

Figure B.2 Electron injection and regeneration reaction. Instead of TiO_2 nanocrystals, a porous ITO layer was used in this work. Taken from Smestad [7]. The TiO_2 nanocrystals were replaced with ITO porous ones.

The energy producing reactions found in a DSSC cell are [7]:

- Dye+light $\Longrightarrow Dye^*$ (1)
- Dye^* + ITO $\Longrightarrow e^-$(ITO) + Dye^*(Oxidised dye) (2)
- Dye^*(Oxidised dye) + $\frac{3}{2}I^- \Longrightarrow$ Dye + $\frac{1}{2}I^{3-}$ (3)
- $\frac{1}{2}I^{3-}$ + $e-$(counterelectrode) $\Longrightarrow \frac{3}{2}I^-$ (4)

After having been excited by light (eq. (1)), the coloured dye is able to transfer an electron to the porous semiconducting ITO layer via a process called electron injection or sensitization (eq. (2)). The dye used in this study was a ruthenium-based organic compound called “Ruthenium 535”. It has to be noticed that this dye can be as simple as pure blackberry, carrot or beetroot juice diluted in pure ethanol. Extracting green chlorophyll from young leaves is also an option. Usually, the dye layer is so thin that almost all of the excited electrons produced from light absorption can be injected into the porous ITO and collected in the underlying conducting ITO layer. It is then “injected” into the circuit so that it produces electricity. This electrode (often called a “photoelectrode” or “photoanode”) has to be made as porous as possible to enhance the surface area so that the dye molecules can collect as many photons as possible. This enhancement is necessary to achieve full light absorption over the absorbing range of the composite when the porous electrode is coated with a monolayer of dye.

As for the electrolyte, it contains a redox couple. In this study, an iodide/trio-iodide redox couple was used. It is a low viscosity electrolyte formulation with a tri-iodide

concentration of 50 mM. The oxidised dye is transformed back into its non-oxidised form via light absorption and eq. (3). The platinum-coated electrode serves as a catalyst for the tri-iodide/iodide regeneration reaction with the incoming electron (eq. (4)). As an alternative to the platinum coating, the counter electrode can be prepared by chemically depositing a transparent, fine-grained carbon layer. Therefore, an electrical current is effectively produced with the circulation of one electron though an external load.

B.3 Experimental method

B.3.1 Resources

The solar cell was built as much as possible from resources available in the department. However, a few elements had to be ordered from a manufacturer in Switzerland (Solaronix [223]) as they could not be made:

- The electrolyte
- The platinum paint
- The coloured dye

The resources used from this department were:

- A syringe to inject the coloured dye
- A hot plate to seal the electrodes and fire the platinum painting
- A PLD deposition set-up. Only chamber 2 was used in this work

B.3.2 Preparation of the porous electrode (photoanode) and counter electrode

The “standard”, or at least the most common way in the literature to make a porous electrode is to deposit a layer of TiO_2 several microns thick on top of a conductive ITO or SnO_2 thin film. In this work, a different approach was used. Only one ITO target was used to deposit the conductive ITO thin film on a glass substrate and the porous ITO layer right on top of it. The temperature and the atmosphere were changed. A summary of the conditions used to make the photoanode is given in Table B.1.

Table B.1 Growth conditions used for manufacturing the photoanode in chamber 2.

Layer name	Temperature (°C)	Atmosphere composition (mT)	Thickness (nm)
Conductive ITO	200	5 mT O_2	~300
Porous ITO	450	1 mT O_2 + 430 mT N_2	~1000

The electrodes were generally made as thin as possible: 300 nm for the conductive ITO layer and 1000 nm for the porous one. Making cells thinner reduces the time required for deposition and thereby reduces capital costs.

In order to obtain a reasonably porous ITO layer, the deposition atmosphere was chosen to be a mix of pure nitrogen and oxygen. After numerous trials and errors, the optimum nitrogen/oxygen pressure ratio was found to be 430. The surface microstructure was evaluated using a SEM. A plan view and cross-sectional SEM micrograph are shown in Fig. B.3.

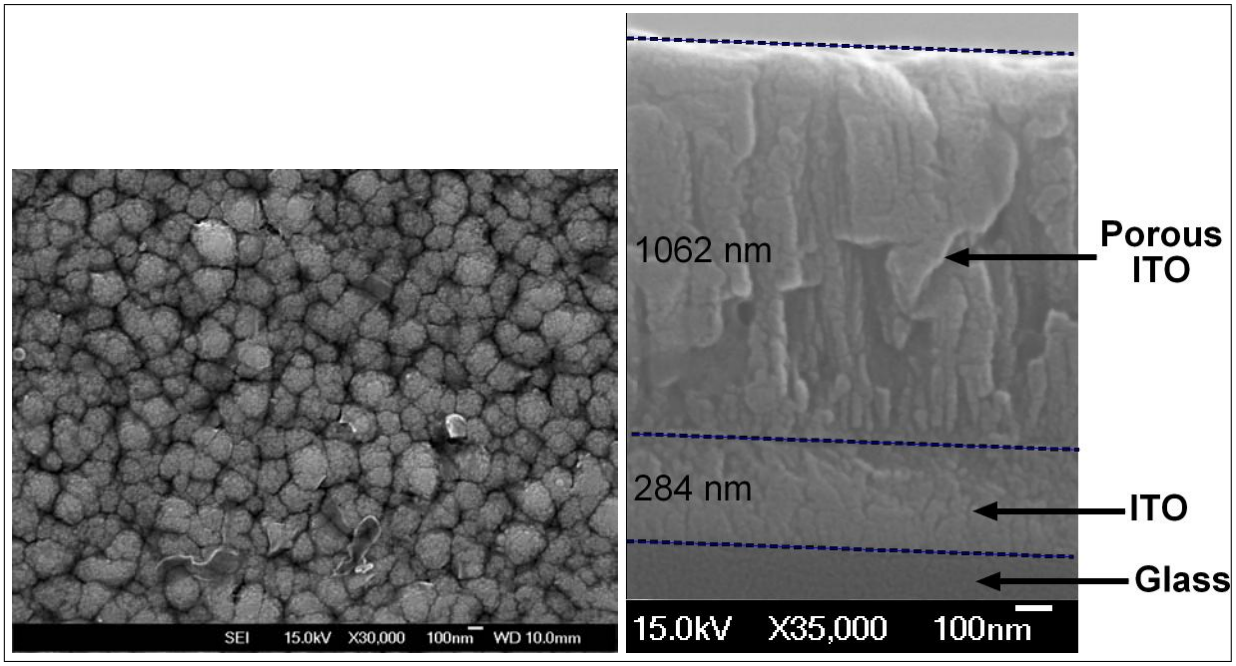

Figure B.3 Plan view SEM micrograph showing the surface microstructure of the porous ITO (left). Cross-sectional SEM micrograph of the same porous ITO/photoanode showing the 284 nm thick conductive ITO thin film on top of which a 1062 nm porous ITO layer was deposited (right). The growth conditions used for both layers are listed in Table B.1.

The achievement of a porous microstructure is believed to arise from the Vapour-Liquid-Solid (VLS) growth mechanism [224]. The nitrogen/oxygen pressure ratio was found to be critical to obtaining the porous microstructure as also found in [225]. If the latter was too low or too high, the surface microstructure appeared to be quite dense. This is

illustrated in Fig. B.4 with N_2/O_2= 140 and 700.

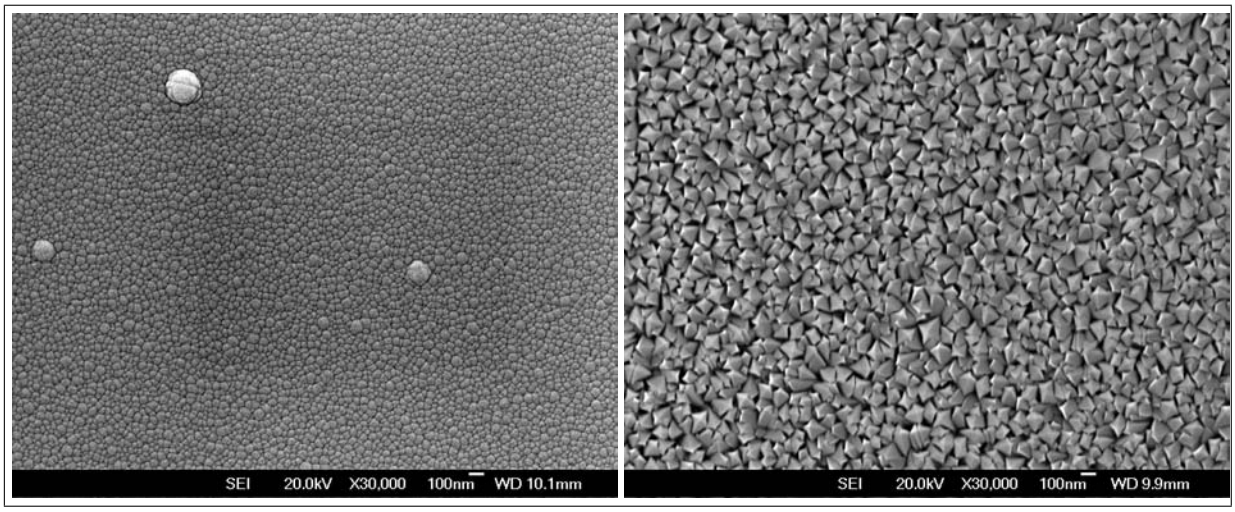

Figure B.4 Plan view SEM micrographs showing the surface microstructure of the porous ITO electrode at two different N_2/O_2 pressure ratios: 140 (left) and 700 (right). The substrate temperature was kept at $450°$C.

The porous electrode must be sensitized with a monolayer of dye molecules. Ruthenium 535 was used. The sensitization was accomplished by diluting 10 mg of dye (Ruthenium 535) in 50 ml of absolute ethanol. The electrode was then gently heated on a hot plate at 70°C before putting it slowly into the sensitizer solution, face-up. The impregnation process was carried out at RT and left overnight to ensure the success impregnation process.

The counter electrode was easier to make. It consisted of a simple ITO thin film on a glass substrate using the optimal growth conditions for chamber 2 found earlier in this work (see sections 5.1.3.4, 5.2.2.4 and 5.3.2.4): 5000 pulses, $P(O_2)$=5 mT and T_s=$200°$C. On top of it, a platinum catalyst was deposited. It was obtained by using a platinum catalyst precursor paint. It was then brush-painted onto the conductive ITO film before firing at 450°C on the hot plate for 5 minutes.

B.3.3 DSSC assembling

Prior to the actual assembling, both electrodes were cleaned with absolute ethanol and dried in air with a hair-drier. DSSCs were assembled following the procedure described in the literature [7]. The catalyst-coated counter electrode was placed underneath the photoanode so that the conductive side of the counter electrode faces the porous ITO film (see Fig. B.5). A hot melt sealing polymer film was used to seal the electrodes together. Sealing was carried out at 120°C with the hot plate. The electrolyte solution was then injected with a syringe into small holes on the edges of the cell. Only 65 μm

separates the two electrodes. Hence, injecting the electrolyte through one hole caused lots of bubbles. To circumvent this, two to three more holes (depending on the cell size) were made using a diamond blade. This way, the liquid was succesfully drawn into the space between the electrodes. These holes were plugged by placing on top of them a few mm^2 of hot melt polymer film, melting it with a soldering iron. The electrodes were slightly displaced from one another to create space for electrical contacts as shown in Fig. B.5.

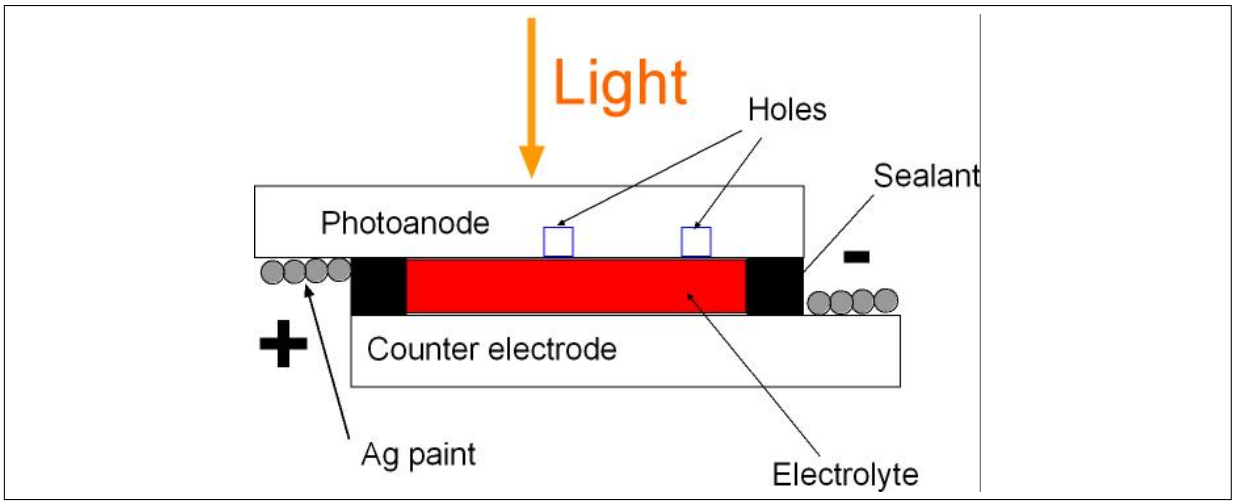

Figure B.5 Schematic of how the two electrodes are arranged in the built DSSCs. Two contacts (+ and -) are formed and covered with Ag paint.

Two cells were built: one cell with a 10×10 mm active area (cell 1) and another one with a larger active area of 15×15 mm (cell 2). Unfortunately, cell 2 dried out because of defective hole plugging. Injection of new electrolyte did not restore the previous performance of this cell.

B.3.4 Characterisation and measurements

B.3.4.1 Electrical measurements

The cells were illuminated by a 60 W tungsten Halogen lamp equipped with an integral parabolic reflector and UV and IR blocking filters. The light intensity was adjusted simply by changing the distance from the cell to the light source. For characterisation, the latter was chosen to be 10 cm for both cells. A light irradiance of 60 W/m^{-2} was evaluated for the electrical measurements. Using a ruler, the dimensions of the active (stained) area of both solar cells was calculated. It is found to be: 100 and 225 mm^2 for cells 1 and 2 respectively. A simple set-up was used consisting of a multimeter attached to both electrodes. Both electrodes were painted with Ag paint to ensure a better electrical

contact between the multimeter probes and the electrodes themselves. The wires used were copper based. This is illustrated for both assembled cells in Fig. B.6.

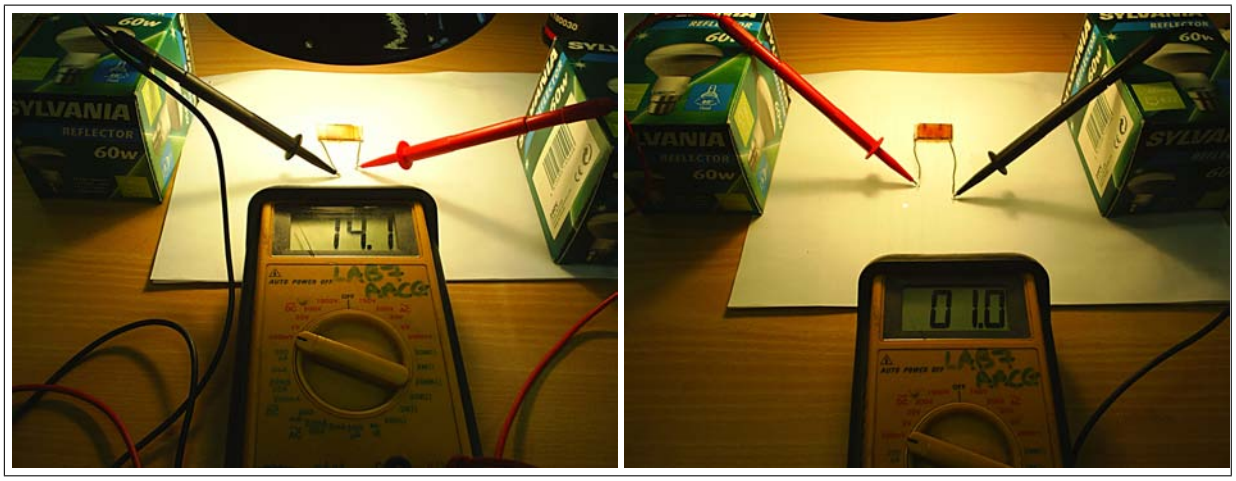

Figure B.6 Electrical characterisation set-up for the two assembled cells. Cell 1 is on the left while cell 2 is on the right.

The chosen calibration on the multimeter was 200 mV. 14.1 mV could be measured for cell 1 while only 1 mV was measured for cell 2. The initial drying-out of the electrolyte of cell 2 is probably responsible for such a low voltage output. Unfortunately, no measurable current could be detected on either cell.

B.3.4.2 Optical measurements

A spectrophotometer was used to derive the transmittance of both cells over the 250 - 1000 nm wavelength range. Results are illustrated in Fig. B.7.

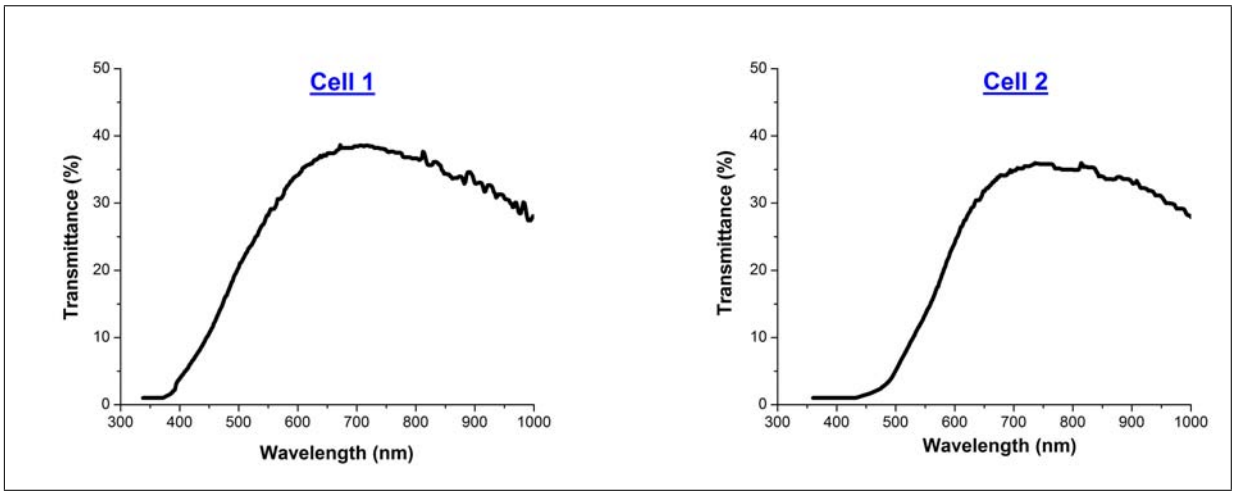

Figure B.7 Transmittance of cell 1 (left) and 2 (right) over the 300 - 1000 nm wavelength range.

The two cells show similar transmittance in the visible range with a maximum transmittance of 40% around 700 nm. A small shift towards higher wavelengths is observed

for cell 2 as compared with cell 1. This is attributed to inhomogeneities within the electrolyte due to the presence of bubbles.

B.4 Summary

Two transparent and operational DSSCs were built using electrodes deposited according to the optimal growth conditions found in this work for chamber 2. A potential difference was measured (14.1 and 1.0 mV for cells 1 and 2 respectively) under a light irradiance of 60 W/m^{-2}. However, no measurable current could be detected in either cell. Hence, no energy conversion efficiency calculation could be performed. It is suggested that the porosity of the ITO thin film deposited under an N_2/O_2 pressure ratio of 430 was not large enough as compared with the conventional TiO_2 layer. Its thickness ($\sim$1000 nm) might be too low as well. Nonetheless, it was demonstrated that with a single target/material but different growth conditions depending on the layer deposited, a potential difference could be measured showing the potential of such a method. The cells showed a maximum transparency of 40%. Such a transmittance could be suitable for their integration in a window making electricity generation possible.

B.5 Further work on Dye-Sensitized solar cells

Although beetroot juice or chlorophyll as dyes could not be tested with our set-up, it would be relevant to investigate them as such dyes would be inexpensive to manufacture, making the scale up of such a technology more likely. Regarding a possible scaling-up, the Platinum coating is an important issue as Platinum is not an abundant metal on Earth; the same is true of Indium. The two electrodes made here could be made with a unique doped-ZnO target circumventing the use of Indium. Possibly, graphite could have been used in place of Platinum, although it is not as efficient as a catalyst [226]. In chamber 2, films with good electro-optical properties were grown and could be used to manufacture inexpensive solar cells. However, the effect of the deposition of the porous layer on the underlying ITO electrode needs to be studied.

Another aspect related to such applications is the study of possible aging effects of our amorphous and polycrystalline samples. Clearly, it is important to know the effects of the environment on the microstructure and subsequently on the properties of the films/electrodes. These effects could be studied by TEM after a suitable period of aging under normal atmosphere conditions.

Bibliography

[1] C.R. Bradley and N.J. Zaluzec. Atomic sputtering in the analytical electron microscope. *Ultramicroscopy*, 28:335–338, 1989.

[2] Testbourne Ltd. Tripod polisher - Model 590. Website, April 2010. `http://www.testbourne.com/instruments/sbt-products/20/Tripod-Polisher/`.

[3] NIST: physical measurement laboratory. The Hall effect. Website, February 2010. `http://www.nist.gov/pml/semiconductor/hall_effect.cfm`.

[4] C. Kittel. *Introduction to Solid State Physics*. Wiley, New York, 1976.

[5] D. Mergel, W. Stass, G. Ehl, and D. Barthel. Oxygen incorporation in thin films of In_2O_3:Sn prepared by radio frequency sputtering. *J. Appl. Phys.*, 88(5):2437–2442, 2000.

[6] R.B. Dingle. Scattering of electrons and holes by charged donors and acceptors in semiconductors. *Philos. Mag.*, 46:831–840, 1955.

[7] G.P. Semstad. Education and solar conversion: Demonstrating electron transfer. *Sol. Energ. Mat. Sol. C.*, 55(1-2):157–178, 2008.

[8] L. Tian. *Study of Indium Tin Oxide and its microwave applications*. PhD thesis, University of Birmingham, UK, 2008.

[9] R.L. Weiher and R.P. Ley. Optical properties of indium oxide. *J. Appl. Phys.*, 37(1):299–302, 1966.

[10] J.H.W. De Wit. Electrical properties of In_2O_3. *Journal of Solid State Chemistry*, 8(2).

[11] M. Marezio. Refinement of the crystal structure of In_2O_3 at two wavelengths. *Acta Cryst.*, 20:723–728, 1966.

[12] A.J.C. Wilson. *The international Union of Crystallography, International Tables for Crystallography*. Kluwer Academic, 1992.

[13] H. Kostlin and G. Frank. Electrical properties and defect model of tin-doped oxide layers. *Appl. Phys. A-Mater.*, 27(4):197–206, 1982.

[14] Z. Ovadyahu, B. Ovryn, and H.W. Kraner. Microstructure and electro-optical properties of evaporated indium-oxide films. *J. Electrochem. Soc.*, 130(4):917–921, 1983.

[15] C.A. Pan and T.P. Ma. High-quality transparent indium oxide films prepared by thermal evaporation. *Appl. Phys. Lett.*, 37(2):163–165, 1980.

[16] Z.M. Jarzebski. Preparation and physical properties of transparent conducting oxide films. *Phys. Stat. Sol. (a)*, 71:13–41, 1982.

[17] I.A. Rauf and J. Yuan. Effect of microstructure on the optical properties of tin-doped indium oxide thin films studied by electron energy loss spectroscopy. *Mat. Lett.*, 25:217–222, 1995.

[18] J. C. C. Fan and J.B. Goodenough. X-ray photoemission spectroscopy studies of Sn-doped indium-oxide films. *J. Appl. Phys.*, 48(8):3524–3531, 1977.

[19] F. Lopez-Aguillar, J. Costa-Quintana, and J.S. Munos. Coulomb (or strong) correlation effects in the band structure of Eu_2O_3. *Phys. Stat. Sol. (b)*, 111:659–669, 1982.

[20] N.F. Mott. *Metal-Insulator transitions*. Taylor and Francis, 1974.

[21] E. Burstein. Anomalous optical absorption limit in InSb. *Phys. Rev.*, 93:632–633, 1954.

[22] M. Batzill and U. Diebold. The surface and materials science of tin oxide. *Progr. Surf. Sci.*, 79:47–154, 2005.

[23] J.W. Orton and M.J. Powell. The Hall effect in polycrystalline and powdered semiconductors. *Rep. Prog. Phys*, 43:1264–1307, 1980.

[24] R. B. H. Tahar, Y. Ohya T. Ban, and Y. Takahashi. Tin doped indium oxide thin films: Electrical properties. *J. Appl. Phys.*, 83(5):2631–2645, 1998.

[25] H. Kim, C.M. Gilmore, A. Pique, J.S. Horwitz, H. Mattoussi, H. Murata, Z.H. Kafafi, and D.B. Chrisey. Electrical, optical and structural properties of indium-tin-oxide thin films for organic light-emitting devices. *J. Appl. Phys.*, 86(11):6451–6460, 1999.

[26] Y. Wu, C.H.M. Maree, R.F. Haglund, J.D. Hamilton, M.A. Morales Paliza, M.B. Huang, and L.C. Feldman. Resistivity and oxygen content of indium tin oxide films deposited at room temperautre by pulsed-laser ablation. *J. Appl. Phys.*, 86:991–994, 1999.

[27] M. Bender, N. Katsarakis, E. Gagaoudakis, E. Hourdakis, E. Douloufakis, V. Cimalla, and G. Kiriakidis. Dependence of the photoreduction and oxidation behaviour of indium oxide films on substrate temperature and film thickness. *J. Appl. Phys.*, 90(10):5382–5387, 2001.

[28] H. Kostlin, R. Jost, and W. Lems. Optical and electrical properties of doped In_2O_3 films. *phys. stat. sol (a)*, 29(1):87–93, 1975.

[29] J.C.C. Fan and F.J. Bachner. Properties of Sn-doped In_2O_3 films prepared by rf sputtering. *J. Electrochem. Soc.*, 122:1719–1724, 1975.

[30] M. Hecq, A. Duboisa, and J. Van Cakenberghe. Etude par diffraction de rayons X de films a base d'oxydes d'etain et d'indium. *Thin Solid Films*, 18:117–125, 1973.

[31] Y. Shigesato, Y. Hayashi, and T. Haranoh. Doping mechanisms of tin-doped indium oxide films. *Appl. Phys. Lett.*, 61:73–75, 1992.

[32] J.R. Bellingham, W.A. Phillips, and C.J. Adkins. Electrical and optical properties of amorphous indium oxide. *J. Phys.: Condens. Matter*, 2:6207–6221, 1990.

[33] E.J. Moore. Quantum-transport theories and multiple scattering in doped semiconductors. *Phys. Rev.*, 160(3):607–617, 1967.

[34] T. Pisarkiewicz, K. Zakrzewskaand, and E. Leja. Scattering of charge carriers in transparent and conducting thin oxide films with a non-parabolic conduction band. *Thin Solid Films*, 174:217–223, 1989.

[35] Y. Shigesato, D.C. Paine, and T.E. Haynes. Lattice defects in O^+ implanted tin-doped indium oxide films. *Jpn. J. Appl. Phys.*, 32(9):L1352–L1355, 1993.

[36] C.Erginsoy. Neutral impurity scattering in semiconductors. *Phys. Rev.*, 79:1013–1014, 1950.

[37] R. B. H. Tahar, Y. Ohya T. Ban, and Y. Takahashi. Optical, structural, and electrical properties of indium oxide thin films prepared by the sol-gel method. *J. Appl. Phys.*, 82(2):865–870, 1997.

[38] Y. Shigesato and D.C. Paine. Study of the effect of Sn doping on the electronic transport properties of thin film indium oxide. *Appl. Phys. Lett.*, 62(11):1268–1270, 1993.

[39] J.W. Orton M.J. Powell. The Hall effect in polycrystalline and powdered semiconductors. *Rep. Prog. Phys.*, 43(11):1263–1307, 1980.

[40] Y. Shigesato, D.C. Paine, and T.E. Haynes. Study of the effect of ion implantation on the electrical and microstructural properties of tin-doped indium oxide thin films. *J. Appl. Phys.*, 73(8):3805–3811, 1993.

[41] F.O. Adurodija, H. Izumi, T. Ishihara, H. Yoshioka, and M. Motoyama. The electro-optical properties of amorphous indium tin oxide films prepared at room temperature by pulsed laser deposition. *Sol. Energ. Mat. Sol. C.*, 71:1–8, 2002.

[42] V.F. Korzo and V.N. Chernyaev. Electrophysical properties of indium oxide pyrolytic films with disordered structure. *Phys. Stat. Sol. (a)*, 20:695–705, 1973.

[43] N.F. Mott. Conduction in glasses containing transition metal ions. *J. Non-Cryst. Solids*, 1:1–17, 1968.

[44] J.-C. Manifacier, M. De Murcia, and J.P. Fillard E. Vicario. Optical and electrical properties of SnO_2 thin films in relation to their stoichiometric deviation and their crystalline structure. *Thin Solid Films*, 41(2):127–135, 1977.

[45] J.-C. Manifacier, J.F. Bresse L. Szepessy, M. Peretin, and R. Stuck. In_2O_3 : (Sn) and SnO_2: (F) films - application to solar energy conversion - 2 electrical and optical properties. *Mater. Res. Bull.*, 14:163–175, 1979.

[46] H.K. Muller. Electrical and optical properties of sputtered In_2O_3 films. *Phys. Stat. Sol.*, 27:723–41, 1968.

[47] J. I. Pankove. Absorption edge of impure gallium arsenide. *Phys. Rev.*, 140(6A):A2059–A2065, Dec 1965.

[48] L-J. Meng and M.P. Dos Santos. Properties of indium tin oxide films prepared by reactive magnetron sputtering at different substrate temperatures. *Thin Solid Films*, 322:56–62, 1998.

[49] I. Hamberg, A. Hjortsberg, and C.G. Granqvist. High quality heat reflectors of reactively evaporated indium tin oxide. *Appl. Phys. Lett.*, 40(5):362–364, 1982.

[50] S. Fahler and H.U. Krebs. Calculations and experiments of material removal and kinetic energy during pulsed laser ablation of metals. *Appl. Surf. Sci.*, 96-98:61–65, 1996.

[51] D.B. Geohegan, A.A. Puretzky, G. Duscher, and S.J. Pennycook. Time-resolved imaging of gas phase nanoparticle synthesis by laser ablation. *Appl. Phys. Lett.*, 72(23).

[52] S.S. Harilal, C.V. Bindhu, V.P.N. Nampoori, and C.P.G. Vallabhan. Influence of ambient gas on the temperature and density of laser produced carbon plasma. *Appl. Phys. Lett.*, 72(2).

[53] S.S. Harilal. Expansion dynamics of laser ablated carbon plasma plume in helium ambient. *Appl. Surf. Sci.*, 172:103–109, 2001.

[54] A.V. Bulgakov and N.M. Bulgakova. Gas-dynamic effects of the interaction between a pulsed laser-ablation plume and the ambient gas: Analogy with an underexpanded jet. *J. Phys. D: Appl. Phys.*, 31.

[55] V. Berardi, S. Amoruso, N. Spinelli, M. Armenante, R. Velotta, F. Fuso, M. Allegrini, and E. Arimondo. Diagnostics of $YBa_2Cu_3O_{7-x}$ laser plume by time-of-flight mass spectrometry. *J. Appl. Phys.*, 76(12):8077–8087, 1994.

[56] M. Han, S. Kiyama, M. Muto, A. Fukuda, T. Sawada, and Y. Iwata. Cluster formation dynamics in a locally-confined gas layer mixed with the plume ablated by pulsed laser irradiation. *Nucl. Instrum. Meth. B*, 153:302–308, 1999.

[57] J.P. Zheng, Q.Y. Ying, S. Witanachchi, Z.Q. Huang, D.T. Shaw, and H.S. Kwok. Role of the oxygen atomic beam in low-temperature growth of superconducting

films by laser deposition. *Appl. Phys. Lett.*, 54:954–956, 1989.

[58] J.P. Zheng, Z.Q. Huang, D.T. Shaw, and H.S. Kwok. Generation of high-energy atomic beams in laser-superconducting target interactions. *Appl. Phys. Lett.*, 54:280–282, 1989.

[59] J. Gonzalo, C.N. Afonso, and I. Madariaga. Expansion dynamics of the plasma produced by laser ablation of $BaTiO_3$ in a gas environment. *J. Appl. Phys.*, 81(2):951–955, 1997.

[60] P.M. Ossi and A. Bailini. Cluster growth in an ablation plume propagating through a buffer gas. *Appl. Phys. A*, 93:645–650, 2008.

[61] P.R. Willmott and J.R. Huber. Pulsed laser vaporization and deposition. *Rev. Mod. Phys.*, 72(1):315–328, 2000.

[62] D.C. Paine, T. Whitson, D. Janiac, R. Beresford, and C.O. Yang. A study of low temperature crystallization of amorphous thin film indium-tin-oxide. *J. Appl. Phys.*, 85(12):8445–8450, 1999.

[63] M. Ohring. *The Materials Science of Thin Films*. Academic Press; 2nd edition, 2001.

[64] R. Eason. *Pulsed laser deposition of thin films*. Willey-Interscience, 2007.

[65] R.W. Vook. Structure and growth of thin films (vacuum evaporation). *Int. Metals rev.*, 27(4):209–245, 1982.

[66] J.A. McMillan and E.M. Peterson. Kinetics of decomposition of amorphous hydrogenated silicon films. *J. Appl. Phys*, 50(8):5238–5241, 1979.

[67] H-C. Lee. Electron scattering mechanism in indium-tin-oxide thin films prepared at the various process conditions. *Appl. Surf. Sci.*, 252:3428–3435, 2006.

[68] F.O. Adurodija, H. Izumi, T. Ishiara, H. Yoshioka, H. Matsui, and M. Motoyama. Low-temperature growth of low-resistivity indium-tin oxide thin films by pulsed laser deposition. *Vacuum*, 59:641–648, 2000.

[69] F. Hanus, A. Jadin, and L.D. Laude. Pulsed laser deposition of high quality ITO thin films. *Appl. Surf. Sci.*, 96-98:807–810, 1996.

[70] F.O. Adurodija, H. Izumi, T. Ishiara, H. Yoshioka, K. Yamada, H. Matsui, and M. Motoyama. Highly conducting indium tin oxide (ITO) thin films deposited by pulsed laser ablation. *Thin Solid Films*, 350:79–84, 1999.

[71] D. Beena, K.J. Lethy, R. Vinodkumar, and V.P. Mahadevan Pillai. Influence of substrate temperature on the properties of laser ablated indium tin oxide lms. *Sol. Energ. Mat. Sol. C.*, 91:1438–1443, 2007.

[72] I. Hamberg and C.G. Granqvist. Evaporated Sn-doped In_2O_3 films: basic optical properties and applications to energy-efficient windows. *J. Appl. Phys.*, 60(11):R123–R159, 1986.

[73] J.P. Zheng and H.S. Kwok. Preparation of indium tin oxide films at room temperature by pulsed laser deposition. *Thin Solid Films*, 232:99–104, 1993.

[74] J.P. Zheng and H.S. Kwok. Low resistivity indium tin oxide films by pulsed laser deposition. *Appl. Phys. Lett.*, 63(1):1–3, 1993.

[75] K. Ellmer and R. Mientus. Reactive magnetron sputtering of tin-doped indium oxide (ITO): influence of argon pressure and plasma excitation mode. *Surf. Coat. Technol.*, 142-144:748–754, 2001.

[76] W-F. Wu and B-S. Chiou. Mechanical properties of r.f. magnetron sputtered indium tin oxide films. *Thin Solid Films*, 293:244–250, 1997.

[77] F.O. Adurodija, L. Semple, and R. Brening. Real-time in situ crystallization and electrical properties of pulsed laser deposited indium oxide thin films. *Thin Solid Films*, 492:153–157, 2005.

[78] S. Naseem, I.A. Rauf, K. Hussain, and N.A. Malik. Effects of oxygen partial pressure on the properties of reactively evaporated thin films of indium oxide. *Thin Solid Films*, 156(1).

[79] H. Aharoni, T.J. Coutts, T. Gessert, R. Dhere, and L. Schilling. Ion-beam sputtered indium tin oxide for InP solar cells. *J. Vac. Sci. Technol. A*, 4(3).

[80] E. Holmelund, B. Thestrup, J. Schou, N.B. Larsen, M.M. Nielsen, E. Johnson, and S. Tougaard. Deposition and characterization of ITO films produced by laser ablation at 355 nm. *Appl. Phys A*, 74(2):147–152, 2002.

[81] S.W. Jan and S.C. Lee. Preparation and characterization of indium-tin-oxide deposited by direct thermal evaporation of metal indium and tin. *J. Electrochem. Soc.*, 134:2056–2061, 1987.

[82] B. Aiterkop, N. Parkansky, R.L. Boxman, and S. Goldsmith. Influence of a parallel electric field on the conductivity of a growing indium oxide film. *Thin Solid Films*, 290-291:10–12, 1996.

[83] R. Pommier, C. Gril, and J. Marucchi. Sprayed films of indium tin oxide and fluorine-doped tin oxide of large surface area. *Thin Solid Films*, 1-3:91–97, 1981.

[84] S. Muranaka. Crystallization of amorphous In_2O_3 films during film growth. *Jpn. J. Appl. Phys.*, 30(12A):L2062–L2064, 1991.

[85] M. Hoheisel, A. Mitwalsky, and C. Mrotzek. Microstructure and etching properties of sputtered indium-tin oxide (ITO). *phys. stat. sol. (a)*, 123:461–472, 1991.

[86] Y. Shigesato, S. Takaki, and T. Haranou. Crystallinity and electrical properties of tin-doped indium oxide films deposited by dc magnetron sputtering.

[87] H. Kim, J.S. Horwitz, G.P. Kushto, Z.H. Kafafi, and D.B. Chrisey. Indium tin oxide thin films grown on flexible plastic substrates by pulsed-laser deposition for organic light-emitting diodes. *Appl. Phys. Lett.*, 79(3):284–286, 2001.

[88] E.J. Tarsa, E.A. Hachfeld, F.T. Quinlan, J. S. Specka, and M. Eddy. Growth-related stress and surface morphology in homoepitaxial $SrTiO_3$ films. *Appl. Phys. Lett.*, 68:490–492, 1996.

[89] D.P. Norton, C. Park, J.D. Budai, S.J. Pennycook, and C. Prouteau. Plume-induced stress in pulsed-laser deposited CeO_2 films. *Appl. Phys. Lett.*, 74(15):2134–2136, 1999.

[90] A. Suzuki, T. Matsushita, T. Aoki, A. Mori, and M. Okuda. Highly conducting transparent indium tin oxide films prepared by pulsed laser deposition. *Thin Solid Films*, 411(1):23–27, 2002.

[91] F.O. Adurodija, H. Izumi, T. Ishihara, H. Yoshioka, and M. Motoyama. High quality indium tin oxide films by combined pulsed laser ablation and in-situ pulsed laser irradiation. *Thin Solid Films*, 19(19):1719–1721, 2000.

[92] H. Kim, A. Pique, J.S. Horwitz, H. Mattoussi, H. Murata, Z.H. Kafafi, and D.B. Chrisey. Indium tin oxide thin films for organic light-emitting devices. *Appl. Phys. Lett.*, 74(23):3444–3446, 1999.

[93] S.H. Kim, N.-M. park, T.Y. Kim, and G.Y. Sung. Electrical and optical characteristics of ito films by pulsed laser deposition using a 10 wt.% SnO_2-doped In_2O_3 ceramic target. *Thin Solid Films*, 475(1-2).

[94] F.O. Adurodija, H. Izumi, T. Ishihara, H. Yoshioka, and M. Motoyama. Effects

of stress on the structure of indium-tin-oxide thin films grown by pulsed laser deposition. *J. Mater. Sci-Mater. El.*, 12(1).

[95] J.B. Choi, H. Kim, K.A. Sang, and S.Y. Lee. Properties of ITO films on glass fabricated by pulsed laser deposition. *Mater. Sci. Eng.*, B102:376–379, 2003.

[96] C Coutal, A. Azema, and J.-C. Roustan. Fabrication and characterisation of ITO thin films deposited by excimer laser evaporation. *Thin Solid Films*, 288:248–253, 1996.

[97] J.-C. Manifacier, J.F. Bresse L. Szepessy, M. Peretin, and R. Stuck. In_2O_3 : (Sn) and SnO_2: (F) films - Application to solar energy conversion; part 1 - Preparation and characterization,.

[98] J. Aranovich, A. Ortiz, and R.H. Bube. Optical and electrical properties of ZnO films prepared by spray pyrolysis for solar cell applications. *J. Vac. Technol.*, 16(4):994–1003, 1979.

[99] J. Sanz Maudes and T. Rodriguez. Sprayed SnO_2 films: growth mechanism and film structure characterization. *Thin Solid Films*, 69:183–189, 1980.

[100] A. Raza, O.P. Agnihotri, and B.K. Gupta. Preparation and intrinsic absorption in the band edge in chemically sprayed In_2O_3 layers. *J. Phys. D: Appl. Phys.*, 10(13):1871–189, 1977.

[101] E. Shanthi, A. Banerjee, V. Dutta, and K.L. Chopra. Annealing characteristics of tin oxide films prepared by spray pyrolysis. *Thin Solid Films*, 71(2):237–244, 1980.

[102] M. Higuchi, S. Uekusa, R. Nakano, and K. Yokogawa. Micrograin structure influence on electrical characteristics of sputtered indium tin oxide films. *J. Appl. Phys.*, 74(11):6710–6713, 1993.

[103] Y. Shigesato, S. Takaki, and T. Haranoh. Electrical and structural properties of low resistivity tin-doped indium oxide films. *J. Appl. Phys.*, 71(7):3356–3364, 1992.

[104] S. Schiller, U. Heisig, C. Korndorfer, G. Beister, J. Reschke, K. Steinfelder, and J. Strumpfel. Reactive dc high-rate sputtering as production technology. *Surf. Coat. Technol.*, 33:405–423, 1987.

[105] A. Salehi. The effects of deposition rate and substrate temperature of ITO thin films on electrical and optical properties. *Thin Solid Films*, 324:214–218, 1998.

[106] T. Maruyama and K. Tabata. Indium-tin oxide thin films prepared by chemical vapor deposition from metal acetates. *Jpn. J. Appl. Phys.*, 29(2):L355–L357, 1990.

[107] T. Maruyama and K. Fukui. Indium-tin oxide thin films prepared by chemical vapor deposition. *J. Appl. Phys.*, 70(7):3848–3851, 1991.

[108] T. Maruyama and K. Fukui. Indium-tin oxide thin films prepared by chemical vapor deposition. *Thin Solid Films*, 203:297–302, 1991.

[109] H. Dislich and E. Hussmann. Amorphous and crystalline dip coatings obtained from organometallic solutions. procedures, chemical processes and products. *Thin Solid Films*, 77:129–139, 1981.

[110] D. Gallagher, F. Scanlan, R. Houriet, R.J. Mathieu, and A. Ring. Amorphous and crystalline dip coatings obtained from organometallic solutions. Procedures, chemical processes and products. *J. Mater. Res.*, 8(12):3135–3144, 1993.

[111] T. Maruyama and A. Kojima. Indium-tin oxide thin films prepared by thermal decomposition of metallic complex salts. *Jpn. J. Appl. Phys.*, 27(10):L1829–L1831, 1988.

[112] T. Furusaki, K. Kodaira, M. Yamamoto, S. Shimada, and T. Matsushita. Preparation and properties of tin-doped indium oxide thin films by thermal decomposition of

organometallic compounds. *Mat. Res. Bull.*, 21:803–806, 1986.

[113] J.J. Xu, A.S. Shaikh, and R.W. Vest. Indium tin oxide films from metallo-organic precursors. *Thin Solid Films*, 161:273–280, 1988.

[114] W-F. Wu and B-S. Chiou. Properties of radio-frequency magnetron sputtered ITO films without *in-situ* substrate heating and post-deposition annealing. *Thin Solid Films*, 247:201–207, 1994.

[115] J. Szczyrbowski, A. Dietrich, and H. Hoffmann. Optical and electrical properties of rf-sputtered indium-tin oxide films. *phys. stat. sol. (a)*, 78:243–252, 1983.

[116] D.T.J. Hurle. *Handbook of crystal growth*, volume 3. North Holland-Elsevier, 1994.

[117] A. Rogozin, N. Shevchenko, M. Vinnichenko, F. Prokert, V. Cantelli, A. Kolitsch, and W. Moller. Real-time evolution of the indium tin oxide film properties and structure during annealing in vacuum. *Appl. Phys. Lett.*, 85(10):212–214, 2004.

[118] W.P. Barr. The production of low scattering dielectric mirrors using rotating vane particle filtration. *J. Phys. E.*, 2(12):1112–1114, 1969.

[119] T. Yoshitake, G. Shiraishi, and K. Nagayama. Elimination of droplets using a vane velocity filter for pulsed laser ablation of $FeSi_2$. *Appl. Surf. Sci.*, 197-198:379–383, 2002.

[120] S.V. Gaponov, A.A. Gudkov, and A.A. Fraerman. Processes occurring in an erosion plasma during laser vacuum deposition of films. condensation in gas flows during laser vaporization of materials. *Soviet Physics-Technical Physics*, 27(39).

[121] D. Lubben, S.A. Barnett, K. Suzuki, S. Gorbatkin, and J.E. Green. Laser-induced plasmas for primary ion deposition of epitaxial Ge and Si films. *J. Vac. Sci. Technol.*, B3(4):968–974, 1985.

[122] G. Koren, R.J Baseman, A. Gupta, M.I. Lutwyche, and R.B. Laibowitz. Particulates reduction in laser-ablated $YBa_2Cu_3O_{7-x}$ thin films by laser-induced plume heating. *Appl. Phys. Lett.*, 56(21):2144–2146, 1990.

[123] H. Chiba, K. Murakami, O. Eryu K. Shihoyama, T. Mochizuki, and K. Masuda. Laser excitation effects on laser ablated particles in fabrication of high T_c superconducting thin films. *Jpn. J. Appl. Phys.*, 30(4B):L732–L734, 1991.

[124] H. Sankur, W.J. Gunning, J. DeNatale, and J.F. Flintoff. High-quality optical and epitaxial Ge films formed by laser evaporation. *J. Appl. Phys. Lett.*, 65(6):2475–2478, 1989.

[125] J.A. Greer and M.D. Tabat. Large-area pulsed laser deposition: Techniques and applications. *J. Vac. Technol. A*, 13(3):1175–1190, 1995.

[126] J.A. Greer. High quality YBCO films grown over large areas by pulsed laser deposition. *J. Vac. Sci. Technol. A*, 10(4):1821–1826, 1992.

[127] J.A. Greer and M.D. Tabat. Properties of laser-deposited yttria films on CdTe and silicon substrates. *Mater. Res. Soc. Symp. Proc.*, 341:87–94, 1997.

[128] S.R. Foltyn, R.E. Muenchausen, and X.D. Wu R.C. Dye, L. Luo, D.W. Cooke, and R.C. Taber. Large-area two-sided superconducting $YBa_2Cu_3O_{7-x}$ films deposited by pulsed laser deposition. *Appl. Phys. Lett.*, 59(11):1374–1376, 1991.

[129] H. Buhay, S. Sinharoy, M.H. Francombe, W.H. Kasner, J. Talvacchio, B.K. Park, N.J. Doyle, D.R. Lampe, and M. Polinsky. Pulsed laser deposition (PLD) of oriented bismuth titanate films for integrated electronic applications. *Integr. Ferroelectr.*, 1(2-4):213–222, 1992.

[130] M. Lorenz, H. Hochmuth, H. Borner, and D. Natusch. Large area pulsed laser deposition of YBCO thin films on 3-inch wafers. *Physica C*, 235-240:639–640,

1994.

[131] Anil K. Jain, Lin Hong, and Sharath Pankanti. Energy dispersive x-ray microanalysis hardware explained - technical briefing. Technical Report MSU-CSE-00-2, Oxford Instruments Analytical, High Wycombe Bucks, England, 2002.

[132] D.B. Williams and C.B. Carter. *Transmission Electron Microscopy - Spectrometry*. Number 4. Plenum Press, New York, 1996.

[133] P.E. Champness, G. Cliff, and G.W. Lorimer. The identification of asbestos. *J. Microsc.*, 103:231–249, 1976.

[134] D.E. Newbury. Microanalysis to nanoanalysis: measuring composition at high spatial resolution. *Nanotechnology*, 1:103–130, 1990.

[135] P.C. Tiemeijer. Measurement of coulomb interactions in an electron beam monochromator. *Ultramicroscopy*, 78:53–62, 1999.

[136] R. Erni and N.D. Browning. The impact of surface and retardation losses on valence electron energy-loss spectroscopy. *Ultramicroscopy*, 108:84–89, 2008.

[137] R.F. Egerton. *Electron Energy-Loss Spectroscopy in the electron microscope*. Plenum Press, New York, 1996.

[138] D.B. Williams and C.B. Carter. *Transmission Electron Microscopy - Spectrometry*. Number 1. Plenum Press, New York, 1996.

[139] P. Moreau, N. Brun, C.A. Walsh, C. Colliex, and A. Howie. Relativistic effects in electron-energy-loss-spectroscopy observations of the Si/SiO_2 interface plasmon peak. *Phys. Rev. B*, 56(11):738–739, 1997.

[140] R.T. Tung. Recent advances in Schottky barrier concepts. *Mat. Sci. Eng. R.*, 35(1-3):738–739, 2001.

[141] C.C. Ahn and O.L. Krivanek. Library of electron energy loss spectra at 1 eV resolution. *Proceedings - Electron Microscopy Society of America*, pages 738–739, 1982.

[142] I.P. Jones. *Chemical microanalysis using Electron Beams*. Institute of materials, 1992.

[143] R.F. Loane, E.J. Kirkland, and J. Silcox. Visibility of single heavy atoms on thin crystalline silicon in simulated annular dark-field STEM images. *Acta Crystallogr. A*, 44:912–927, 1988.

[144] J.R. Michael, D.B. Williams, C.F. Klein, and R. Ayer. The measurement and calculation of the x-ray spatial resolution obtained in the analytical electron microscope. *J. Microsc*, 160:41–53, 1999.

[145] C.A. Andersen and M.F. Hassler. *Proc. 4th Int. Conf on X-ray Optics and Microanalysis*, 1966.

[146] R. Brydson. *Electron Energy Loss Spectroscopy*. BIOS Scientific Publishers Ltd, 2001.

[147] Gatan, editor. *EELS manual - EL/P 3.0*. 1997.

[148] M. Stoger-Pollach, A. Laister, and P. Schattschneider. Treating retardation effects in valence EELS spectra for Kramers-Kronig analysis. *Ultramicroscopy*, 108:439–444, 2008.

[149] M. Stoger-Pollach and P. Schattschneider. The influence of relativistic energy losses on bandgap determination using valence EELS. *Ultramicroscopy*, 107:1178–1185, 2007.

[150] W.A Knox. Contamination formed around a very narrow electron beam [and film

thickness measurement]. *Ultramicroscopy*, 1:175–180, 1976.

[151] R.K. Hart, T.F. Kassner, and J.K. Maurin. The contamination of surfaces during high-energy electron irradiation. *Philos. Mag.*, 21:453–467, 1970.

[152] L. Reimer and M. Wachter. Contribution to the contamination problem in transmission electron microscopy. *Ultramicroscopy*, 3:169–174, 1978.

[153] R.D. Leapman and D.E. Newbury. Trace elemental analysis at nanometer spatial resolution by parallel-detection electron energy loss spectroscopy. *An. Chem.*, 65:2409–2414, 1993.

[154] L.E Thomas. High spatial resolution in STEM X-ray microanalysis. *Ultramicroscopy*, 9:311–318, 1981.

[155] Y. Chen, R.E. Palmer, E.J. Shelley, and J.A. Preece. HREELS studies of gold nanoparticles with dialkyl sulphide ligands. *Surf. Sci.*, 502-503:208–213, 2002.

[156] O.S. Oenr. Ornl report - tm-4897,. 1973.

[157] P.A. Egerton, R.F.; Feng Wang; Crozier. Beam-induced damage to thin specimens in an intense electron probe. *Microscopy and Analysis*, 12(1):65–71, 2006.

[158] Center for X-Ray Optics Berkeley USA. X-ray interactions with matter. Website, March March 2010. `http://henke.lbl.gov/optical_constants/atten2.html`.

[159] J.R. Bellingham, A.P. Mackenzie, and W.A. Phillips. Precise measurements of oxygen content: Oxygen vacancies in transparent conducting indium oxide films. *Appl. Phys. Lett.*, 58(22):2506–2508, 1991.

[160] D. Drouin. Monte carlo simulation of electron trajectory in solids: CASINO v 2.42. Website, November 2010. `http://www.gel.usherbrooke.ca/casino/index.html`.

[161] Uppsala university Department of Physics and Materials Science. Atomic force microscopy (AFM). Website, April 2010. `http://surfint.fysik.uu.se/techniques_afm.html`.

[162] G.J. Simpson, D.L. Sedin, and K.L. Rowlen. Surface roughness by contact versus tapping mode atomic force microscopy. *Langmuir*, 15(4):1429–1434, 1999.

[163] P.D.T. Huibers and D.O. Shah. Multispectral determination of soap film thickness. *Langmuir*, 13:5995–5998, 1997.

[164] M. Iliescu, V. Nelea, J. Werckmann, and I.N. Mihailescu. Transmission electron microscopy investigation of pulsed-laser deposited hydroxylapatite thin films prepared by tripod and focused ion beam techniques. *Surf. Coat. Tech.*, 187(1).

[165] A. De Veirman and L. Weaver. The use of a focused-ion-beam machine to prepare transmission electron microscopy samples of residual photoresist. *Micron*, 30(1).

[166] F.M. Smits. Measurement of sheet resisitivities with the Four-point probe. *, The Bell System Technical Journal*, 37:711–718, 1958.

[167] School of Physics Trinity College Dublin. Ellipsometry. Website, February 2010. `http://www.tcd.ie/Physics/Surfaces/ellipsometry2.php`.

[168] Y. Yang, X.W. Sun, B.J. Chen, C.X. Xu, T.P. Chen, C.Q. Sun, B.K. Tay, and Z. Sun. Refractive indices of textured indium tin oxide and zinc oxide thin films. *Thin Solid Films*, 510:95–101, 2006.

[169] A. Savitzky and M.J.E. Golay. Smoothing and differentiation of data by simplified least squares procedures. *Anal. Chem.*, 36(8):1627–1639, 1964.

[170] J.F. Pocza, A. Barna, and P.B. Barna. Formation processes of vacuum-deposited indium films and thermodynamical properties of submicroscopic particles observed

by in situ electron microscopy. *J. Vac. Sci. Technol.*, 6(4):472–475, 1969.

[171] H.P. Singh and L.E. Murr. Electron microscopy of nucleation and growth of indium and tin films. *Philos. Mag.*, 26(3):649–663, 1972.

[172] H.P. Singh and L.E. Murr. Nucleation and growth characteristics of palladium and indium thin films. *Met. Trans.*, 3(4):983–988, 1972.

[173] A.K. Saxena, S.P. Singh, R. Thangaraj, and O.P. Agnihotri. Thickness dependence of the electrical and structural proeprties of In_2O_3:Sn films. *Thin Solid Films*, 117:95–100, 1984.

[174] F. Simonis, M. van der Leija, and C.J. Hoogendoorn. Physics of doped tin dioxide films for spectral-selective surfaces. *Solar Energy Materials*, 80:221–231, 1979.

[175] E. Bertrana, J.L. Morenza, J. Estevea, M. Varela, A. Figueras, , and J.M. Tura. Indium thin films on metal-coated substrates. *Thin Solid Films*, 129:103–109, 1985.

[176] J.Y.W. Seto. The electrical properties of polycrystalline silicon films. *J. Appl. Phys.*, 46(12):5247–5254, 1975.

[177] H.S. Kwok, X.W. Sun, and D.H. Sim. Pulsed laser deposited crystalline ultra-thin indium tin oxide films and their conduction mechanisms. *Thin Solid Films*, 335(1):199–302, 1998.

[178] W-F. Wu and B-S. Chiou. Effect of oxygen concentration in the sputtering ambient on the microstructure, electrical and optical properties of radio-frequency magnetron-sputtered indium tin oxide lms. *Semicond. Sci. Technol.*, 11:196–202, 1996.

[179] M. Shiojiri, T. Miyano, and C. Kaito. Electron microscopic studies of structure and crystallization of amorphous metal oxide films. *Jap. J. Appl. Phys.*, 18(10):1937–1945, 1979.

[180] R.L. Petritz. Theory of semiconductivity in semiconductor films. *Phys. Rev.*, 104(6):1508–1516, 1956.

[181] J.M. Marshall. Carrier diffusion in amorphous semiconductors. *Rep. Prog. Phys.*, 46:1235–1282, 1983.

[182] G. Frank, H. Kostlin, and A. Rabeneau. X-ray and optical measurements in the In_2O_3-SnO_2 system. *Phys. stat. sol.*, 52:231–238, 1979.

[183] M. Tariq Bhatti, A. Manzoor Rana, and A. Faheem Khan. Characterization of rf-sputtered indium tin oxide thin lms. *Mater. Chem. Phys.*, 84:126–130, 2004.

[184] H. Morikawa and M. Fujita. Crystallization and electrical property change on the annealing of amorphous indium-oxide and indium-tin-oxide thin films. *Thin Solid Films*, 359:61–67, 2000.

[185] H. Gestlinger. The influence of chemisorption on the defect equilibrium of metal oxide thin films. *J. Appl. Phys.*, 80(3):1370–1380, 1996.

[186] U. Betz, M.K. Olsson, J. Marthy, M.F. Escola, and F. Atamny. Thin films engineering of indium tin oxide: Large area flat panel displays application. *Surf. Coat. Tech.*, 200:5751–5759, 2006.

[187] M.E. Cowher and T.O. Sedgwick. Chemical vapor deposited polycrystalline silicon [deposition process and hall mobility]. *J. Electrochem. Soc.*, 119(11):5247–5254, 1972.

[188] R.L. Weiher. Electrical properties of single crystals of indium oxide. *J. Appl. Phys*, 33(9):33–34, 1962.

[189] H. De Waal and F. Simonis. Tin oxide coatings: Physical properties and applications. *Thin Solid Films*, 77:253–258, 1981.

[190] J. Tauc, R. Grigorovici, and A. Vancu. Optical properties and electronic structure of amorphous germanium. *Phys. Stat. Sol.*, 15(2):627–637, 1966.

[191] V.I. Fistul and V.M. Vainshtein. Mechanism of electron scattering in In_2O_3 films. 8(11).

[192] P. Thilakan and J. Kumar. Investigations on the annealing effects on reactively deposited ITO thin films. *phys. stat. sol. (a)*, 160:97–104, 1997.

[193] L. Gupta, A. Mansingh, and P.K. Srivastava. Band gap narrowing and the band structure of tin-doped indium oxide films. *Thin Solid Films*, 176:33–34, 1989.

[194] I. Hamberg, C.G. Granqvist, K.-F. Berggren, B.E. Sernelius, and L. Engstrom. Band-gap widening in heavily Sn-doped In_2O_3. *Phys. Rev. B*, 30:3240–3249, 1984.

[195] S.A. Knickerbocker and A.K. Kulkarni. Estimation and verification of the optical properties of indium tin oxide based on the energy band diagram. *J. Vac. Sci. Technol. A*, 14:757–761, 1996.

[196] J.A. Woollam, W.A. McGahan, and B. Johs. Spectroscopic ellipsometry studies of indium tin oxide and other flat panel display multilayer materials. *Thin Solid Films*, 241(1-2):44–46, 1994.

[197] T. gerfin and M. Gratzel. Optical properties of tin-doped indium oxide determined by spectroscopic ellipsometry. *J. App. Phys.*, 79(3):1722–1729, 1995.

[198] A.G. Spencer, R.P. Howeson, and R.W. Lewis. Pressure stability in reactive magnetron sputtering. *Thin Solid Films*, 158:141–149, 1988.

[199] S. Major, A. Banerjee, and K.L. Chopra. Optical and electronic properties of zinc oxide films prepared by spray pyrolysis. *Thin Solid Films*, 125(1-2):179–185, 1985.

[200] I.W. Boyd. Thin film growth by pulsed laser deposition. *Ceramics international*, 22:429–434, 1996.

[201] G. P. Williams. X-ray data booklet - section 1.1 electron binding energies. Website, May 2010. `http://xdb.lbl.gov/Section1/Sec_1-1.html`.

[202] R. Kwok. Xpspeak 4.1. Website, June 2010. `http://www.uksaf.org/software.html`.

[203] S. Evans, R. Pritchard, and J.M. Thomas. Relative differential subshell photoionisation cross section (Mg K_α) from Lithium to Uranium. *J. Elec. Spec. Relat. Phenom.*, 14:341–358, 1978.

[204] C.G. Choi, K. No, W.-J. Lee, H.-G. Kim, S.O. Jung, W.J. Lee, W.S. Kim, S.J. Kim, and C. Yoon. Effects of oxygen partial pressure on the microstructure and electrical properties of indium tin oxide films prepared by d.c. magnetron sputtering. *Thin Solid Films*, 258:274–278, 1995.

[205] D. Dobrev. Ion-beam-induced texture formation in vacuum-condensed thin metal films. *Thin Solid Films*, 92(1-2):41–53, 1982.

[206] A. Dietrich, K. Schmalzbauer, and H. Hoffmann. The effect of annealing on the optical properties of indium tin oxide films. *Thin Solid Films*, 122(1):19–29, 1984.

[207] F. Zhu, K. Zhang C.H.A. Huan, and A.T.S. Weeb. Investigation of annealing effects on indium tin oxide thin films by electron energy loss spectroscopy. *Thin Solid Films*, 359:244–250, 2000.

[208] Y. Gassenbauer and A. Klein. Electronic and chemical properties of tin-doped indium oxide (ITO) surfaces and ITO/ZnPc interfaces studied in-situ by photoelectron spectroscopy. *J. Phys. Chem. B*, 110:4793–4801, 2006.

[209] A.K. Kulkarni, K.H. Schulz, T.-S. Lim, and M. Khan. Electrical, optical and structural characteristics of indium-tin-oxide thin films deposited on glass and polymer substrates. *Thin Solid Films*, 308-309:1–7, 1997.

[210] Y. Chen, Y. Zhou, Q.Zhang, M. Zhu, and F. Liu. The correlation between preferred orientation and performance of ITO thin films. *J. Mater. Sci-Mater. El.*, 18:411–414, 2007.

[211] P. Thilakan and J. Kumar. Studies on the preferred orientation changes and its influenced properties on ITO thin films. *Vacuum*, 48:464–466, 1997.

[212] J.C.C. Fan, F.J. Bachner, and G.H. Foley. Effect of O_2 pressure during deposition on properties of rf-sputtered Sn-doped In_2O_3 films. *Appl. Phys. Lett.*, 31:773–775, 1975.

[213] H. Enoki, J. Echigoya, and H. Suto. The intermediate compound in the In_2O_3 - SnO_2 system. *J. Mater. Sci*, 26(15):4110–4115, 1991.

[214] Q. X. Jia, J. P. Zheng, H.S. Kwok, and W.A. Anderson. Indium tin oxide on InP by pulsed laser deposition. *Thin Solid Films*, 258:260–263, 1995.

[215] F. Shinoki Y. Ohhata and S. Yoshida. Optical properties of r.f. reactive sputtered tin-doped In_2O_3 films. *Thin Solid Films*, 59:369–372, 1979.

[216] S. Kulaszewicz and I. Lasocka Cz. Michalski. Properties of transparent conducting films of SnO_2:Sb and In_2O_3:Sn deposited by hydrolisis. *Thin Solid Films*, 59:283–288, 1979.

[217] R.A. Synowicki. Spectroscopic ellipsometry characterization of indium tin oxide film microstructure and optical constants. *Thin Solid Films*, 313-314:394–397, 1998.

[218] U. Bangert and R. Barnes. Electron energy loss spectroscopy of defects in diamond. *phys. stat. sol. (a)*, 204(7):2201–2210, 2007.

[219] E.F. Egerton. Kramers-Kronig analysis FORTRAN program. Website, December 2009. `http://laser.phys.ualberta.ca/~egerton/programs/krakro.for`.

[220] M. Stoger-Pollach. Optical properties and bandgaps from low loss EELS: Pitfalls and solutions. *Microns*, 39:1092–1110, 2008.

[221] B. O'Regan and M. Gratzel. A low-cost, high-efficiency solar cell based on dye-sensitized colloidal TiO_2 films. *Nature*, 353(6346):737–740, 1991.

[222] H.J. Snaith and L. Schmidt-Mende. Advances in liquid-electrolyte and solid-state dye-sensitized solar cells. *Adv. Mater*, 19:3187–3200, 2007.

[223] Solaronix. Website, March 2010. `http://solaronix.com/`.

[224] Q. Wan, E.N. Datolli, W.Y. Fung, W. Guo, Y. Chen, X. Pan, and W. Lu. High-peformance transparent conduction oxide nanowires. *Nanoletters*, 6:2909–2915, 2006.

[225] R. Savu and E. Joanni. Low temperature, self-nucleated growth of indium-tin oxide nanostructures by pulsed laser deposition on amorphous substrates. *Scripta Mater.*, 55:979–981, 2006.

[226] T.N. Murakami and M. Gratzel. Counter electrodes for DSC: Application of functional materials as catalysts. *Inorganic Chimica Acta*, 361:572–580, 2008.

List of publications

- Microstructure-property relationships in thin film ITO, G. Giusti, L. Tian, I.P. Jones, J.S. Abell, J. Bowen, *Thin Solid Films*, 518:1140-1144, 2009.
- Dielectric properties modelling of ITO thin films by Electron Energy Loss Spectroscopy and Spectroscopic Ellipsometry, *in preparation*.
- Electro-optical properties of PLD deposited ITO thin films for dye-senstized solar cell applications, *in preparation*.